SANDIA REPORT
SAND2010-7052
Unlimited Release
Printed December 2010

Analysis of SNL/MSU/DOE Fatigue Database Trends for Wind Turbine Blade Materials

John F. Mandell, Daniel D. Samborsky, Pancasatya Agastra, Aaron T. Sears and Timothy J. Wilson
Department of Chemical and Biological Engineering
Montana State University, Bozeman, MT

Sandia Technical Managers: Thomas D. Ashwill and Daniel L. Laird

Prepared by
Sandia National Laboratories
Albuquerque, New Mexico 87185 and Livermore, California 94550

Sandia National Laboratories is a multi-program laboratory managed and operated by Sandia Corporation, a wholly owned subsidiary of Lockheed Martin Corporation, for the U.S. Department of Energy's National Nuclear Security Administration under Contract DE-AC04-94AL85000.

Issued by Sandia National Laboratories, operated for the United States Department of Energy by Sandia Corporation.

Available to DOE and DOE contractors from
U.S. Department of Energy
Office of Scientific and Technical Information
P.O. Box 62
Oak Ridge, TN 37831

Telephone: (865) 576-8401
Facsimile: (865) 576-5728
E-Mail: reports@adonis.osti.gov
Online ordering: http://www.osti.gov/bridge

Available to the public from
U.S. Department of Commerce
National Technical Information Service
5285 Port Royal Rd.
Springfield, VA 22161

Telephone: (800) 553-6847
Facsimile: (703) 605-6900
E-Mail: orders@ntis.fedworld.gov
Online order: http://www.ntis.gov/help/ordermethods.asp?loc=7-4-0#online

SAND2010-7052
Unlimited Release
Printed December 2010

Analysis of SNL/MSU/DOE Fatigue Database Trends for Wind Turbine Blade Materials

John F. Mandell, Daniel D. Samborsky, Pancasatya Agastra, Aaron T. Sears and Timothy J. Wilson
Department of Chemical and Biological Engineering
Montana State University, Bozeman, MT 59717

Thomas Ashwill and Daniel Laird, Sandia Technical Managers

Abstract

This report presents an analysis of trends in fatigue results from the Montana State University program on the fatigue of composite materials for wind turbine blades for the period 2005-2009. Test data can be found in the SNL/MSU/DOE Fatigue of Composite Materials Database which is updated annually. This is the fifth report in this series, which summarizes progress of the overall program since its inception in 1989. The primary thrust of this program has been research and testing of a broad range of structural laminate materials of interest to blade structures. The report is focused on current types of infused and prepreg blade materials, either processed in-house or by industry partners. Trends in static and fatigue performance are analyzed for a range of materials, geometries and loading conditions. Materials include: sixteen resins of three general types, five epoxy based paste adhesives, fifteen reinforcing fabrics including three fiber types, three prepregs, many laminate lay-ups and process variations. Significant differences in static and fatigue performance and delamination resistance are quantified for particular materials and process conditions.

When blades do fail, the likely cause is fatigue in the structural detail areas or at major flaws. The program is focused strongly on these issues in addition to standard laminates. Structural detail tests allow evaluation of various blade materials options in the context of more realistic representations of blade structure than do the standard test methods. Types of structural details addressed in this report include ply drops used in thickness tapering, and adhesive joints, each tested over a range of fatigue loading conditions. Ply drop studies were in two areas: (1) a combined experimental and finite element study of basic ply drop delamination parameters for glass and carbon prepreg laminates, and (2) the development of a complex structured resin-infused coupon including ply drops, for comparison studies of various resins, fabrics and pry drop thicknesses. Adhesive joint tests using typical blade adhesives included both generic testing of materials parameters using a notched-lap-shear test geometry developed in this study, and also a series of simulated blade web joint geometries fabricated by an industry partner.

Acknowledgements

The work presented in this report was carried out by Montana State University under Sandia National Laboratories purchase order 680272 and subcontract Z3609 between 2004 and 2009. In addition to the authors listed, significant contributions to the studies were made by Ole Kils (Clipper Wind) and Patrick Flaherty (undergraduate, MSU).

The Air Force Office of Scientific Research co-funded development of the complex structured laminate coupon. Industry materials suppliers and collaborators include: The Wind Technology Center/Delft University, Global Energy Concepts, G E Wind, Clipper Wind, TPI, Vectorply, Hexion, U-Pica, Dow, Ashland, Emerald Performance Plastics, Saertex, OCV, Zoltek, Toray, Newport Adhesives and Composites, PPG, 3M, EFI and Rhino. Their interest and participation are greatly appreciated.

Table of Contents

List of Figures

List of Tables

SECTION 1. EXECUTIVE SUMMARY

1.1 Overview

This report presents an analysis of results from the Montana State University program on the fatigue of composite materials for wind turbine blades for the period 2005-2009. Test data can be found in the SNL/MSU/DOE Fatigue of Composite Materials Database [1] which is updated annually. This is the fifth report in this series [2-8], which summarizes progress of the overall program since its inception in 1989. Many additional details are contained in various student theses and published papers cited in the report, copies of which are available either on the MSU program website, www.coe.montana.edu/composites/ or the Sandia website www.sandia.gov/wind/.

The program has benefitted from numerous ongoing interactions with turbine and blade manufacturers and materials suppliers cited in the Acknowledgements. Associated interactions under which significant test results were generated include: (1) the Wind Technology Center and Delft University under which the doctoral research by Rogier Nijssen [2] was carried out both at MSU and in The Netherlands, the latter under the European OPTIMAT Blades program; and (2) a cooperative testing effort with the Blade System Design Study [9] at Global Energy Concepts (now DNV Global Energy Concepts, Inc.).

The primary thrust of this program has been research and testing of a broad range of structural laminate materials of interest to blade structures. The report is focused on current types of infused and prepreg blade materials, either processed in-house or by industry partners. Trends in static and fatigue performance are analyzed for a range of materials, geometries and loading conditions. Materials include: sixteen resins of three general types, five epoxy based paste adhesives, fifteen reinforcing fabrics including three fiber types, three prepregs, many laminate lay-ups and process variations. Significant differences in static and fatigue performance and delamination resistance are quantified for particular materials and process conditions.

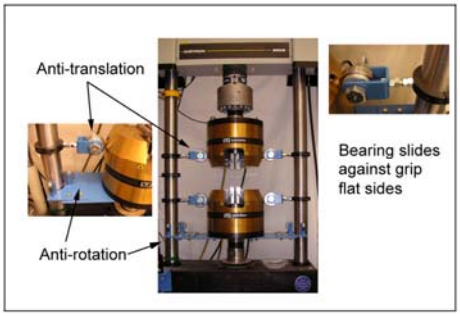

Testing Equipment

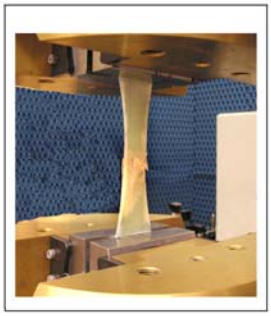

Standard Tests

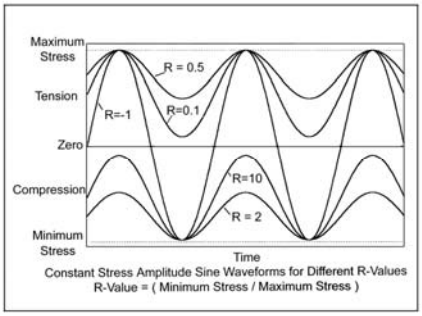

Waveforms, R-values

When blades do fail, the likely cause is fatigue in the structural detail areas or at major flaws, as distinct from undisturbed laminate areas. The program is focused strongly on these issues in addition to standard laminate characterization. Structural detail tests allow evaluation of various blade materials options in the context of more realistic representations of blade structure than do

the standard test methods. Structural details addressed in this report include ply drops used in thickness tapering as well as adhesive joints, each tested over a range of fatigue loading conditions. Ply drop studies were in two areas: (1) a combined experimental and finite element study of basic ply drop delamination parameters for glass and carbon prepreg laminates, and (2) the development of a complex structured resin-infused coupon including ply drops, for comparison studies of various resins, fabrics and ply drop thicknesses. Adhesive joint tests using typical blade adhesives included both generic testing of materials parameters using a notched-lap-shear test geometry developed in this study, and also a series of simulated blade web joint geometries fabricated by an industry partner.

Relative to more elaborate full scale blade or substructure testing, the structural detail test methods are designed to allow for efficient evaluation of materials and geometric design parameters under varied fatigue loading conditions. The test coupons are easily fabricated and tested in conventional fatigue testing equipment.

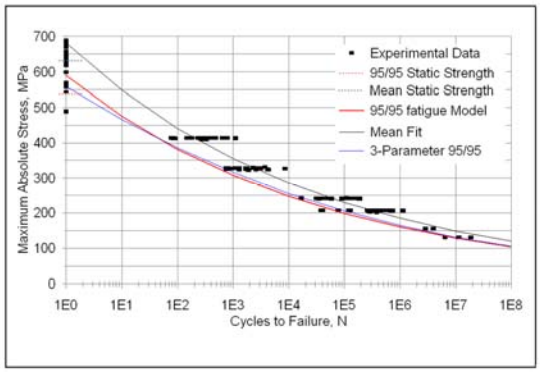

Typical Data Fits (Fig. 33)

MATERIAL QQ1

Lay-up = [±45/0$_6$/±45], V_f = 0.52, Ave. thickness = 4.088 mm, S.D. = 0.132 mm (range = 3.937 - 4.242 mm (50% - 54% V_f)), Vantico TDT 177-155 Epoxy Resin, Saertex U14EU920-00940-T1300-100000 0's (0°-864g/m^2, 90°-79 g/m^2, stitching 12 g/m^2), VU-90079-00830-01270-000000 45's (800 g/m^2)

TEST & SAMPLE ID #		STRESS Max./Min. MPa	R	Q Hz	E GPa	e %	CYCLES TO FAIL	WIDTH (mm) and Notes
9281	QQ1-100	855	*	13	34.6	2.47	1	25
9284	QQ1-105	448/45	0.1	2	34.7	1.33	1109	25
9288	QQ1-106	241/24	0.1	4	34.5	0.72	34816	25
9290	QQ1-112	172/17	0.1	5	32.3	0.53	329999	25
9294	QQ1-110	138/14	0.1	8	33.6	0.4	2471561	25
9295	QQ1-123	138/14	0.1	10	33.6	0.41	3580200	25
9296	QQ1-117	138/14	0.1	8	33.6	0.41	4657452	25

SNL/MSU/DOE Data Base Sample

1.2 Typical Blade Laminates

The historical focus of this program has been to characterize, compare, and analyze a broad range of structural laminate materials of interest to blade manufacturers. Early years of the program explored the fatigue properties of low fiber content laminates typical of hand lay-up blades over a range of materials parameters, loading conditions and environments [4, 7]. This work has been extended in recent years to resin infusion and prepreg materials of current interest. This report compares the performance of glass, carbon and WindStrand fibers, many different polyester, vinyl ester and epoxy resins, a range of reinforcing fabric architectures, process details, and the full range of (uniaxial) loading conditions experienced by blades. Laminates were either fabricated at MSU or by industry partners, the latter providing the closest approximation to actual blade processing.

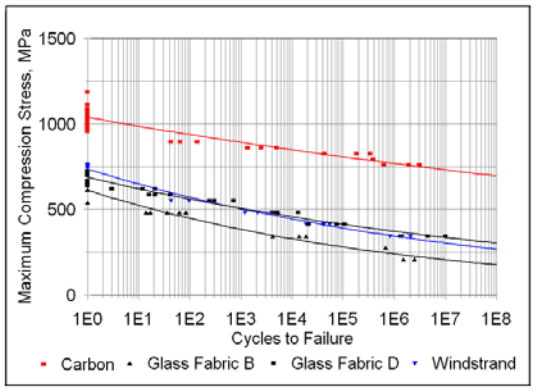

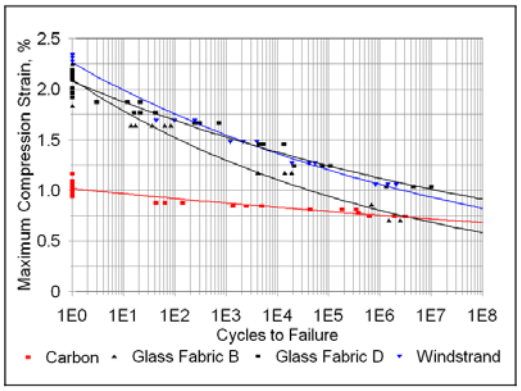

Effects of Fiber and Fabric Type, Stress and Strain Comparison, Tensile Fatigue (Fig. 41)

The most notable materials trends are briefly summarized in this section. In terms of fiber types, carbon fibers provide the greatest stiffness and fatigue resistance under all loading conditions for fiber dominated laminates (laminates containing a significant portion of the plies in the main load (0^o) direction), as demonstrated in comparisons of constant life diagrams (CLD's) with glass laminates. While the compression properties of carbon can be limiting, particularly with fiber waviness, new infusion fabrics provide compression properties equal to those of well aligned prepreg. Lower cost, infused glass fabrics and prepreg are slightly more fatigue sensitive than carbon in compression (with greater strain capability), but are much more fatigue sensitive under loading cycles with a significant tensile component. WindStrand fibers produce improved stiffness compared with lower cost glass, with fatigue resistance similar to the best of the glass laminates.

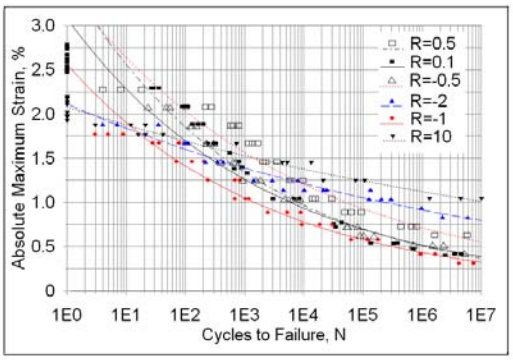

Different R-values, Glass Fabric B/epoxy (Fig. 54)

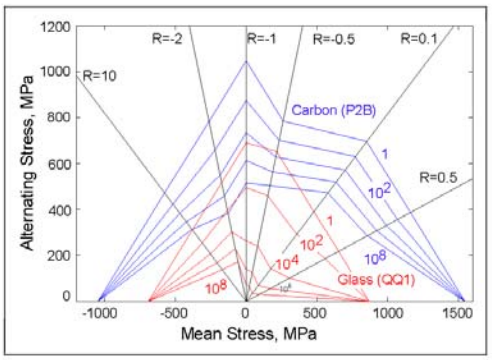

Stress Based Constant Life Diagram, Carbon vs. Glass (Fig. 63)

Particular commercial glass fabrics have now been identified which provide improved tensile fatigue resistance at typical infusion fiber contents for multidirectional laminates, but some process sensitivity has become evident in recent testing. Epoxies tend to provide the best fatigue resistance, lower cost polyesters the poorest. Effects are similar, but less pronounced, for various types of biax (±45) fabric laminates; these fabrics show significant effects of construction, such as the presence of mat. In laminates which contain both biax and unidirectional plies, failure of the laminate occurs after significant resin cracking in the biax plies; the best unidirectional

fabrics survive for one to two decades of cycles after severe resin cracking develops in the biax plies.

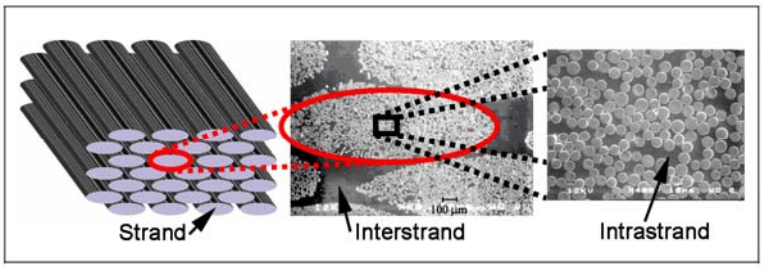

Fabric Structure (Fig. 1)

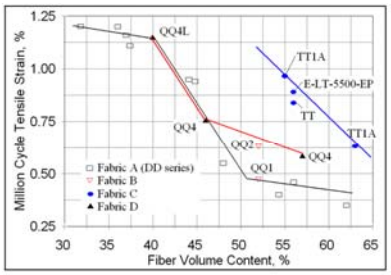

Effect of Fabric Structure (Fig. 48)

1.3 Delamination

Composite structures frequently fail, not by fiber failure, but by the delamination of the reinforcing plies. Delamination between plies is an issue in areas of the structure with significant third-dimension stress components, as at ply drops, shape changes and other structural detail areas. The initiation and growth of cracks which separate plies of a composite structure are best treated by fracture mechanics concepts. The resistance to delamination is characterized through experimental opening mode I and shearing mode II tests which allow determination of the critical strain energy release rates G_{Ic} and G_{IIc}. Mixed Mode I and II testing has also been carried out, since typical delamination crack fronts are mixed mode.

Delamination resistance is a resin-dominated property which correlates with the toughness of the neat resin. Findings in this report are consistent with earlier observations that G_{Ic} and G_{IIc} are consistently higher for typical epoxy resins than for polyester resins, with vinyl esters intermediate between the two. Mixed mode results show the same trend with resin type. Toughened versions of resins show greater delamination resistance than do the base resins.

Many applications, including wind blades, do not design their products with the complex and limited technology of fracture mechanics. A more useful approach for wind blades is to test materials of interest in geometries where delamination is important, as at ply drops, but to represent the performance in terms of strain levels and fatigue cycles to produce significant damage, which can be incorporated into traditional blade design. Detailed analysis of these methods is also carried out to identify the important more basic failure mode and property dependence.

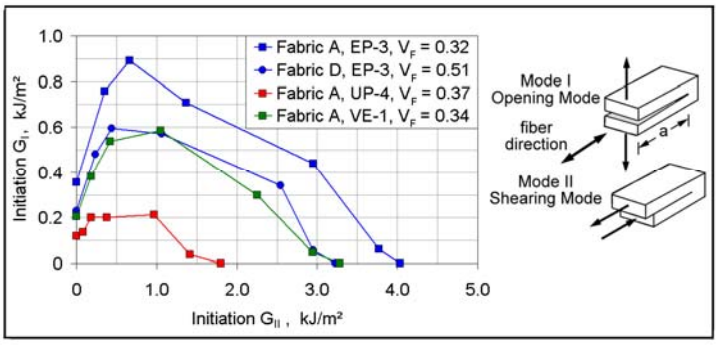

Delamination Resistance, Three Resins (Fig. 68)

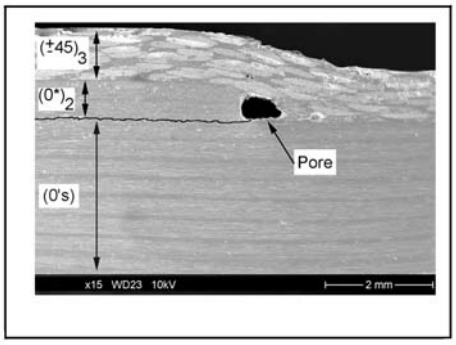

Delamination at Ply Drop Pore (Fig. 80)

1.4 Delamination at Ply Drops

This study explored the basic geometric and materials parameters involved with ply drops for large tow carbon and glass prepreg materials, all with the same epoxy resin system. Detailed finite element analysis of a broad range of geometries for ply drops, ply joints, and material transitions was carried out in association with the experimental study.

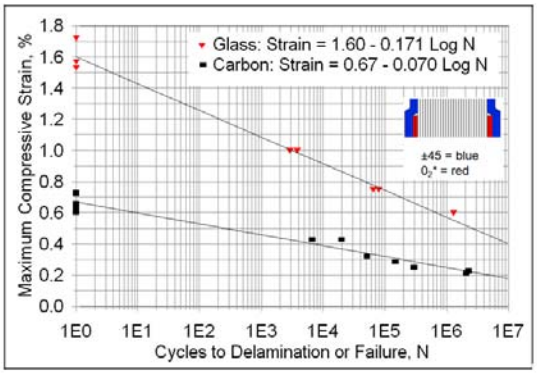

Delamination Strain,
Glass vs. Carbon (Fig. 79)

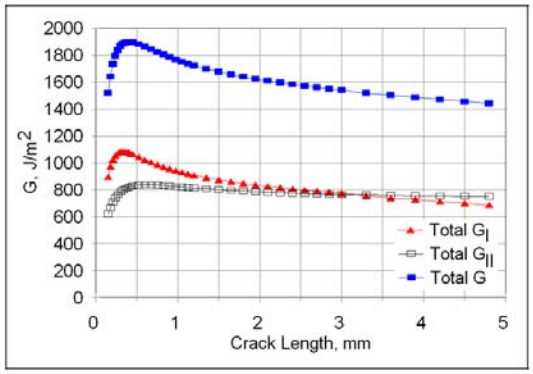

FEA Predicted Internal Ply Drop Fracture Parameters vs. Delamination Length (Fig. 83)

The results indicate that ply drops can lead to ply delamination at relatively low applied strains under fatigue loading. Findings were similar for various loading conditions including tension, compression and reversed loading and, in compression, for relatively thin and thick laminates. Ply drops involving ply thicknesses of about 0.3 mm had adequate fatigue resistance with carbon fibers, while ply thicknesses of 0.6 mm and greater delaminated at maximum strains of 0.3% and below at one million cycles. By contrast, glass laminates using the same resin and prepreg manufacturing delaminated at strains about three times higher than for carbon; in terms of stresses, slightly higher stresses were required to delaminate the carbon compared with glass.

The experimental results can be understood through both approximate strength of materials estimates and detailed FEA, which identifies the mode I and mode II strain energy release rates for various geometries. The difference in performance between glass and carbon fibers is related directly to the differences in elastic constants.

1.5 Complex Structured Coupon with Ply Drops

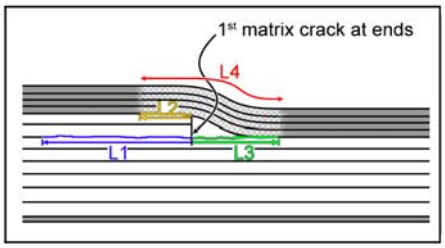

(Fig. 85)

The concept in this study was to develop a complex structured coupon test for infused laminates, representative of thickness tapered blade structure with ply drops. The resulting test method was then run to compare the performance of different resin types and ply drop thicknesses, under tension, compression and reversed loading, in terms of both damage growth characteristics and strain knockdowns.

The complex coupon provides a basis for comparing infusion blade material and lay-up parameters for a case which is more representative of real blade structure than are plain laminate tests. The sequence of damage initiation and growth depends on both in-plane properties of the fabric layers and interlaminar properties, the latter dominated by the resin. The test coupon geometry, designed by FEA, shows minimal effects of non-symmetry, which allows for increased thickness coupons more representative of blades. Results from the static and fatigue tests again indicate improved performance epoxy relative to vinyl ester or polyester; a toughened vinyl ester performed on a par with epoxy. Test results for various resins with the complex coupon are consistent with delamination data for mode I and mode II tests.

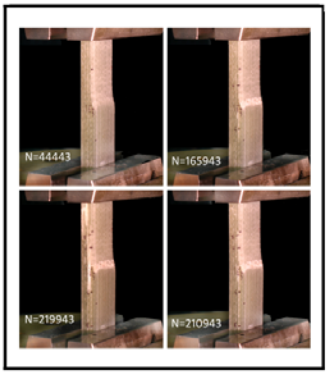

Complex Coupon Damage Sequence (Fig. 84)

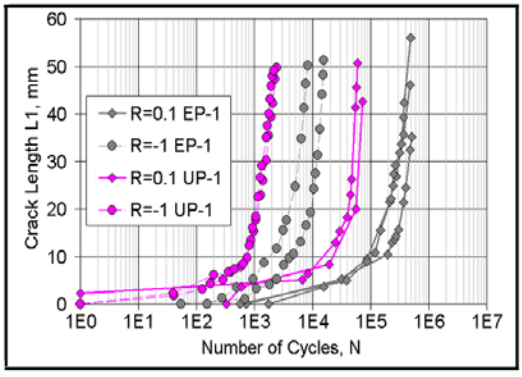

Epoxy (EP) vs. Polyester (UP), Tension and Reversed Loading, R = 0.1 and -1 (Fig. 94)

In terms of loading and geometry, significantly higher strain knockdowns are found for greater thicknesses (up to 5 mm) of dropped material. The results also show much increased fatigue sensitivity under reversed fatigue loading compared with either tensile or compressive loading alone, for both epoxy and polyester resins. In terms of fabrics, test data show sensitivity to the biax surfacing fabrics of different constructions.

1.6 Adhesive Joints

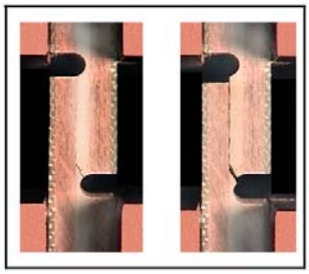

Notched Lap Shear Test (Fig. 28)

Adhesive joint failure in blades has been a persistent industry problem. While inspection methods are most critical with severe problems like adhesive gaps, there has also been a lack of test data relevant to typical quality joints, in terms of high viscosity paste adhesives, laminates and peel ply surfaces, adhesive thickness, and appropriate fatigue loading conditions like reversed loading. A notched lap shear test method has been adapted from standard tests under this program, for generic studies of the various adhesive joint parameters, and a second study with simulated blade joint geometries has been carried out with an industry partner. Extensive static and fatigue test data and finite element results including flaw modeling are reported for both test series.

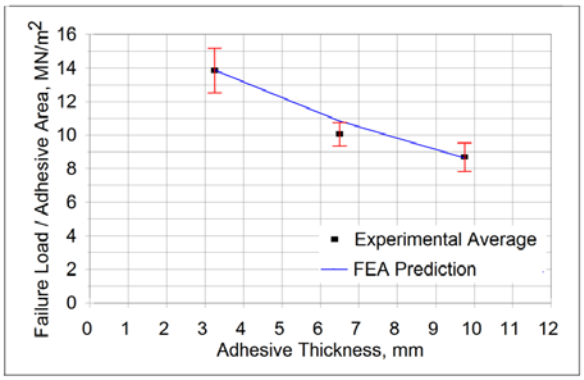

Adhesive Thickness Effect (Fig. 107)

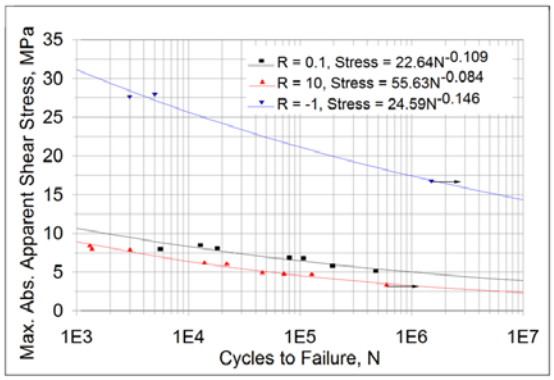

Lap Joint Fatigue, R = 0.1, -1, 10 (Fig. 101)

The notched lap shear joint test method produced consistent results for several high viscosity, thick paste adhesives for a range of adhesive thicknesses (3 mm-9 mm), overlap lengths (12.7 and 25.4 mm), laminate adherends, laminate peel plies and loading conditions (tension, compression and reversed loading). Failure initiated under tension and reversed loading as a crack in the notch root area, at a stress concentration in the adhesive, then propagated along the interface, either inside the laminate surface or on the peel ply interface. Compressive failures appeared to initiate at the interface in an area of local tensile stress, then propagate diagonally across the adhesive and along the interfaces. Linear and nonlinear finite element predictions correlated with the various results for geometric effects, using measured neat adhesive stress-strain data. The first known fatigue data for various R-values are given for a common blade adhesive under tension, reversed, and compression fatigue loading.

Simulated blade joint tests involved testing of baseline and reinforced web joint geometries fabricated by an industry partner. Included in the series of over 250 tests were four geometries, two static loading rates, and two fatigue loading conditions. The test geometries are representative of typical blade web joints using a relatively brittle, thick paste adhesive. Various flaws and failure modes have been identified, and some have been explored with finite element modeling. The joint strength and fatigue statistics were significantly affected by several types of flaws, including poor adhesive mixing, pores, poor surface preparation and porosity in the laminate surface. The reinforced geometries were significantly stronger but slightly more fatigue sensitive, but still retaining significantly greater fatigue strength at high cycles.

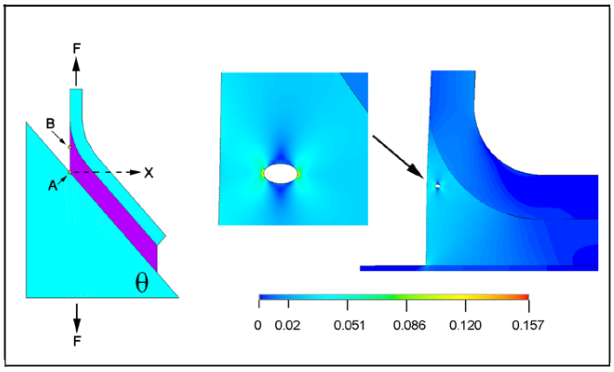

Simulated Blade Web Joint FEA, Pore Effects (Figs. 29 and 125)

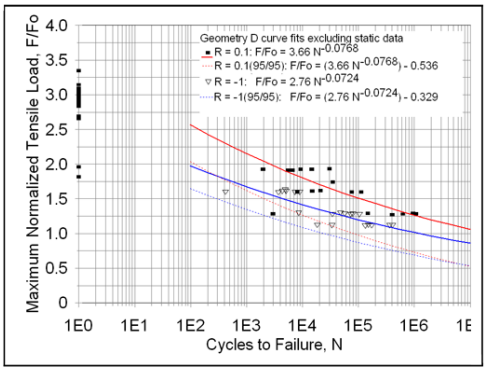

Fatigue Data for Simulated Web Joint (Fig. 117)

1.7 Spar Split Tests

Blade spars are thick, predominantly unidirectional laminate which could be prone to splitting parallel to the fibers due to relatively small off-axis loads. Off-axis plies, either distributed through the thickness or bonded to the surfaces, can resist splitting. A series of static fracture mechanics-type tests have been conducted to explore these parameters for prepreg and VARTM processed carbon and glass fiber laminates. The results show that small amounts of off-axis plies are effective in increasing split resistance under static loads. Little sensitivity was found to the way the off-axis material was distributed through the thickness.

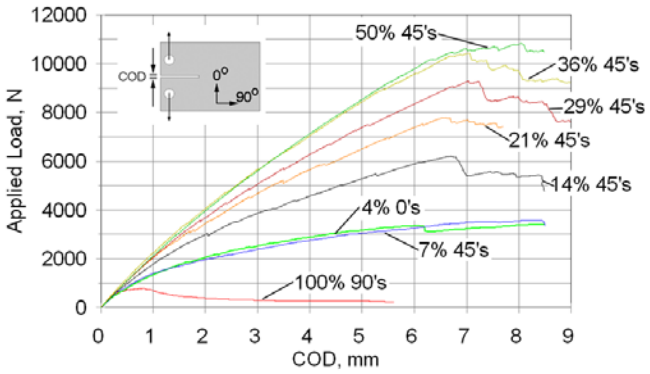

Effect of Off-Axis Plies on Splitting of Spar Cap Laminate (Fig. 129)

SECTION 2. INTRODUCTION AND BACKGROUND

2.1 Introduction

This report presents results from the Montana State University program on the fatigue of composite materials for wind turbine blades for the period 2005-2009. Test data can be found in the DOE/MSU Fatigue of Composite Materials Database [1] which is updated annually in March. This is the eighth report in this series [2-7], which summarizes progress of the overall program since its inception in 1989. References 4, 5 and 6 provide the broadest overview of the program prior to this report. Many additional details are contained in various student theses and published papers cited in the report, copies of which are available either on the MSU program website, www.coe.montana.edu/composites/ or the Sandia website www.sandia.gov/wind/.

Of special note for this time period is the cooperative effort with the Wind Technology Center and Delft University under which the doctoral research by Rogier Nijssen [2] in the area of spectrum loading and residual strength effects was carried out both at MSU and in The Netherlands, the latter under the European OPTIMAT Blades program. A second cooperative effort under which some of the results contained in this report were generated is the Blade System Design Study [3] at Global Energy Concepts (now DNV Global Energy Concepts, Inc.). The program has also benefitted from numerous recent interactions with turbine and blade manufacturers and materials suppliers.

The report contains a broad range of static and fatigue data obtained from standard test methods for laminate materials of current or potential interest in wind turbine blades, as well as new test methods representing more complex blade structural details. Included in the latter category is an improved coupon for quantitative comparison of different infusion resin systems and fabrics in the context of realistic laminate structure with ply drops for thickness tapering. A second category of structural detail tests is adhesive joints with thick adhesive layers, including generic notched lap shear and simulated blade joint geometries. Trends in static and fatigue performance are analyzed for a range of parameters including: many different fibers, resins and adhesives, fabric architecture, laminate lay-up, process variations, loading conditions, constant life diagrams, ply drop thickness and spar cap splitting.

2.2 Background

2.2.1 Overview

Wind turbine blades are designed to several major structural conditions, including tip deflection, strength and buckling during severe loading, as well as very high numbers of fatigue cycles during operation, varying between tension, compression and reversed tension-compression loads according to the particular loads spectrum for the turbine and wind conditions. The major static strength and stiffness properties depend primarily on fiber type, content, and orientation, following composite mechanics predictions widely available in the literature. The fatigue of composite laminates appropriate for wind turbine blades has been the topic of research studies for more than two decades; a general review of this area can be found in Reference [2]. The findings of these studies are summarized in recent reports [2-7], and in two

current public databases [1, 10]. Recent publications [11-15] are summarized here, with additional new data in several areas. The databases provide adequate constant amplitude fatigue data for the range of loading conditions necessary to compare materials, define constant life diagrams and predict failure under spectrum loading [2, 16]. The latter requires testing for at least five or six load conditions, as described in detail in References 2 and 16. Precise laminate configurations for particular blades may not be included in the databases, but, in the absence of data for particular laminates, the fatigue trends may be assumed to apply in terms of strains.

Structural details such as ply drops used in thickness tapering, and special features such as sandwich panel close-outs and joints require separate attention. The fatigue response of structural details is typically dominated by crack initiation and growth in the matrix or adhesive [5, 17]. Recent studies have focused on those materials issues which appear most likely to produce damage and failure for otherwise well designed and constructed blades [12, 17, 18]:

1. tensile fatigue loading of glass fiber laminates,
2. compression static and fatigue loading of carbon fiber laminates,
3. ply delamination under a range of fatigue loading conditions,
4. combined in-plane and interlaminar response for complex blade structure,
5. matrix cracking and transverse direction failure, and
6. adhesive joint failure.

The major sections describe the sensitivity to these issues of a range laminates of current interest in blades, in terms of fiber and matrix differences, fiber content and laminate construction, infused fabric architecture, processing, loading conditions, ply drop geometry and complex structure interactions, and adhesive joint characteristics. Introduction and background discussion is provided for each area in the remainder of this section.

2.2.2 Typical blade laminates

Data for blade laminates of current interest can be found in two public databases: the Sandia/MSU/DOE Database (1989-present) [1] and the European OptiDAT Database (2006) [10]. The Sandia/MSU/DOE database contains results for earlier materials as well as materials of current and, potentially, future interest (such as carbon and WindStrand fibers). The OptiDAT database contains data for an E-glass/epoxy material of current interest, in several constructions. Another source of significant, currently relevant data is Reference [3]. An extensive review of the composite laminate fatigue area is available in Reference 2; only a review of fabric effects will be included in this section.

The fatigue behavior of laminates based on a broad range of fabrics often used in hand lay-up processes has been reported earlier [5, 6]. Detailed analysis was presented for the effects of fiber content, fabric architecture, resin, and laminate construction parameters such as fiber orientation and fraction of plies in the axial (load) direction. This section provides a brief overview of these results as they apply to studies of current glass fabrics used in resin infusion. The resins used in most of the earlier studies were polyesters, but comparisons with vinyl esters and epoxies showed little effect on tensile fatigue [5].

Figure 1 is a diagram and micrographs representing a unidirectional laminate containing D155 weft unidirectional stitched fabric (stitching not shown). The inter-strand areas are mostly free of fibers, allowing for rapid resin wet-out. The intra-strand areas contain closely packed fibers with a continuous resin phase. At one extreme are fabrics with relatively large inter-strand channels, such as the D155 fabric. At the other extreme are laminates with no significant inter-strand areas, such as prepreg with uniformly dispersed fibers, which would appear entirely like the intra-strand micrograph. Current unidirectional infusion fabrics as shown in Figure 2(a) (fabrics and laminates defined in Section 3.1.1), tend to have large rectangular shaped strands which pack closely together, as well as small amounts of transverse strands or mat to which the main uni-strands are stitched [12, 15]; fiber contents can then approach typical prepreg values of 50-60% by volume, producing high stiffness and strength. Figure 2(b) shows typical strand nesting and fiber content variations ply-by-ply in thicker laminates. Fabrics having fibers oriented in other directions, such as biax at ±45°, can also be stitched to the (0°) uni-strands to produce typical triaxial fabrics. As noted in Table 1, the actual in-situ ply thickness and fiber content vary depending on position through the thickness and fabric details. Biax plies, especially with mat, tend to hold more resin than do the densely packed uni-fabric plies, resulting in lower fiber contents for these plies. (V_f is the fiber volume fraction or %.)

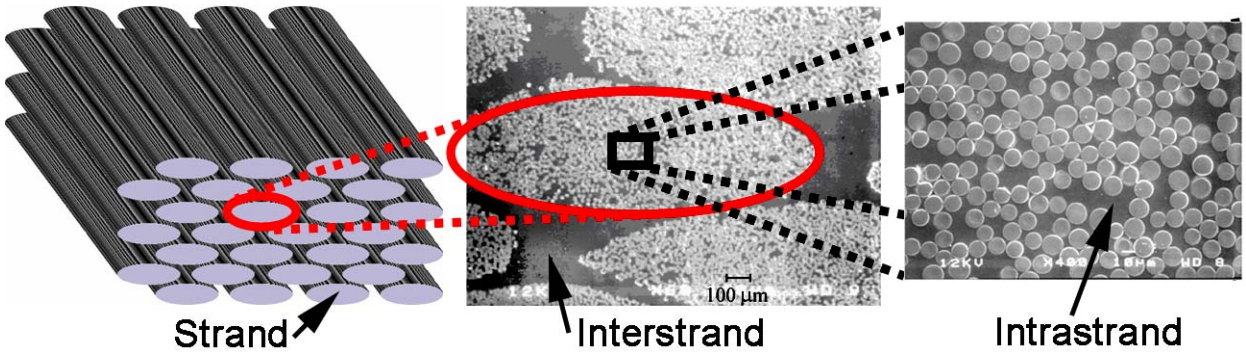

Figure 1. Exploded view of Fabric A composite showing inter-strand channels and intra-strand structure [15].

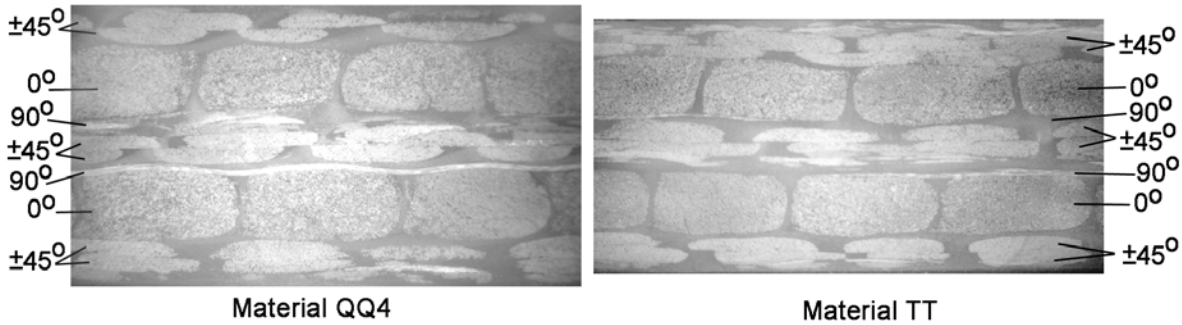

Figure 2(a). VARTM processed laminates QQ4 (fabric C), and TT (fabric D) [15].

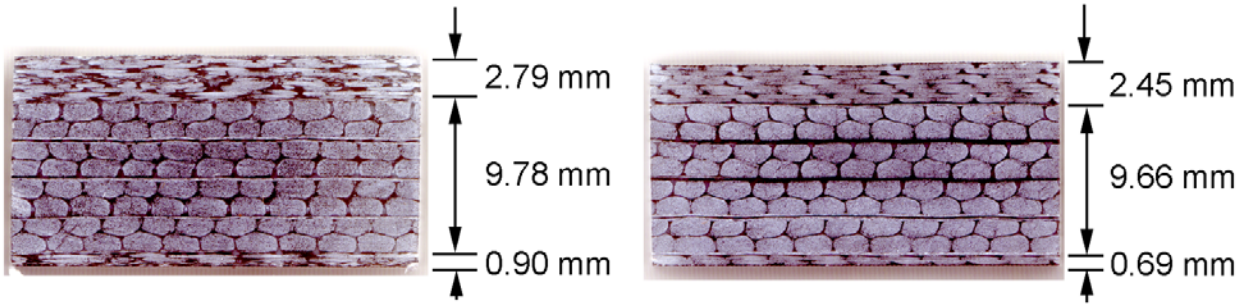

Figure 2(b). Infusion processed complex coupon (Section 3.1.3), thick side, showing in-situ ply thicknesses and fiber contents and strand nesting and distortion, fabrics D (0^o) and M ($\pm 45^o$) (left) or L ($\pm 45^o$) (right).

Figure 2. Comparison of cross-section views of laminates.

Table 1. Typical breakdown of in-situ ply thicknesses and fiber contents for laminates in Figure 2(b); comparison for different biax fabrics, L and M, both with uni-fabric D (Table 2(b).

Type of Fabric	Number of Layers	Calculated Thickness (mm)	Thickness per Layer (mm/ply)	V_F
Fabric M	4	2.79	0.70	48%
Fabric D	8	9.78	1.22	61%
Fabric M	1	0.90	0.90	37%
TOTAL	---	13.48*	---	57%***

Type of Fabric	Number of Layers	Calculated Thickness (mm)	Thickness per Layer (mm/ply)	V_F
Fabric L*	4	2.45	0.61	54%
Fabric D	8	9.66	1.21	62%
Fabric L*	1	0.69	0.69	47%
TOTAL	---	12.79**	---	59%***

* Ply thickness is calculated from photographs, Figure 2(b).
**The total thickness measured.
***This is the calculated average fiber volume content for the laminate based on the areal weight of fabric and the glass density.

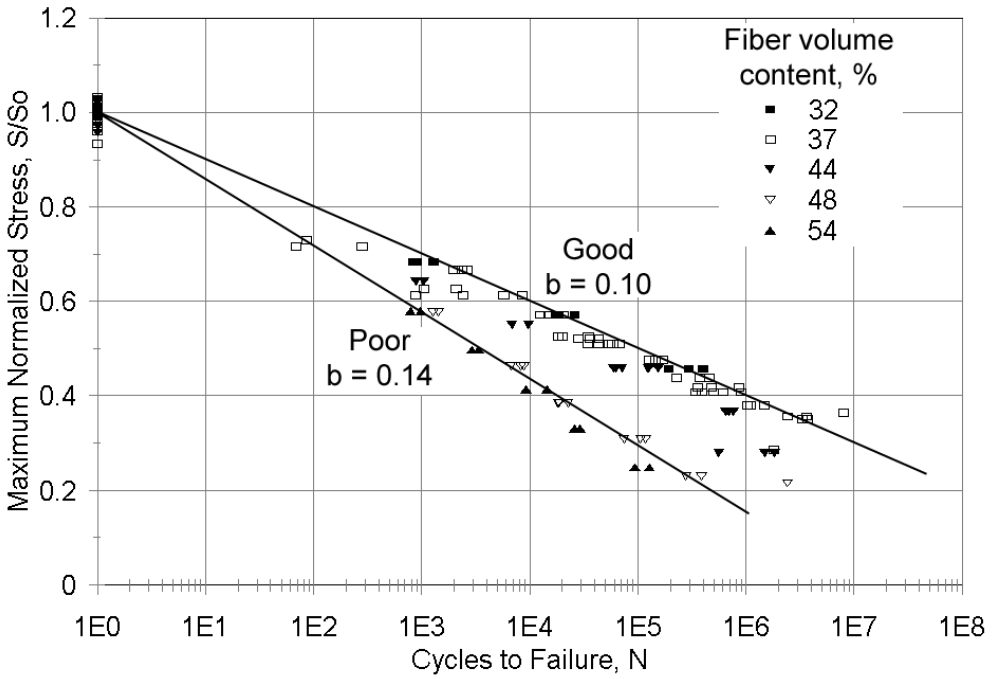

Figure 3. Normalized stress vs. log cycles to failure for DD-series E-glass/polyester laminates at various fiber contents, configuration $[0/\pm45/0]_s$, R = 0.1 [2].

The D155 fabric (A) was used in a variety of earlier studies as a baseline material, and compared with a broad range of stitched and woven fabrics from various manufacturers [5, 6]. The results which follow are typical for fabrics with significant inter-strand channels, whether stitched or woven. Laminates in the DD series in the DOE/MSU Database [1] contain D155 0^o fabric and DB120 biax $\pm45^0$ fabric with a polyester resin. The fiber content was varied by controlling the spacing between the two-sided hard molds during RTM. Resin flow was primarily in-plane. Figure 3 gives typical S-N (maximum stress vs. log cycles) fatigue data for laminates with different fiber contents. The mean lifetime trend was fit with an exponential model

$$S/S_o = 1.0 - b \log N \tag{1}$$

where S is the maximum tensile stress, S_o the ultimate tensile strength at the fatigue load rate, N the cycles to fail (complete separation) and b is the slope of the normalized S-N curve. Tests were run at various maximum stress values with a constant R-value of 0.1, a typical tensile fatigue loading condition, where

$$R = \text{minimum load/maximum load} \tag{2}$$

The results from Figure 3 and similar laminates are plotted in Figures 4 and 5 as the slope of the S-N curves, b, and the maximum strain which can be sustained for a million cycles, respectively. These are both useful parameters to represent the fatigue resistance. As the fiber content increases above about 40% by volume, the S-N curves become significantly steeper and the million cycle strain decreases sharply. By both measures, the laminates become less fatigue

resistant at higher fiber contents. This fatigue response is in contrast to the steadily increasing static strength, S_o (Fig. 3), and elastic modulus with increasing fiber content [6]. The typical triax fabric laminate shown in Figure 4 (based on CDB 200 fabric [5, 6]) has poor fatigue resistance over the entire fiber content range, and fails along the stitch lines, where the local fiber content is high [5, 6]. Laminates with low fiber content and associated good fatigue resistance shifted to poor resistance when flaws like ply drops were added, which caused local strand compaction and distortion [5].

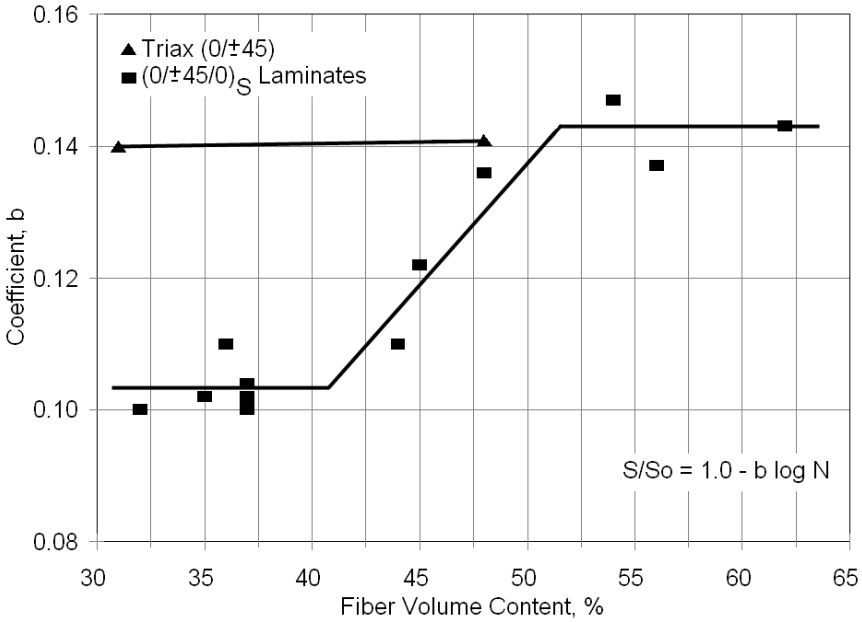

Figure 4. Fatigue coefficient, b, from Eq. (1) vs. fiber volume content for DD-series laminates, R = 0.1 [4].

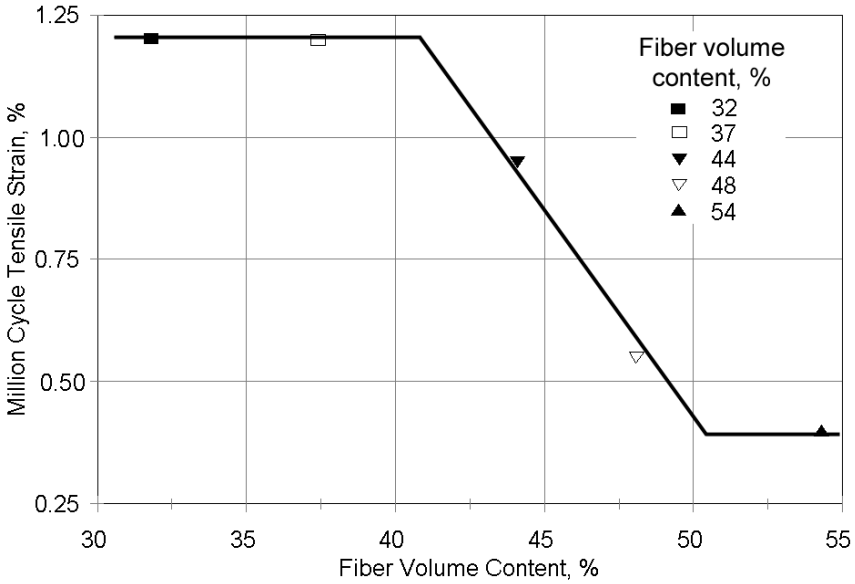

Figure 5. Million cycle tensile strain vs. fiber volume content for DD-series laminates, R = 0.1 [4].

The transition to poorer fatigue resistance at higher fiber contents has been associated with distortion and compaction of the strands as the fabric is squeezed at higher mold pressures. This produces very high local fiber contents within the strands, especially at stitch points, resulting in more fiber contacts, shown in Figure 6 [5]. Mold pressure, strand distortion and fiber content are considered in detail later. When the fabric structure is compact, as in Figure 2(a), the natural fiber content at low mold pressure is much higher. Little strand compaction and distortion are present for compact fabrics in the typical blade infusion range of 50-60% by volume (see Figure 49).

In essence, a fabric like the D155 in Figure 1 has a typical fiber content at low mold pressures as in vacuum bag molding. While compaction to higher fiber contents can be achieved by increasing the mold pressure, this compresses the strands into the inter-strand (channel) areas, and results in poor fatigue performance for glass fibers. To achieve the higher properties associated with higher fiber contents while maintaining good fatigue resistance, the fabric architecture must be changed to reduce the inter-strand areas. A reduction in inter-strand channels has the negative effect of decreasing fabric permeability and ease of wet-out.

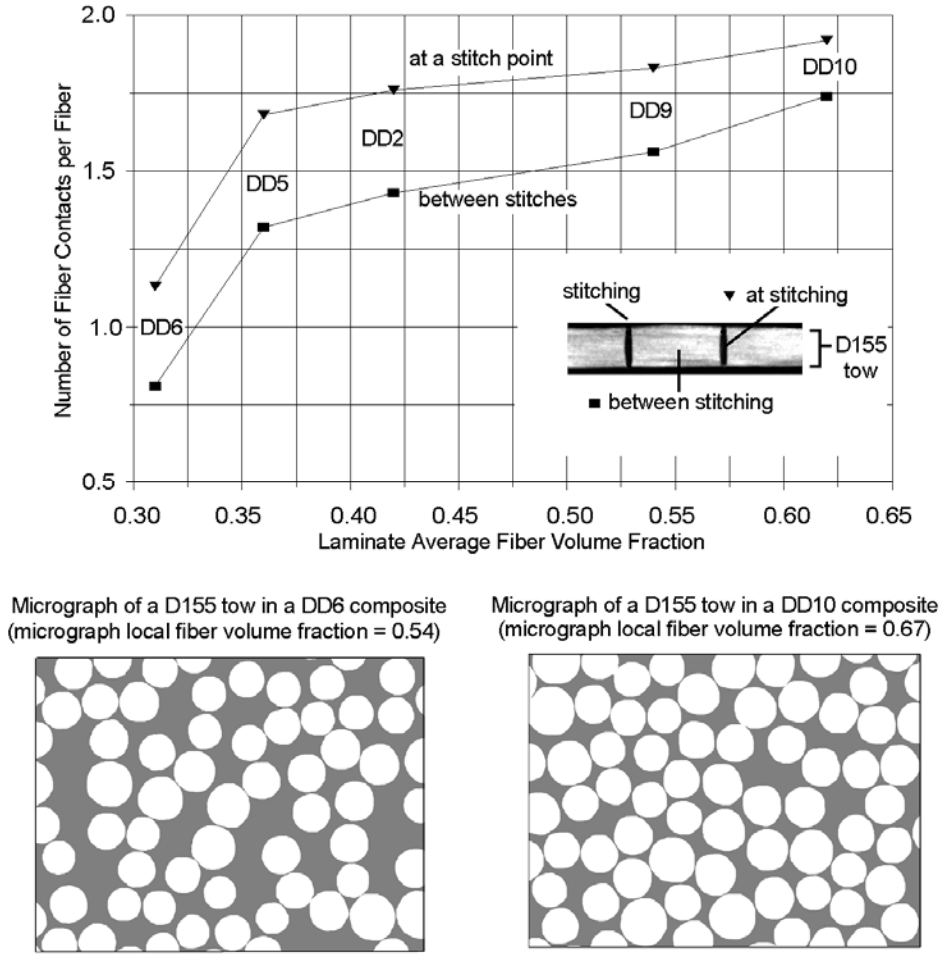

Figure 6. Number of contacts per fiber from neighboring fibers along stitch line and between stitch lines vs. average laminate fiber volume fraction, also showing micrographs (bottom) for intra-strand fiber packing, selected DD-series laminates.

2.2.3 Delamination at ply drops

The primary structural elements in most wind turbine blades are spars with tapering thickness along their length. Thickness tapering in laminated composites is accomplished by a series of terminations of individual plies or groups of plies, called ply drops. When loads are applied to a blade, these ply drops cause stress concentrations in adjoining plies and can also serve as an initiation site for the separation, or delamination, of the plies. Ply delamination, if widespread, can cause a general loss in structural integrity of the blade. Delamination and ply drops have received extensive attention in the general composites literature [19-23] and, to a lesser extent, in wind turbine blade technology [24, 25]. Methodologies for predicting delamination under static and fatigue loading using finite elements have been demonstrated [22, 24]. Recent attention has been given to this problem in the aerospace community in the area of tapered flex beams for helicopter rotors [26, 27].

The ply drop problem is of particular concern for wind turbine blades using carbon fibers for three reasons: first, the more directional elastic constants of carbon fiber laminates often increase the tendency to delaminate relative to glass; second, to reduce cost, the plies are often thicker in composites for wind turbine blades relative to aerospace applications; and third, the ultimate and fatigue strains in compression for lower cost forms of carbon fiber laminates are lower than for glass, [28, 29], and may be design drivers in some cases.

This study has concentrated on exploring the strain levels for delamination and/or gross failure with several variations, including carbon vs. glass fibers, ply drop location through the thickness, number of plies dropped at one location (simulating changes in ply thickness), laminate thickness, and loading conditions (tension, compression and reversed loading.) While fracture mechanics based methodology is available to predict delamination growth under defined conditions [22, 24], the most useful data for material selection and design of wind turbine blades is in the form of stress and strain levels to produce significant delamination, which doesn't require complex analysis.

2.2.4 Complex structured coupon

Blade structural details are complex and often involve major transitions in materials (joints and cores) and thickness (ply drops). Standard laminate coupon tests do not adequately address blade structure issues of thicker material transitions and laminates, interactions of delamination growth with damage in adjacent plies such as surface $\pm 45^{o}$ skins, or materials parameters such as resin type. Delamination tests generally show a strong dependence on resin toughness, with epoxies more resistant than vinyl-esters, which are in turn more resistant than polyesters [5]; toughened versions of vinyl esters and epoxies are available, commonly at additional cost, and with some associated viscosity increase. Compared with prepreg, resin infusion structures involve many available options in resins, fabrics, process variations and local geometry. Testing of blades or substructural elements which include structural details is limited in the parameters which can be explored due to the required time and cost. This study involved the development of a relatively simple test coupon geometry which is inexpensive to fabricate and test, but represents the thickness tapering areas of blade spars which contain ply drops. Establishing a standard test coupon geometry allows comparisons of resins and other materials parameters, where the

performance of unidirectional plies, biax plies and delamination between plies can all play a role, similar to larger substructure tests. This is the first known approach of this type, which allows a more quantitative approach to materials selection in the context of complex composite structure.

2.2.5 Adhesive joints

Adhesive bonding has become an issue of increasing importance as wind blade size has increased. Typical blade joints use paste adhesives several millimeters thick, of varying geometry. They can be expected to experience significant static and fatigue loads under various environmental conditions over their service life. The limited data available for joints of this class with metal or composite adherends indicate significant sensitivity to adherend properties and surface preparation, adhesive composition (chemistry, additives, mixing, curing), adhesive thickness, temperature, and moisture, as well as joint geometry. Cyclic fatigue and time dependent creep/stress relaxation are major loading issues, in addition to static loading conditions and multi-axial loads. The variability of joint strength can be greater than that of typical laminates due to a higher sensitivity to flaws such as porosity in the adhesive, poor mixing, unbonded areas or poor dimensional control. Extreme strength issues not generally included in coupon test programs are large areas where the adhesive does not fill the bond gap, and large unbonded or partially bonded areas; these are inspection issues.

Joint design and structural adhesives technology have been the subjects of many studies. References 30-34 provide reviews of the structural adhesives literature as it pertains to fatigue testing, design and lifetime prediction. A series of reports by Tomblin, et. al, [31, 35-37] explore many of the adhesive joint parameters for general aircraft, which are also of relevance to wind blades in many instances. The strengths of lap-shear and many other joint designs for relatively brittle adhesives are dominated by stress concentrations at corners and edges of the adhesive, rather than an average stress condition across the joint [30, 38, 39]. The interpretation of test results must consider the stress concentration problem, even if strength data are represented by the average stress across the joint. Because of this problem, the failure of joints is often considered in a fracture mechanics context, with artificial or assumed cracks [32, 33, 40, 41].

Failure modes in adhesive joints are broadly represented in the literature [30, 31] as cohesive within the adhesive layer, or interfacial between the adhesive and the adherend; both may be dominated by either shearing or peeling stresses depending on factors such as adherend thickness [31]. Failure may also occur away from the joint in the adherend, or in the adherend adjacent to the adhesive. Delamination between plies, particularly the first ply below the adhesive, has been reported as a failure mode for composite adherends [31].

The fatigue lifetime of adhesive joints may be determined using the same general test methods as for static strength and fracture mechanics [30-36, 42-48]. Fatigue tests used to determine the lifetime (cycles to failure) of standard test specimen or application oriented geometries can include a significant component of the lifetime for the initiation of a fatigue crack, followed by a period of crack propagation, until the joint finally separates completely [49]. Fracture mechanics based fatigue tests generally measure the growth rate of an artificially induced crack as a function of stress intensity or strain energy release rate loading parameters [21, 22, 42-48]. Prediction of joint lifetime using fracture mechanics then requires additional information as to

the assumed initial and critical flaw sizes, and does not explicitly include crack initiation cycles [32, 33]. A practical approach based on crack growth thresholds determined in a fracture mechanics context might overcome these limitations [25, 50, 51]. Since a significant portion of the fatigue lifetime may be consumed in crack initiation (as for bulk materials), improved joint designs potentially may be based on increasing the crack initiation cycles by prudent choices of adhesive and the details of joint geometry. Thus, particularly for application related joint testing, determination of the fatigue resistance of joints which accurately represent the application may be important.

Lap shear tests have been the basis for most of the cited literature studies. Joint geometries which simulate blade joints have also been a major subject of this research, including adhesive layers on the order of 4 mm thick; limited studies of thickness effects in this range have reported reduced joint static and fatigue strength for thick joints in lap shear geometries, which was related to increased eccentricity of the load path [2]; data for simulated T-geometry intersections showed increased strength for thicker joints, apparently due to increased bending stiffness [49]. In neither case was any inherent adhesive strength change due to increasing bond thickness suggested.

SECTION 3. EXPERIMENTAL METHODS

3.1 Materials and processing

3.1.1 Typical blade laminates

A broad range of potential blade materials have been included in the course of this study, including E-glass, WindStrand™ and Carbon fibers; polyester, vinyl ester and epoxy resins; a variety of laminate constructions and fiber contents, many stitched fabrics and several prepregs. The various resin systems are listed in Table 2(a), fabrics in Table 2(b), strands used in fabrics, where known, in Table 2(c) and laminate definitions are given in Table 2(d). Fabric details given indicate the content of stitching and transverse strands or mat to which the primary strands are stitched. The laminate nomenclature corresponds to the Sandia/MSU/DOE Database. Laminates were processed by resin transfer molding (RTM), vacuum assisted RTM (VARTM), infusion through resin distribution layers, SCRIMP™ infusion, and vacuum bag prepreg molding. VARTM and infusion processes are described in Figures 7 and 8. The materials list covers most materials and process details. Other materials will be described in the results sections.

Most of the materials are in the form of multidirectional laminates containing 0^o and $\pm 45^o$ plies, with fiber volume fractions in the range of current infused or prepreg blades. Laminates used in blades typically vary in extreme cases from all unidirectional in some spars to all $\pm 45^o$ in some skins and webs. Testing experience both in this program [5, 6, 12, 13] and European OPTIMAT program [2] has found that it is increasingly difficult, often impossible, to obtain gage-section fatigue failures under many testing conditions for laminates with strong fibers, high fiber contents and high fractions of 0^o plies. One outcome of this problem is a focus of the databases on laminates with significant $\pm 45^o$ ply content. The testing philosophy is then to represent fatigue results in terms of strain rather than stress. Since all plies experience the same strains, other laminate configurations with a significant fraction of 0^o (main load direction) plies, including unidirectional, are assumed to fail at consistent strain-cycle conditions; this assumption is supported by test data in this study.

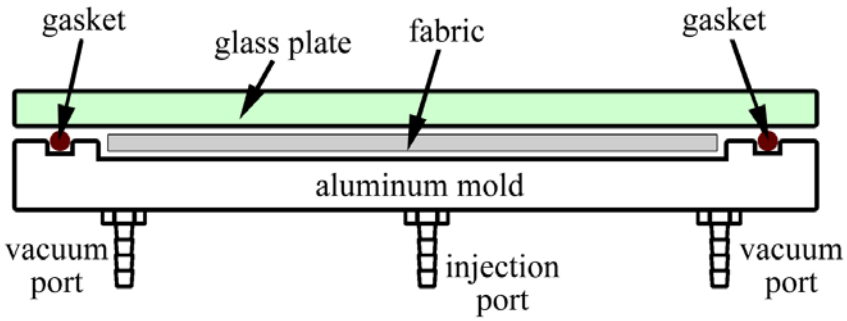

Figure 7. Schematic of the VARTM process

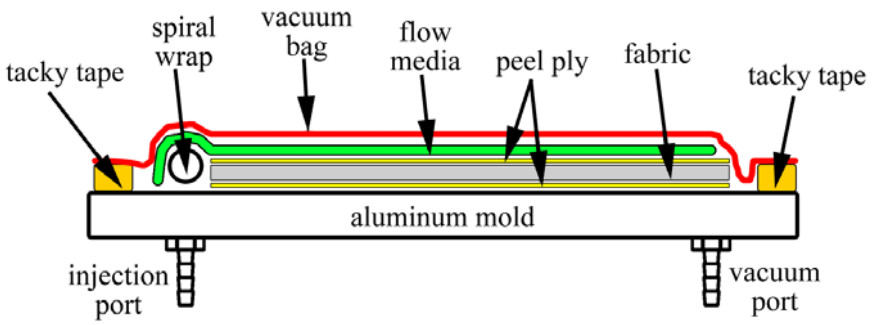

Figure 8. Schematic of the resin infusion process

Table 2(a). RTM/Infusion Resins and Post Cure Conditions

Name	Type	Resin	Cure (if not RT) and Post Cure* Temperature, ^{o}C
EP-1	Epoxy	Hexion MGS RIMR 135/MGS RIMH 1366	90
EP-2	Epoxy	Vantico TDT 177-155	70
EP-3	Epoxy	SP Systems Prime 20LV	80
EP-4	Epoxy	Huntsman Araldite LY1564/XB3485	60 and 82
EP-5	Epoxy	Hexion MGS L135i/137i	35 and 90
EP-6	Epoxy	Jeffco 1401	60 and 82
EP-7	Epoxy	DOW un-toughened epoxy	90
EP-8	Epoxy	DOW toughened epoxy	90
UP-1	Polyester	U-Pica/Hexion TR-1 with 1.5% MEKP	90
UP-2	Polyester	CoRezyn 63-AX-051 with 1% MEKP	65
UP-3	Polyester	Ashland AROPOL 1101-006 LGT with 1.5% DDM-9 MEKP	65
UP-4	Polyester	CoRezyn 75-AQ-010 with 2.0% MEKP	65
VE-1	Vinyl ester	Ashland Derakane Momentum 411 with 0.1% CoNap, 1% MEKP and 0.02 phr 2,4-Pentanedione	100 65 (mixed mode)
VE-2	Vinyl ester	Ashland Derakane 8084 with 0.3% CoNap and 1.5% MEKP	90
VE-3	Vinyl ester	Ashland Derakane 411-200	NA

*Actual temperatures used for test panels; may not comply with manufacturer recommendations for blades.

Table 2(b). Fabric specifications (from manufacturers).

	Manuf.	Designation	Areal Wt. (g/m^2)	Component Strands* Warp Dir.(wt.%)				
				0^o	$\pm45^o$	90^o	Mat	Stitch
A	Knytex	D155	527	0	0	99	0	1
B	Saertex	U14EU920-00940-T1300-100000	955	91	0	8	0	1
C	Saertex	S15EU980-01660-T1300-088000	1682	97	0	2	0	1
D	Vectorply	E-LT-5500	1875	92	0	6	0	2
E	Vectorply	E-LM-1810	932	67	0	0	32	1
F	Vectorply	E-LM-3610	1515	80	0	0	20	0
G	Knytex	A260	868	98	0	0	0	2
K	Knytex	DB120	393	0	97	0	0	3
L	Saertex	VU-90079-00830-01270-000000	831	0	97	2	0	1
M	Fiber Glass Ind.	SX-1708	857	0	68	0	30	2
N	Vectorply	E-BX-1700	608	0	99	0	0	1
O	OCV	WindStrand DB1000	1000	5	94	0	0	1
P	Knytex	DB240	837	0	98	0	0	2
R	Saertex (11)	MMWK Triax Glass/carbon/glass	970	69	31	0	0	NA
S	Toray	ACM-13-2 carbon (300-48k-10C yarn)	600	100	0	0	0	NA

*Fabrics are glass fiber with the exceptions: O is WindStrand, R is hybrid glass/carbon, and S is carbon

Table 2(c). Strands used in selected fabrics.

Fabric (Table 2(b))	Direction (Deg.)	Strand
B	0	NA
C	0	NA
D	0	PPG Hybon 2026 4400 TEX
F	0	PPG Hybon 2026 4400 TEX
L	±45	NA
M	±45, mat	FGI 675/1334
O	0	OCV WindStrand 17-1200 SE2350M2,
S	0	Toray carbon 300-48k-10C

Table 2(d). Laminate Definition

Database Laminate Designation	Resin	Fabrics	Layup	V_f (%)	Thickness (mm)	Process	Processed by (if not MSU)
Glass, 0^o and $\pm45^o$ Plies							
DD series	UP-2	A, K	$(0/\pm45/0)_S$	Var.	Var.	VARTM	
QQ1	EP-2	B, L	$(\pm45/0_2)_S$	53	4.09	VARTM	
QQ1I	EP-1	B,L	$(\pm45/0_2)_S$	52	4.10	infusion	
QQ2	EP-2	B, L	$(\pm45/0/\pm45)_S$	52	3.96	VARTM	
QQ4	EP-2	C, M	(±45/0/±45/0/±45)	57	4.03	VARTM	
QQ4I	EP-1	B, L	$(\pm45/0/\pm45)_S$	50	4.59	infusion	
QQ4-L	EP-2	C, M	(±45/0/±45/0/±45)	40	5.70	VARTM	
QQ4-M	EP-3	C, M	(±45/0/±45/0/±45)	46	4.85	VARTM	
SLA	UP-3	D, N	(±45/0/±45/0/±45)	54	4.29	Scrimp	Vectorply
SLB	UP-3	E,N	(±45/0/±45/0/±45)	43	2.69	Scrimp	Vectorply
SLC	UP-3	F,N	(±45/0/±45/0/±45)	51	3.67	Scrimp	Vectorply
TT-TPI-EP	EP-4	D, M	(±45/0/±45/0/±45)	55	4.59	Scrimp	TPI
TT-TPI-VE	VE-3	D, M	(±45/0/±45/0/±45)	55	4.60	Scrimp	TPI
TT	EP-3	D, M	(±45/0/±45/0/±45)	55	4.60	VARTM	
TT	EP-1	D, M	(±45/0/±45/0/±45)	55	4.60	Infused	
TT	UP-1	D, M	(±45/0/±45/0/±45)	52	4.60	Infused	
TT2	EP-1	D,M	(±45/0/0/0/±45)	54	6.60	infused	
TT1A	EP-2	D, L	(±45/0/±45/0/±45)	55	4.37	VARTM	
TT1A	EP-1	D, L	(±45/0/±45/0/±45)	55	4.37	infusion	
TT1A-H	EP-2	D, L	(±45/0/±45/0/±45)	63	3.98	VARTM	
Glass, $\pm45^o$ plies only							
DH	EP-1	M	$[(RM/-45/45)s]_3$	44	4.57	infusion	
DTR1	UP-1	M	$[(RM/-45/45)s]_3$	44	4.52	infusion	
45D	VE-1	M	$[(RM/-45/45)s]_3$	46	4.12	infusion	
45D2	VE-2	M	$[(RM/-45/45)s]_3$	44	4.41	infusion	
SWA	EP-1	L	$(\pm45)_{3S}$	45	4.20	infusion	
DE2	EP-7	M	$(\pm45)_{3S}$	40	4.93	infusion	
DE4	EP-8	M	$(\pm45)_{3S}$	40	4.85	infusion	
WindStrand Laminates							
WS1	EP-5	O, *	(±45/0*/±45)	61	2.56	infusion	OCV
WS2	EP-5	O, *	$(\pm45/0*/\pm45)_S$	60	5.19	infusion	OCV
W45	EP-1	O	$(\pm45)_6$	49	4.10	infusion	
Carbon 0^o and Glass $\pm45^o$ Plies							
CGD4E	EP-3	S, K	$(\pm45/0_3/\pm45)$	50	2.61	VARTM	
P2B	**	**	$(\pm45/0_4)s$	55	2.75	vac. bag	
MMWK-C/G-EP	EP-6	R	(0_4)	56	4.30	Scrimp	TPI

*0^o WindStrand is 1000g/m^2 17-1200 SE2350M2 aligned strands

**Newport prepregs; 0^o: NCT-307-D1-34-600 and $\pm45^o$: NB-307-D1-7781-497A

3.1.2 Prepreg Ply Drop Materials

Three different prepregs, supplied by Newport Adhesives and Composites, Inc, were used in this study. Two unidirectional prepregs: carbon (NCT307-D1-34-600-G300) and E-glass (NCT307- D1-E300), and one E-glass 0/90 woven fabric (NB307-D1-7781-497A) orientated at 45° for ±45 plies. All three prepregs employed the same epoxy 307 resin system. All test laminates utilized external ±45 glass plies. Plies were cut from the prepreg roll and individually laminated together using a rubber roller. To facilitate the tapering thickness of the laminate at the ply drops, sacrificial plies of the same prepreg type and number of dropped plies, were placed in the dropped regions, separated from the ply drop laminate by a Teflon sheet (See Reference 28). This allowed the use of simple flat and parallel caul plates. The prepreg was cured for 3 hours at 121°C in a vacuum bag with a vacuum of 75 kPa.

Thin laminates (<4 mm thick) in the base configuration ($\pm45/0_9/\pm45$) were used for exploratory tests under tensile, compressive, and reversed fatigue loading. Thicker laminates, $[(\pm45)_3/0_{27}/(\pm45)_3]$ (10 – 13 mm thick) were used for the main study, subjected only to compressive loading.

Additional 3 mm thick fiberglass G10 tabs were bonded to the test coupons with Hysol 9309.2 NA epoxy and cured for two hours at 60°C. Test coupons were sized so that the length of coupon would fit to the hydraulic wedge grip pistons to allow for end loading. A photo of a typical ply-drop specimen is shown in Figure 21, along with a schematic giving specimen dimensions.

3.1.3 Complex Structured Coupon

Panels containing ply drops were infused under vacuum through two flow medium layers and one peel ply layer on the top and the bottom surfaces of the laminate. Table 2 (b) gives the construction details for the fabrics L and M, ±45 (biax) and fabric D, 0^o mostly unidirectional. A typical infused panel, containing three ply drop transition lines from which test coupons were cut, is shown in Figure 9. Several infusion resins listed in Table 2 (a) were included in the study, all with the same fabrics and layups. The nominal fiber volume fraction for the ply drop panels was 54%, giving a thin-side and thick-side panel thickness of 13.7 mm and 11.5 mm, respectively with biax fabric M. Fiber content differences between systems are proportional to the thicknesses given later (in Table 14).

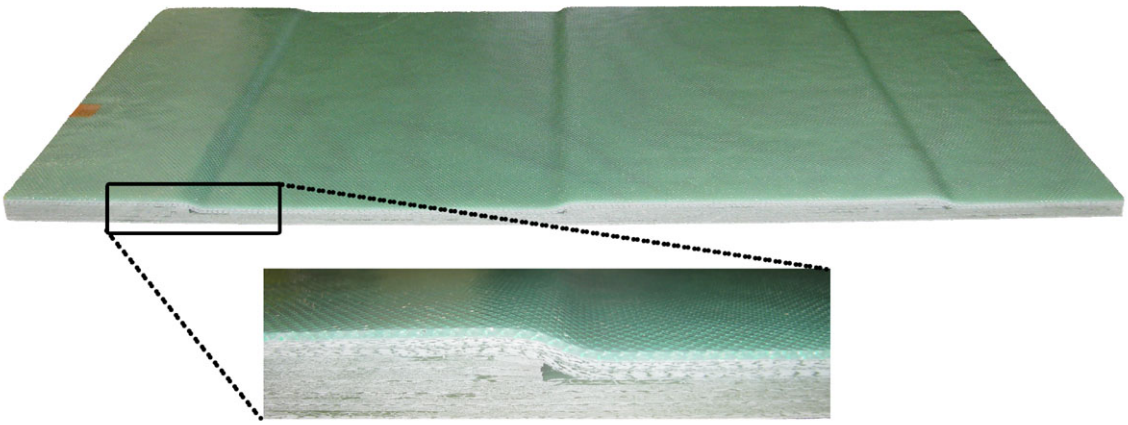

Figure 9. Infused panel with four dropped plies along three lines, from which complex coupons are machined.

3.1.4 Adhesive joints

Notched lap shear adhesive joint fatigue test specimens were prepared using unidirectional laminate adherends consisting of five plies of fabric D (Table 2) infused with either epoxy EP-1 or polyester UP-3 (Table 2(a); the latter supplied by Vectorply). ASTM A36 steel was used as one of the adherends in the tests with the UP-3 resin. Adherend laminates using EP-1 were infused through two layers of the resin distribution medium (Figure 8) and one of the following peel-plies: Super Ply F, Econoply E, or Econostitch, all supplied by Airtech International, Inc.. The adhesives were all epoxy based, and included (Table 3) a high performance unfilled adhesive, ADH-2, and several blade or potential blade adhesives, ADH-1, 3, 4 and 5. Test samples were fabricated as a sandwich with the cured laminate adherends on the outside and the adhesive layer between (Figure 10); specimens were machined as strips, with notches then machined to provide the specified overlap length, as described later. The joints with steel adherends were fabricated as individual specimens with gaps at the notches to avoid adhesive damage during machining. The designation given in Table 4 follows the Database.

Simulated blade web adhesive joint test specimens were prepared by an industry partner using ±45 fabric, epoxy resin adherends, and an epoxy based paste adhesive, shown in the schematic in Figure 11. Specimens are described in Figure 11.

Table 3. Adhesives, mixing and cure temperature.

Designation	Adhesive	Mixing	Cure temp (^{o}C)
ADH-1	Hexion EP135G3/EKH1376	Hand	70
ADH-2	3M DP460 NS	Mixer Head	50
ADH-3	EFI 20236/50219	Hand	70
ADH-4	Rhino 105	Hand	70
ADH-5	Rhino 402	Hand	70

Table 4. Notched lap shear adhesive joint materials and nominal dimensions.

Lap Joint Case	Adhesive	Adherend Material	Adherend Peel Ply	Overlap Length (mm)	Adhesive Thickness (mm)
LS-1	ADH-1	EP-1, $(0)_5$, Fabric D	Super Ply F	25.4	3.25
LS-2	ADH-2	EP-1, $(0)_5$, Fabric D	Super Ply F	25.4	3.25
LS-3	ADH-1	EP-1, $(0)_5$, Fabric D	Econo ply E	12.7	3.25
LS-4	ADH-1	EP-1, $(0)_5$, Fabric D	Econo ply E	25.4	3.25
LS-5	ADH-2	EP-1, $(0)_5$, Fabric D	Econo ply E	12.7	3.25
LS-6	ADH-2	EP-1, $(0)_5$, Fabric D	Econo ply E	25.4	3.25
LP-7	ADH-1	EP-1, $(0)_5$, Fabric D	Econo stitch	12.7	3.25
LP-8	ADH-1	EP-1, $(0)_5$, Fabric D	Econo stitch	25.4	3.25
LP-9	ADH-2	EP-1, $(0)_5$, Fabric D	Econo stitch	12.7	3.25
LP-10	ADH-2	EP-1, $(0)_5$, Fabric D	Econo stitch	25.4	3.25
LP-11	ADH-3	EP-1, $(0)_5$, Fabric D	Econo ply E	12.7	3.25
LP-12	ADH-4	EP-1, $(0)_5$, Fabric D	Econo ply E	12.7	3.25
LP-13	ADH-5	EP-1, $(0)_5$, Fabric D	Econo ply E	12.7	3.25
LP-14	ADH-1	EP-1, $(0)_5$, Fabric D	Econo ply E	25.4	6.50
LP-15	ADH-1	EP-1, $(0)_5$, Fabric D	Econo ply E	25.4	9.75
LP-16	ADH-1	UP-3, $(0)_5$, Fabric D 2.5 mm Steel, side 2	Econoply E / N/A	25.4	3.25
LP-17	ADH-1	UP-3, $(0)_5$, Fabric D 4.8 mm Steel, side 2	Econoply E / N/A	25.4	3.25
LP-18	ADH-3	UP-3, $(0)_5$, Fabric D Steel side 2	Econoply E/ N/A	25.4	3.25

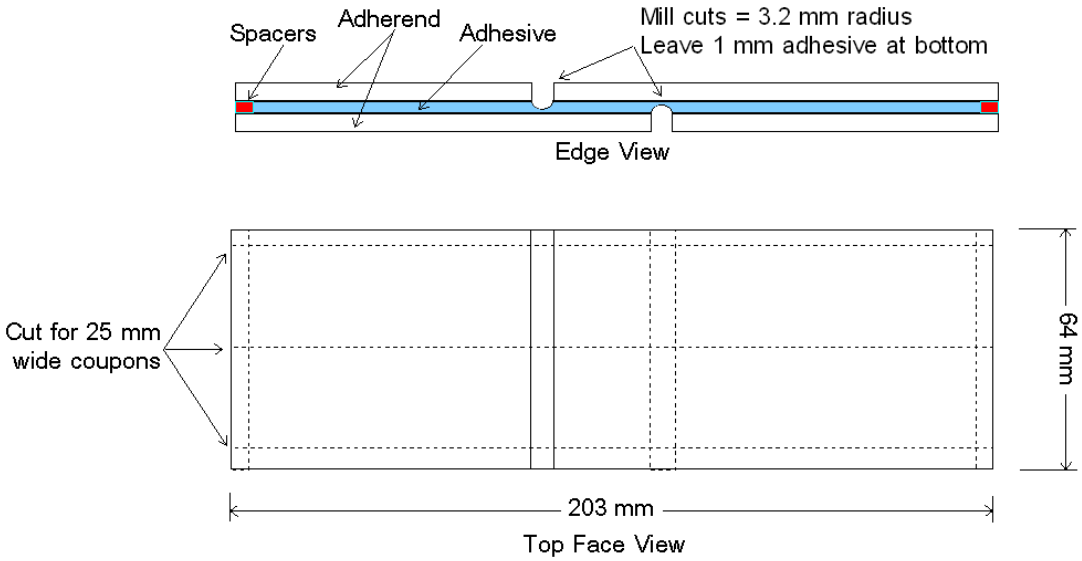

Figure 10. Lay-out of lap-shear adhesive panel (two specimens/panel).

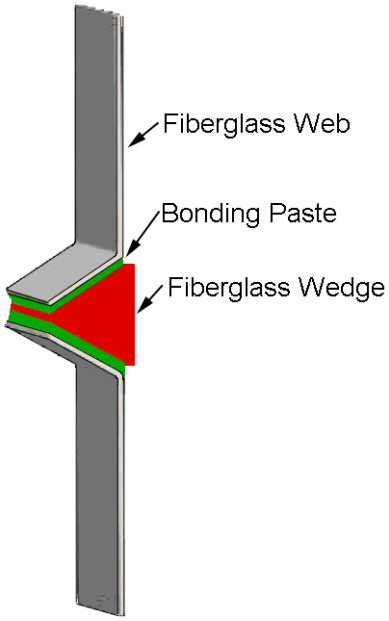

Figure 11. Simulated blade web adhesive joint specimen.

3.1.5 Spar cap split tests

Laminate plates were fabricated by VARTM or prepreg molding to 10-12 mm thick as defined in Table 5. The VARTM laminates used fabrics A and K, which are typical for hand lay-up, with isopolyester UP-4, and were post cured at 60^{o}C for two hours following 24 hrs. at room temperature. The prepreg laminates were fabricated from (NCT307-D1-34-600) Newport carbon fiber prepreg 0° plies and (NB307-D1-7781-497-A) Newport glass prepreg ±45°. The laminates were vacuum bag, net resin cured at initially at 85^{o}C for 2 hours; the temperature was then increased at 1^{o}C/min. to 121^{o}C, held for 3 hours and oven cooled to room temperature.

Table 5. Summary of spar cap split test laminates.

Fiber and Matrix Material	Lay-up	% 0^O	% 90^O	% 45^O	Thickness mm
VARTM Fabric A with Resin UP-4 (V_F = 48 %)	$(90)_{28}$	0	100	0	12.6
	$((90)_2/0)_{4S}$	28.6	71.4	0	10.9
	$(90/0)_{7S}$	50	50	0	12.6
	$(0/90)_{7S}$	50	50	0	12.6
	$(90)_{14}/0/(90)_{13}$	3.6	96.4	0	12.7
	$[(90)_{13}/45]_S$	0	92.9	7.1	12.7
	$[(90)_7/\pm45/(90)_5]_S$	0	85.7	14.3	12.7
	$[((90)_4/\pm45)_2/(90)_2]_S$	0	71.4	28.6	12.7
	$[((90)_2/\pm45)_3/90/45]_S$	0	50	50	12.7
VARTM Fabric G (0's), K (±45* and P (±45) with Resin UP-4 (V_F = 48 %)	$(90)_{16}$	0	100	0	11.5
	$(\pm45^*/(90)_7)_S$	0	94.7	5.3	11.0
	$(\pm45/(90)_7)_S$	0	88.8	11.2	11.8
	$((\pm45)_2/(90)_6)_S$	0	78.7	21.3	11.5
	$(\pm45/(90)_4/\pm45/(90)_2)_S$	0	78.7	21.3	11.1
	$((\pm45/(90)_2)_3/90/(\pm45/(90)_2)_2/\pm45)$	0	66.4	33.6	11.3
	$(\pm45)_2/(90)_5/\pm45/\pm45/(90)_6/(\pm45)_2$	0	66.4	33.6	10.9
	$(\pm45/90)_4)/90/(90/\pm45)_4$	0	55.2	44.8	11.8
	$(\pm45)_4/(90)_9/(\pm45)_4$	0	55.2	44.8	11.7
PREPREG NCT307-D134600 Newport Carbon fiber prepreg 0° plies and NB307-D1-7781-497A Newport Glass prepreg ±45° plies (V_F = 53%)	$(90)_{42}$	0	100	0	13.2
	$90_{20}/\pm45/90_{20}$	0	95.9	4.1	12.8
	$[90_{13}/\pm45/90_6]_S$	0	91.7	8.3	12.3
	$[90_9/\pm45]_3\ /90_9$	0	87.4	12.6	11.9
	$[(90_7/\pm45)_2\ /90_3]_S$	0	83.1	16.9	11.9
	$[(90_3/\pm45)_4\ /90)]_S$	0	65.3	34.7	10.8
	$[(90_2/\pm45)_5\ /90]_S$	0	56.1	43.9	9.8
	$[(90_4/(\pm45)_2)_2\ /(90)_3/\pm45]_S$	0	56.1	43.9	9.8
	$[\pm45]_{21}$	0	0	100	11.4

3.2 Test Methods and Test Development

3.2.1 Overview

Test methods fall into two categories: first, in-plane and interlaminar tests which follow recognized ASTM or ISO test methods, modified in some cases to accommodate materials variations which produce problems with failure modes; second, tests related to more complex structural detail areas such as ply drops, adhesive joints and sandwich cores.

New test methods have been developed for structural details including ply drop areas and thick adhesive joints. The purpose of the structural detail test development is to establish test methods for comparison of blade materials, but which represent more realistic blade geometries and loading conditions than do available test standards. The new tests still conform to the conventional coupon concept, utilizing standard testing equipment, as compared to the considerable demands and limitations of blade substructure testing. Thus, while standard test methods exist which are useful in comparing different adhesives on the basis of peel and lap shear performance, most of these do not allow evaluation in the context of typical thick paste adhesives, composite laminate adherends or compression and reversed loading fatigue conditions, which are typical for blade structures.

3.2.2 Standard laminate test.

In-Plane Tests. Test coupons were machined from panels supplied by industry or molded at MSU (Figures 7 and 8). Typical test geometries for static and fatigue tests are given in Figure 12, with failed specimens shown in Figure 13. The short rectangular specimens were used for tests involving compression loads, or as noted. Failure locations were usually adjacent to or inside the grips for rectangular specimens regardless of whether tabs were used [14, 15]. This testing problem has also been reported in other programs with similar materials [2]. Tensile fatigue tests using the dog-bone geometries failed consistently in the gage section, Figure 13. Tensile fatigue test data for the wide and narrow dog-bone shape specimens were indistinguishable as illustrated in Figure 14; the narrower specimen was generally used with the exception of laminates QQ1 and TT-TPI-EP and VE as noted in individual database entries.

Fatigue tests were run under load control, constant amplitude as illustrated for various minimum to maximum stress ratios, R, in Figure 15. The test frequency was typically below 10 Hz and specimen surfaces were air cooled with fans to avoid heating of more than a few ^{o}C [5, 6]. The frequency was also selected so as to approximately maintain a constant average load rate, increasing with decreasing maximum load [6]. For tensile fatigue tests the strains given are initial strains measured on the first few cycles. Strains for other R-value tests, using the short rectangular specimens shown, were determined from the stresses through the tensile modulus given in each case. In either event, the strains are lower than those which will accumulate during the fatigue lifetime [5 - 7]. A useful description of the effects of the method of strain determination on strain based fatigue curves for several of the materials reported here is given in Reference [3].

Four different Instron servo-hydraulic test systems were used depending on the force and frequency of the test. All test systems are equipped with servo-hydraulic grip systems; for compression loading the lower grip is constrained against rotation and lateral movement as shown in Figure 16 and discussed in more detail in Reference 5.

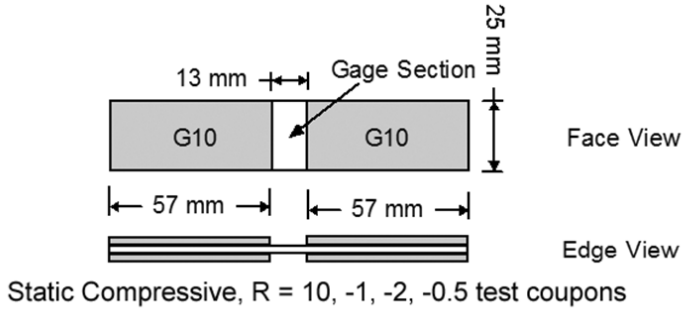

Static Compressive, R = 10, -1, -2, -0.5 test coupons

Static Tensile, R = 0.1, 0.5 test coupons (smaller geometry)

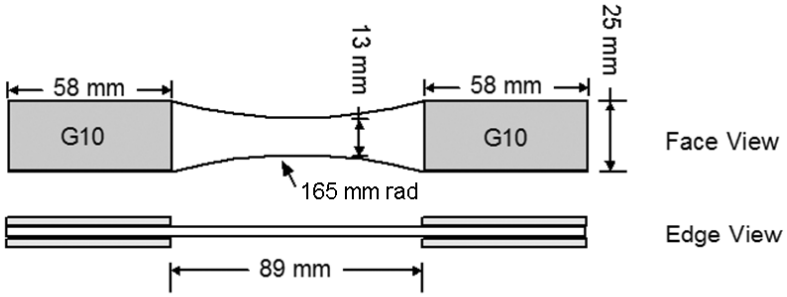

Static Tensile, R = 0.1, 0.5 test coupons (larger geometry)

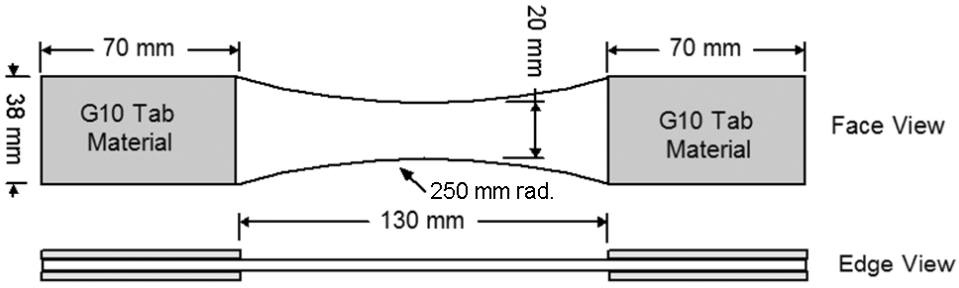

Figure 12. Dog-bone (DB) and rectangular (top) test geometries; test specimens may or may not include tabs.

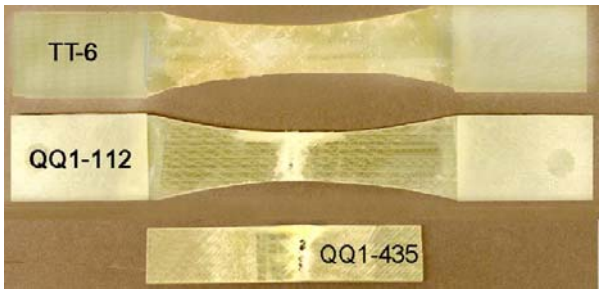

Figure 13. Failed fatigue dog-bone and rectangular specimens, showing grip-edge failure for a rectangular specimen (bottom) and gage section failure for a dog-bone specimen.

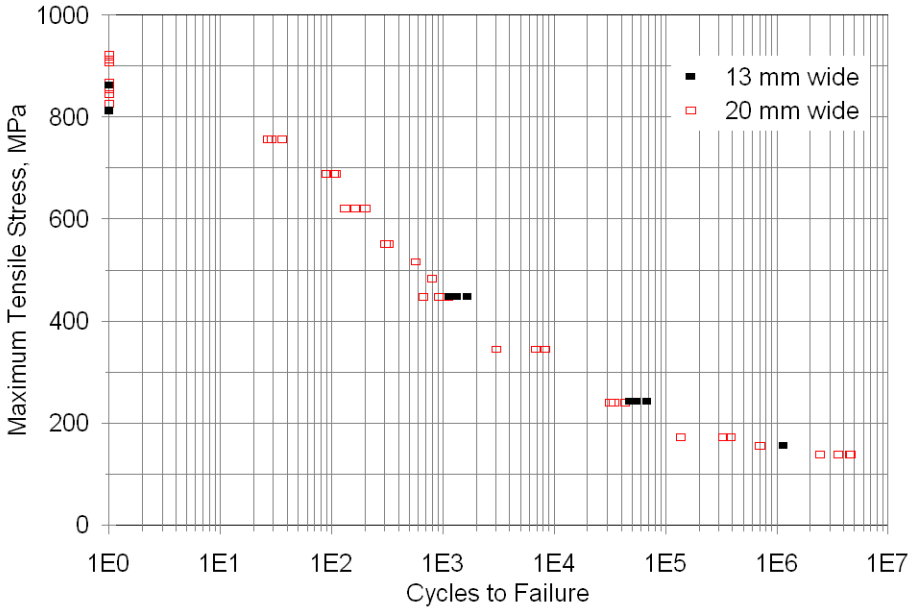

Figure 14. Comparison of tensile fatigue data for wide and narrow dog-bone specimens, Laminate QQ1, R = 0.1.

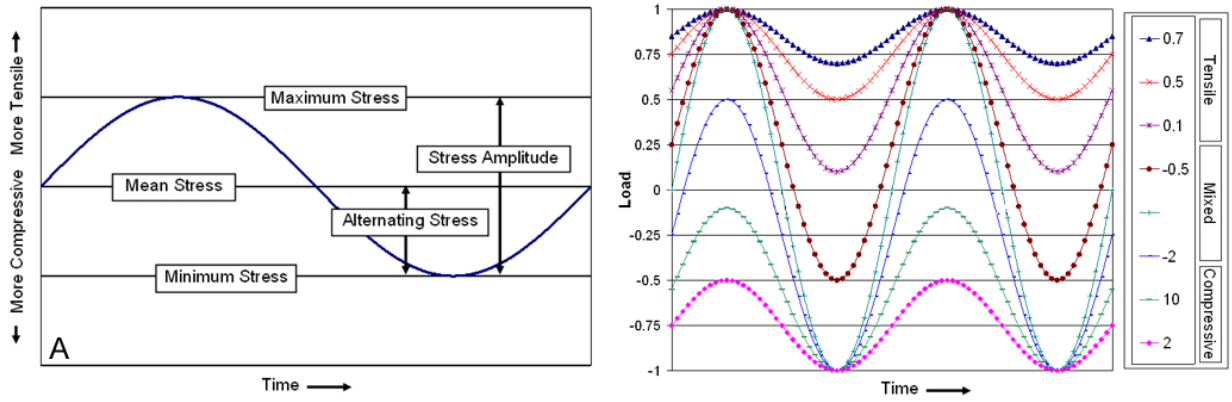

Figure 15. Load waveforms showing definition of terms (left) and illustration of R-values (right, R = minimum stress/maximum stress).

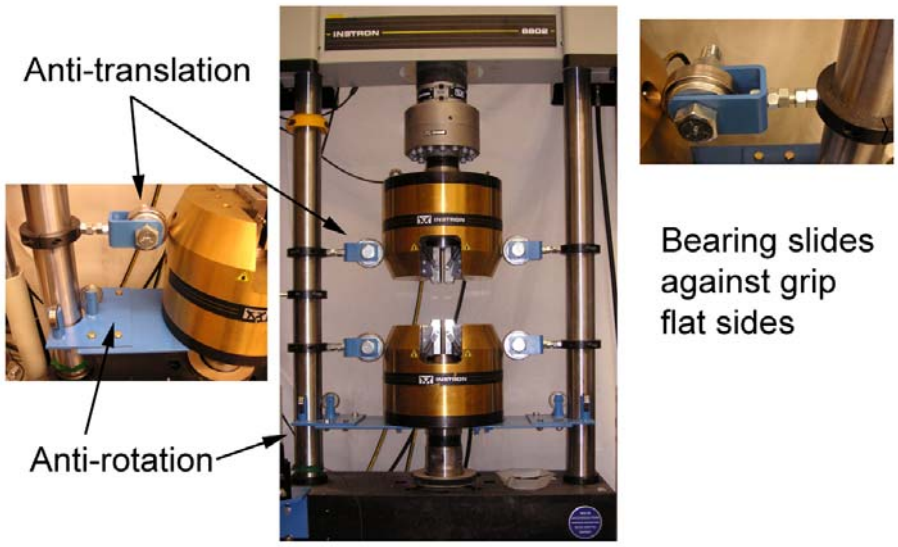

Figure 16. Hydraulic grip with lateral restraint.

Delamination Tests. Delamination test methods for pure and mixed modes (I and II) used double cantilever beam (DCB), end notch flexure (ENF) and mixed mode bending (MMB) geometries described in more detail in References 5 and 52. These test methods are used to determine a critical strain energy release rate for crack propagation, G. This critical value must be experimentally determined for each material system. The critical value usually differs for each mode and is denoted with subscripts as G_{IC} and G_{IIC}. In practical terms, materials that are "tougher" have higher critical values of G, requiring more energy to grow a crack in that material. The interlaminar toughness relates directly to the resin toughness [53]. The Teflon insert starter cracks were 0.040 mm thick.

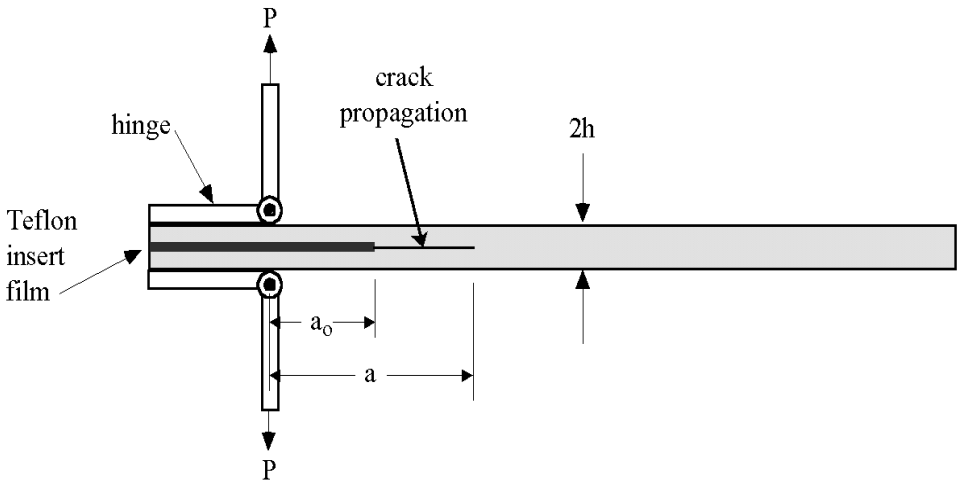

Figure 17. Mode I DCB geometry and loading (ASTM D5528).

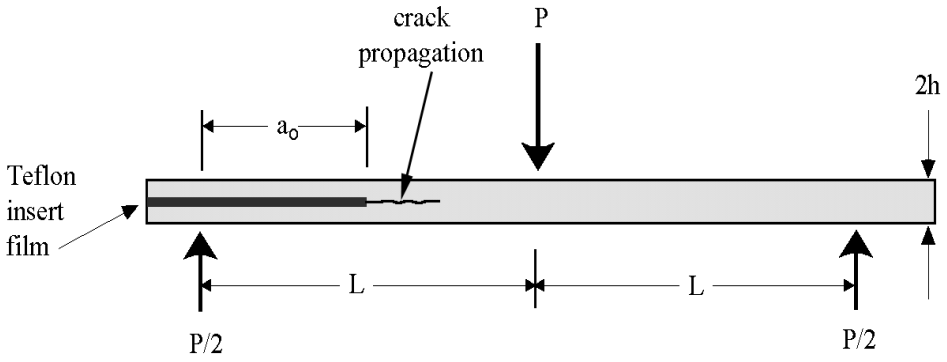

Figure 18. Mode II ENF geometry and loading.

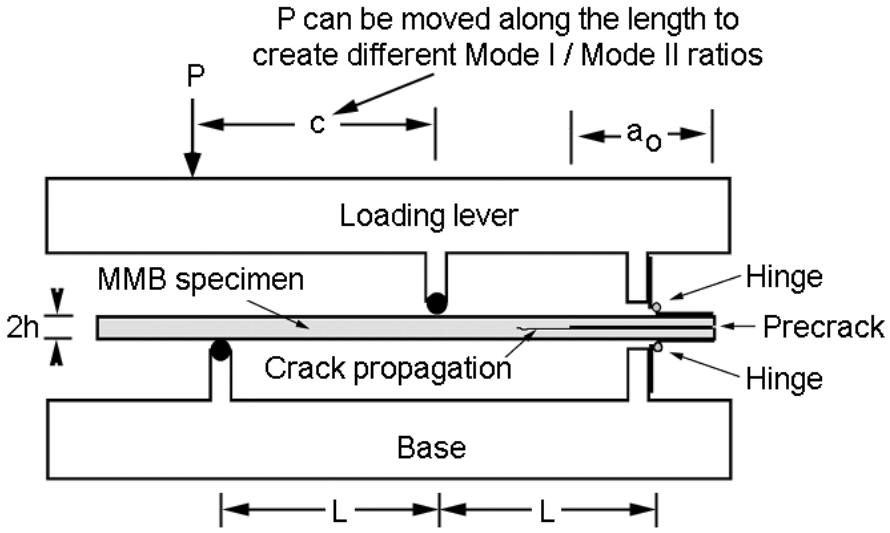

Figure 19. Mixed mode bending test specimen and apparatus.

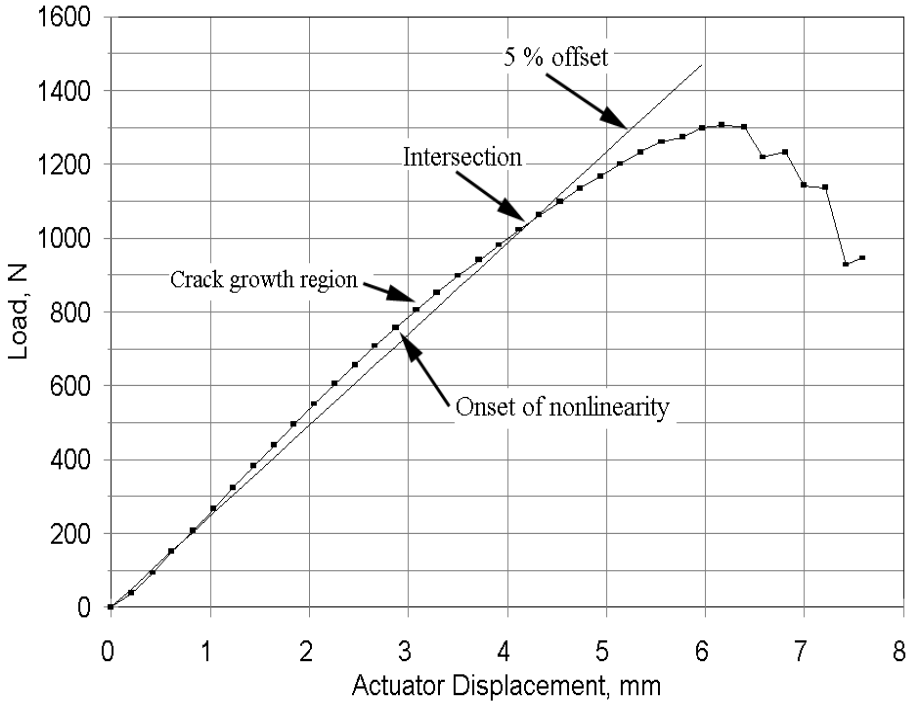

Figure 20. Typical load versus actuator displacement and critical load determination for an ENF Specimen.

To obtain critical values for G in static loading conditions, a variety of tests are used for the various modes of crack extension. For Mode I fracture, the standard test specimen is the double cantilever beam (DCB) as described in ASTM standard D5528 and shown in Figure 17. The critical strain energy release rate to grow a crack in the material can be obtained by the use of the load versus displacement curve of the test and the modified beam theory (MBT) method [54]:

$$G_{IC} = \frac{3P\delta}{2ba} \tag{3}$$

where: P = critical load at crack propagation
δ = displacement between DCB cantilever arms at critical load
b = specimen width
a = crack length measured from the center of the load pins

The end-notched flexure (ENF) test has emerged as the standard test method for measuring Mode II type crack growth, although questions remain as to crack closure problems. Typical specimen geometry and loading for an ENF specimen are shown in Figure 18. This specimen produces shear at the mid-plane of a composite loaded in three-point bending. When a critical load is reached, the crack advances, usually in an unstable manner [55]. The formula used to calculate G_{IIC} based on beam theory [56] is given by:

$$G_{IIC} = \frac{9P^2a^2C}{2b(2L^3 + 3a^3)} \tag{4}$$

where: P = critical load at propagation
a = initial crack length measured from support point
b = specimen width
C = specimen compliance (= center point deflection/P)
L = one-half support spacing distance

The mixed mode bending (MMB) test developed by Reeder and Crews [70] allows G_I and G_{II} calculation under mixed mode conditions. This test allows the mixed mode ratio, G_I/G_{II}, can be varied by a single adjustment. Figure 19 illustrates the mixed mode bending test.

In their analysis of this test, Reeder and Crews incorporated effects of both shear deformation and elastic foundation [70]. The Reeder and Crews analysis is used in this study, and an analysis by Williams [57] that includes large rotation and beam-root rotation, is discussed but not used.

Shear deformation must be considered if the shear modulus is relatively small compared to the longitudinal modulus, as in most polymer matrix composites. Shear deformation is a function of specimen thickness (h), longitudinal modulus (E_{11}), and shear modulus in the 1-2 or 1-3 planes (G_{12} or G_{13}). The shear moduli G_{12} and G_{13} are taken to be the same, based on the usual transversely isotropic assumption. As the beams become shorter, this correction becomes more significant. This correction applies to both DCB and ENF tests.

Elastic foundation analysis is required for the DCB specimen because the two beams are supporting each other and act elastically, instead of acting as a rigid body [52]. The elastic foundation correction is a function of thickness, and longitudinal and transverse moduli. A large deflection correction can be applied to pure modes when deflection can be obtained experimentally. In the MMB test, large deflection correction is not applicable because the deflection contributed by each mode is not measurable. While the mode-II deflection may be determined, the mode-I deflection component (in mixed mode) is no longer symmetric as in pure mode-I. Since the modal deflections cannot be determined, corrections for them are unavailable prior to the test [52].

The rotation correction renders the testing substantially more difficult and the accuracy is limited by the accuracy of the equipment as well as the measurements. Rotation of the beam root can be measured approximately, but not at the accuracy of the other measurements. The accuracy of the toughness determination is not any better than the least accurate measurement. Large deflection and beam-root rotation corrections are not used in this study.

The G_I and G_{II} values formulated by Reeder and Crews are the following [70]:

$$G_I = \frac{12P_I^2}{b^2h^3E_{11}}\left(a_o^{\,2} + \frac{2a_o}{\lambda} + \frac{1}{\lambda^2} + \frac{h^2E_{11}}{10G_{13}}\right) \tag{5}$$

$$G_{II} = \frac{9P_{II}^2}{16b^2h^3E_{11}}\left(a_o{}^2 + \frac{h^2E_{11}}{5G_{13}}\right) \tag{6}$$

$$\lambda = \frac{1}{h}\sqrt[4]{\frac{6E_{22}}{E_{11}}} \tag{7}$$

$$P_I = P_C\left(\frac{3c - L}{4L}\right) \tag{8}$$

$$P_{II} = P_C\left(\frac{c + L}{L}\right) \tag{9}$$

where,
a_o = initial crack length
b = width of specimen
c = geometric variable that changes the G_I/G_{II} ratio
E_{11}, E_{22} = longitudinal and transverse moduli, respectively
G_{13} = in-plane shear modulus
G_I, G_{II} = strain energy release rate in mode I and II, respectively
h = half-thickness of specimen
L = half-length of the bottom support
P_C = critical loading determined from load-deflection curve
P_I, P_{II} = mode I and II loadings, respectively
λ = elastic foundation correction
See the illustration of the apparatus in Figure 19 for the geometric variables a_o, c, h and L. Lambda is the parameter in the elastic foundation correction and is a function of h, E_{11} and E_{22}. The critical load was determined using the 95% slope method illustrated in Figure 20.

3.2.3 Prepreg Ply Drop Tests

Ply drop studies were carried out on specimen geometries illustrated in Figure 21. Mechanical testing was performed in Instron 8501 and 8802 servo-hydraulic test machines with capacities of 100 and 250 kN respectively. The static (1-cycle) tests were performed under displacement control with a linear ramp rate of 13 mm/s, which produced a similar loading rate to the fatigue tests. The fatigue tests were performed under load control with a sinusoidal waveform with frequencies between 1 and 6 Hz. Figure 21 shows a typical ply drop specimen.

Compression tests of the thin laminates with no ply drops used 25 mm wide rectangular specimens having a gage length of 13 mm, with no lateral constraint on the gage section. Thicker laminate tests (10 - 13 mm) and the thin laminate tests with a ply drop used a 25 mm gage length. In all cases, the coupons were monitored for buckling. Specimens were held in hydraulic grips with special anti-rotation and anti-deflection restraints.

Compressive stress-strain curves were generated from specimens without ply drops to obtain modulus values which were used to calculate strain values from the stress determined in the tests. All stresses and strains in the results represent the thin side of the ply drop specimens.

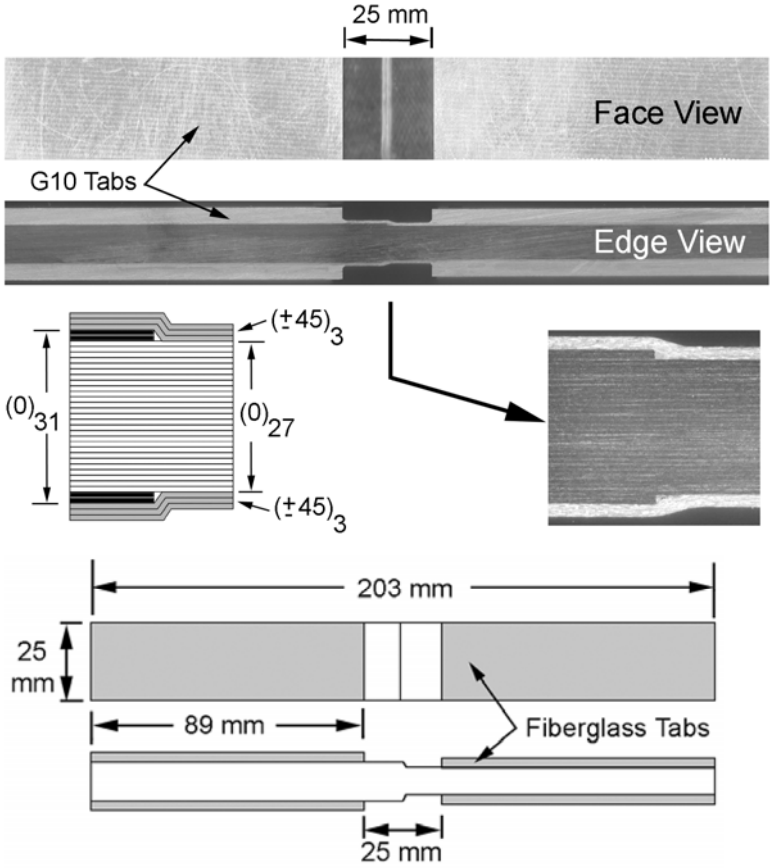

Figure 21. Typical ply drop coupon containing double 0^o ply drop at surface of 0^o ply stack; carbon prepreg 0^o plies, glass prepreg $\pm 45^o$ plies.

3.2.4 Complex Structured Coupon Tests

The complex coupon with ply drops employs an unsymmetrical geometry shown in Figures 22 and 23. This test method required significant test development to arrive at a lay-up and dimensions which would have minimal bending, be compatible with testing machine (250 kN) capacity and grip capacity, while representing blade materials and structure of current interest. The lay-up chosen allows convenient infusion with a variety of resins of interest for blades, and features failure modes including delamination at the ply drops, damage in the $\pm 45^o$ surface layers (which represent blade skin materials) and load redistribution between the surface skins and primary structural 0^o plies as damage develops and extends.

The final dimensions were selected based on FEA including grip interactions. Figure 24 gives FEA results showing the distribution of axial strain along the specimen length, and Figure 25 gives the strain through the thickness at several points. Despite the specimen non-symmetry, the

strains appear to be sufficiently uniform in the gage section around the ply drop to allow them to be meaningfully related to other geometries such as blades. FEA based damage simulations will be carried out in the future, when a complete set of experimental data is available.

Fatigue tests were conducted in sinusoidal tensile loading at minimum to maximum load ratios, R of 0.1, -1 and 10. Frequencies were in the range of 2-5 Hz, with surface heating monitored to be less than 5°C. Delamination in complex specimens with ply drops was monitored by camera and measured periodically using visual inspection (ink marks visible on specimen photographs like Fig. 23). Static ramp tests on these specimens were conducted at a displacement rate of 0.025 mm/s, with periodic interruptions for delamination measurement.

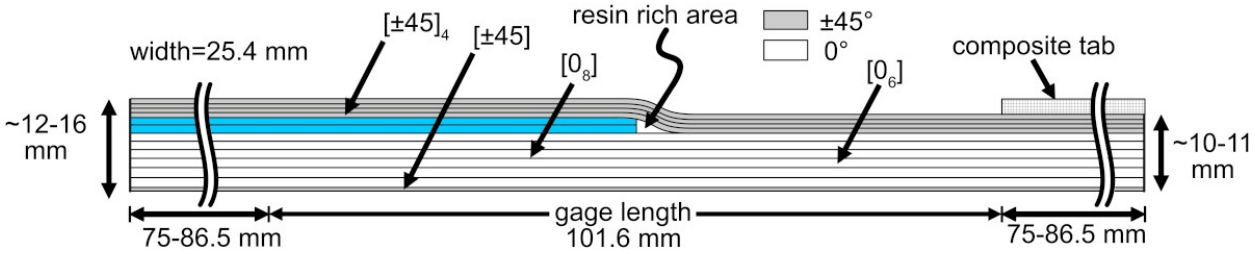

Figure 22. Geometry and layup of MSU complex coupon with two ply drops shown.

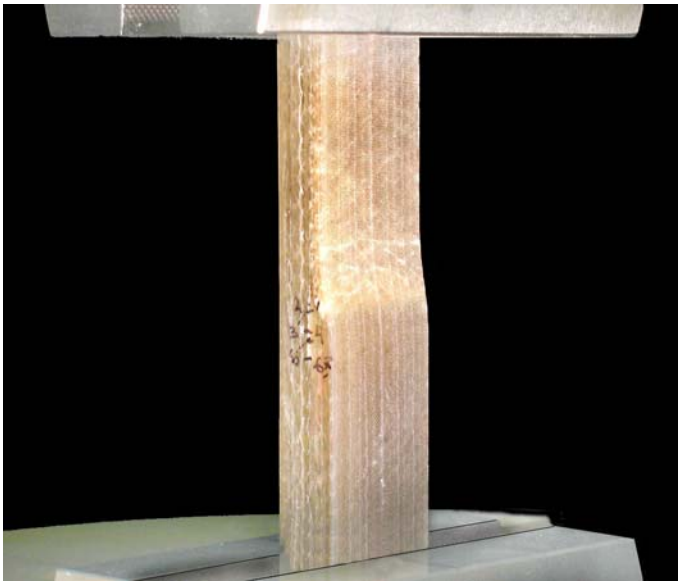

Figure 23. MSU complex coupon with fatigue damage at ply drops, VE-2 resin.

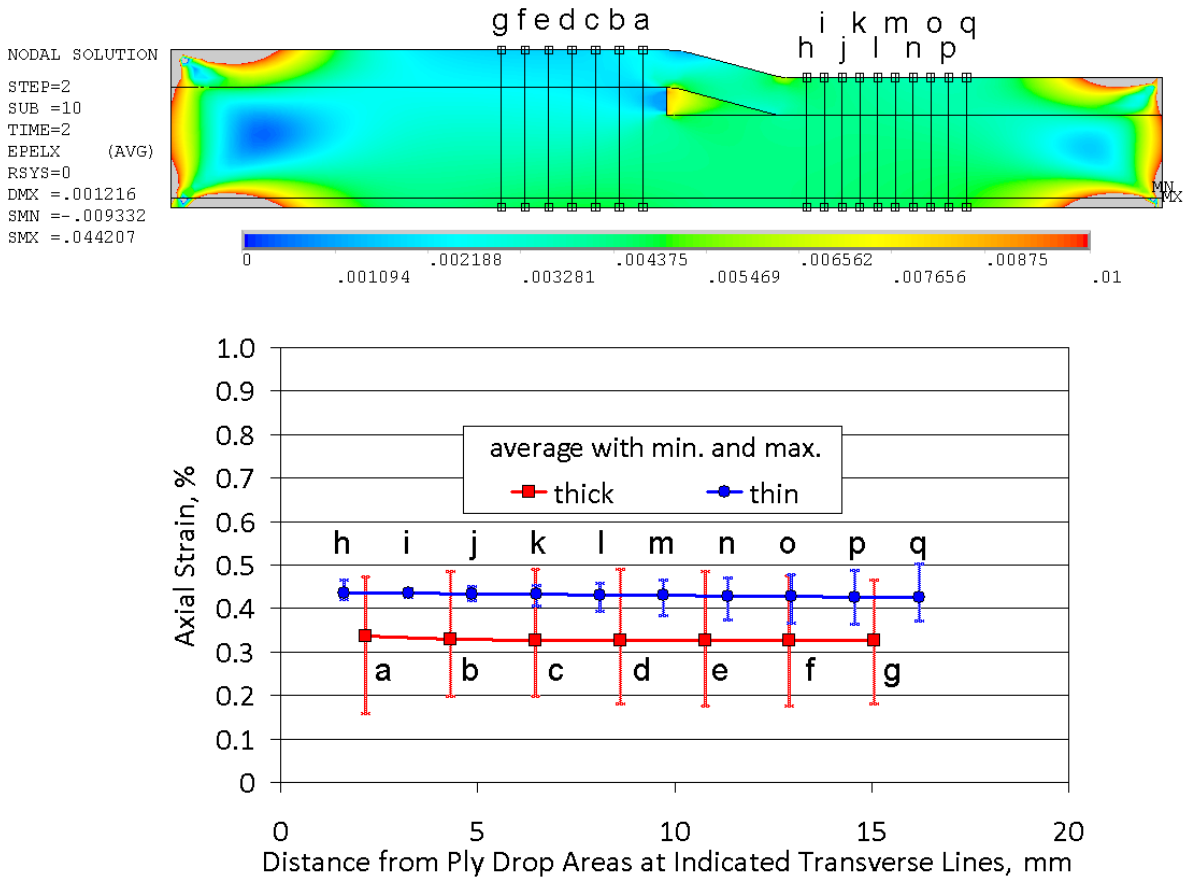

Figure 24. Axial strain distribution (top), and line plots across thickness at indicated axial locations from FEA for a tensile force of 44.5 kN.

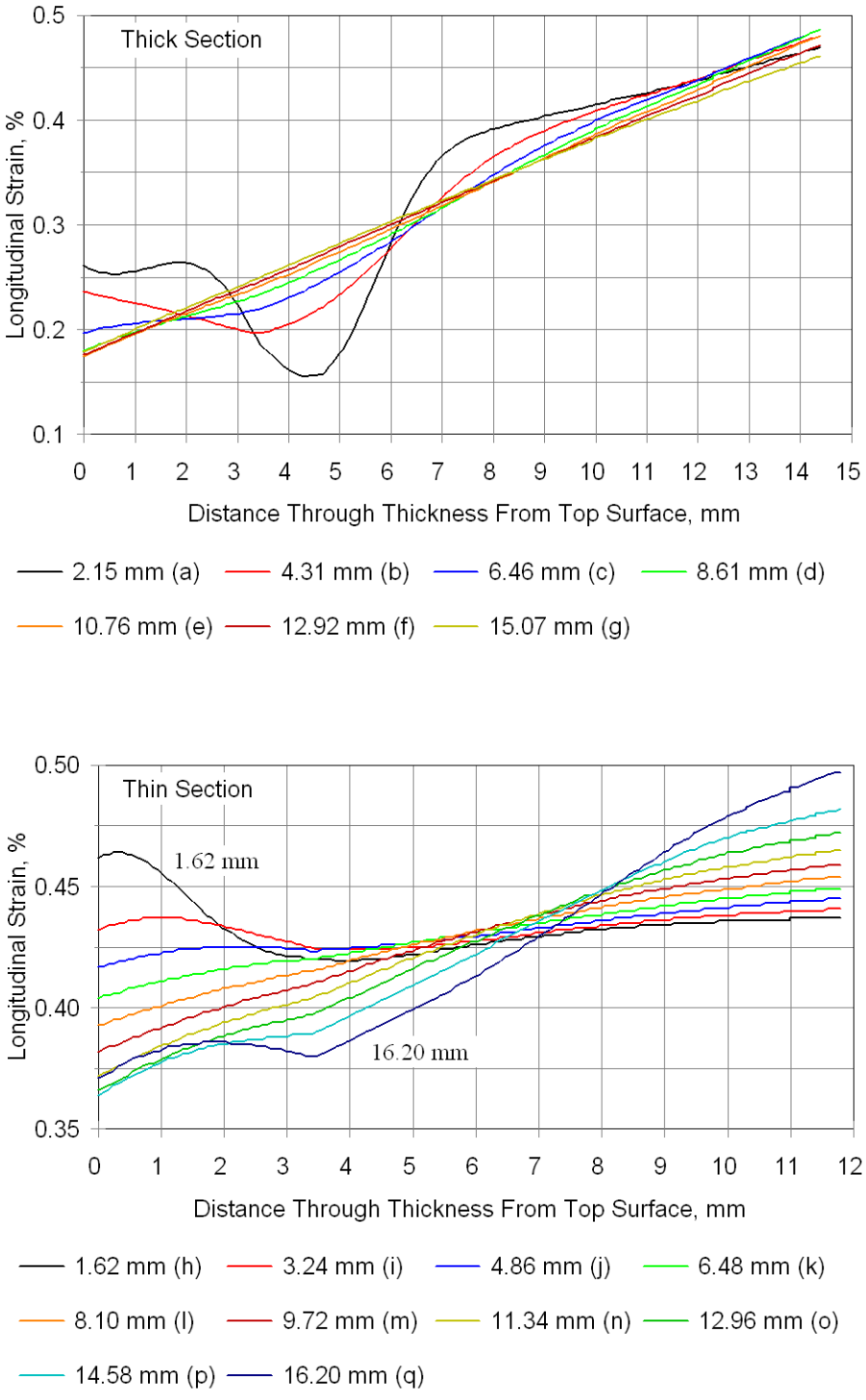

Figure 25. Axial strain distribution through the thickness in gage section: (top): thin side; (bottom): thick side. (letters denote position in Figure 24)

3.2.5 MSU Notched Lap Shear Specimen

A thick adhesive lap shear test method has been developed along the lines of various standard methods (ASTM D1002, D3165, D5656, and D5868), but with improved application to fatigue studies with laminate adherends and thick adhesive layers typical of blade structures. The following were the target attributes of interest:

1. The test should be capable of determining fatigue response under a range of R-values including compressive loads.
2. Loading should be through standard hydraulic grips (with lateral movement constraint).
3. Specimen preparation should be convenient and reproducible.
4. Failure should initiate in the adhesive for a broad range of adhesives of interest (as opposed to failure initiating inside the laminate interface).
5. The overlap length should be sufficient to explore damage initiation and propagation.
6. The test should be able to accommodate a broad range of adhesive properties and thicknesses.

The specimen geometry is depicted in Figure 26. This geometry is similar to that reported by Tomblin, et al [35]. Preliminary tests with other geometries, including notches at various positions in the adhesive, showed inconsistent failure initiation sites and increased scatter. Data are reported later for overlap lengths of 12.7 and 25.4 mm, with the fatigue geometry using 25.4 mm. Laminate adherends are important in that failure may initiate within the laminate for some layups; this is more common for ±45 laminates than for unidirectional laminates with relatively thick plies. The laminate used in these studies was four plies of fabric D with epoxy EP-1 resin; additional tests were conducted using UP-3 polyester and also one steel adherend.

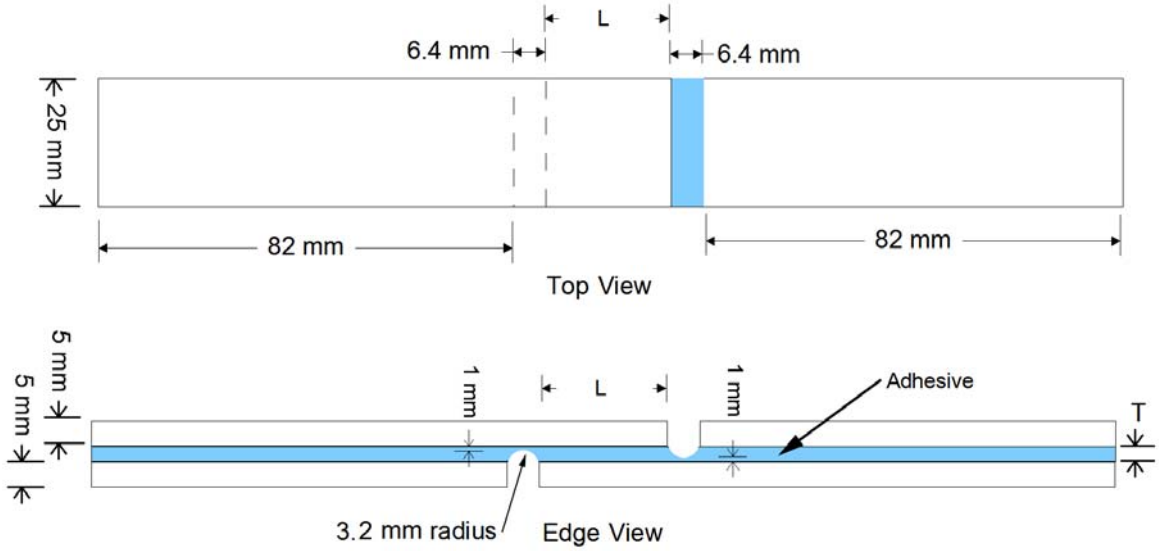

Figure 26. Geometry of MSU notched lap shear fatigue specimen.

Test development included linear and nonlinear finite element analysis discussed in more detail later. Figure 27 gives a maximum tensile strain map for a typical specimen with a 25.4 mm overlap length, L, under tensile load. The strain concentration area at the notch radius is the dominant failure (crack) initiation site as indicated for a typical fatigue specimen in Figure 28. The crack usually propagates through the adhesive to the opposite adherend interface, then along the interface, either in the adhesive or inside the laminate surface, as described in the results.

Static tests were conducted at a displacement rates of 0.025 and 12.7 mm/s; fatigue tests were conducted at a frequency of 1-5 Hz as discussed later.

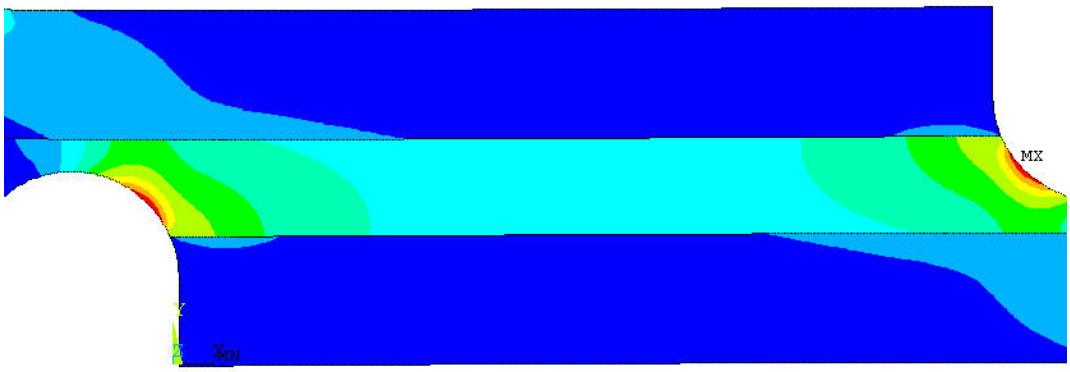

Figure 27. Maximum principal tensile strain linear FEA map.

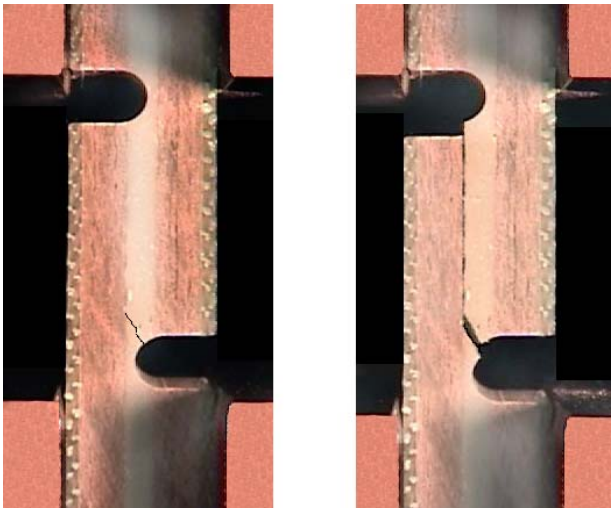

Figure 28. MSU notched lap shear fatigue specimen failing in reversed loading fatigue at 3004 cycles (left) and 3006 cycles (right).

3.2.6 Simulated Blade Adhesive Joint Tests

Specimen geometries were based on that given in Figure 11, with either 45^o or 90^o angles; modified geometries included added reinforcement. The four geometries tested are:

1. Geometry A, 45^o wedge block, no reinforcement
2. Geometry B, 90^o wedge block, no reinforcement
3. Geometry C, 45^o wedge block, with additional reinforcement
4. Geometry D, 90^o wedge block, with additional reinforcement

A schematic of Geometry A, 45^o with no additional reinforcement, is given in Figure 29, and failed specimens of Geometries A and B are given in Figure 30. Each specimen contained two nominally identical joints, top and bottom in Fig. 11; failure in almost all cases occurred on one side only, with no observable damage to the joint on the other side. All laminates were glass/epoxy with a ±45^o orientation; reinforcement in the center wedge block was oriented so that the fabric was in the vertical plane, parallel to the load, coplanar with the web adherend. Adhesive thicknesses varied slightly from specimen to specimen, with a nominal value of 4 mm. Specimens were nominally 50 mm wide, with the straight portion of each web 100 mm long. Web thickness was nominally 4 mm for Geometries A and B.

For tensile testing, specimens were loaded by standard hydraulic wedge grips with a grip separation of 185 mm; reversed loading fatigue tests used grip separations of 175 mm (Geometry C) and 75 mm (Geometry D) to avoid buckling. Loads were uniaxial tension or compression. Static tension tests were run at two displacement rates: slow (0.025 mm/s), consistent with test standards, or fast (13 mm/s), consistent with the fatigue rates. Fatigue tests were conducted under sine wave, constant load amplitude conditions at frequencies ranging from 2-4 cycles per second (varied approximately inversely with maximum load, to maintain an approximately constant load rate). Surface temperatures were monitored during selected tests; the maximum temperature rise measured on the adhesive surface was 2 ^{o}C. Fatigue loading conditions were either tensile fatigue, R = 0.1, or reversed tension-compression, R = -1, where R is the ratio of minimum to maximum load for each cycle. Specimens were conditioned and tested at ambient laboratory conditions, approximately 20^{o}C and 30 % R.H.

Although the specimens were slightly unsymmetrical about the load line, out of plane movement during fatigue loading was small. A typical out of plane lateral movement at a load of 25 kN at the mid-height was 0.2 mm for Geometry C.

The adhesive strains were not monitored directly as by shear extensometry [36], but the load-deflection curve was determined for Geometry A with an extensometer across the entire joint. The response was moderately nonlinear for the load range used in the static and fatigue tests, but was similar to that for the adherend without a joint. Thus, direct measurements of the strain in the adhesive would be required to characterize the extent of adhesive nonlinearity. A range of conditions have been reported [37] for paste adhesives in this class for different temperatures and moisture contents, as to adhesive yielding and nonlinearity, for loads which produce fatigue failure in the cycle range of interest in this study. As described later, failures in this study appeared brittle in character, originating at a flaw or stress concentration.

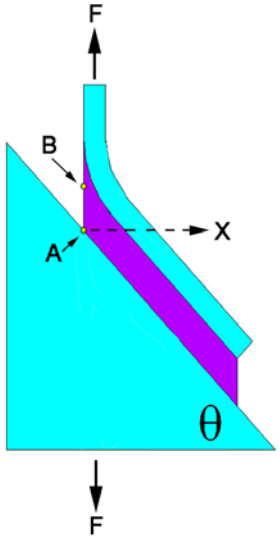

Figure 29. Geometry and location of points of interest and line plot axis.

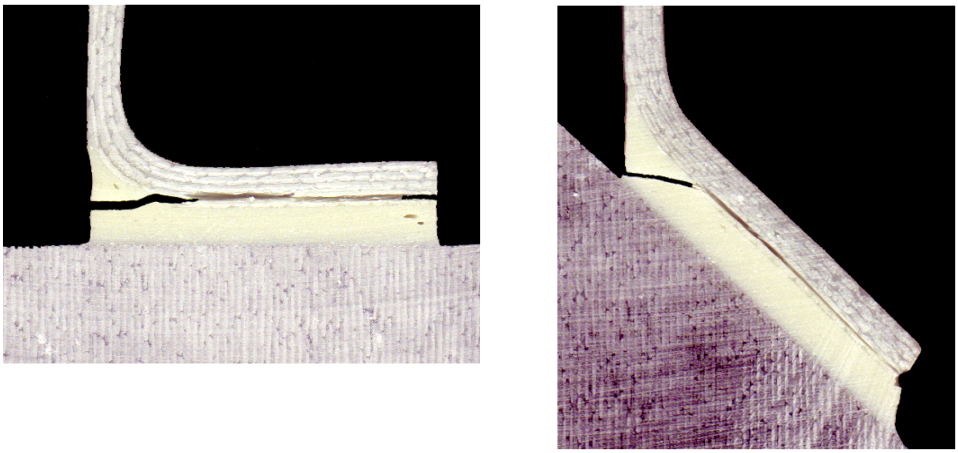

Figure 30. Typical failed specimens of Geometries A (right) and B, edge view.

3.2.7 Spar Cap Split Tests

The edges of the fabricated plates were trimmed off to eliminate any edge composition variability, ensuring representative, uniform material properties. The trimmed plates were then cut to produce flat rectangular coupons for testing. The plates were cut into rectangular 127 mm by 89 mm coupons, shown in Figure 31, with a 20 cm diameter diamond coated blade rotating at 3450 rpm (36 m/s), which was water cooled and lubricated. The feed rate of the composite plates during cutting was less than approximately 2 mm/second to ensure clean, perpendicular cut edges. The initial crack was sharpened with a razor blade.

Tests were performed on an Instron 8562 servo electric universal testing machine at a linear displacement ramp rate of 1.5 mm/minute under tensile loading. An extensometer was used as the crack opening displacement (COD) measurement device across the precrack.

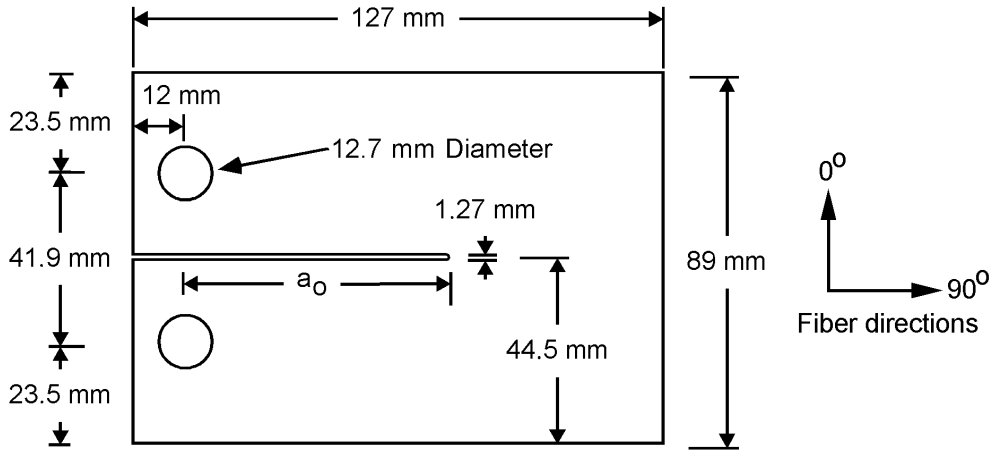

Figure 31. Spar cap split test coupon geometry.

3.3 Fatigue Models and Data Reduction

Data reduction for standard laminate fatigue tests includes least squares fitting of the fatigue trends with a power law model (Eq. 10) illustrated for a DD series material dataset in Figure 32, which compares the power law fit to exponential (Eq. 1) and three-parameter (Eq. 11) models. The power law provided a better fit to the fatigue data than the exponential model in most cases investigated, discussed later; cases where the exponential model (Eq. 1) provided an improved fit include some low amplitude R-values, carbon hybrid laminates and, laminates with ply drops. The exponential model tends to better fit the low cycle and static data as shown, but the power law provides a better fit to the higher cycle data, and has also been shown to represent small impregnated glass strand data to 10^{10} cycles [4]. The three-parameter model shown provides an improved fit to the overall dataset, but does not provide a consistent set of fitting parameters compared to the power law, and is inconvenient to manipulate [58, 59]. Most of the datasets in this study are fit by Eq. (10) to the fatigue data for cycles above about 10^3; the fits represent the mean lifetimes. The fits include static data for most carbon laminates except material P2B, due to improved fits for the relatively less steep S-N curves. Other representations such as the 95/95 confidence limits for these datasets can be found in the Appendix.

$$S = A\, N^B \tag{10}$$

$$S_O - S = aS\left[\frac{S}{S_O}\right]^b (N^c - 1) \tag{11}$$

where S is the maximum applied stress, S_O is the ultimate tensile or compressive strength (obtained at a strain rate similar to the fatigue tests), N is fatigue cycles, and A, B, a, b, and c are the fitting parameters. Additionally, for Eq. (11), the maximum stress value extrapolated to 10^9

cycles was kept within 10% of the extrapolated stress from a power law fit to the data for cycles above 10^3 [58].

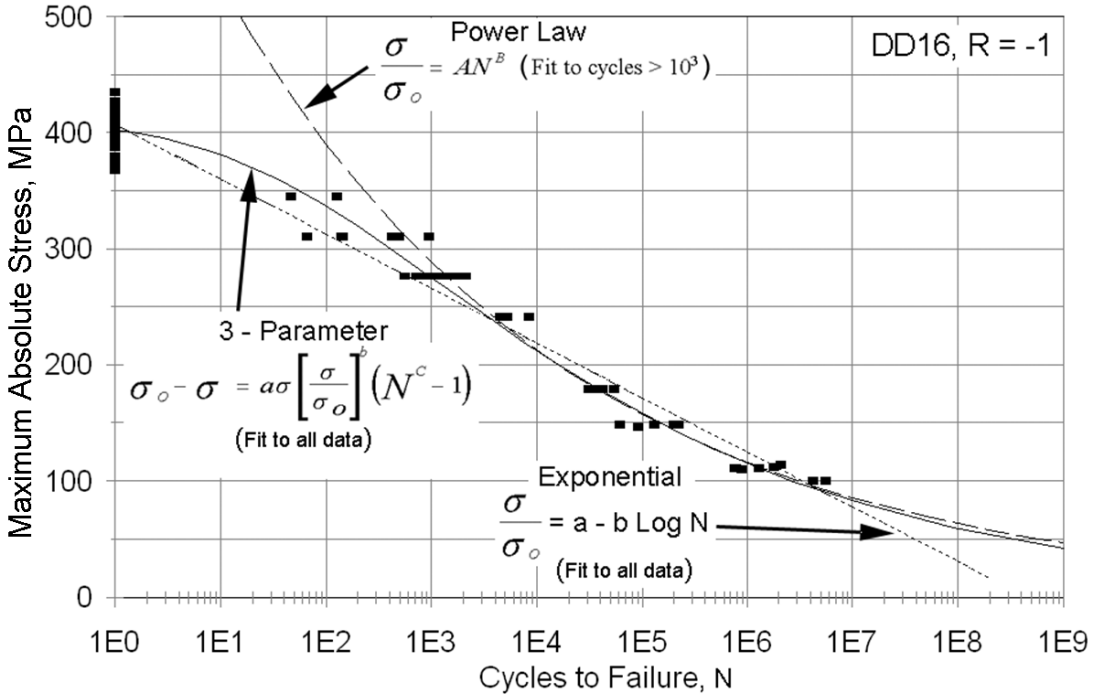

Figure 32. Material DD16, R = -1 S-N dataset with three curve fits, glass/polyester laminate (shown with static compressive strength).

A statistical treatment to establish 95/95 confidence limits [60, 61] has been carried out for the more complete datasets for materials QQ1 (glass) and P2B (hybrid). The confidence limits were established on the log stress (or log strain) relative to the mean power law fit (Eq. 10) following Echtermeyer et al. [62]. This representation allows inclusion of the static (one cycle) strength values in the fits, which can be useful for some very flat fatigue curves, as for carbon, described later. Equation 12 gives the mean fit on a log stress-log cycles plot

$$\log_{10}(S(N)) = m \cdot \log_{10}(N) + b \tag{12}$$

The standard deviation is then determined from individual data points, log S_i and log N_i as:

$$SD = \sqrt{\frac{1}{n-1}\sum_{i=1}^{n}\left(\log_{10}(S_i) - m \cdot \log_{10}(N_i) + b\right)^2} \tag{13}$$

Using the one sided tolerance limit multiplier, $c_{1-\forall,(}$, where the confidence level is 1-$\forall$ and the probability of survival is (, the tolerance limit is [2,5]:

$$S_{CL}(N) = 10^{\left(\log_{10}(N) + b - c_{1-\alpha,\gamma} \cdot SD\right)} \tag{14}$$

In the results, the intercept, b, in Eq. 12 and the term $c_{1-\forall,(}$ · SD in Eq. 14 are combined into a term "b-tol" resulting in:

$$S_{CL}(N) = 10^{(\log_{10}(N)+(b-tol))} \tag{15}$$

The same procedure is used to find the confidence limit for the static strengths.

Figure 33 shows typical mean and 95/95 fits to a material DD16 tensile fatigue dataset using Eqs. (10) and (15), comparing this treatment with the 95/95 fit using a three-parameter model to fit the mean data and 95/95 confidence limits based on log cycles [63]. The agreement between the two 95/95 lines is good over the range of the fatigue data (as noted above, the three parameter mean fit is more accurate for S-N datasets which are nonlinear at low cycles, such as the reversed loading dataset for the same material in Figure 32).

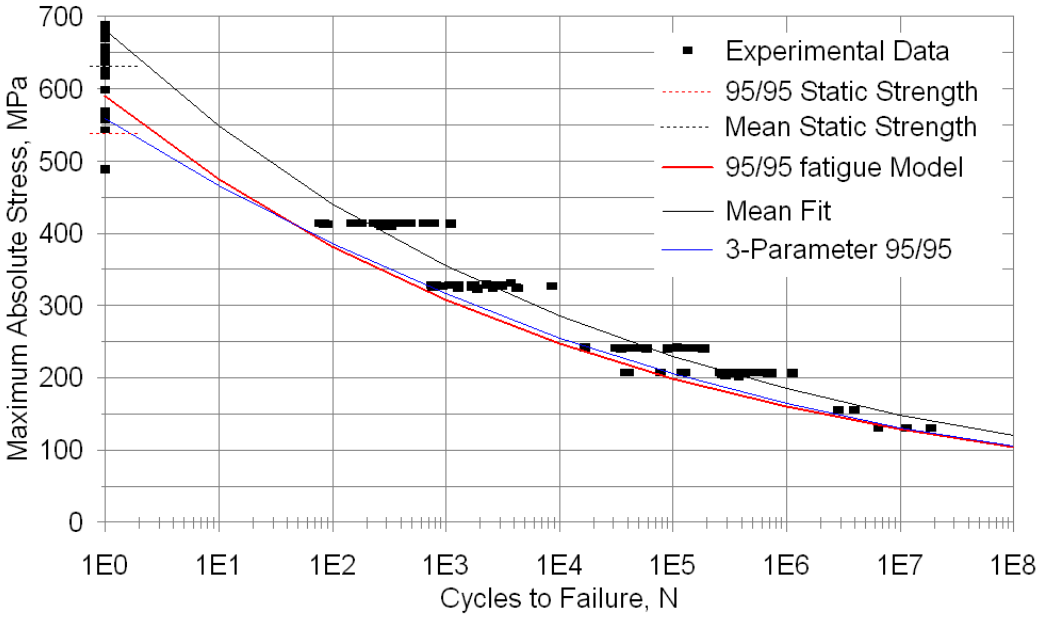

Figure 33. Typical stress vs. cycles to failure dataset showing mean and 95/95 Fits, and 95/95 fit from a log cycles model using a three-parameter S-N model [63], R = 0.1, material DD16, axial direction.

SECTION 4. BLADE LAMINATE RESULTS

4.1 Summary

This section provides an overview of the results of recent studies of plain composite laminates (plain indicating the absence of structural details or artificial flaws) of interest for wind turbine blade construction. Materials included are representative of current infused and prepreg blades with fiber volume fractions in the 50-60% range for unidirectional fabrics, usually slightly lower for biax ($\pm 45^o$) fabrics; lower fiber content materials have been reported in earlier contractor reports [5-7]. Static and fatigue results are presented for glass, carbon and WindStrand™ fibers in various fabrics and prepreg and epoxy, polyester, and vinyl ester resins. Laminates were prepared by MSU, blade manufacturers and materials suppliers using processes including vacuum assisted resin transfer molding (VARTM), infusion using flow medium layers or SCRIMP™, and vacuum bag prepreg processes. Specific processes are discussed in Chapter 3.

Test results are presented for static and fatigue properties of two types of laminates: multidirectional and biax. Multidirectional laminates contain varying amounts of both 0^o and $\pm 45^o$ plies, where the 0^o plies are predominantly unidirectional strands; the properties of multidirectional laminates tend to be dominated by the unidirectional fibers. The biax laminates contain only $\pm 45^o$ biax fabrics, which may also contain small amounts of 0^o or 90^o strands or chopped mat, and are more resin dominated in properties. Fabric construction details are given in Table 2.

Important differences in performance are shown for the major fiber and resin types. Details of fabric construction, fiber content and processing also produce major differences in performance, particularly under fatigue loading. Materials and conditions are identified where failure can occur at particularly low strain levels at high cycles.

4.2 Static Properties

Unidirectional laminate tests establish ply properties for use in analysis such as FEA. Table 6 lists ply properties for several fabrics and prepregs of current interest. The essential static stiffness property provided by the fibers is the elastic modulus in the longitudinal direction of the 0^o plies, E_L, compared in Table 7 for several glass, WindStrand and Carbon unidirectional laminates; data are normalized proportionally with fiber volume fraction to 53% fiber (actual unidirectional laminates varied from 53 to 57 %). The advantage of the higher modulus (and higher cost) WindStrand and carbon fibers is evident. This advantage is diluted somewhat as biax plies are added to form multidirectional laminates.

Carbon fiber laminates were noted earlier as having great advantages in terms of stiffness and strength, as is evident in Table 6 and will be discussed later. The strain performance of carbon is limited relative to glass, particularly in static loading. Compression ultimate strains fall well below 1.0 % in the presence of fiber waviness, even at the low levels inherent in many infusion fabrics [4]. An encouraging result for direct strain measurements on a blade containing carbon laminate has been reported in a Sandia study [64], with recorded compression strain values exceeding 0.8% before blade failure.

Table 6. Measured ply properties in material principle directions for E - Glass and Carbon prepregs and infused fabrics (static longitudinal, transverse, simulated shear).

Laminate Definition			Longitudinal Direction								Shear
			Elastic Constants				Tension		Compression		
	lay-up	V_F %	E_L GPa	E_T GPa	υ_{LT}	G_{LT} GPa	UTS_L MPa	ε_{max} %	UCS_L MPa	ε_{min} %	τ_{TU} MPa
VARTM Fabric/resin											
Fabric B/EP-3	$[0]_2$	52	38.4	12.0	0.27	----	863	2.71	-583	-1.58	----
Fabric C/EP-3	$[0]_2$	60	45.9	15.8	0.26	----	1233	2.80	-676	-1.65	----
Fabric D/EP-3	$[0]_2$	54	41.8	14.0	0.28	2.63	1151	2.97	-740	-1.79	30
Fabric L/EP-3	$[\pm45]_4$	51	13.8	11.8	----	----	95.4	1.46	-166	-1.44	----
Fabric M/EP-3	$[\pm45]_4$	44	13.6	13.3	----	----	144	2.16	-213	-1.80	----
Prepreg											
NB307-D1 7781 497A Glass	0/90	39	19.2	19.2	0.13	3.95	337	2.21	-497	-2.60	115
NCT307-D1-34-600 Carbon	$[0]_4$	53	123	8.20	0.31	4.71	1979	1.32	-1000	-0.90	103
NCT307-D1-E300 Glass	$[0]_4$	47	35.5	8.33	0.33	4.12	1005	2.83	-788	-2.22	112

Notes: All coupons for this Table were tested at 0.25 mm/s, with a 100 mm gage length. Compression tests used a 13 mm gage length with unsupported edges following ASTM D6641.
E_L - Longitudinal modulus, υ_{LT} - Poisson's ratio, G_{LT} and τ_{TU} - Shear modulus and ultimate shear stress from a simulated shear (±45) ASTM D3518 test. UTS_L - Ultimate longitudinal tensile strength, ε_{MAX} - Ultimate tensile strain, UCS_L - Ultimate longitudinal compressive strength. ε_{MIN} - Ultimate compressive strain.

Laminate Definition			Transverse Direction			
			Tension		Compression	
	lay-up	V_F %	UTS_T MPa	ε_U %	UCS_T MPa	ε_U %
VARTM Fabrics						
Fabric B/EP-3	$[0]_2$	52	66.7	0.63	-197	-1.40
Fabric C/EP-3	$[0]_2$	60	41.9	0.29	-150	-0.98
Fabric D/EP-3	$[0]_2$	54	59.0	0.46	-202	-1.47
Fabric L/EP-3	$[\pm45]_4$	51	94.7	1.11	-157	-1.50
Fabric M/EP-3	$[\pm45]_4$	44	87.5	1.61	-203	-1.68
Prepreg						
NB307-D1 7781 497A	0/90	39	337	2.21	-497	-2.60
NCT307-D1-34-600 Carbon	$[0]_4$	53	59.9	0.76	-223	-2.72
NCT307-D1-E300 Glass	$[0]_4$	47	51.2	0.74	-168	-2.02

Table 7. Comparison of unidirectional longitudinal elastic modulus for several fabrics and carbon prepreg (normalized to a fiber volume fraction of 53%).

Fabric or Prepreg	Fiber	Matrix	0^O Ply Modulus, E_L, at $V_f = 53\%$, GPa
Fabric B	E-glass	EP-3	42.5
Fabric D	E-glass	EP-3	41.6
NCT307-D1-34-600	Carbon	Epoxy	123
WS1, 0^o plies	WindStrand	EP-1	48.3

Table 8. Comparison of displacement rate effects on mean strengths (rates represent standard static and fatigue displacement rates in the axial direction).

Laminate	Tensile Strength, 13 mm/s (MPa)	Tensile Strength, 0.02 mm/s (MPa)	% Difference
QQ1	869	691	-21
DD16	632	549	-13
WS1	865	754	-13
TT-TPI-EP	837	732	-13
P2B	1546	1516	-2
DH	224	164	-27
DTR1	214	210	-2
45D	238	197	-17
45D2	207	167	-19
SWA	174	124	-29
WS1	223	157	-30

Typical static stress-strain curves are presented in Figures 34-40. Figures 34 and 35 compare the tensile and compressive stress-strain curves for a typical multidirectional laminate in the longitudinal direction, along with the component 0^o and $\pm 45^o$ plies. As noted in Figure 2 and Table 1, the actual local fiber content of biax and mat layers in infused multidirectional laminates are well below that in the more closely packed uni-plies. The multidirectional laminate stress-strain curves are dominated by the 0^o plies in terms of modulus and failure strain. However, the nonlinear $\pm 45^o$ (biax) plies contribute to the slight nonlinearity of the multidirectional laminate behavior in tension, as matrix cracking develops in these plies well before failure of the 0^o fibers. The process of matrix crack accumulation and material softening is typical of multidirectional laminates in tension [5-7, 65]. Compression failure in the 0^o plies generally occurs before wide-scale matrix cracking is observed in the $\pm 45^o$ plies, but after the response becomes nonlinear. Laminate static modulus, strengths and ultimate strains are listed with the fatigue parameters in Table 9.

Static data are determined both for standard displacement rate, 0.02 mm/s, and also at a faster rate, 13 mm/s, representative of the displacement rate in fatigue. As indicated in Table 8 for

typical laminates, this approximately three orders of magnitude rate difference produces a 13-21% strength increase for the glass laminates with 0^o strands at the high rate; rate effects are small for carbon (2% increase), and some biax fabrics. Rate effects on static strength values should be considered carefully in using results such as S-N datasets and constant life diagrams. For example, while static data at the faster rate are generally used with the datasets in this study (specified in each case) and indicated in the database, the slower, standard static strength testing rate was used in the OPTIMAT program [2, 10].

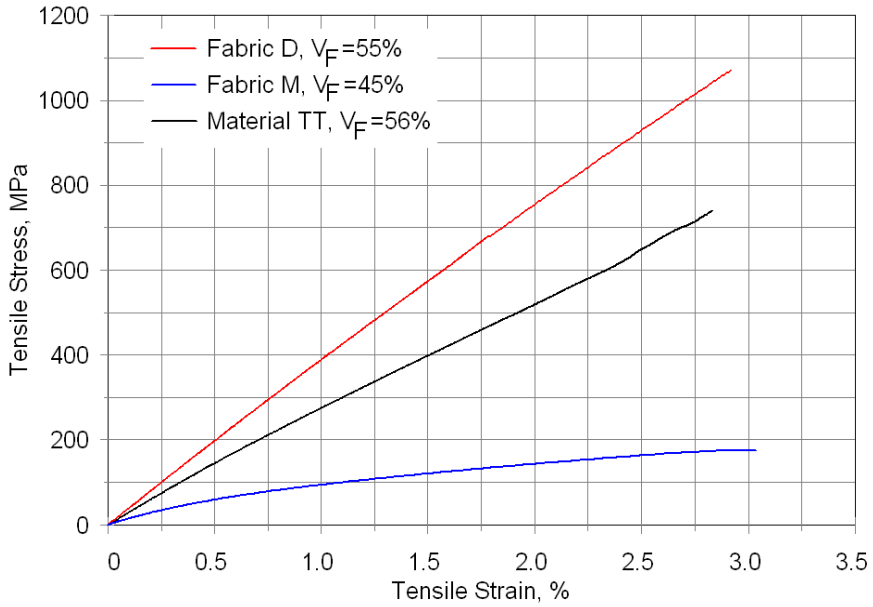

Figure 34. Tensile stress-strain curves for laminate TT in the axial direction, with epoxy EP-1, comparison with component 0^o and $\pm 45^o$ plies.

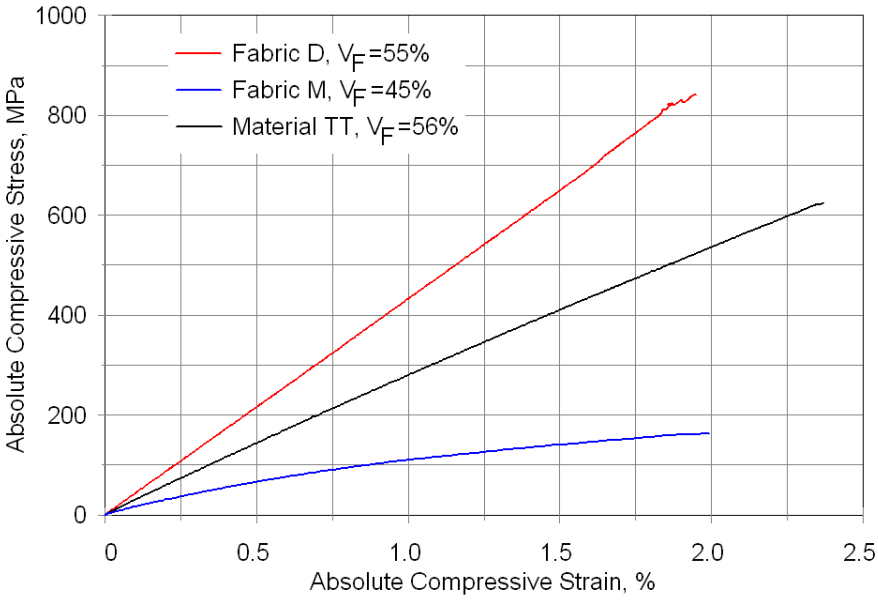

Figure 35. Compressive stress-strain curves for laminate TT in the axial direction, with epoxy EP-1, comparison with component 0^o and $\pm 45^o$ plies.

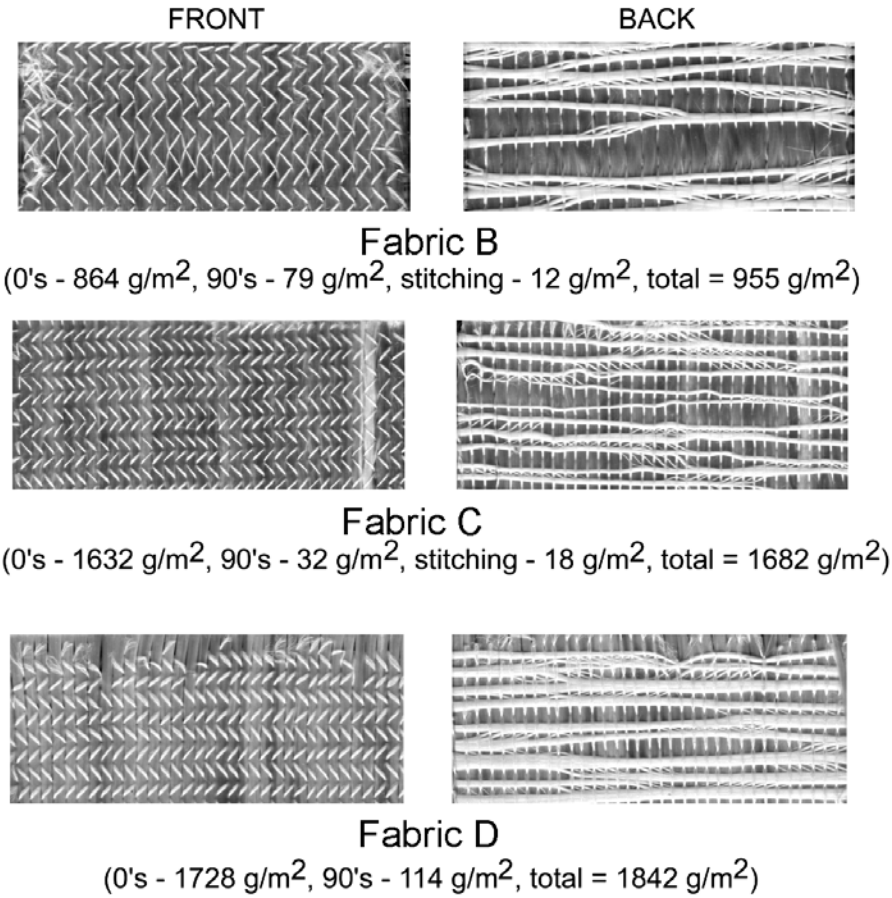

Figure 36. Photographs of front and back of unidirectional fabrics B, C and D (Table 2).

Unidirectional fabric laminates are much weaker when tested in the transverse direction, depending on the content of mat or transverse material added in fabric construction (Table 2). Figure 36 is a photograph of the two sides of fabrics B, C, and D, showing the irregular construction on the backside of the unidirectional fabrics. These "warp unidirectional" fabrics contain the primary 0^{O} strands in the warp, or long direction of the fabric roll. The transverse strands are in the "weft", or transverse direction of the fabric roll. Figure 37 compares the transverse tensile stress-strain curves for fabric D unidirectional laminates for resins EP-1 and UP-3, and gives a simulated shear stress-strain curve with resin EP-1. The apparent knee in the curves identifies the strain where cracking occurs along the primary fabric strands; the specimen is then held together by the few transverse strands until failure, at a much reduced modulus. The epoxy shows a clear advantage over polyester in increasing the knee stress and strain where transverse cracking occurs. The simulated shear response shows matrix cracking above where the curve becomes significantly nonlinear. Figure 38 gives a comparison of axial and transverse stress-strain curves for two multidirectional laminates.

Laminates containing only biax (±45) fabric of three types have been tested with several resins (Figures 39 and 40). While fabric construction and direction have significant effects in Figure 39 (a and b), the resin has limited effect for a particular fabric (Figure 40). Matrix cracking accumulates above where the tensile curves become nonlinear (see Figure 42), and intensifies to

include delamination prior to failure. The compressive tests showed little matrix cracking prior to failure despite significant nonlinearity.

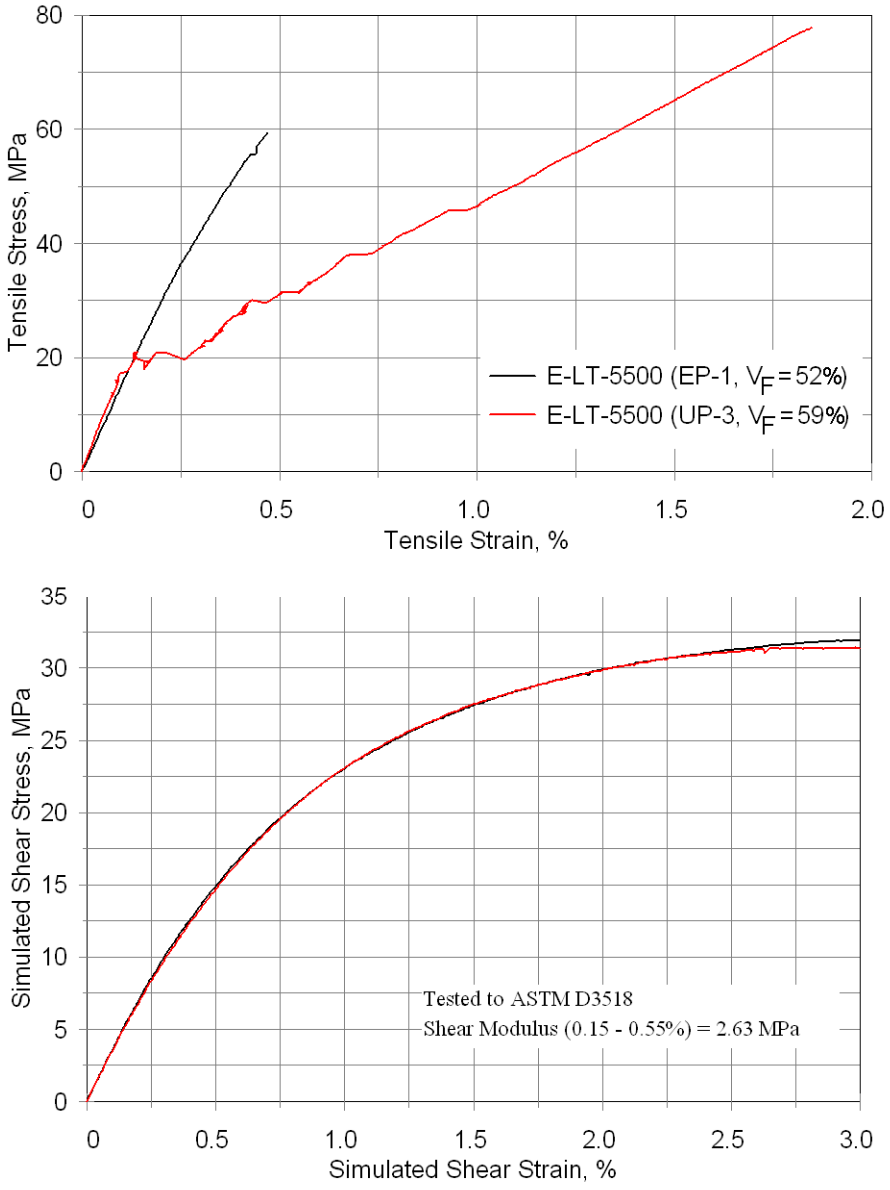

Figure 37. Transverse and shear stress-strain curves for fabric D laminates: (top) transverse tensile stress-strain curves for unidirectional fabric D laminates with epoxy EP-1 and polyester UP-3; (bottom) simulated shear stress-strain curve with epoxy EP-1.

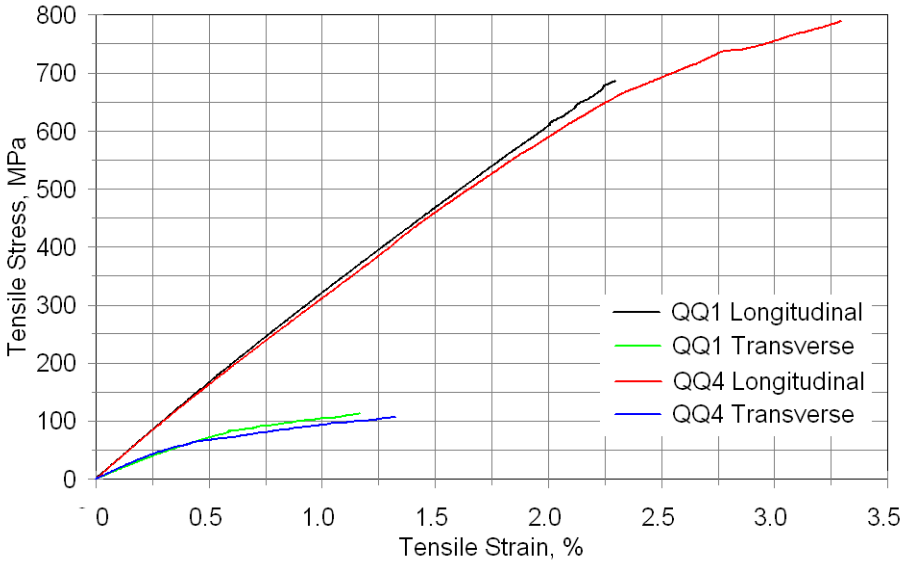

Figure 38. Axial and transverse tensile stress-strain curves for multidirectional laminates QQ1 and QQ4.

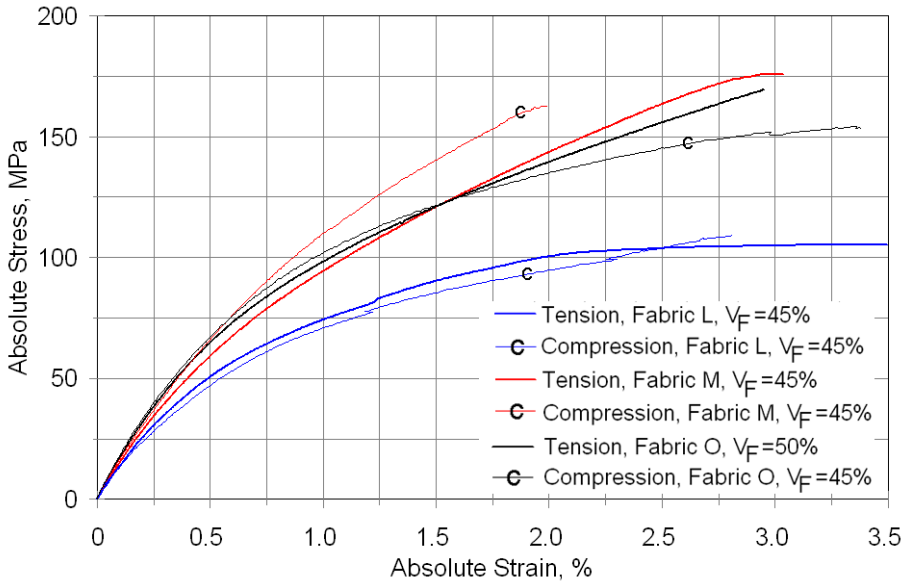

Figure 39a. Tensile and compressive stress-strain curves for biax fabrics; L , M, and O in the warp direction, epoxy EP-1.

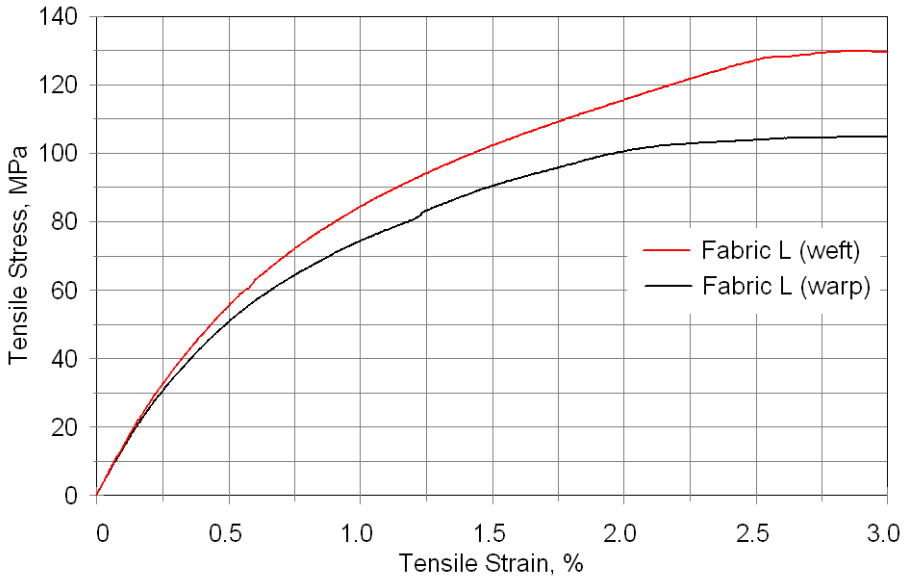

Figure 39b. Tensile stress-strain curves for biax fabric L in the warp and weft directions, epoxy EP-1.

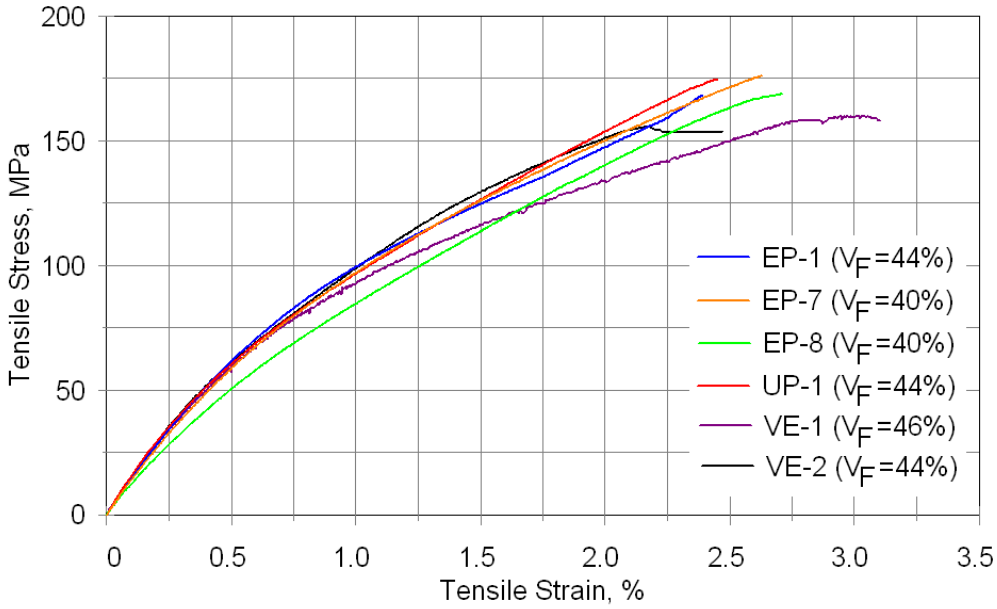

Figure 40. Comparison of tensile stress-strain curves for biax fabric M laminates with several resins, warp direction.

4.3 Fatigue Results for Multidirectional Laminates

4.3.1 Effects of fiber type

Figure 41 gives a comparison of the tensile stress and strain based fatigue resistance in tension (R = 0.1) and compression (R = 10), for four laminates representing three main fiber types, all with epoxy resins: glass, QQ1 and TT-TPI-EP; WindStrand^{TM}, WS1 and WS2; and carbon prepreg hybrid, P2B. The laminates have differing contents of 0^o plies relative to $\pm 45^o$ plies, slightly different fiber contents, and different processing, as defined in Table 2. Table 9 gives the average static modulus, strength and ultimate strain data as well as the fatigue curve fit parameters for various materials. Notable differences in fatigue performance are that the carbon hybrid is superior in terms of stress, and shows a much less steep fatigue curve compared to the glass fiber materials at R = 0.1 (tension). The compression fatigue curve for carbon is again less steep. Of the glass laminates, QQ1 is notably less tensile fatigue resistant, as discussed in the next section, and TT-TPI-EP is less compression fatigue resistant. WindStrand^{TM} is generally similar to the best of the glass laminates in each case, but slightly stronger in terms of stress, in tension. The aligned strand structure of the WindStrand^{TM} WS1 and WS2 laminates may be advantageous compared with stitched fabrics used for QQ1 and TT-TPI-EP. By way of comparison, E-glass laminates MD2 in the European OPTIMAT program, fabricated by blade manufacturer LM, show slightly lower failure strains in tension than TT-TPI-EP, with a similar trend; these laminates were infused uni-fabric (0^o strands stitched to mat, Combimat 1250) as well as $\pm 45^o$ fabric [2].

The failure sequence for all of the laminates in tension started with matrix cracking in the $\pm 45^o$ plies, shown in Figure 42, as is commonly observed for most multidirectional polymer composites as noted in the previous section under static properties. The matrix damage can significantly reduce the modulus, increasing the strain in the constant stress amplitude tests [5, 6]. Matrix damage for the more tensile fatigue resistant laminates like WS1 and TT-TPI-EP was excessive prior to total failure (see Fig. 13, specimen TT-6). Compression fatigue failures were sudden, with little matrix cracking before total failure.

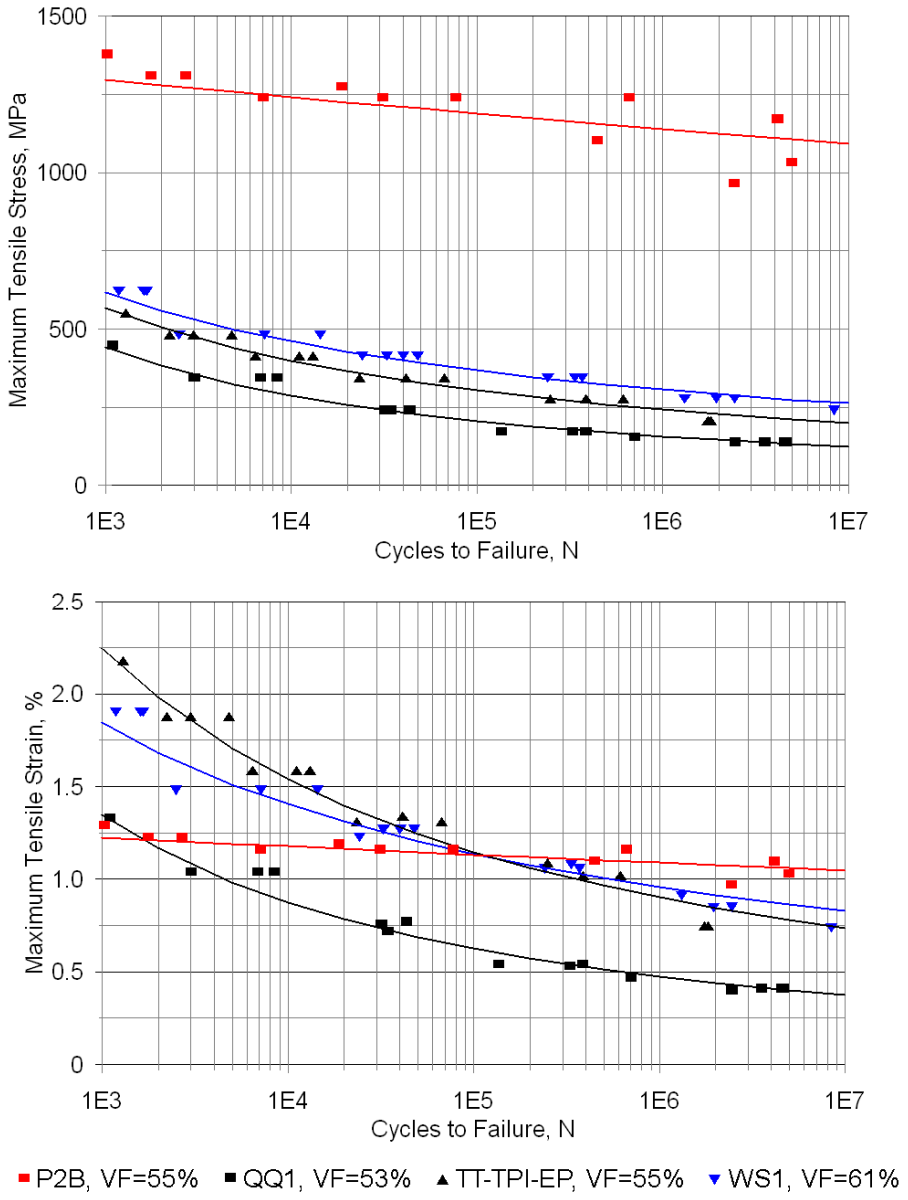

Figure 41a. Tensile fatigue comparison of multidirectional laminates based on E-glass (QQ1 and TT-TPI-EP), WindStrand™ (WS1) and carbon (P2B) fibers at similar fiber contents, in terms of stress (top) and strain (bottom), epoxy resins, R = 0.1.

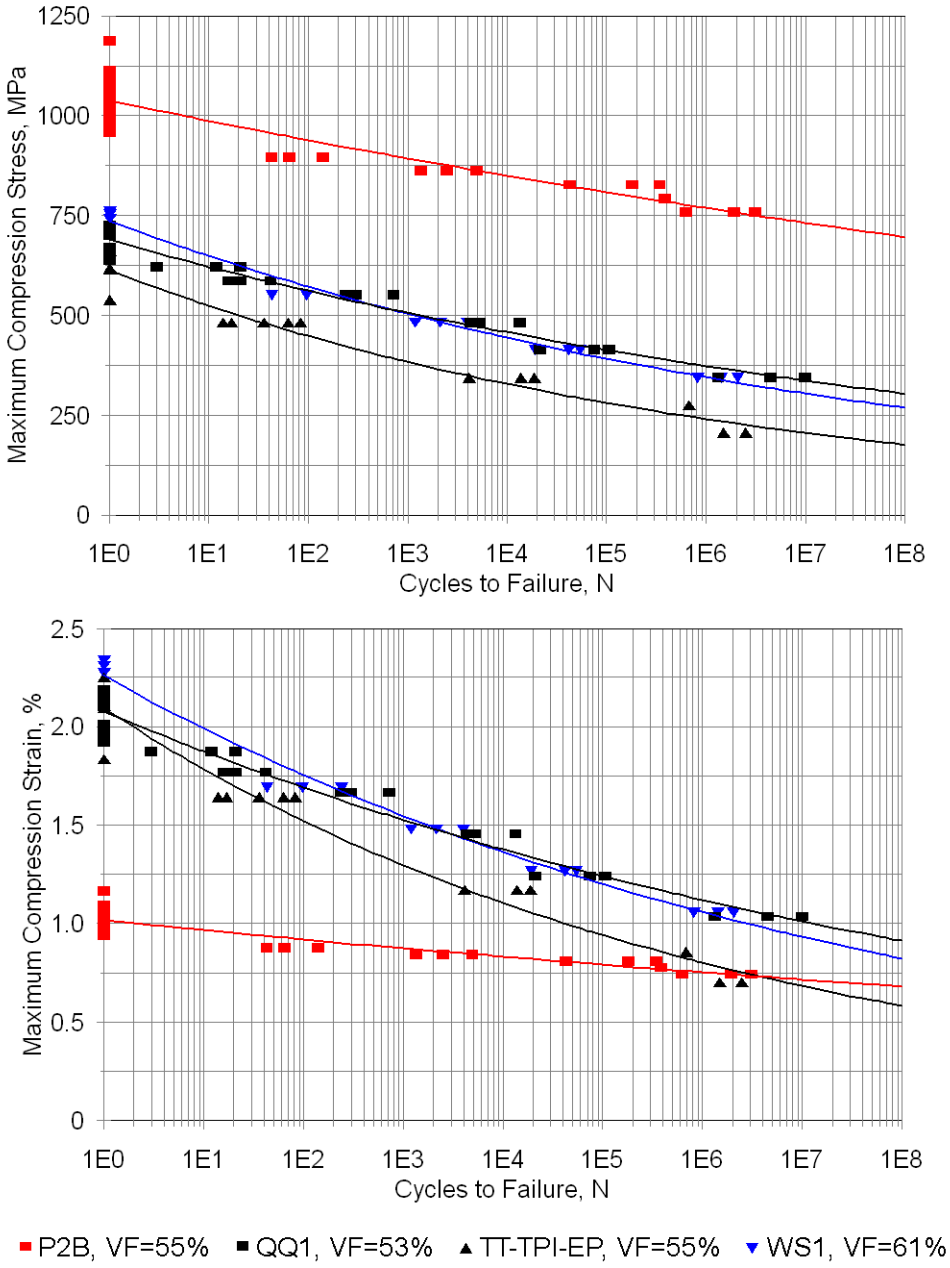

Figure 41b. Compressive fatigue comparison of multidirectional laminates based on E-glass (QQ1 and TT-TPI-EP), WindStrand™ (WS1) and carbon (P2B) fibers at similar fiber contents, in terms of stress (top) and strain (bottom), epoxy resins, R = 10.

Table 9. Average static data and fatigue fit parameters.

Material	V_f %	R	Static* Strength, MPa	Ultimate Strain, %	Elastic Modulus, GPa	10^6 cycle strain, % (from fit eqn.)	Eq. 10 Mean Fit Parameters**			
							Strain		Stress	
							A	B	A	B
QQ1	53	10	-683	-2.05	----	-1.12	2.078	-0.0447	690	-0.0445
		-2				-0.92	2.111	-0.0604	698	-0.0600
		-1				0.43	2.557	-0.1289	931	-0.1378
		-0.5				0.51	3.535	-0.1405	1173	-0.1407
		0.1				0.47	4.032	-0.1558	1328	-0.1556
		0.5	843	2.56	33.1	0.71	3.426	-0.1136	1359	-0.1313
QQ1T	53	10	-274	-1.59	----	-0.76	1.380	-0.0431	281	-0.1042
		-2				-0.38	1.628	-0.1044	281	-0.1042
		-1				0.20	1.014	-0.1171	175	-0.1170
		-0.5				0.21	0.961	-0.109	166	-0.1087
		0.1				0.28	0.841	-0.0806	145	-0.0806
		0.5	149	0.86	17.1	0.23	0.896	-0.0976	155	-0.0709
		0.7				0.42	0.8138	-0.0480	141	-0.0480
QQ2	52	0.1	552	2.50	23.3	0.63	3.731	-0.1288	735	-0.1216
QQ4	57	0.1	986	3.10	31.8	0.59	3.589	-0.1313	1048	-0.1263
		10	-601	-1.89		-0.82	2.331	-0.0759	742	-0.0759
QQ4L	40	0.1	673	3.13	21.5	1.15	4.474	-0.0983	939	-0.0979
QQ4M	46	0.1	790	3.09	25.6	0.76	5.038	-0.1372	1071	-0.1284
DH	42	0.1	224	----	13.4	0.53	3.790	-0.1420	225	-0.0920
	42	10	-212	----	13.4	1.02	1.610	-0.0330	211	-0.0600
	42	-1	----	----	13.4	0.38	2.110	-0.1240	172	-0.0960
DTR1	44	0.1	214	----	17.7	0.41	3.292	-0.1500	208	-0.0980
45D	46	0.1	239	----	16.9	0.44	2.886	-0.1360	239	-0.0900
45D2	44	0.1	207	----	15.2	0.43	4.586	-0.1710	208	-0.0890
DE 2	40	0.1	220	----	13.5	0.55	3.690	-0.1377	242	-0.1002
DE 4	40	0.1	215	----	13.1	0.75	3.675	-0.1151	216	-0.0829
SWA	45	0.1	172	----	11.9	0.73	3.99	-0.1230	174	-0.0690
	45	10	-176	-1.48	11.9	1.12	4.341	-0.0980	175	-0.0510
	45	-1	----	----	11.9	0.36	1.984	-0.1240	156	-0.1040
SLA	54	0.1	770	2.57	30.0	0.42	4.350	-0.1700	1035	-0.1500
SLB	43	0.1	588	2.59	22.7	0.34	4.720	-0.1900	1053	-0.1900
SLC	51	0.1	626	2.53	26.7	0.47	3.730	-0.1500	967	-0.1500

*Positive stress and strain = tensile. Negative stress and strain = compressive. ** Curve fits do not include static data except for materials MMWK-C/G-EP and CGD4E.

Table 9 (cont). Average static data and fatigue fit parameters.

Material	V_f %	R	Static* Strength, MPa	Ultimate Strain*, %	Elastic Modulus, GPa	10^6 cycle strain, % (from fit eqn.)	Eq. 10 Mean Fit Parameters**			
							Strain		Stress	
							A	B	A	B
TT-TPI-EP	55	0.1	837	3.36	29.4	0.89	5.322	-0.1301	1264	-0.1208
		10	-552	-1.88		-0.80	2.138	-0.0713	623	-0.0691
TT-TPI-VE	55	0.1	809	2.47	30.5	0.72	4.624	-0.1344	1146	-0.1384
		10	-670	-2.09		-0.94	2.527	-0.0712	811	-0.0712
TT (VARTM)	55	0.1	858	2.96	29.0	0.84	5.309	-0.1336	1523	-0.1327
TT (Infused)	48	0.1	842	2.82	26.7	0.79	6.270	-0.1500	1201	-0.1310
TT1A (VARTM)	55	0.1	899	3.24	27.7	0.97	3.965	-0.1023	1176	-0.1093
TT1AH	63	0.1	930	2.95	31.5	0.63	3.694	-0.1279	1163	-0.1301
WS1	61	0.1	865	2.72	32.6	0.98	2.902	-0.0787	932	-0.0778
WS2	61	10	-755	-2.31	32.6	-1.06	2.260	-0.0548	737	-0.0548
W45	49	0.1	223	----	16.8	0.68	2.560	-0.0960	206	-0.0690
P2B	54	10	-1047	-1.03	----	-0.76	0.9455	-0.0154	964	-0.0151
		-2				-0.58	1.089	-0.0451	1114	-0.0455
		-1				0.60	1.017	-0.0378	1038	-0.0379
		-0.5				0.72	0.9094	-0.0166	972	-0.0166
		0.1				1.09	1.424	-0.0194	1549	-0.0226
		0.5	1564	1.43	101	1.19	1.315	-0.0073	1406	-0.0073
MMWK C/G-EP	55	10	-873	-1.37	67.2	-0.70	1.377	-0.0485	874	-0.0410
CGD4E	43	10	-684	-0.81	86.2	-0.53	0.781	-0.0286	673	-0.0286

*Positive stress and strain = tensile. Negative stress and strain = compressive. ** Curve fits do not include static data except for materials MMWK-C/G-EP and CGD4E.

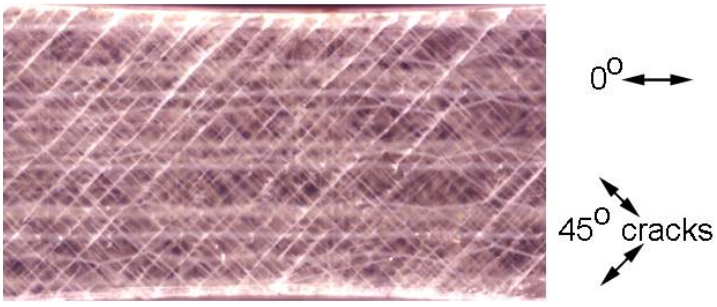

Figure 42. Cracking in ±45 plies of material QQ2 specimen prior to total failure.

4.3.2 Effects of resin type

Comparison of different resins with the same process, fiber content, and fabrics is not yet available for all multidirectional laminates in this general series; such a comparison is given later for the biax laminates. Figure 43a compares the tensile fatigue performance of the TT multidirectional glass laminate structure (±45/0/±45/0/±45, with fabrics M and D, Table 2) with carefully controlled infusion conditions for baseline resins epoxy EP-1 and polyester UP-1. The epoxy has a clear advantage over the polyester for this typical laminate layup. Results published recently [18] for the same laminate configuration with different resins and processing showed a similar difference, with vinyl ester (TT-TPI-VE) results intermediate between those for the epoxy and polyester resin laminates (Figure 43b). These comparisons clearly show a performance ordering of epoxy>vinyl ester>polyester for tensile fatigue of multidirectional laminates. Earlier data for lower fiber content laminates showed no significant difference between these three resin types using VARTM and DD series construction [5]. Compression fatigue results in Figure 44 show an advantage for vinyl ester over epoxy for these particular laminates [3].

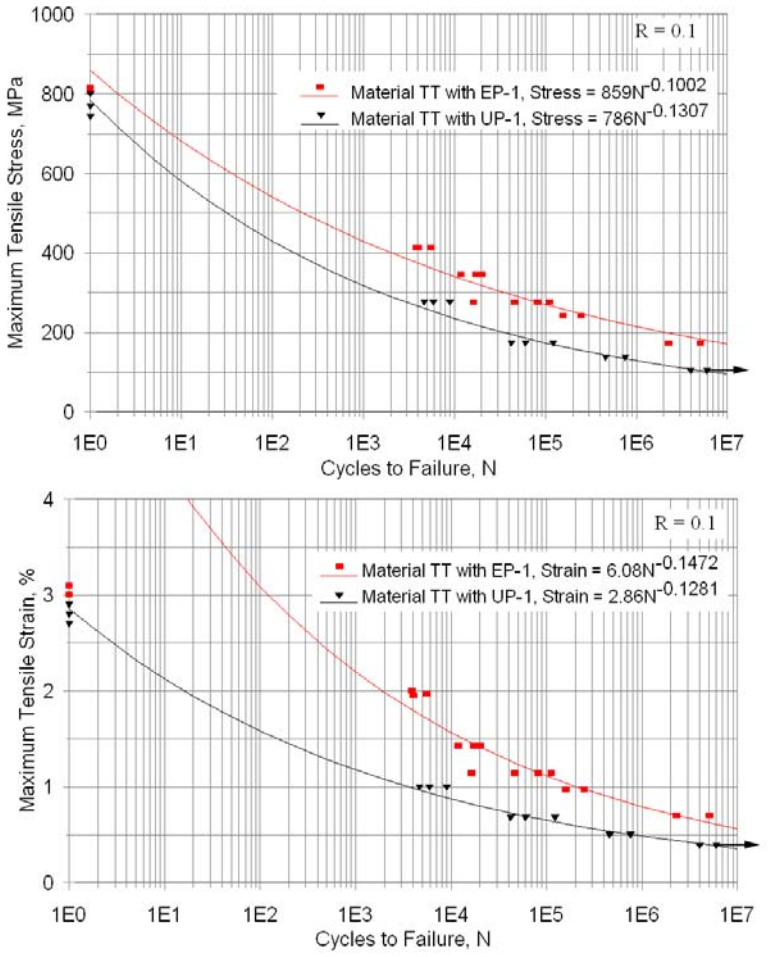

Figure 43a. Stress (top) and strain vs. log cycles data for (±45/0/±45/0/±45) multidirectional infused laminates containing fabrics D and M, TT-EP-1 (epoxy, V_f = 52%), TT-UP-1 (polyester, V_f = 52%), R = 0.1.

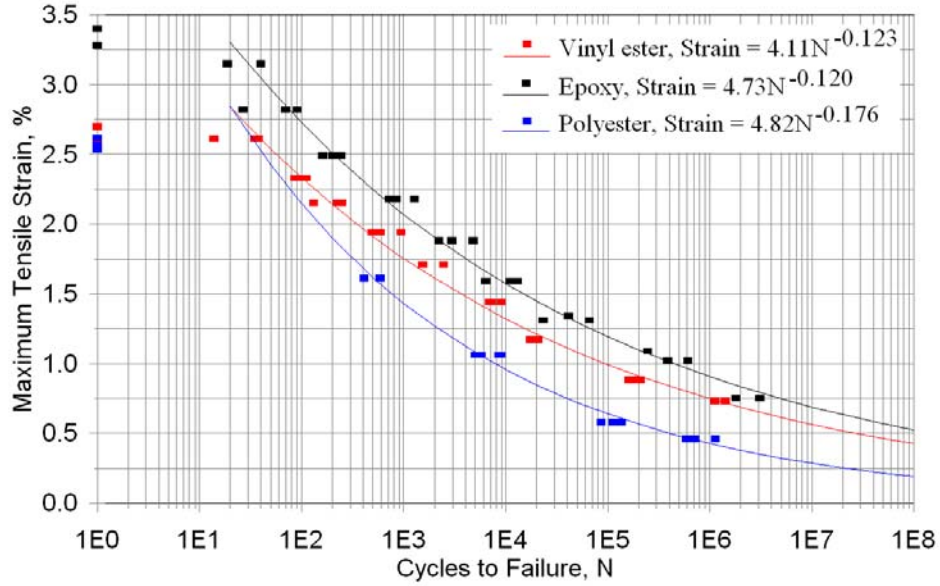

Figure 43b. Strain vs. log cycles data for (±45/0/±45/0/±45) multidirectional SCRIMP laminates containing uni-fabric D: TT-TPI-EP (epoxy), TT-TPI-VE (vinyl ester) and SLA (polyester).

4.3.3 Effects of Reinforcing Fabric, Resin and Process, Multidirectional Laminates

Glass Reinforcement, epoxy resins. Different materials based on different reinforcing fabrics (see Table 2) are compared in terms of the maximum tensile fatigue strain which can be withstood for a million cycles, determined from the curve fits in Table 9. Other measures of fatigue resistance such as the exponents of the S-N fits in Table 9 would show consistent trends. The results in Figure 45 for the VARTM processed QQ1, QQ2, and QQ4 series of laminates containing 0^o fabrics B and C show tensile fatigue resistance typical of many fabrics in this fiber content range, with improving resistance at lower fiber contents (QQ4L, $V_f = 40\%$), below the typical infused blade range [4, 7]. Figure 46 compares the tensile fatigue resistance of laminates based on unidirectional Fabric D; these perform much better under VARTM processing than those in Figure 45 except at the highest fiber content range (TT1A-H, $V_f = 63\%$), above the typical infused blade range. Figure 47 compares selected results (QQ1, QQ4 and TT-TPI-EP, V_f 53-57 %) from Figures 45 and 46; the SCRIMP processed TT-TPI-EP laminate based on unidirectional fabric D can withstand fatigue strains 50 to 100 % higher than those for the laminates based on the generally similar fabrics B and C. (Note that many other commercial fabrics from these and other manufacturers are available, but were not included in this study.)

The general trend of the results is clear for the DD Series laminates based on Fabric A, shown in Figure 48. As the fiber content increases (as determined by the mold opening in the VARTM process with hard molds on both sides), the fatigue resistance as represented by the million cycle strain decreases rapidly above about 40% fiber by volume. The strain capacity at higher fiber contents drops to less than half the value at lower fiber contents. At the other extreme, materials

based on fabric D retain good tensile fatigue resistance to above 55% fiber by volume, then drop above 60% fiber; these results approach those for prepreg and aligned strand laminates [5]. Fabric C in the QQ4 series laminates is very similar in construction and weight to fabric D, but when VARTM processed, shows a transition to lower fatigue resistance at much lower fiber contents, close to fabric A. The lighter weight but otherwise similar fabric B (materials QQ1 and QQ2) shows even lower fatigue strains than fabric C. Fabrics B, C, and D are shown in Figure 36. Of the data in Figure 48, only the TT-TPI-EP material follows current infusion methods; all other data are for VARTM with two sided hard molds, to which Fabric C appears sensitive, as noted later.

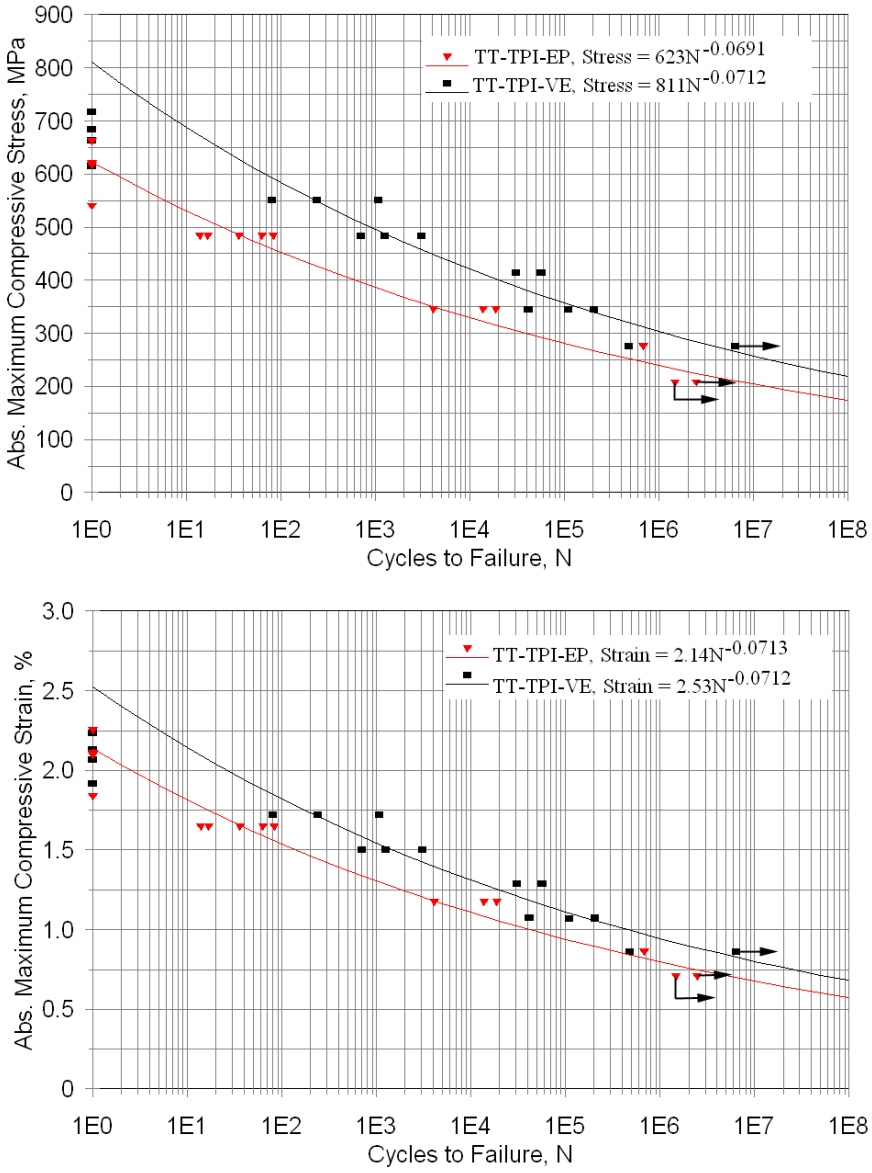

Figure 44. Comparison of compression fatigue S-N results for (±45/0/±45/0/±45) multidirectional SCRIMP laminates with epoxy (TT-TPI-EP) and vinyl ester (TT-TPI-VE) resins, based on Fabrics D and M, R = 10.

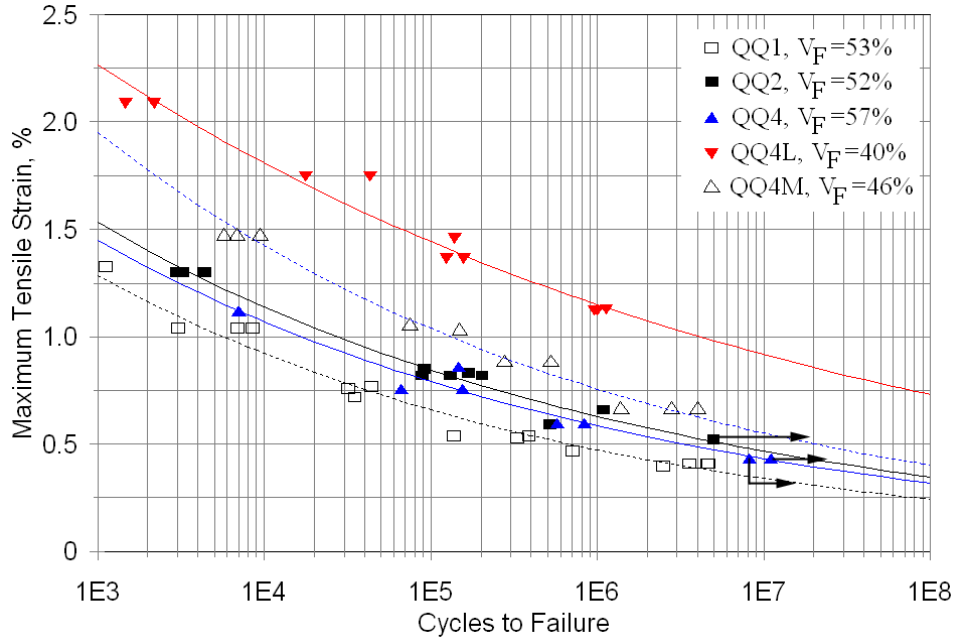

Figure 45. Tensile fatigue strain-cycles data for multidirectional laminates based on unidirectional fabrics B and C, VARTM processed.

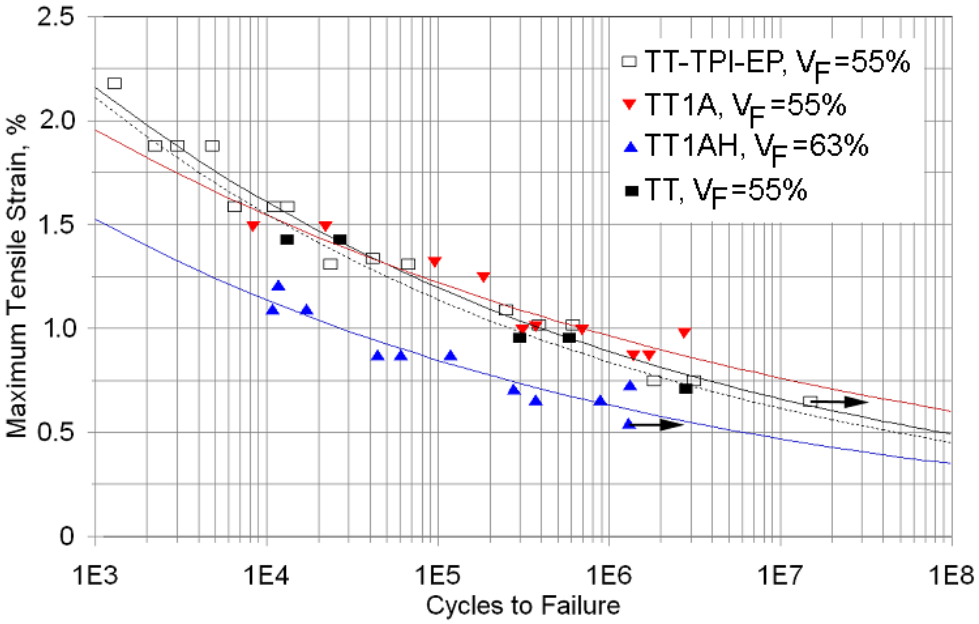

Figure 46. Tensile fatigue strain-cycles data for multidirectional laminates based on unidirectional fabric D, VARTM processed except TT-TPI-EP.

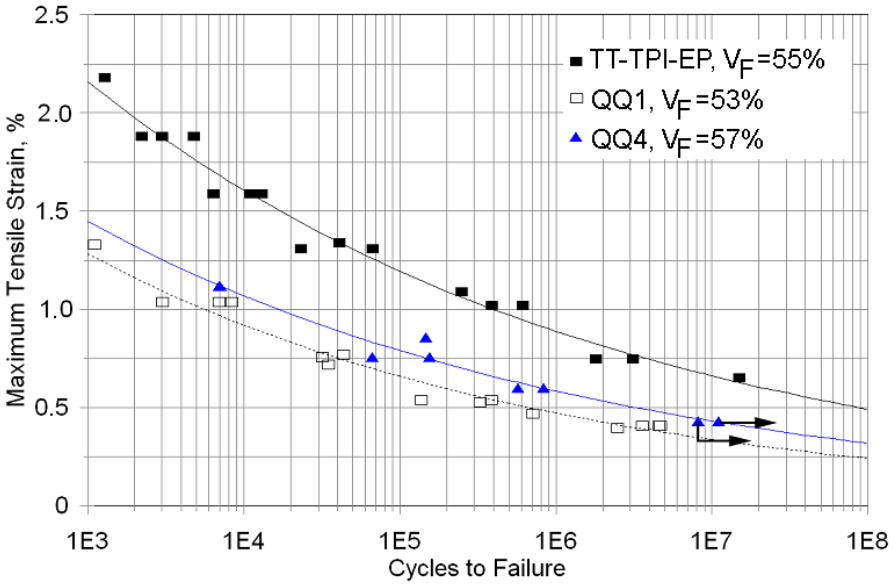

Figure 47. Comparison of tensile fatigue resistance for multidirectional laminates based on unidirectional fabrics B (QQ1), C (QQ4), both VARTM processed, and D (TT-TPI-EP), SCRIMP processed.

The differences in materials such as QQ1 and QQ4 (fabrics B and C) and TT and TT-TPI-EP (fabric D) at similar fiber contents (Figure 48) and overall fabric specifications (Table 2) is pervasive over entire panels and for different batches. No individual fatigue test results (Figure 45) for the more fatigue sensitive materials approach the worst performing specimens from the less fatigue sensitive materials (Figure 46) at the same strain level and fiber content range. This is observed despite similar static properties. Thus, the increase in fatigue sensitivity is not due to some form of occasional flaw, but is inherent in the gage section of every test specimen. The differences observed between these fabrics relates primarily to the extent of distortion (Figure 2) and compaction (Figure 6) in the strands when the fiber content is increased, apparently raising some local strand fiber contents sufficiently to reduce the fatigue resistance. The main advantage of fabric D appears to be in the stitching details rather than the general fabric specifications (Table 2). However, other factors including fiber sizing could also play a role. As noted later, the fatigue resistance of the TT and TT1A series may be reduced compared to TT-TPI-EP for some resins and process variations, and QQ4 is similar to TT when infusion processed.

In cross-section, fabrics C and D are densely packed compared with fabric A due to their rectangular strand cross-sections and large strands, with small inter-strand areas (Figure 2). The fiber content as a function of mold pressure has been determined (Figure 49) for Fabrics A, C, and D, following methods described elsewhere [4]. Fabrics C and D are very similar in terms of the fiber content reached as a function of mold pressure, while fabric A reaches much lower fiber contents for the same pressure. At low pressure conditions like 10-20 kPa, fabric A fiber content is around 40%, while fabrics C and D are around 55% fiber by volume; these ranges are typical of hand lay-up vs. infusion processes for which the fabrics are apparently designed. Transitions to poor fatigue resistance occur only as the fiber content is raised above the low pressure range for fabrics A and D, and for fabric C when infusion processed; however, the transition occurs well below this point for fabric B (VARTM and infusion) and fabric C (VARTM only), noted

later. Whether the fatigue resistance transitions demonstrated in Figure 48 would occur for one-sided molds used in infusion (Figure 8) is unknown, since the fiber content cannot easily be varied over a wide range for a particular fabric in this process. However, Fabric C showed marked improvement when infusion processed at 50% fiber volume content compared with the VARTM data in Figures 45-48. A tentative conclusion is that Fabric C is adversely affected when using two sided molding by VARTM, perhaps due to local compression at high points in the preform stack. Earlier data for many triaxial fabrics (one shown in Figure 4) showed poor fatigue resistance even at very low fiber contents, apparently due to local compaction at stitch points regardless of mold pressure [5, 6].

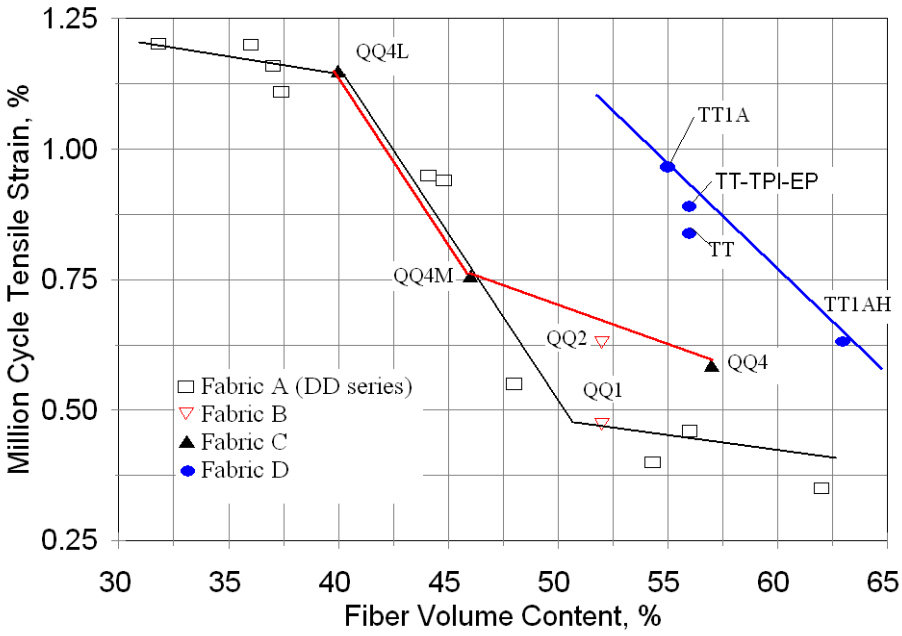

Figure 48. Million cycle strain vs. fiber volume content for various VARTM laminates and one SCRIMP laminate (TT-TPI-EP) showing transitions to reduced fatigue resistance as a function of 0^o fabric, R = 0.1.

Materials in the TT and TT1A series (Table 2), with the best tensile fatigue resistance of the various multidirectional laminates in Figure 48, and QQ4, which performs less well under VARTM processing, are the subject of on-going study to explore the effects of resin and processing. These laminates contain unidirectional Fabrics C and D with biax fabrics M and L which differ in that M contains mat while in L the $\pm 45^o$ strands are stitched to a light 90^o strand (warp direction), Table 2. Figure 50 gives tensile fatigue data for several batches, with variations in process type and epoxy resin. The data which are lowest in this figure are for the highest fiber contents, which are not controlled with infusion and SCPIMP processes. The infused QQ4 with fabric C is now similar to the various fabric D laminates in the 50% fiber content range, contrary to figures 47 and 48 where VARTM QQ4 was shown. However, infused QQ1 (with the lighter fabric B) showed only marginal improvement relative to the VARTM version in Figures 47 and 48. Differences in the fatigue resistance for the materials shown in Figures 48 and 50 relate to the survivability of the 0^o plies after cracking of the ± 45 plies; the more fatigue resistant laminates show severe damage, matrix cracking and sometimes ply delamination, in the ± 45 plies prior to

total failure, while the less fatigue resistant laminates show only localized damage near the failure site (see Figure 13, specimen TT-6, top, vs QQ1).

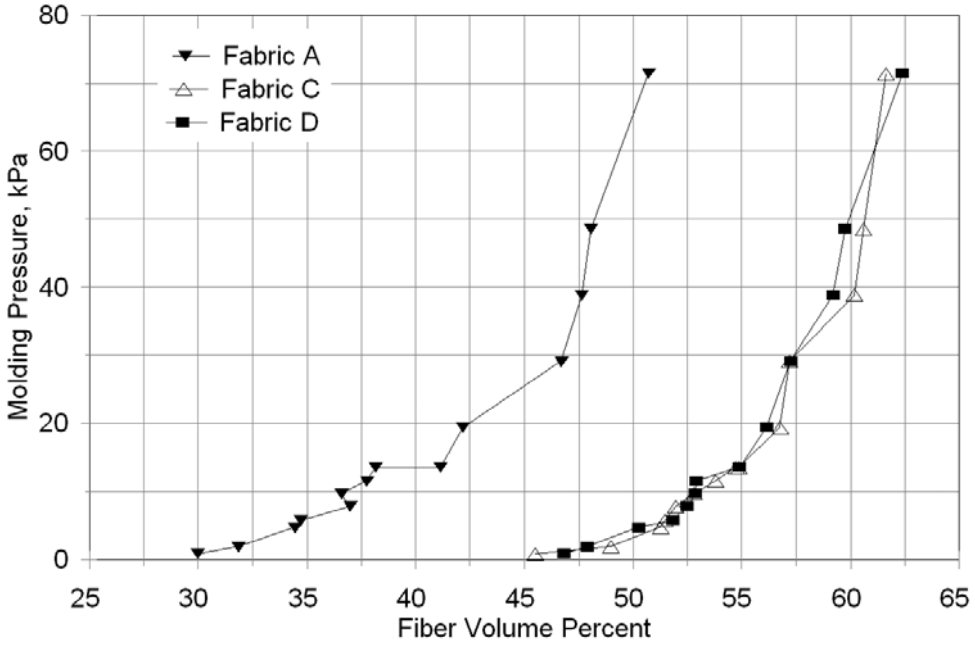

Figure 49. Mold pressure vs. fiber content for fabrics A, C, and D, measured for fully wet-out [0_2] laminates.

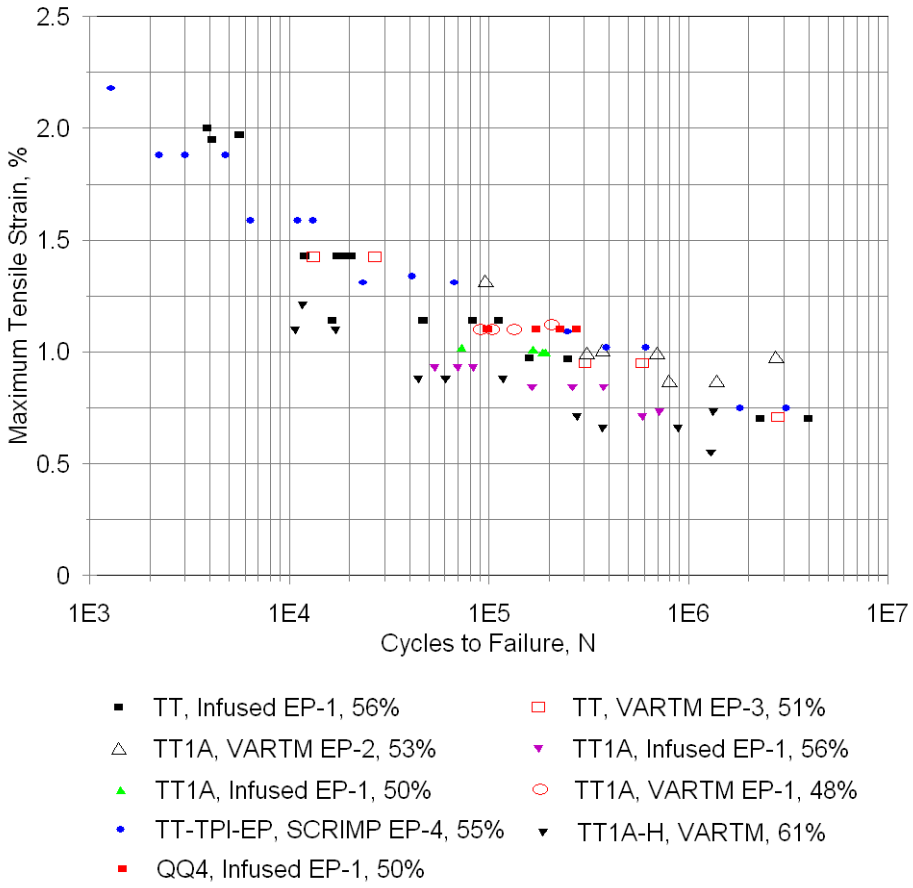

Figure 50. Tensile fatigue strain-cycles comparison for multidirectional laminates based on unidirectional fabrics C and D, different epoxy resins, batches, and processes.

The following summarizes findings for different fabrics, layups and processing in terms of million cycle tensile fatigue failure strain differences:

1. Thick uni-fabrics C and D, infusion processed, produce the most tensile fatigue resistant laminates (laminate groups TT, TT1A, QQ4).
2. When VARTM processed, fabric C laminates QQ4 were significantly less resistant, while fabric D laminates TT and TT1A were not significantly affected unless the fiber content was increased.
3. Stacking several uni-fabric plies had little effect relative to laminates with interspersed 0's and ±45's (TT vs. TT2).
4. On average, laminates of type TT, with biax fabric M, performed slightly better than type TT1A, with biax fabric L (both types use uni-fabric D), despite higher fatigue failure strains for fabric L compared with M, when tested without uni-fabrics (see Figure 60).

Glass Reinforcement, Polyester Resins. Figure 50a compares tensile fatigue performance for two polyester resins, UP-1 and UP-3 in the same multidirectional layup, TT, with uni-fabric D (biax fabric and process details differ, Table 2). The laminates had similar fiber volume contents, SLA (54%) and TT-UP-1 (52%). The results in Figure 50a show only minor differences in

fatigue resistance between the two laminates. As noted earlier (Figure 43a), the UP-1 resin showed greater fatigue sensitivity than an epoxy in identical layups. However, other multidirectional laminates with epoxy resins, like QQ1 in Figure 47, show similar fatigue sensitivity to SLA and TT-UP-1.

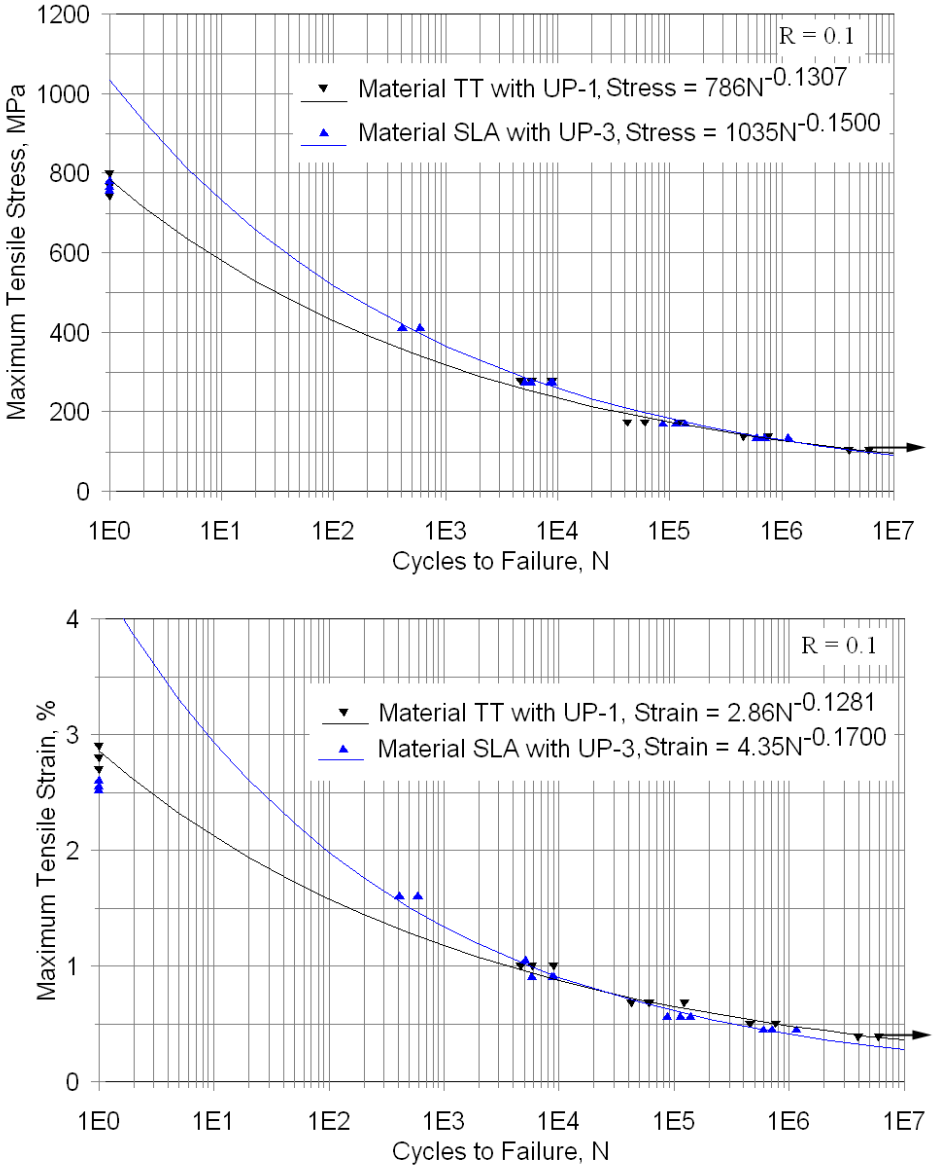

Figure 50a. Comparison of stress (top) and strain performance of two similar (±45/0/±45/0/±45) laminates (TT-UP-1 and SLA) with fabric D 0° plies, with two polyester resins, UP-1 and UP-3.

Carbon Reinforcement. Carbon fiber reinforced laminates for wind blades are most limited by compressive strength and ultimate strain [5, 12, 28]. The presence of even minor amounts of fiber misalignment has been shown to reduce static and fatigue properties significantly [28].

Maximum compressive properties are obtained with strands which have the least misalignment, generally unidirectional prepreg 0° plies; poorest properties have been found with woven fabrics, particularly with large tows. Figure 51 compares the compressive static and fatigue properties for three laminates (see Table 2): P2B, relatively thick (0.3 mm) prepreg with unidirectional carbon fiber 0° plies; MMWK C/G-EP, infused triaxial fabric R with +45° and -45° E-glass plies sandwiching 0° carbon strands; and CGD4, VARTM processed 0° stitched carbon fabric with E-glass ±45° plies. The P2B laminate gave properties typical of other large tow prepregs reported in Reference 3. The CGD4 laminate was among the best stitched or bonded carbon fabrics tested [5], but inferior to the prepreg, apparently due to slight misalignment in the fabric strands. The MMWK- C/G-EP laminate properties were at least equivalent to various prepregs tested in this program, with very straight strands held in place by the 45's; this fabric contains about 25 % off-axis material by volume which reduces the strength and modulus values relative to unidirectional carbon laminates [3] (Table 9).

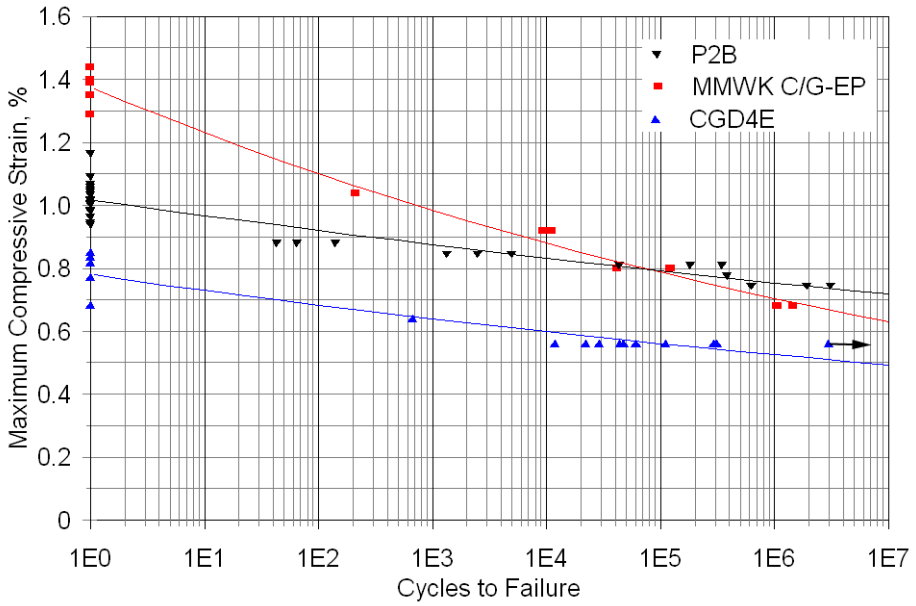

Figure 51. Comparison of compressive fatigue resistance of hybrid laminates with carbon 0° plies and E-glass ±45° plies: materials P2B (prepreg); MMWK C/G-EP (infused stitched hybrid triaxial fabric); and CGD4E (VARTM stitched fabrics), R = 10.

4.4 Laminates for small turbine towers

Tensile fatigue data for a polyester resin with three different fabrics, SCRIMP™ infusion processed by Vectorply, are given in Figure 52. SLA, SLB and SLC laminates were tested in cooperation with a development effort on small wind turbine towers. The unidirectional fabrics D and F are slightly superior to fabric E in this comparison. Laminates SLA and TT-UP-1 gave very similar results with different polyester resins (Figure 50a).

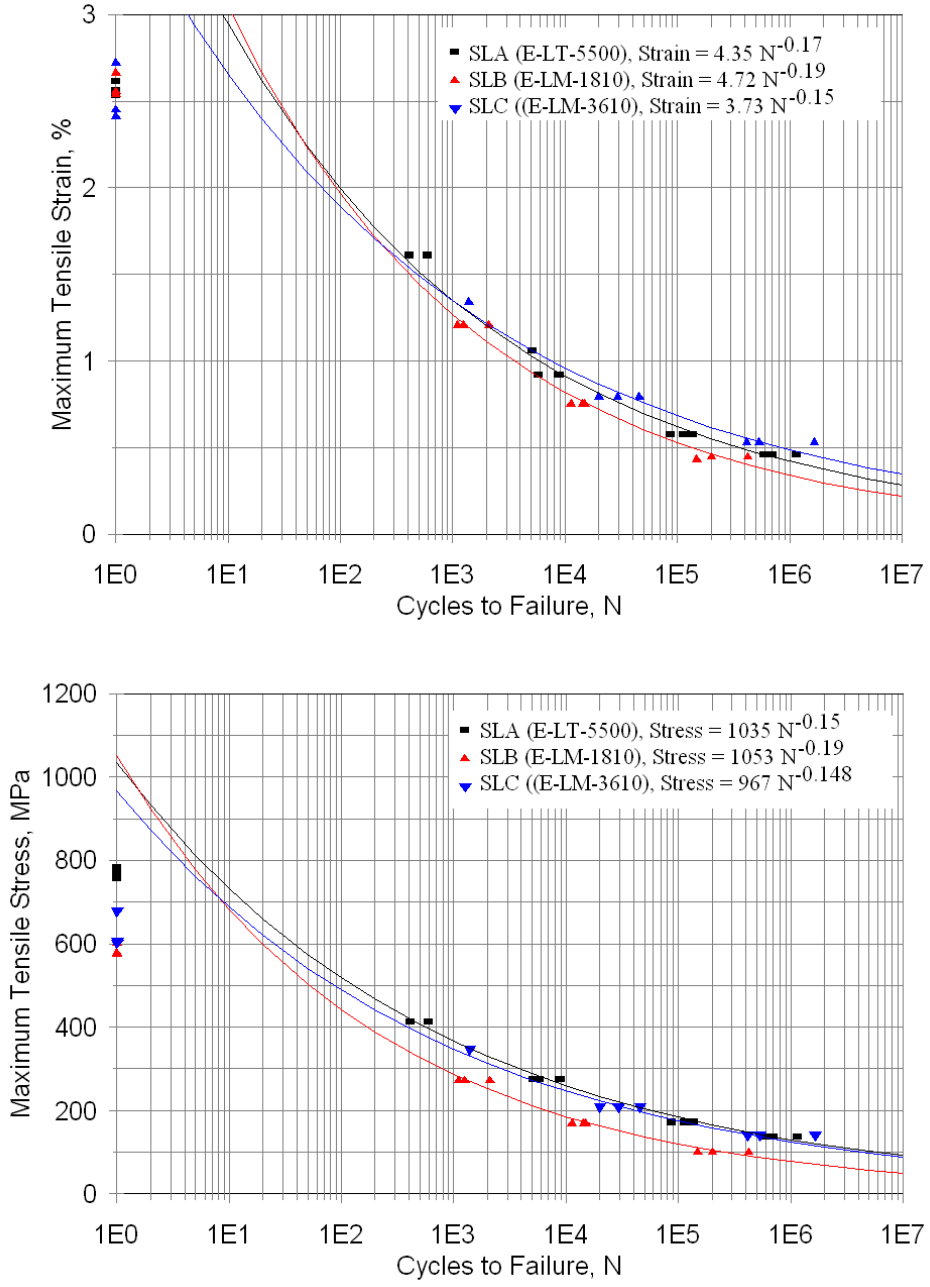

Figure 52. Tensile (R = 0.1) data for polyester UP-3 resin laminates SLA (V_F=54%), SLB (V_F=53%), SLC (V_F=51%), Scrimp process, three fabrics (differences in uni-fabrics given in Table 2).

4.5 Effects of R-value

This section presents results for multidirectional glass and hybrid laminates tested at a variety of loading conditions (R-values). The data are also presented in the next section in the form of constant life diagrams. An early laminate, DD16, typical of hand lay-up fabrication at low fiber content using an ortho-polyester resin was tested at thirteen R-values, the most complete such dataset available [58]; the results in Figure 53 (a-c) indicate the greater sensitivity to fatigue cycles containing significant tension, shown in (b) and (c). Reversed loading, R = -1, produces the shortest lifetimes at particular maximum stress values. The data in Figure 53 are fit with the three parameter model Eq. 11, and fit parameters are also given for Eq. 10 in Table 11. Figure 54 gives another dataset for VARTM E-glass laminate QQ1 at six R-values. Fit parameters can be found in Table 11. It should be noted that only the R = 0.1 specimens failed consistently in the gage section (Fig. 12). This laminate is more sensitive to tensile fatigue in this fiber content range than those based on fabric A at low fiber content (Figure 53), or Fabric D, as noted earlier, but is typical of many laminates using stitched and woven fabrics [5, 6]. The loading conditions with the greatest tensile amplitudes, R = 0.1, -0.5 and -1 again fail at the lowest maximum strains at high cycles. As indicated in Figures 46 and 47, laminate TT-TPI-EP and other laminates based on fabrics C and D show significantly higher tensile fatigue strains compared to QQ1. Extensive data of this type for infused glass/epoxy have also been reported in Reference [2].

Compared to Figure 54 for glass/epoxy, much less steep fatigue trends are demonstrated for carbon hybrid laminate P2B in Figure 55 at each R-value. Very similar trends at the same R-values were given in Figure 51 for the infused triaxial carbon hybrid fabric laminate MMWK C/G-EP. Mean lifetime fits for carbon materials include the static data, since the goodness of fit is improved [59], see Appendix A.

The effects of R-value on the strain-cycles data for laminates QQ1 and P2B loaded in the transverse direction are given in detail in Appendix A. Laminates in this class, having 0^o and $\pm 45^o$ plies, are relatively weak and brittle in the transverse direction in tension, as noted under static properties, with much improved properties in compression. Testing is relatively simple compared to the axial direction, using straight sided specimens with few grip interactions.

Results for the effects of R-value on fatigue resistance are presented throughout this report for the dominant cases R = 0.1, -1 and 10. Except for the transverse direction, the lowest absolute maximum stress and strain for a particular lifetime are invariably under reversed loading, R = -1, including ply drop delamination and adhesive joints. Cases with the greatest sensitivity to reversed loading tend to be shear dominated, such as Mode II delamination and ±45 plies, where the shear direction is reversed and the effects of amplitude doubling relative to pure tension or compression can be seen in the damage mechanisms [65, 66]. Associated with this sensitivity to reversed loading is difficulty in testing due to grip interactions, since the grips introduce load through shear stress transfer.

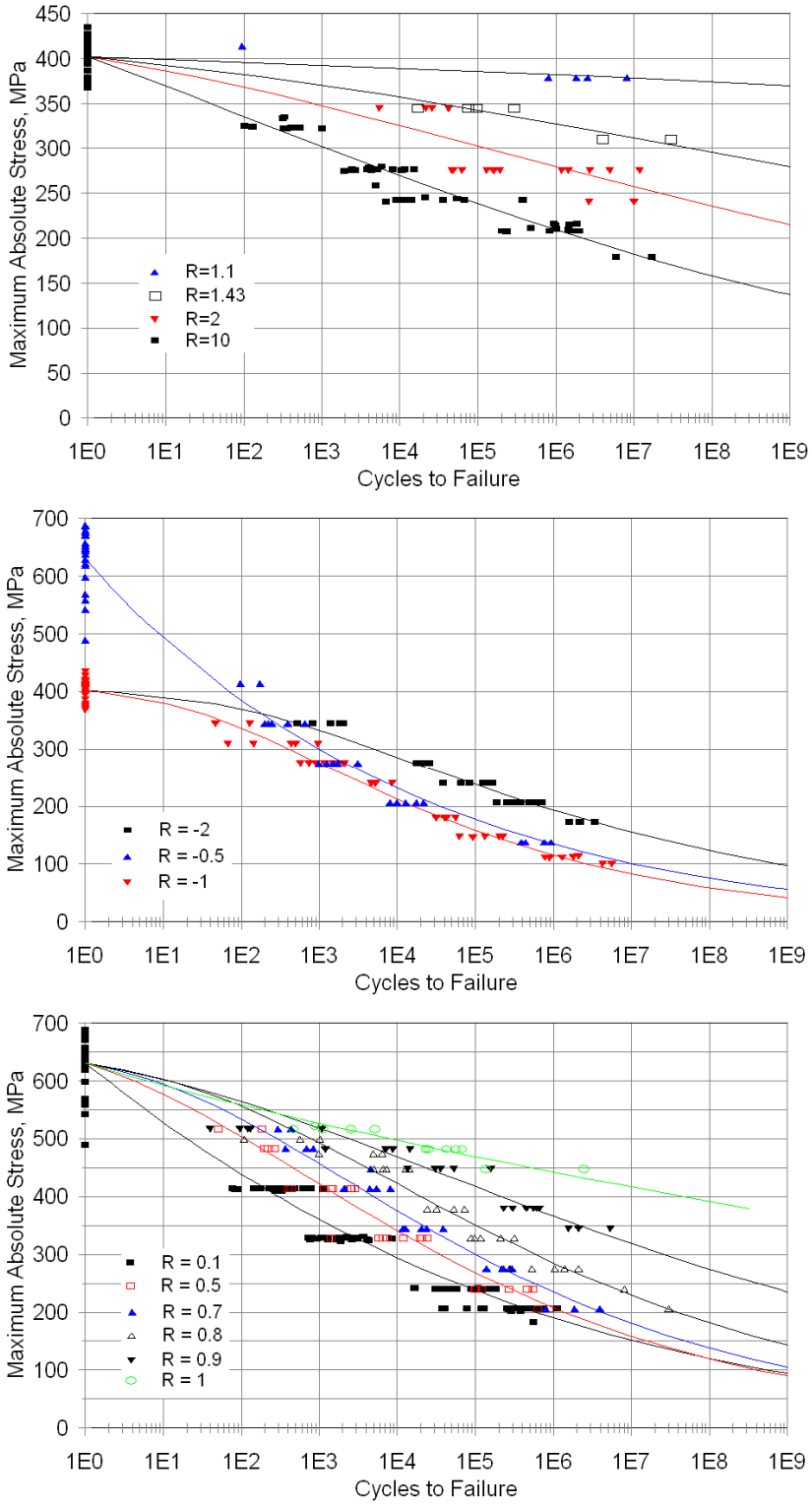

Figure 53 Stress-cycles data for early (low fiber content glass/polyester) material DD16 at thirteen R-values, axial direction, fit with three parameter model (Eq. 11).

Table 10. Equations 10 and 11 parameters for the thirteen R-values for material DD16.

R – Value	Equation 11			Equation 10	
	a	b	c	A	B
1.1	0.060	3.0	0.05	402	-0.0038
1.43	0.060	3.0	0.15	402	-0.0148
2	0.060	4.0	0.25	458	-0.0372
10	0.100	4.0	0.35	391	-0.0445
-2	0.010	4.0	0.55	648	-0.0876
-1	0.020	3.0	0.62	717	-0.1317
-0.5	0.450	0.85	0.25	622	-0.1134
0.1	0.420	0.58	0.18	630	-0.0865
0.5	0.075	2.5	0.43	833	-0.0997
0.7	0.04	2.5	0.45	996	-0.1059
0.8	0.035	2.5	0.40	1007	-0.0924
0.9	0.060	2.5	0.28	811	-0.0574
1*	0.21	3.0	0.14	599	-0.0205

*Assumes a frequency of 10 Hz

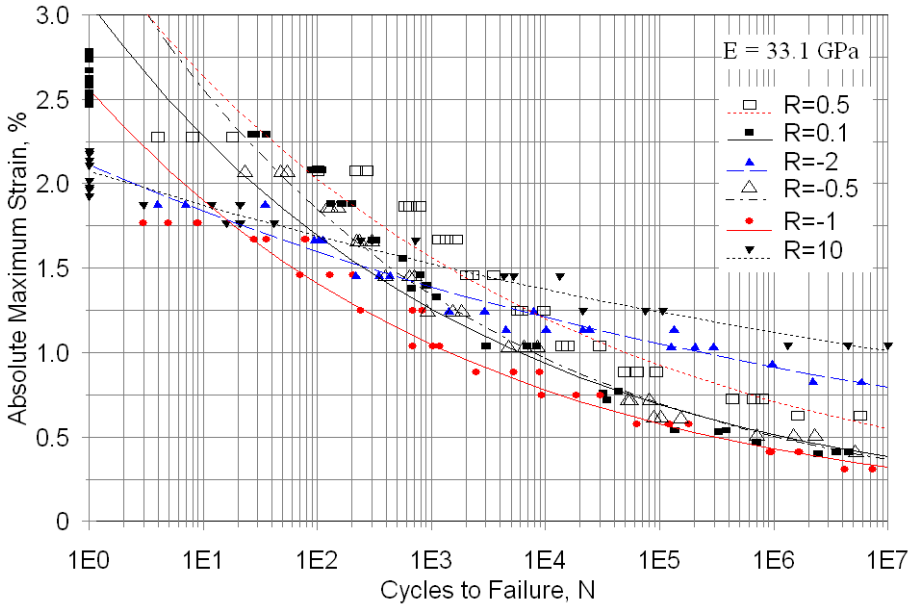

Figure 54. Effect of loading conditions (R-value) on fatigue strain vs. lifetime for E-glass/epoxy laminate QQ1 in the axial direction.

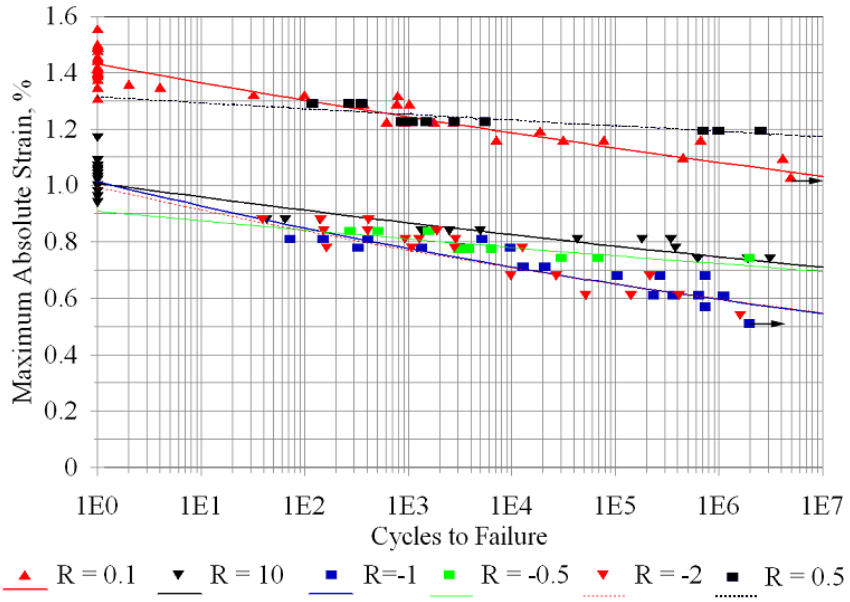

Figure 55. Effect of loading conditions (R-value) on fatigue strain vs. lifetime for hybrid laminate P2B, axial direction.

4.6 Biax (±45) laminates

The laminates consisting only of "biax" fabrics such as L and M in Table 2 have reduced mechanical properties in the axial direction, since most of the fibers are at ±45° (with the exception of small contents of mat or other 0° or 90° strands used in stitching the fabrics). These fabrics are common in skins and webs to provide shear and multidirectional properties, and to improve reinforcement handling and stability during assembly and infusion. Stress-strain curves for six resins (Table 2) with ±45 fabric M (which contains 30% mat) are given in Figure 40; the curves are significantly nonlinear in the stress range where fatigue tests were conducted, so fatigue data are given for both stress and initial cyclic strain in Figure 56. Differences in static strength between the Table 9 data and the one cycle data plotted on Figures 56 and 57 are the result of lower (standard) displacement rates for the Table 9 data (0.025 mm/s) compared with the much faster fatigue rate of 13 mm/s (see Table 8); for some ±45 laminates this has a pronounced effect on absolute strength values (higher for the higher rate) as well as the relative values for the different resins. The resin effects are limited for these biax fabric laminates; the most notable differences are improved fatigue strains for toughened epoxy EP-8 [67], and slightly reduced performance for the TR-1 polyester.

The failure of multidirectional laminates may be precipitated by failure of the biax plies; Figure 57 compares tensile failure strains for biax fabric L with several multiaxial laminates which contain fabric L in combination with a uni-fabric. The strain levels are similar and follow a similar S-N trend for the biax fabric and the multidirectional laminates. Multidirectional laminates which fail at lower strains, like QQ1, show limited biax layer damage at failure compared to more fatigue resistant laminates like TT, where the biax layers are heavily cracked prior to laminate failure (see Fig. 13, TT vs QQ1).

Laminates based on ±45 fabrics are known to show significant sensitivity to fatigue loading conditions [5]. Figures 58 and 59 compare fatigue data for the EP-1 resin with fabrics M and L for tensile, reversed and compressive fatigue loading (R = 0.1, -1, and 10, respectively); reversed loading is particularly damaging compared to other R values, apparently as a result of the reversing shear direction as discussed above.

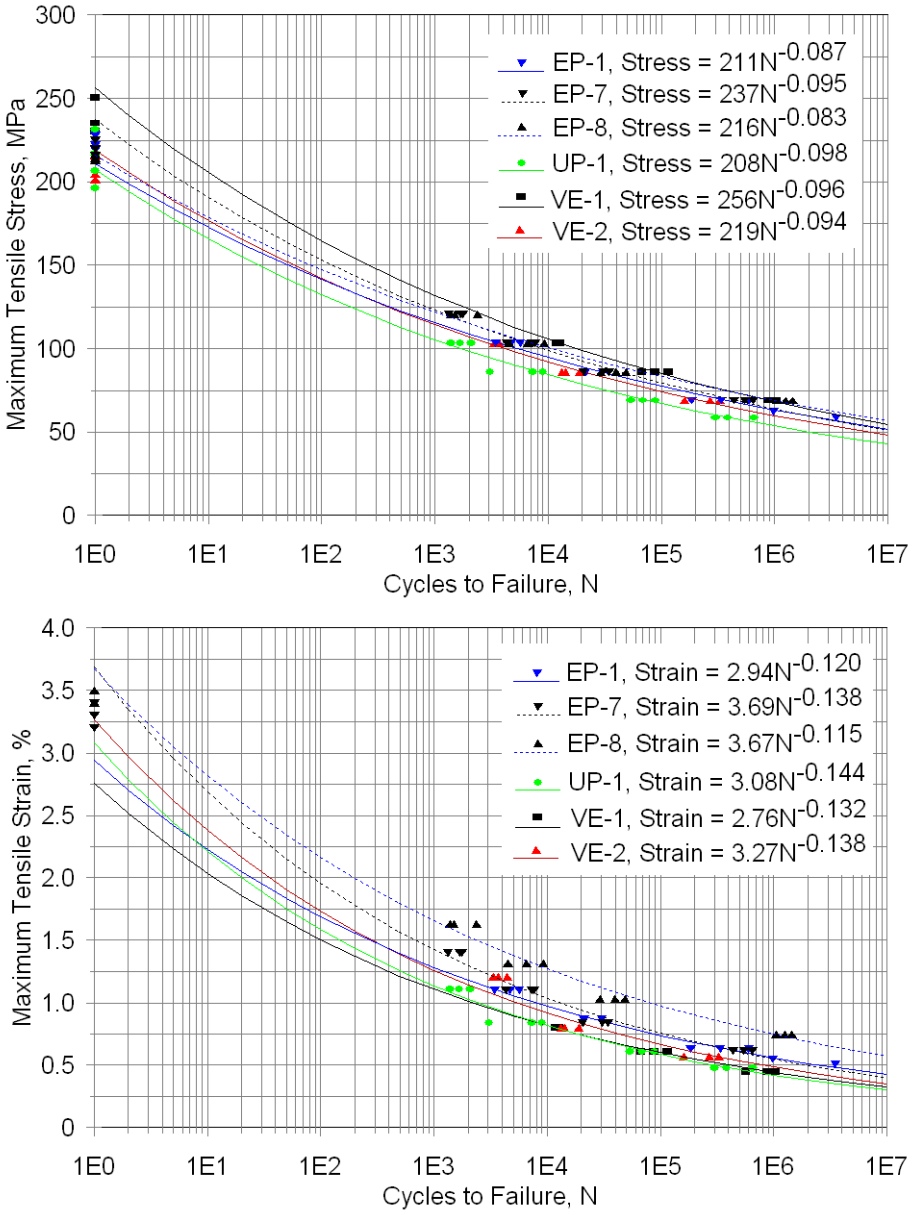

Figure 56. Stress (top) and initial strain (bottom) vs. log cycles data for fabric M ±45 laminates with various resins (R = 0.1).

A comparison of tensile stress-strain curves and tensile fatigue data is given for fabrics L, M and O (WindStrand) in the fabric warp direction, with epoxy EP-1 in Figure 60 [68]. These fabrics differ in construction (Table 2), with fabric L containing 2% 90-deg. strands, M containing 30% mat, and O containing 5% 0^o strands, each of which affects the performance in particular directions. Static behavior (Figure 39(a)) is more sensitive to fabric construction than are fatigue results (Figure 60). Figures 39b and 61 compare fabric L with epoxy EP-1 in the warp (0^o) and weft (90^o) directions, where the effects of the 90^o strands are evident.

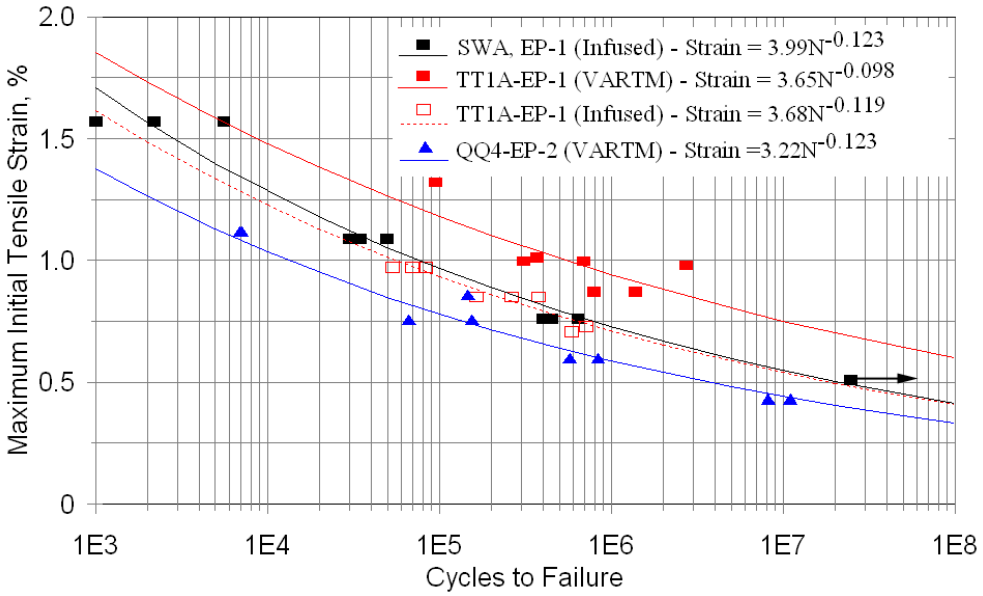

Figure 57. Comparison of fatigue failure strains for biax fabric L alone (laminate SWA) with multidirectional laminates TT1A (VARTM and infusion) and QQ4 (VARTM) containing both fabrics L and D, R = 0.1).

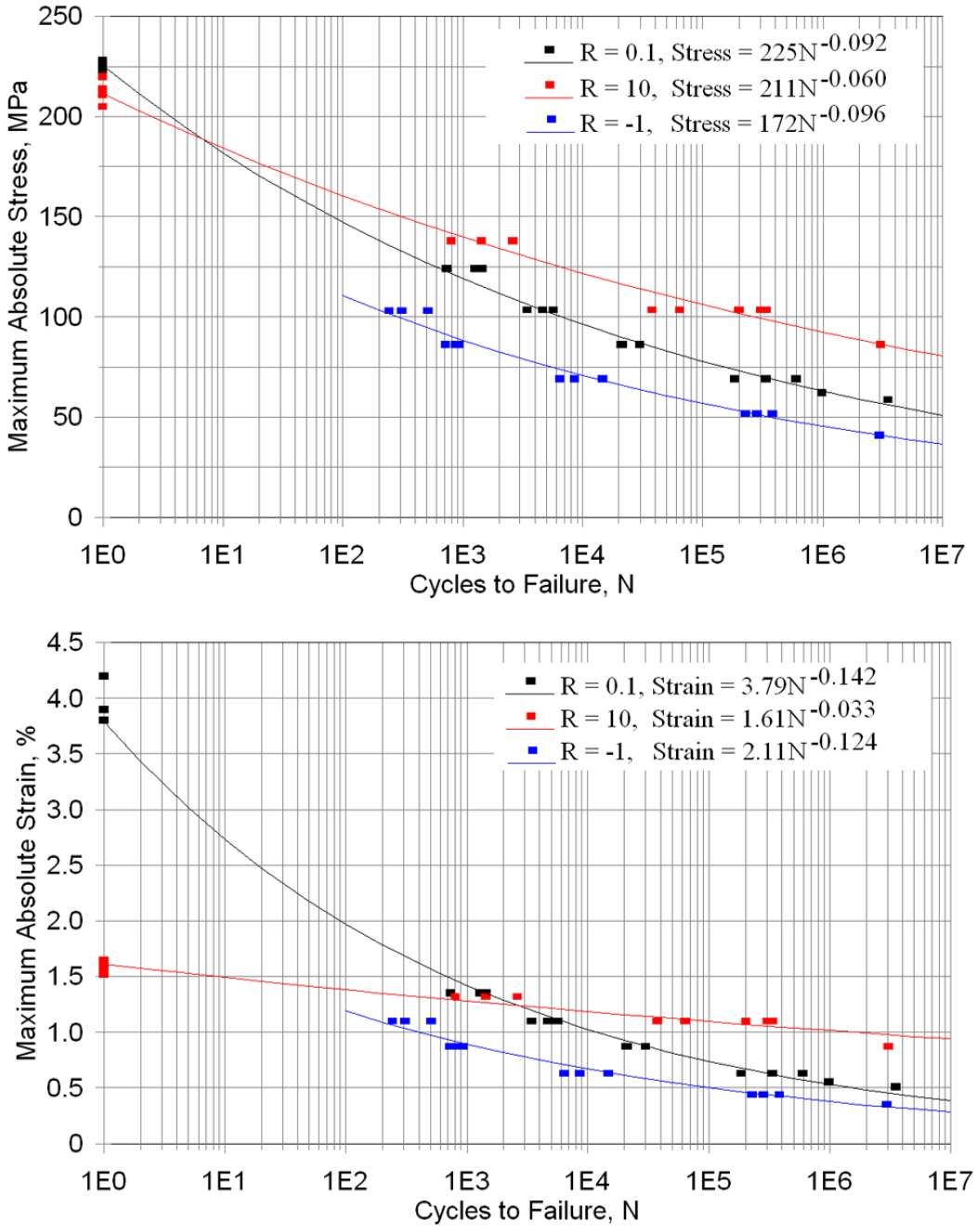

Figure 58. Effect of R-value on stress (top) and strain vs. log cycles, EP-1/fabric M laminates, R-values 0.1, -1, and 10.

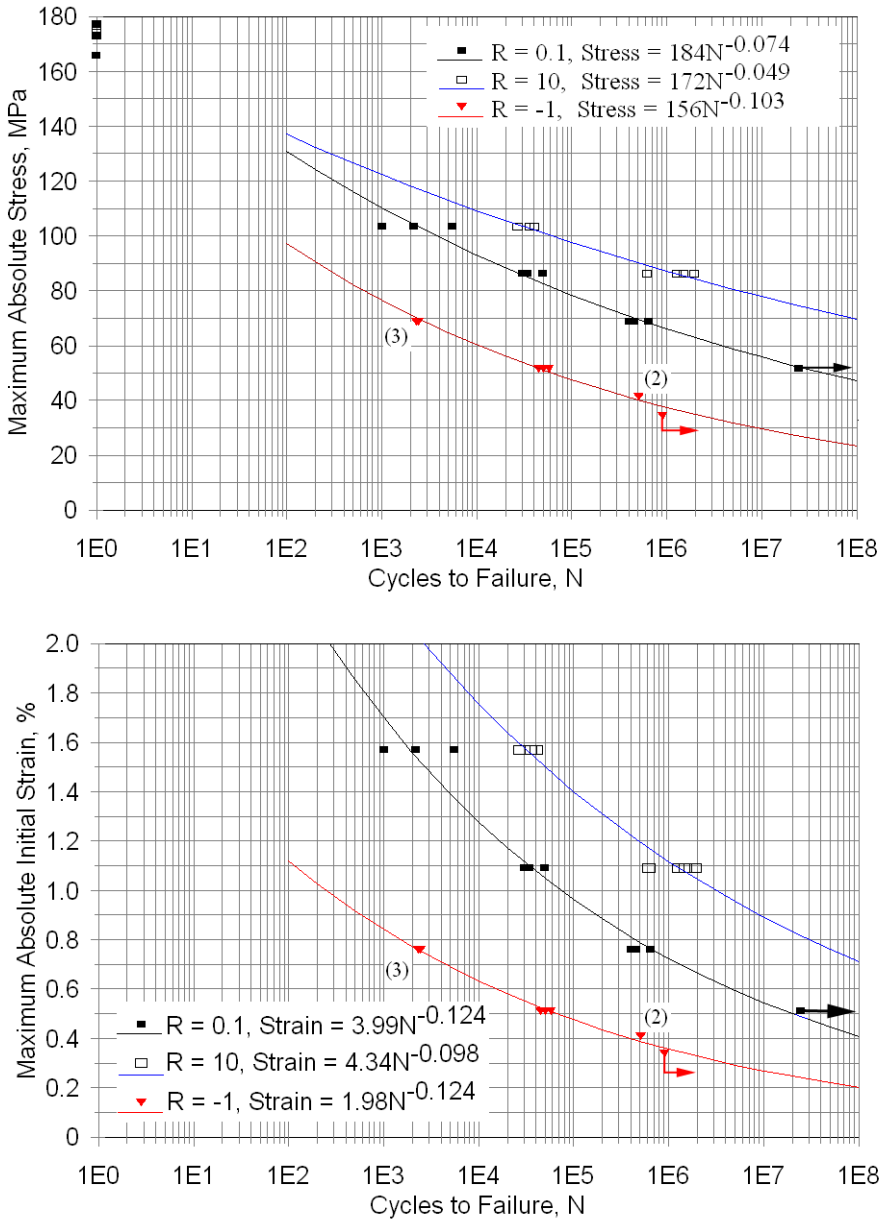

Figure 59. Effect of R-value on biax fabric L with epoxy EP-1.

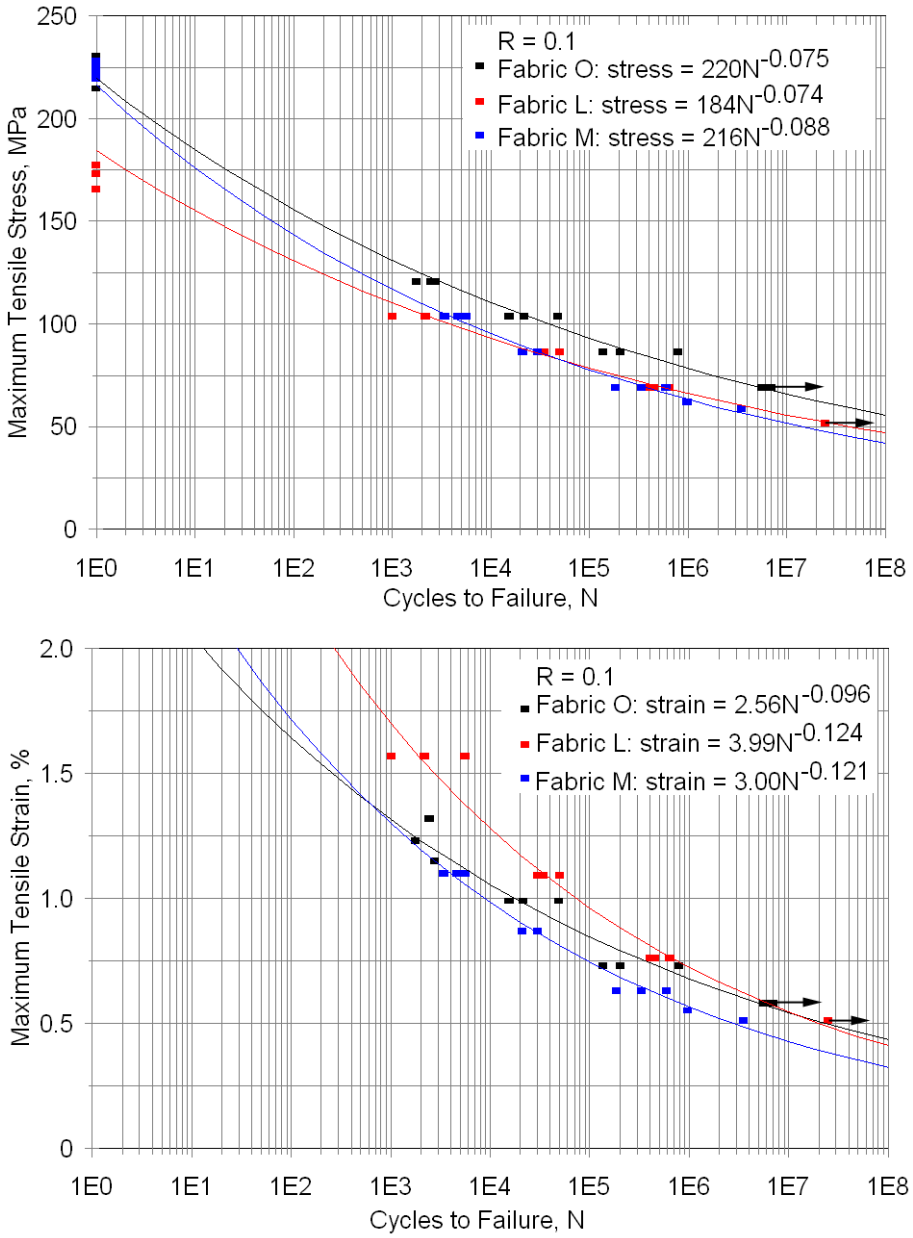

Figure 60. Stress (top) and strain-cycles data for three biax fabrics, warp direction, with epoxy EP-1, R = 0.1.

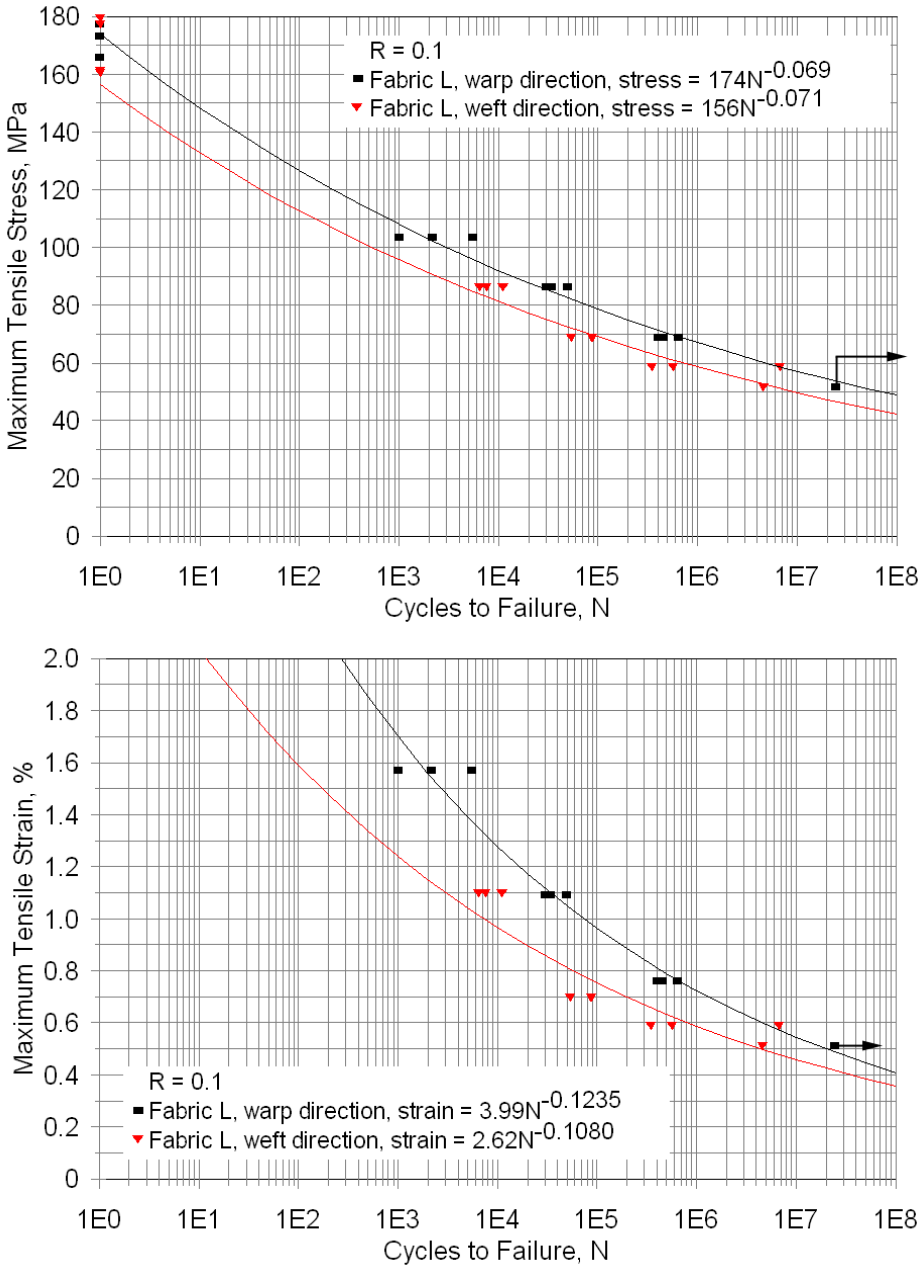

Figure 61. Effect of fabric direction on stress (top) and strain-cycles data, fabric L, epoxy EP-1, R = 0.1.

4.7 Constant Life Diagrams

Constant life diagrams, CLD's, have been prepared for materials QQ1 (glass/epoxy) and P2B (hybrid carbon/glass with carbon 0^o plies), in the axial and transverse directions. The full dataset including mean and 95/95 CLD's is given in Appendix A, and only selected results are given here. The CLD's are constructed from the fit parameters in Table 9. The procedures for constructing CLD's from constant amplitude fatigue data at various R-values is discussed in detail in Ref. [2]. Any point on the CLD represents the (interpolated) lifetime for a particular mean stress and stress amplitude (Fig. 62), which can then be used in conjunction with Miner's Sum or other damage rule to predict the lifetime under spectrum (usually random) loading [2].

The CLD for early laminate DD16, representing hand lay-up at low fiber content (36% by volume) with polyester resin, is given in Figure 62, based on testing at thirteen R-values. The static tensile creep-rupture data are plotted at zero amplitude (R=1) assuming a frequency of 10 Hz. The DD16 laminate is relatively fatigue resistant in terms of strains, with a million cycle fatigue strain of 0.95% at 10^6 cycles for R = 0.1. Current infused laminates usually have significantly higher fiber content, and consequently, higher modulus and strength. In terms of strain capability in tensile fatigue, DD16 falls between QQ1 and TT (Figure 47). This constant life diagram, combined with extensive testing for spectrum loading [5] and residual strength [2], has served as a basis for a variety of spectrum load modeling studies [2, 8, 16, 63]. One result of these and related studies is the conclusion that constant amplitude data for five or six R-values are needed to define the CLD with sufficient accuracy for spectrum load lifetime predictions [2, 16].

Based on the data at various R-values in Figures 54 and 55, CLD's have been prepared for infused glass laminate QQ1 and prepreg hybrid laminate P2B. Figures 63 and 64 compare the mean CLD's based on stress and strain, respectively. As noted above, the QQ1 laminate shows poor tensile fatigue resistance compared to other E-glass/epoxy laminates like the TT series, based on Fabric D, as well as laminate DD16 and results reported for material MD2 in the European OPTIMAT program at similar fiber content to QQ1 [2]. A more controlled set of experiments where fabric parameters are systematically varied is currently underway. The transition from compression to tensile failure modes around R = -1 is particularly severe for this material at high cycles. The carbon hybrid laminate, P2B, is much stronger than QQ1 in both static and fatigue tests (Fig. 63). On the basis of strains (Figure 64) the order is reversed for most conditions, except in the tension quadrant at high cycles. Even on a strain basis, however, the carbon fatigue curves are much less steep (Figures 41), and carbon dominated blade designs may be driven by static rather than fatigue properties, particularly ultimate compressive strain.

The transverse direction mean stress CLD for material QQ1 is given in Figure 65, with strains calculated from the stresses through the transverse modulus (Appendix). These 0^o dominated laminates are relatively weak in the transverse direction (Table 3) as expected, particularly in tension. The CLD shows much better performance in the compressive than the tensile quadrant. A similar transverse direction CLD is reported in the Appendix for material P2B. Comparison of the axial and transverse diagrams for material QQ1 and P2B indicate the general trend that matrix cracking for R-values containing tension occurs at lower strains than does fiber dominated failure, in this case for transverse loading. Laminates loaded in the axial direction will

generally develop matrix cracking in off-axis plies prior to total failure for these conditions, and this stable damage can become severe for materials which are more resistant to fiber failure, like those based on fabric D, as discussed earlier (Section 4.3.3).

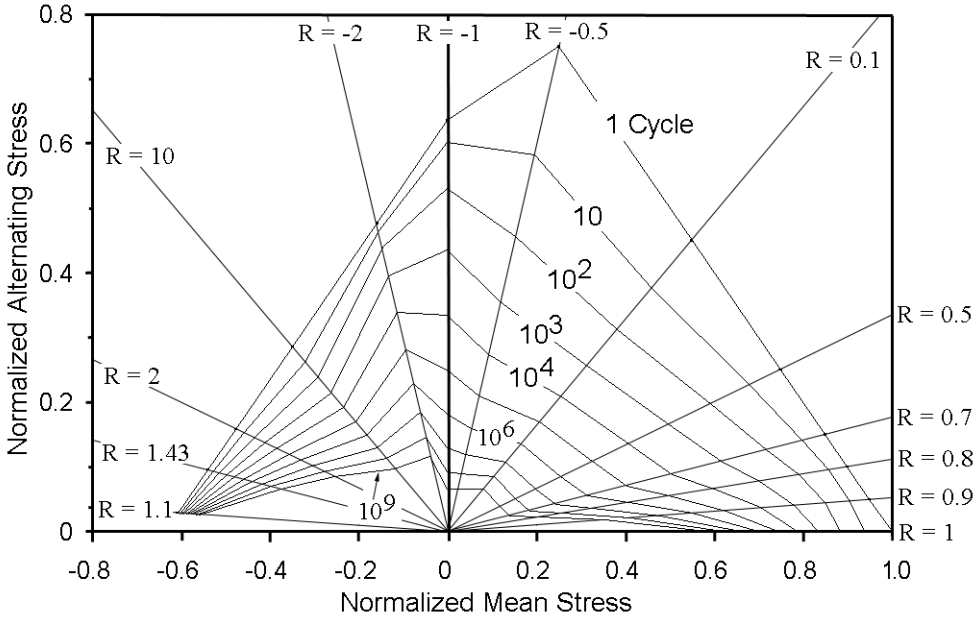

Figure 62. Constant life diagram for laminate DD16 based on thirteen R-values (from Ref. 58).

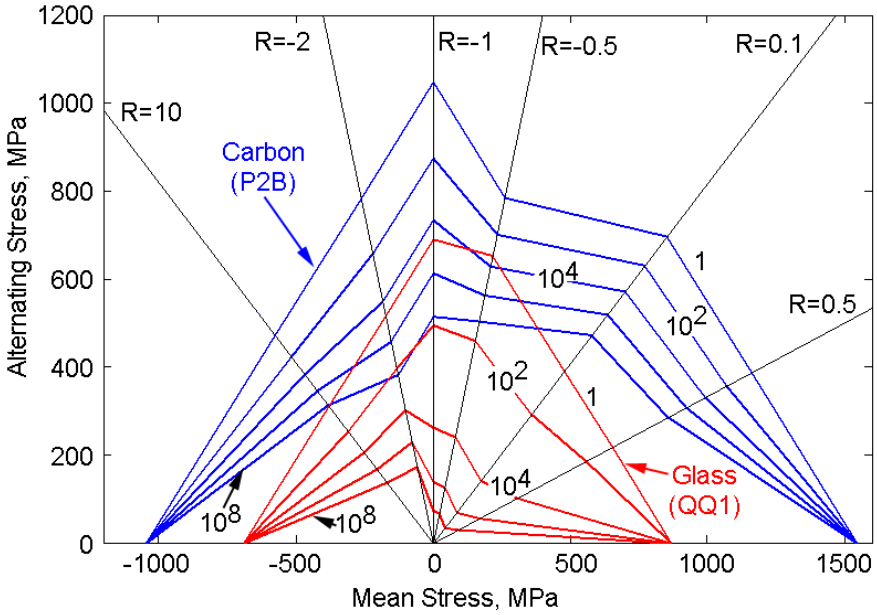

Figure 63. Comparison of materials QQ1 (E-Glass) and P2B (carbon 0^o plies), axial direction, mean stress constant life diagram.

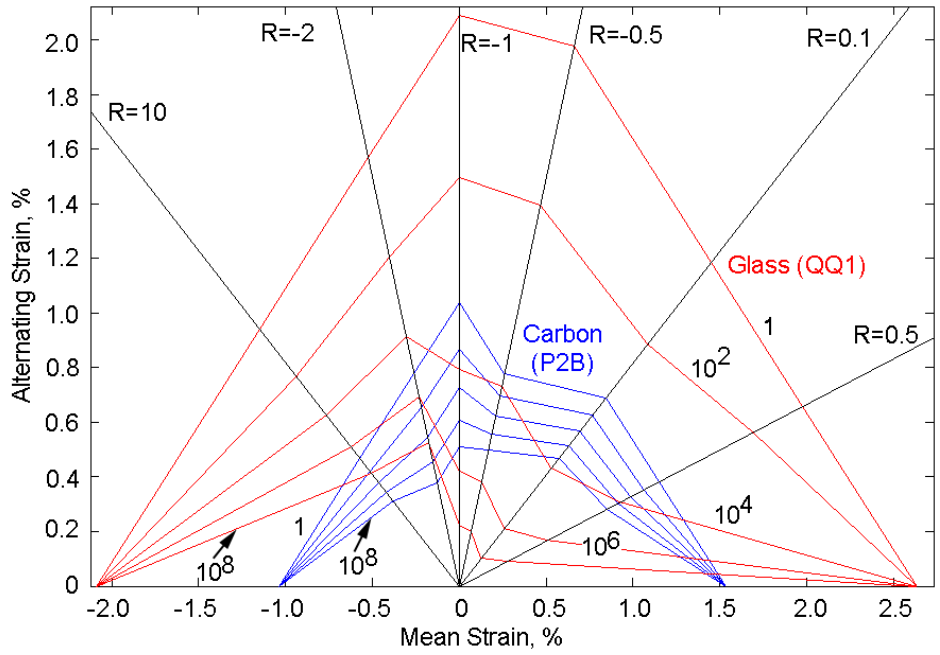

Figure 64. Comparison of materials QQ1 (E-Glass) and P2B (carbon 0^o plies), axial direction, mean strain constant life diagram.

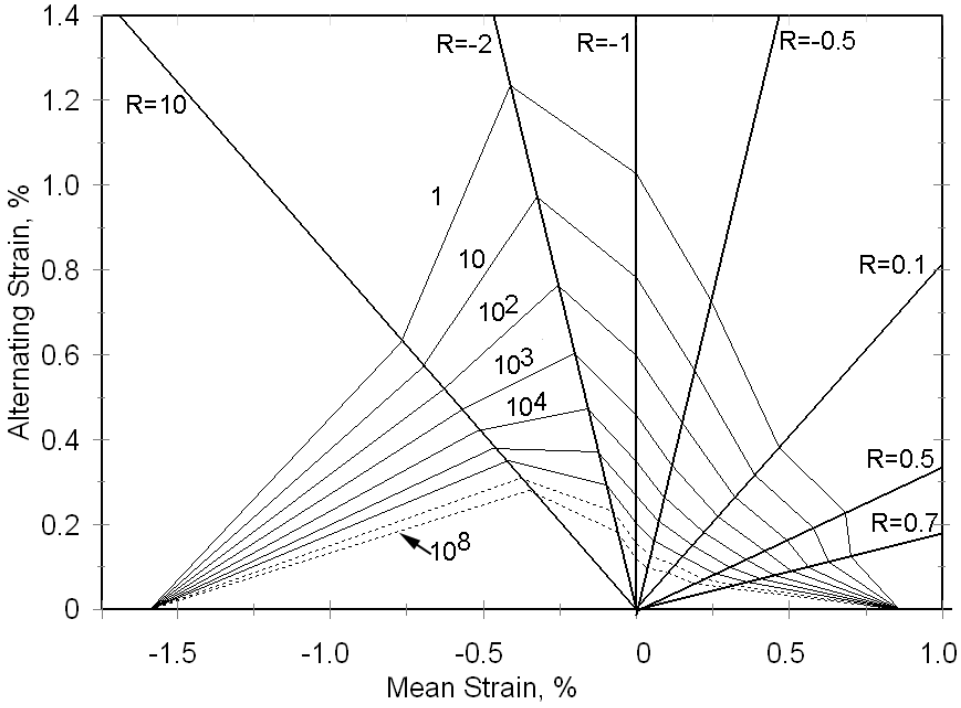

Figure 65. Transverse direction strain constant life diagram for laminate QQ1.

4.8 Spectrum Loading

Spectrum loading predictions and models have been presented elsewhere [2, 8, 63]. Lifetime predictions under several types of spectra have been in good agreement with nonlinear models when the constant amplitude CLD's are represented with sufficient accuracy, as for material DD16 [8, 63] and for material MD2 in the OPTIMAT database [2]. Residual strength lifetime trends have been measured and modeled under a variety of loading conditions for materials DD16 and MD2 in reference [2].

This section presents a brief comparison of predicted spectrum fatigue life based on the CLD's for laminates DD16, QQ1, and P2B in the preceding section. Prediction of their lifetime was carried out under the WISPERX wind turbine loads spectrum (rainflow counted) using their respective mean stress CLD's. This spectrum is a tensile, single high load dominated spectrum developed in Europe, which has been widely used in spectrum loading studies of blade materials [2, 8, 20]. Based on recent findings for different cumulative damage criteria by Nijssen [2], Miner's sum was used to predict failure, although Sutherland and Mandell [11] have found better predictions with nonlinear models. The required magnification factor for the spectrum in stress or strain was calculated such that failure would occur in a specified number of passes through the spectrum, ranging from 1 to 1000. Since the WISPERX spectrum is a reduced version of the original WISPER spectrum which contains 132,000 cycles [59], 1000 passes represents over 10^8 cycles, on the order of the expected 20-year blade lifetime in service.

Figures 66 and 67 present the results in terms of stress and strain, respectively [59]. Carbon based material P2B is predicted to withstand much higher stress scale factors (and therefore loads) compared to the two E-glass based laminates. On a strain based comparison (which correlates with blade deflection) material P2B shows lower fatigue strains but a much less steep trend, analogous to the S-N trends, compared to the E-glass laminate materials, crossing the QQ1 curve and almost intersecting the DD16 curve by 1000 passes. Comparing the two E-glass based laminates, DD16, with lower fiber content, is superior in terms of strain at all levels (Figure 67) and in terms of stress at higher passes. As noted earlier, QQ1 has a higher elastic modulus compared with DD16, but poorer tensile fatigue resistance. Other E-glass laminates at the higher fiber content of QQ1, such as the TT and TT1A series in Table 2, would be expected to show better results than QQ1, based on Figures 47 and 48.

The scale factors in Figures 66 and 67 represent the magnitude of the highest stress or strain in the tensile-dominated spectrum. It is worth noting that the scale factor at 1000 passes, the approximate expected blade 20-year lifetime, is similar in magnitude to the constant amplitude stress and strain data at R of 0.1 at approximately 10^6 cycles (Figures 53-55). Thus, the constant amplitude 10^6 comparisons, as in Figure 48, approximately represent a 20 year lifetime under the WISPERX spectrum. In a sense, testing at constant amplitude in tensile fatigue accelerates the lifetime determination by about a factor of 10^2 for this particular case, apparently due to the single high load in the spectrum.

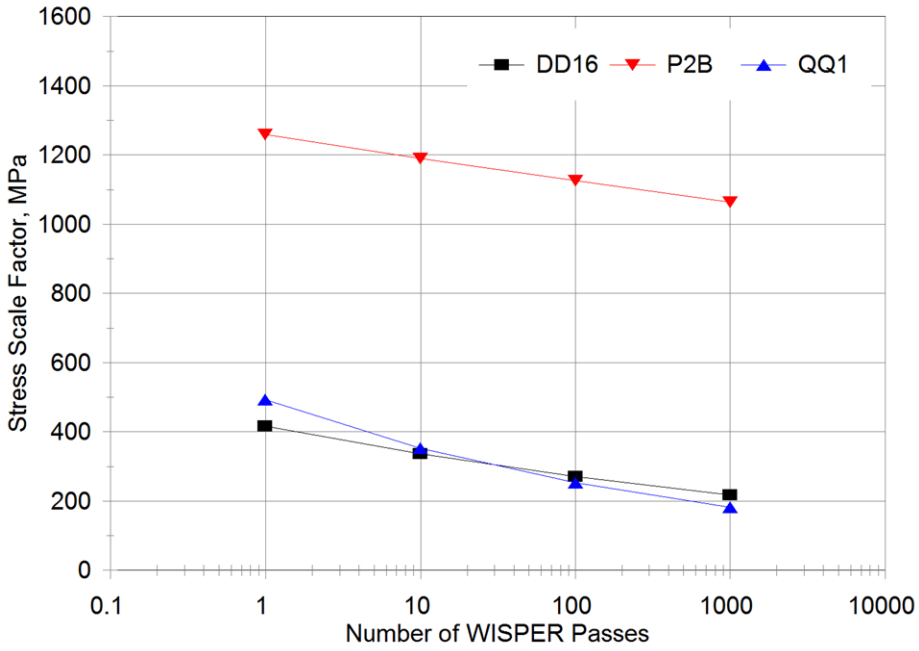

Figure 66. Stress scale factors applied to the WISPERX spectrum to achieve a miner's sum equal to 1 (using the mean stress CLD).

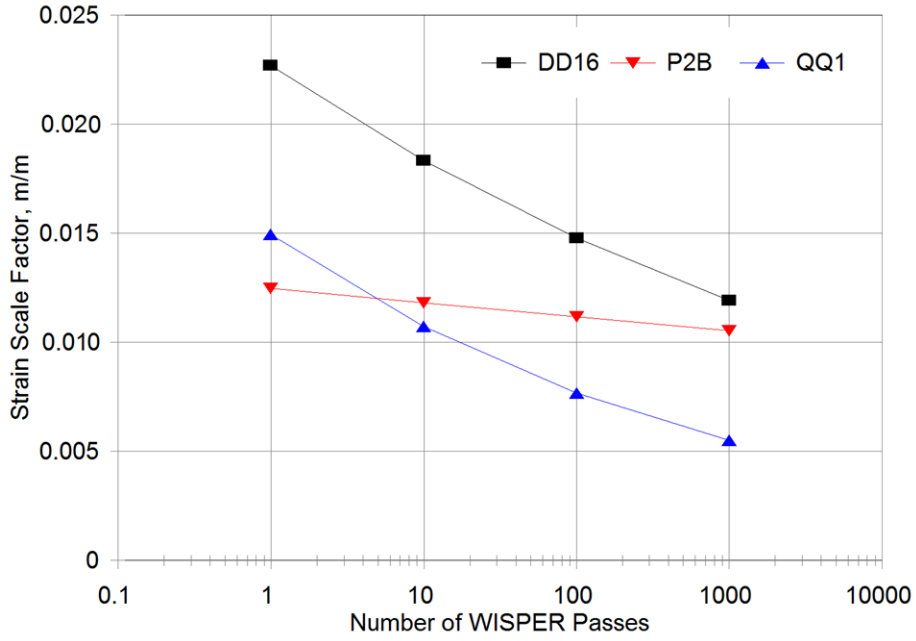

Figure 67. Strain scale factors applied to the WISPERX spectrum to achieve a miner's sum equal to 1 (using the mean stress CLD).

4.9 Ply Delamination Resistance

As noted in Section 2, delamination crack growth resistance is known to be sensitive to resin toughness [5, 53, 66]. Pure mode I and II tests are run on unidirectional laminates with artificial starter cracks, to determine the critical strain energy release rates G_{Ic}, opening mode and G_{IIc}, shearing mode (Section 2). These properties are sensitive to both the resin and the thickness of resin layer between plies. Values of these two properties usually correlate with delamination resistance in structural details for blade materials [5, 18, 69]. Table 11 presents pure mode delamination resistance data for unidirectional Vectorply E-LT-5500 laminates with four resins from Table 2; the fabric has a front face with packed 0^o strands, while the back face has irregularly spaced 90^o strands to which the 0^o strands are stitched (Table 2, Figure 36). Data in Table 11 are given for delamination along back-to-back 0^o and 90^o sides. The toughness values order as epoxy>vinyl ester>polyester as in earlier studies [5] but with the toughened vinyl ester (VE-2) exceeding the epoxy for G_{Ic} on the 0/0 interface.

Mode II toughness is typically much higher than Mode I toughness for relatively brittle resins. Mode I cracks grow in a sharp, coplanar fashion through the resin (in the absence of fiber bridging), much as in neat resin fracture toughness tests. Mode II cracks, while driven by the imposed shear stress, locally develop as tensile cracks normal to the maximum tensile stress, forming a series of sigmoidal shaped local cracks which coalesce to form the main crack [66]. Mode II fracture surfaces show the resulting resin hackles standing off the surface. The complex cracking pattern in Mode II consumes the inter-ply resin layer, resulting in much higher toughness values compared to Mode I. Mixed mode cracks with combinations of Modes I and II experience the effects of the Mode II cracking mechanism, increasing the combined Mode toughness relative to G_{Ic} [5, 65, 70]. Very tough resins yield and deform throughout the resin layer, and are limited in energy absorption by the thickness of the layer. G_{Ic} and G_{IIc} then have similar high values [65].

Delamination cracks at structural details like ply drops are usually mixed-mode [11, 12, 21, 59] with complex interaction between modes for relatively brittle resins. Figure 68 [52] shows data comparing epoxy, vinyl ester, and polyester resins. The three lower fiber content laminates show the same toughness ordering as Table 11, epoxy>vinyl ester>polyester over the entire mixed mode range. The higher fiber content Vectorply E-LT-5500/epoxy shows slightly reduced toughness compared to the lower fiber content epoxy system, as expected. Compared with in-plane properties presented earlier, the delamination resistance is very matrix sensitive. Test results, including environmental effects, have been reported [5, 69] for laminates of the type discussed above. The general trend of the data in Figure 68 with mode mixity is consistent with the model of Reeder and Crews [70] for relatively brittle resins. Results for skin-stiffener structural details show a trend for different resins which is consistent with delamination test results [5]. Thus, data such as those in Figure 68 are generally consistent with structural integrity observations. The delamination tests can also be run in fatigue, to obtain fatigue crack growth trends, but results for this group of materials are only available for the polyester resin [5] in pure modes. The sections which follow explore what is usually mixed mode delamination at ply drops used in thickness tapering.

Table 11. Delamination resistance of unidirectional fabric D laminates with various resins.

Resin	V_f (%)	Initial G_{IC} (J/m^2)*	V_F (%)	G_{IIC} (J/m^2)*
0-0 Interface				
EP-1	60	303 (40)	60	3446 (201)
UP-1	60	166 (17)	60	1662 (200)
VE-1	64	252 (24)	63	2592 (130)
VE-2	61	433 (53)	61	2998 (313)
90-90 Interface				
EP-1	62	321 (38)	61	1887 (97)
UP-1	62	175 (27)	62	928 (353)
VE-1	64	223 (13)	63	1653 (124)
VE-2	61	272 (33)	61	1689 (349)

*numbers in parenthesis are standard deviations for 3-5 tests. The 0 and 90 interfaces refer to the two sides of the E-LT-5500 fabric, which has the primary 0° strands stitched to a few 90° strands (Table 2). Fiber contents vary slightly batch to batch as shown.

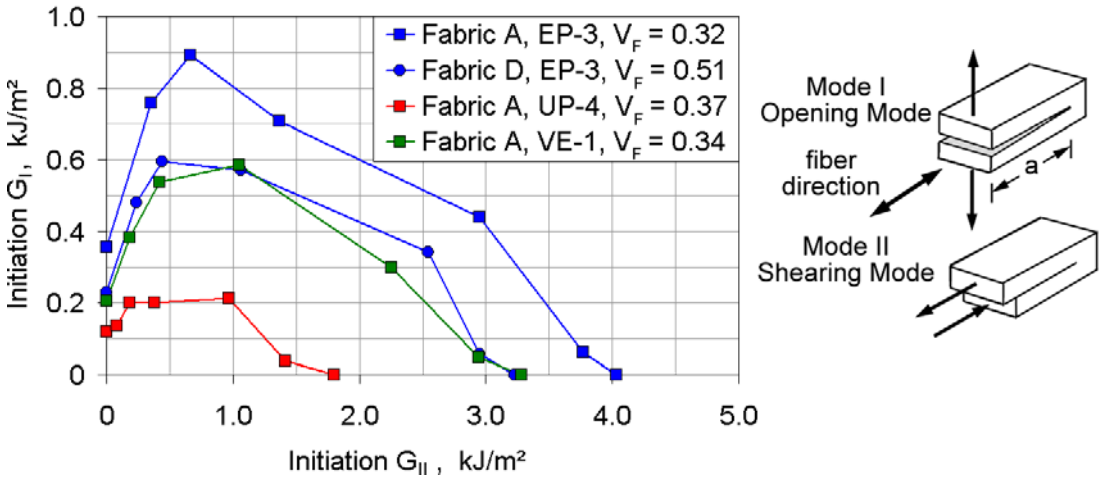

Figure 68. Mixed mode delamination resistance for two unidirectional E-Glass fabrics having different fiber contents, with three resins.

The delamination resistance in Modes I and II has also been measured for unidirectional Newport prepregs used in material P2B and the ply drop study in the following section. Table 12 indicates G_{Ic} and G_{IIc} values in the range of those for the infused fabric D/epoxy EP-1 laminates given in Table 11.

Table 12. Delamination resistance of unidirectional carbon and glass fiber/epoxy prepreg laminates.

Prepreg	Lay-up	V_F %	G_{IC} (J/m^2)	G_{IIC} (J/m^2)
NCT307-D1-34-600 Carbon	$[0]_{20}$	53	364 (62)	1829 (87)
NCT307-D1-E300 Glass	$[0]_{20}$	47	365 (37)	2306 (188)
* 13 to 14 tests, Brackets indicate standard deviation.				

SECTION 5. DELAMINATION AT PLY DROPS IN PREPREG LAMINATES

5.1 Thin Laminates

Ply drop delamination effects are inherently a function of the laminate thickness, ply lay-up and ply thickness. In terms of testing, the thinner the laminate, the less complex are the test methodology and failure modes due to reduced load transfer requirements at the grips. However, since laminates contain plies with a fixed ply thickness, ply drops in thin laminates are not representative of thick blades in terms of the fraction of plies dropped at a particular cross-section. Thus, a series of relatively thin laminates, on the order of 3 mm thick, was tested both with and without ply drops under tensile, compressive, and reversed loading. The results were then compared with data given later from relatively thick laminates for selected cases under compression with combined face and end loading, where meaningful tests could be run [11]. The ply configuration for the thin laminates was $(\pm 45/0_9/\pm 45)$, with additional plies added for half of the coupon length in the case of ply drops. As noted earlier, the 0^o plies contained carbon fibers, while the $\pm 45^o$ plies contained glass fiber. The test specimen geometry was shown in Figure 21. Previous studies of ply drop delamination and knockdown factors have been reported in References 4 and 24.

S-N fatigue curves for coupons without ply drops were reported earlier in Figure 53 for this material system, for the similar ply configuration ($\pm 45/0_8/\pm 45$, laminate P2B) with several R-values. Table 6 gives measured ply properties for these prepregs.

The results for the thin laminates containing ply drops, $(\pm 45/0_2*/0_9/0_2*/\pm 45)$, where the 0_2* plies are dropped at mid-length, are given in Figures 69 and 70. The two double ply drops reduce the static strengths by approximately 45% in tension and 42% in compression (Table 13). These reductions for double ply drops are slightly less severe than those reported for a different prepreg system in Reference 28. However, the effects of ply drops under fatigue loading are severe, producing much steeper S-N curves than for the controls (trend lines from Figure 53). Failure is taken as the growth of a large (6 mm) delamination or combined delamination and separation. Delamination is a matrix dominated failure mode which follows a steeper S-N trend with carbon fibers than do control laminates in directions which are more fiber dominated [11]. Maximum strain levels for 10^6 cycles are below 0.3% for the laminates with double ply drops, compared with 0.6% to 1.0% for the control material, depending on R-value. As with the control material, reversed loading is most severe.

It is noteworthy that all three loading conditions produce delamination in a similar strain range. Since a change from tension to compression changes the opening mode stress intensity from opening to closing, where closing would suppress delamination, this implies that delamination is dominated by the Mode II, or shear component, as discussed later.

Table 13. Comparison of the static strengths of selected materials, with and without ply drops (0° plies are carbon, ±45° plies are glass).

Lay-up	Ultimate compressive strength, MPa	Ultimate compressive strain, %	Ultimate tensile strength, MPa	Ultimate tensile strain, %
$(\pm45/0_8/\pm45)$	-1070	-1.04	1496	1.40
$(\pm45/0_2*/0_9/0_2*/\pm45)$	-617	-0.64	827	0.85
$((\pm45)_3/0*/0_{27}/0*/(\pm45)_3)$	-754	-0.78	----	----
$((\pm45)_3/0_2*/0_{27}/0_2*/(\pm45)_3)$	-642	-0.67	----	----
$((\pm45)_3/0_4*/0_{27}/0_4*/(\pm45)_3)$	-612	-0.64	----	----
* indicates dropped ply; stress and strain values refer to thin side of coupon.				

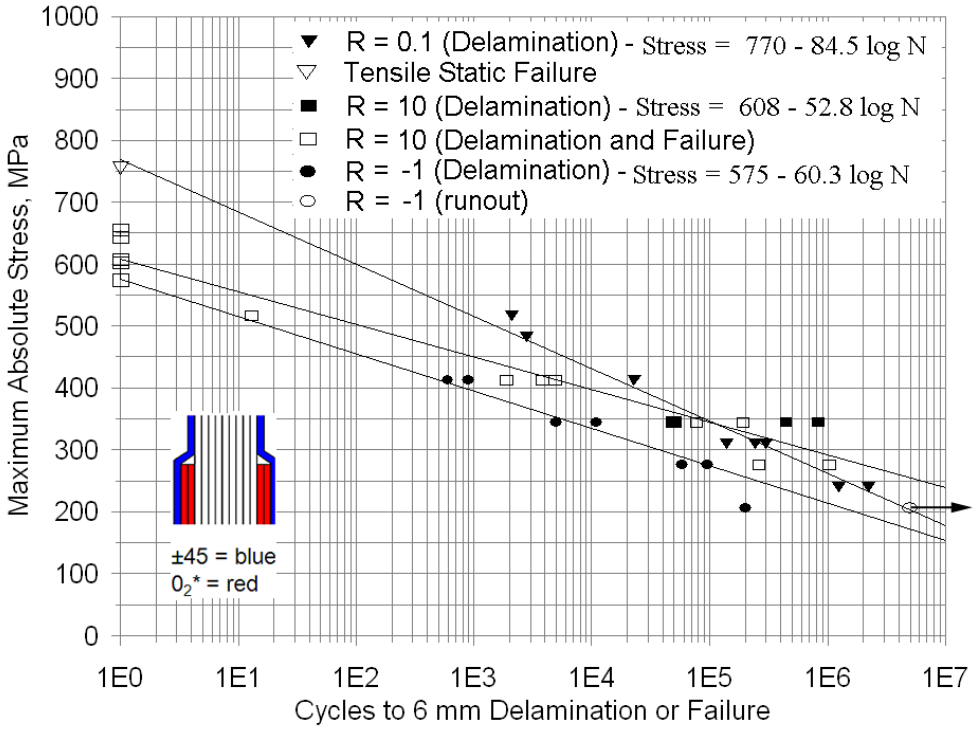

Figure 69. Maximum absolute stress versus cycles to failure for a $[\pm45/0_2*/0_9/0_2*/\pm45]$ laminate, R=0.1, 10 and -1 (contains ply drops for the 0_2* Plies; 0° plies are carbon, ±45° plies are glass).

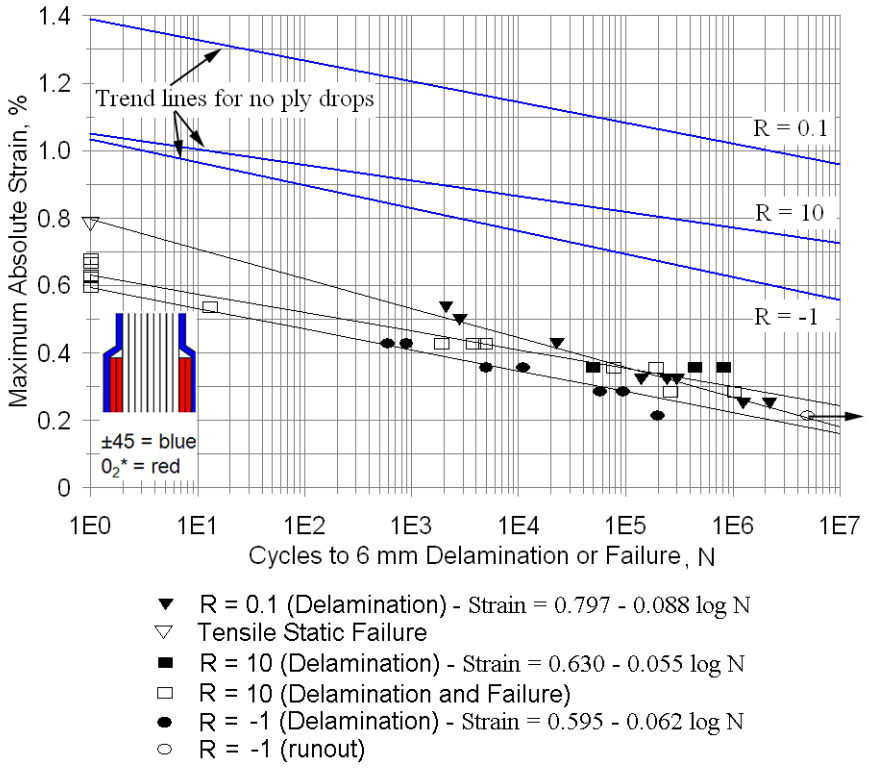

Figure 70. Maximum absolute strain versus cycles to failure for a [±45/0$_2$*/0$_9$/0$_2$*/±45] laminate, R=0.1, 10 and -1 (contains ply drops for the 0$_2$* Plies; 0° plies are carbon, ±45° plies are glass).

5.2. Thick Laminates

The thin laminate results indicate a serious problem with delamination at ply drops in laminates with carbon fiber 0° plies. To better represent actual blade laminates while remaining within the load limits of available testing machines (250 kN), a series of thicker laminates were tested under compression loads only. The number of plies dropped at the same location was varied to simulate unidirectional plies of varying thickness. The laminates are based on the configuration [(±45)$_3$/0$_{27}$/(±45)$_3$] with additional dropped 0° plies running half of the coupon length, designated 0*. The ±45° plies are glass/epoxy while the 0° plies are carbon/ epoxy; the next section compares these laminates with all glass laminates having the same configuration and resin. The test specimen is symmetrical through the thickness (Figure 21) which simplifies interpretation of results but limits the effective thickness compared to the Complex Coupon discussed in the next section.

Figures 71 and 72 give the results for the laminates with varying numbers of plies dropped under the surface ±45 glass plies, [(±45)$_3$/0$_n$*/0$_{27}$/0$_n$*/(±45)$_3$], where n is 1, 2 or 4. Figure 73 compares the results from the thinner laminates with the thick laminates for the double ply drop case. As expected, the trends in Figures 71 and 72 show lower cycles to delaminate and lower

static strength as the number of dropped plies at a location increases. The thick laminate with double ply drops delaminates at about the same strains as do the thin laminates with double ply drops (Figure 73). Thus, little effect of the fraction of 0° plies dropped is evident, indicating that the data should also be representative of still thicker laminates typical of blade spar-caps, and that the R=0.1 and -1.0 data obtained for the thin laminates would also be meaningful for the thick laminates.

The double ply drop data show what may be an unacceptable lifetime decrease for carbon 0° plies, having a total doubled ply thickness of about 0.6 mm. The limited single ply drop (0.3 mm) results show much improved performance over the double ply drops. Data for single ply drops were difficult to obtain because the load levels for delamination in fatigue were sufficiently close to the ultimate strength that failures occurred in the grips prior to delamination at the ply drop. Taking the data as lower limits to the delamination lifetime, the performance with single ply drops appear much less problematic to blade design than do the double ply drops (0.6 mm total dropped thickness).

Earlier work had found only slight effects of the position of the dropped plies through the thickness for static strength [5, 24, 28]. Under fatigue loading the ±45° plies which cover the surface 0° ply drops in this laminate configuration may soften considerably in fatigue, providing less constraint on the Mode I peeling of the surface 0°. The effect of dropping 0° plies on the surface of the 0° stack versus the interior is evident in Figure 74 for the double ply drops. The double interior drops appear to perform only slightly better than do the double surface drops at higher cycles. Still, the single surface ply drop performs much better. The single ply drop results in Figure 71 can be compared to literature data for hybrid glass/carbon flexbeams [26], where single ply drops half as thick as those used here produced delamination at surface strains on the order of 0.5% at 10^6 cycles. Thus, the flexbeam data are consistent with the results of this study for a resin system with similar interlaminar toughness.

5.3 Glass versus Carbon Fibers

To provide a direct comparison to all glass fiber laminates, the thick laminate configurations for carbon were also tested with glass fiber 0° plies, using the same epoxy resin prepreg. The fiber volume fraction for the glass prepreg was lower than the carbon, 47% versus 53%. As noted earlier (Table 12), the static Mode II delamination resistance was considerably higher for the glass, possibly due to the lower fiber content, which provides thicker resin areas and can produce higher toughness [53].

The glass results are given in Figures 75 and 76. The data in Figure 75 indicate much higher strains to cause delamination for the glass 0° plies as compared with the carbon. The effect of the number of plies dropped is similar to the carbon 0° case, except for the static data. The relatively high static strength for the 4 ply drop case may reflect an increased buckling resistance provided by the added thickness. Buckling effects are more pronounced with the lower modulus glass in compression. Even with four 0° glass plies dropped at the same location (the surface of the 0° ply stack), the strains to delaminate are similar to those for a single carbon ply drop; the comparison is different when stresses are considered, Figure 76. Now the carbon 0° performance

is better than the glass for all cases, but not to the extent of the advantage for glass in terms of strains.

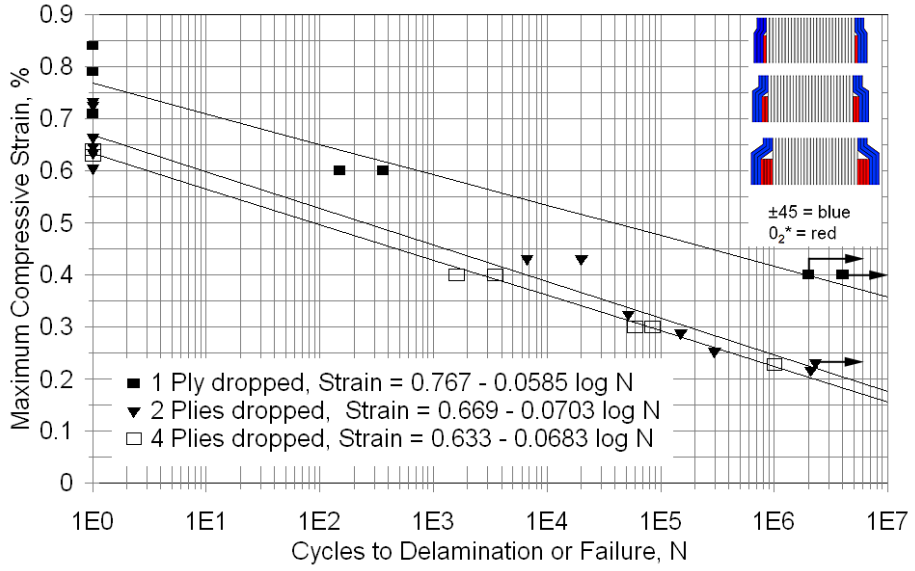

Figure 71. Maximum compressive strain versus cycles to failure for a $[(\pm 45)_3/0_n*/0_{27}/0_n*/(\pm 45)_3]$ laminate with n = 1, 2 and 4 plies dropped at the surface of the 0° stack, R = 10 (0° plies are carbon and ±45° plies are glass).

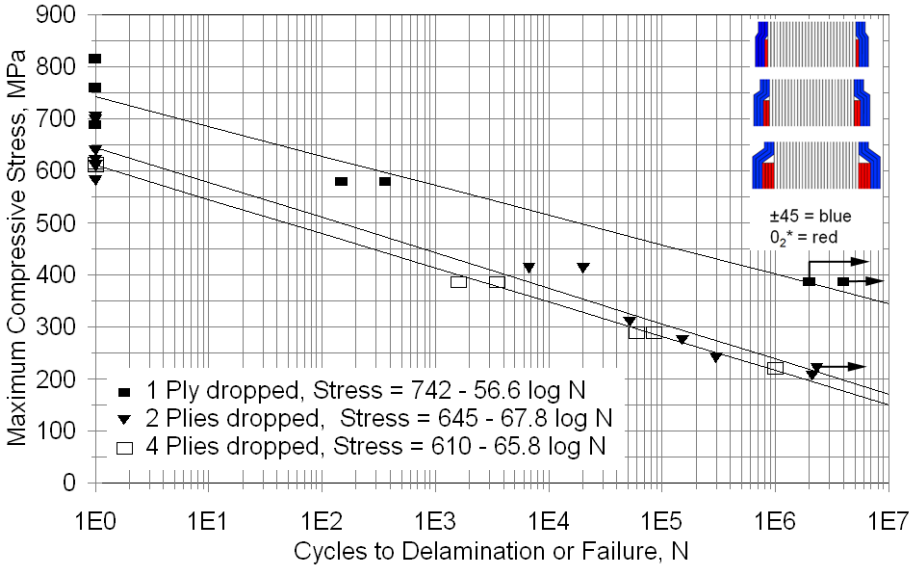

Figure 72. Maximum compressive stress versus cycles to failure for a $[(\pm 45)_3/0_n*/0_{27}/0_n*/(\pm 45)_3]$ laminate with n = 1, 2 and 4 plies dropped at the surface of the 0° stack, R = 10 (0° plies are carbon and ±45° plies are glass).

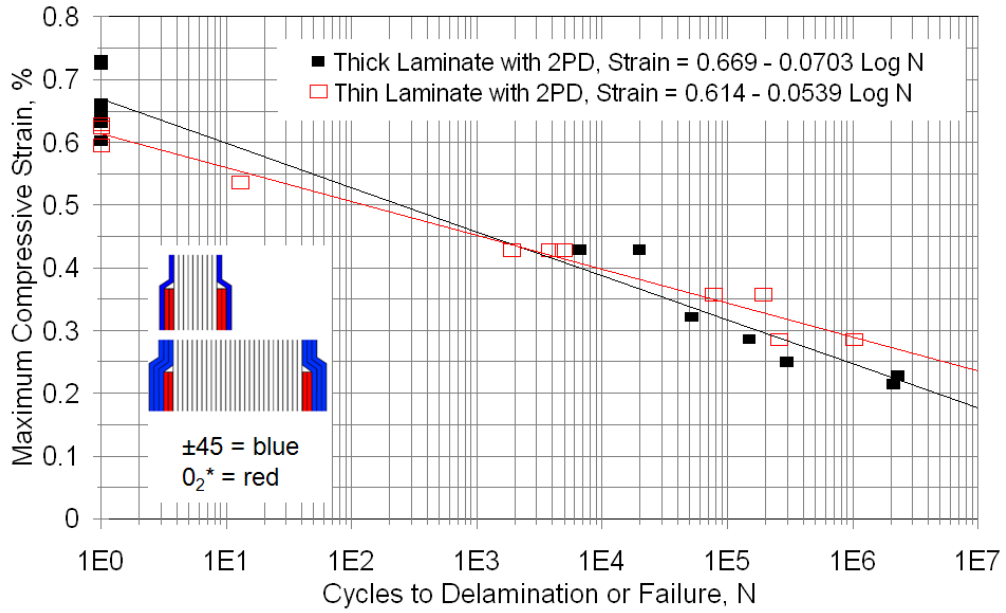

Figure 73. Comparison of maximum compressive strain versus cycles to delamination or failure for a thick $[(\pm45)_3/0_2^*/0_{27}/0_2^*/(\pm45)_3]$ laminate and a thin $[\pm45/0_2^*/0_9/0_2^*/\pm45]$ laminate, both with 2 plies dropped at the surface of the 0° stack (0° plies are carbon and ±45° plies are glass).

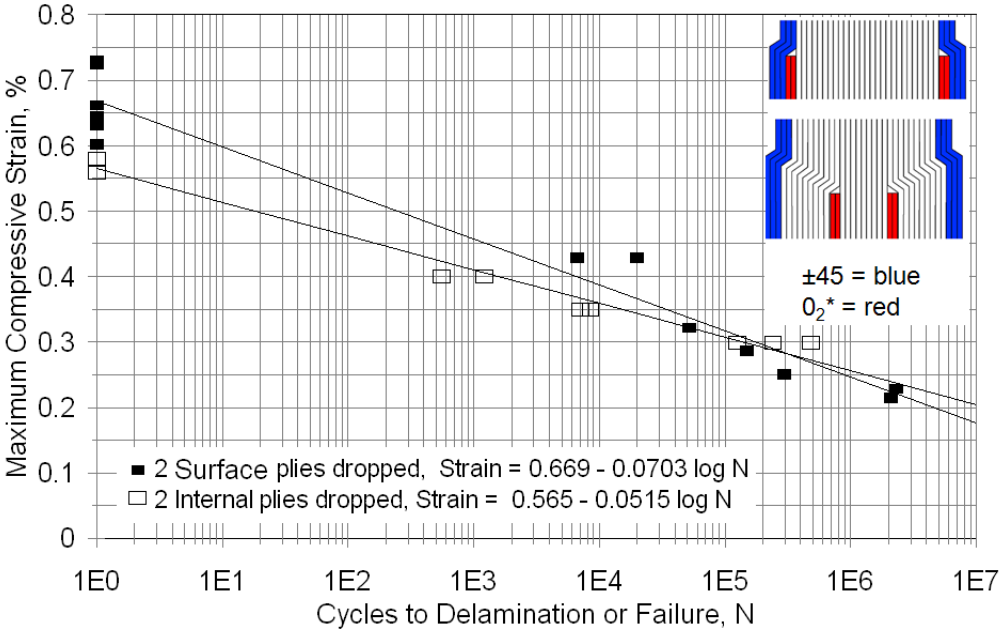

Figure 74. Comparison of the maximum compressive strain versus cycles to delamination or failure for laminates with two plies dropped at the surfaces of the 0° stack $[(\pm45)_3/0_2^*/0_{27}/0_2^*/(\pm45)_3]$ versus laminates with two internal plies dropped at two locations $[(\pm45)_3/0_9/0_2^*/0_9/0_2^*/0_9/(\pm45)_3]$, R = 10 (0° plies are carbon and ±45° plies are glass).

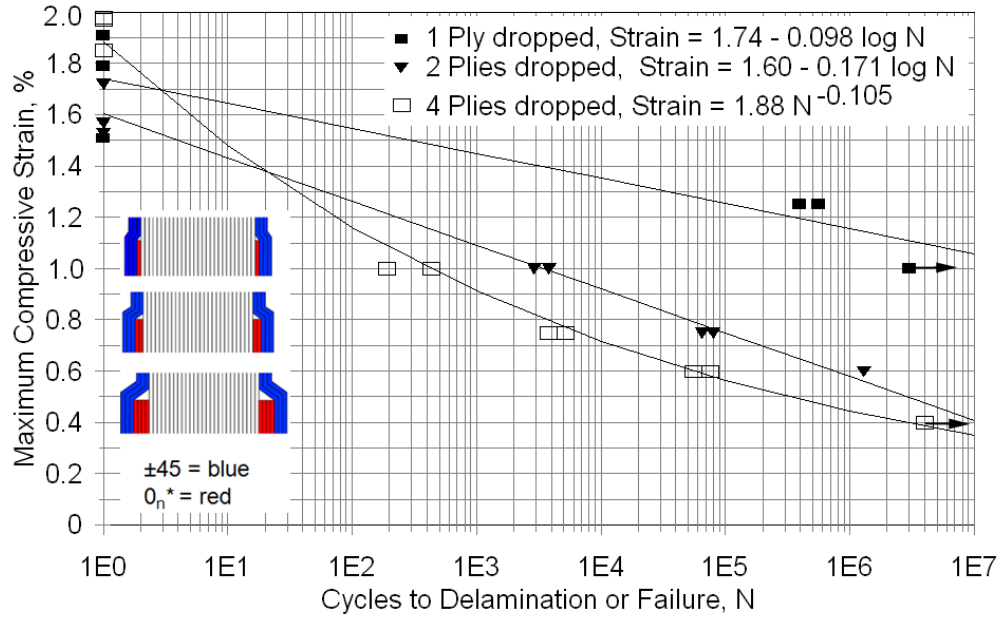

Figure 75. Maximum compressive strain versus cycles to failure for a $[(\pm45)_3/0_n*/0_{27}/0_n*/(\pm45)_3]$ all glass laminate with n = 1, 2 and 4 plies dropped at the surface of the 0° stack, R = 10 (0° and ±45° plies are glass).

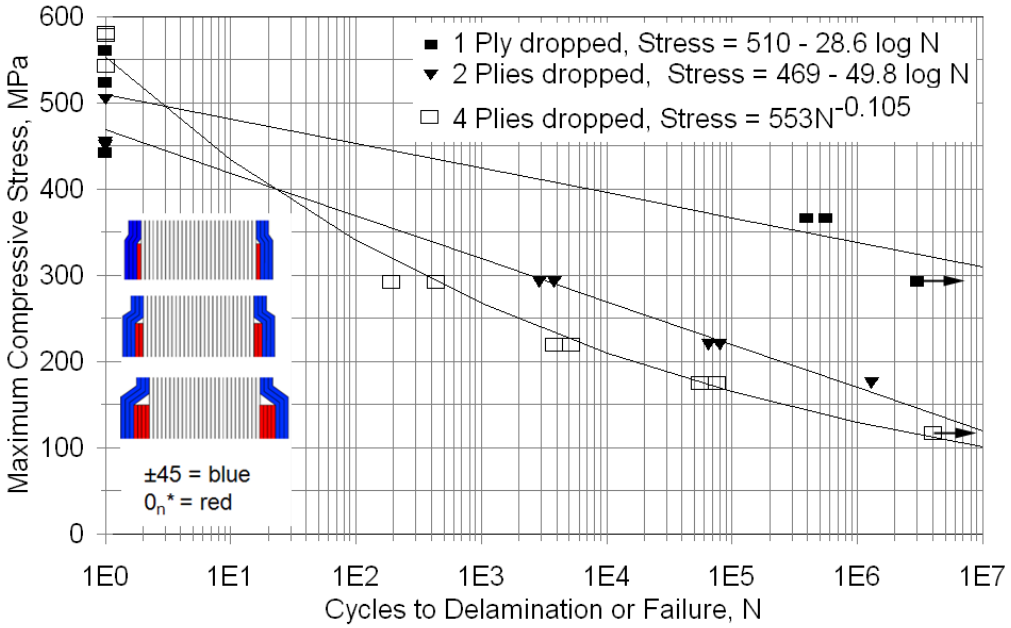

Figure 76. Maximum compressive stress versus cycles to failure for a $[(\pm45)_3/0_n*/0_{27}/0_n*/(\pm45)_3]$ laminate with n = 1, 2 and 4 plies dropped at the surface of the 0° stack, R = 10 (0° and ±45° plies are glass).

Figures 77 and 78 compare laminates with carbon and glass 0° plies for the double internal ply drop case, which has a less complex delamination pattern than the ply drops at the surface of the 0° stack, which have adjacent ±45° layers. As in other cases, the strains for delamination are

much higher for the glass 0° plies, while the stresses are slightly higher for the carbon 0° plies. Figure 79 shows similar strain differences for the double external ply drop case.

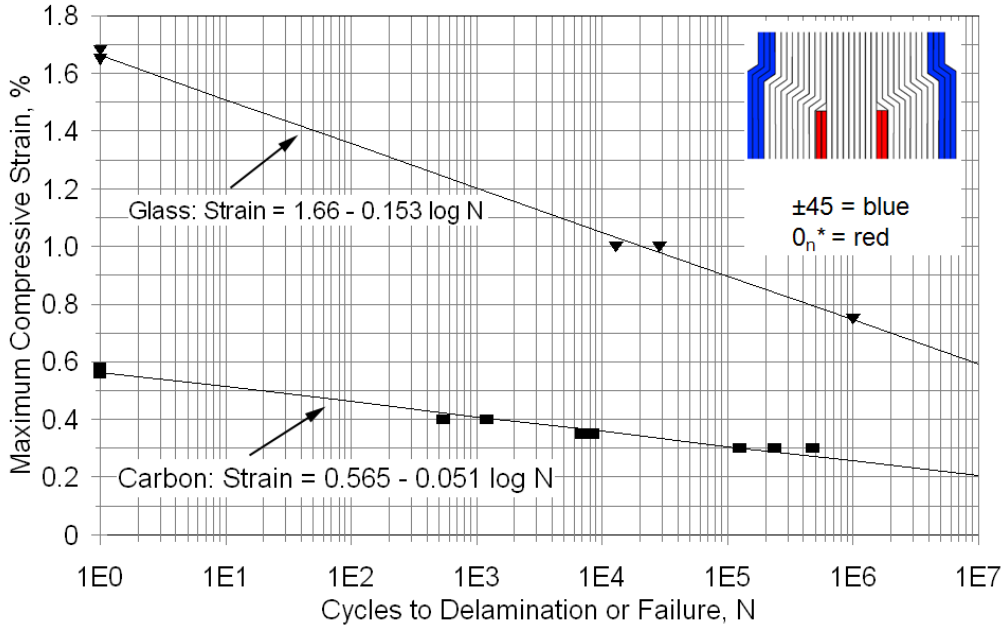

Figure 77. Maximum compressive strain versus cycles to delaminate with two double internal ply drops for thick laminates with carbon and glass 0° plies, ±45° plies are glass, $[(\pm 45)_3/0_9/0_2{*}/0_9/0_2{*}/0_9/(\pm 45)_3]$.

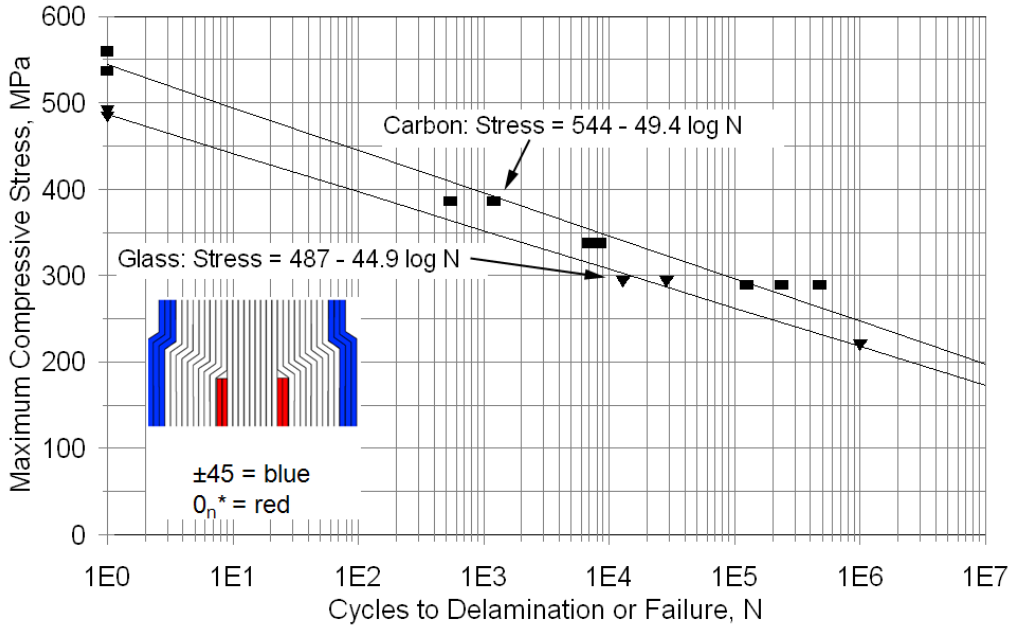

Figure 78. Maximum compressive stress versus cycles to delaminate with two double internal ply drops for thick laminates with carbon and glass 0° layers, all plies are glass, $[(\pm 45)_3/0_9/0_2{*}/0_9/0_2{*}/0_9/(\pm 45)_3]$.

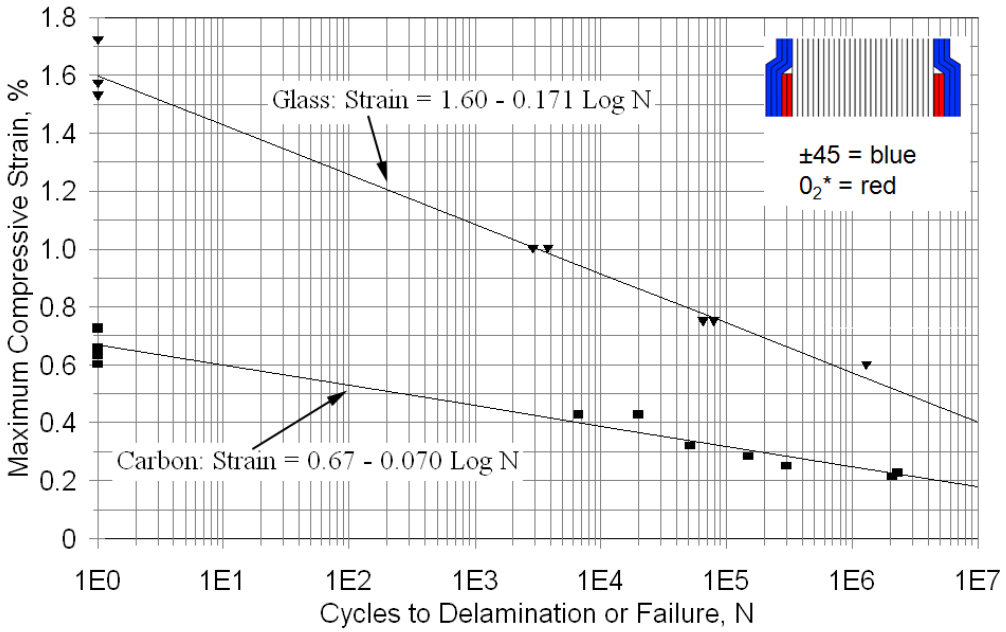

Figure 79. Strain-cycles comparison for laminates with carbon vs. glass 0° plies, double exterior ply drops [$(\pm 45)_3/0_2^*/0_{27}/0_2^*/(\pm 45)_3$] (all plies are glass).

5.4 Finite Element Analysis of Ply Drop Delamination

A detailed finite element analysis of the ply drop geometries tested experimentally, as well as many additional geometries including the ply drop and joint geometries reported in Reference 3, has been carried out by Wilson [59] using the ply elastic constants in Table 12. Reference 59 also includes analysis of special treatment of ply drop edges including chamfering and pinking, the latter explored experimentally in Reference 3. Wilson's Masters Thesis is available at www.coe.montana.edu/composites/, and only a brief summary is presented here. The FEA analysis included contact elements along crack surfaces and used virtual crack closure to obtain the static strain energy release rates for observed crack geometries. The purpose was to assist in interpretation of the experimental results. Full lifetime prediction would require a fatigue crack growth simulation as in Reference 73. Figure 80 shows a typical delamination growing from a double ply drop in a thin carbon laminate (Figures 71 and 72) with a pore at the end of the dropped plies which was typical in the prepreg laminates.

The nature of the delamination problem at ply drops is evident in Figures 81-83 for the internal ply drop geometry reported experimentally in Figures 74, 77 and 78. Figures 82 and 83 represent the strain energy release rates at the delamination crack tips in terms of the opening mode, G_I, shearing mode, G_{II}, and the sum of these, the total G. The opening mode, G_I is insignificant under tension loading, and G_{II} is dominant (Figure 82). Figure 82 compares the shear, G_{II}, values for glass and carbon 0^o plies as a function of crack length at a thin side far-field static strain of 0.5%. (The model assumes equal crack lengths, which was not generally observed experimentally, and the results are given for the total of the G-values at each crack tip.) The results in Figure 82 help explain the various experimental observations, where carbon was much more prone to delamination than glass; the G_{II} values driving crack growth are over three times

as high for carbon as for glass at the same far-field strain. Compared to the critical Mode II G_{IIc} values in Table 12, the carbon is at about half the critical value of 1829 J/m^2, while the glass is much lower. While the finite element results are for static loads, the values are consistent with the fatigue curves in Figure 77 at the same strain level of 0.5%.

The tension case is a relatively simple example due to the low G_I values for crack growth into the thicker side of the ply drop; this growth direction was observed for all experiments in this study. Figure 83 gives results for compression loading of the same geometry, at the same absolute applied strain. Now, both G_I and G_{II} are of the same order of magnitude, and a mixed mode failure criterion is required, which complicates the problem. The surface ply drop geometry used in most of the experiments (Figure 80) shows very low G_I values in both tension and compression, and is, therefore, G_{II} dominated for the single crack. The consistency of the tension and compression data in Figure 69 and 70 is expected from the Mode II domination.

Other finite element analyses indicate that the delamination cracks are predominantly Mode II when growing toward the thick section, but Mode I when growing toward the thin section [20]. Reference 26 argues that the initial delamination in fatigue occurs in Mode I. O'Brien [74] argues for consideration primarily of Mode I toughness as dominating delamination problems in composites. However, the thin laminate ply drops in Figures 69 and 70 showed delamination at similar strains for all three loading conditions. Since the Mode I component would change sign in compression versus tension, causing crack closure, this argues for a Mode II domination in these results. A study of Mode II delamination at various R-values by Tanaka and Tanaka [65] found the highest crack growth rates for R=-1, consistent with Figures 69 and 70; at low maximum G_{II} values, crack growth rates were insensitive to R-value for the same G_{II} range.

5.5 Approximate Theory

Delamination under Mode II domination can be approximately modeled using strength of materials assumptions including the absence of stress gradient and bending effects. These models are based on release of the strain energy in the delaminating plies as they unload. Ignoring effects of the ±45 plies, a solution by Ramkumar and Whitcomb [75] can be rearranged to:

$$G = \frac{\sigma^2 t_p}{2E_L}\left(\frac{t_T}{t_T - t_p}\right) = \frac{E_L \varepsilon^2 t_p}{2}\left(\frac{t_T}{t_T - t_p}\right) \tag{16}$$

where σ is the applied stress, ε the applied strain, t_p the thickness of the dropped material, t_T the total thickness and G the total strain energy release rate. Substituting for the geometry in Figure 81 (using the thick side strains of 0.45% for carbon and 0.44% for glass), the predicted G-values are 921 J/m^2 for carbon and 237 J/m^2 for glass. These are in good agreement with the G_{II} values in Figure 82. However, this type of model cannot separate G_I and G_{II} values for cases like Figure 83, and does not accurately predict many cases with significant G_I values [59].

The predictions based on Eq. (16) again demonstrate that the difference between carbon and glass derives primarily from the modulus, in this case E_L of the dropped plies. G in Eq. (16) is also proportional to t_p, the thickness of dropped material, for relatively thick laminates. For the same applied strain, ε, the ply stress is higher for the carbon than for glass by the ratio of their

longitudinal moduli E_C/E_G, about 3.5 times for the prepregs used here (Table 12); at the same strain, the strain energy available in the dropped plies would differ by the same ratio. Thus, from Equation (16), the G value driving ply delamination will be about 3.5 times higher for the carbon fibers than for the glass fibers, for the same dropped thickness and applied strain. For the same applied stress, σ, the value of G would be about 3.5 times higher for glass due to the lower elastic modulus. The differences in E and G would be expected from Eq. (16) to result in predictable differences in applied strain to produce the same strain energy release rates, and expected fatigue crack growth rates [11]. These differences would translate into about $(3.5)^{1/2}$ or 1.9 times higher strain for the same delamination lifetime for glass, or about 1.9 times higher stress for carbon. The data in Figures 77 and 79 are for the interior and exterior ply drops in compression. As noted above, the G_I component is high for the interior case (Figure 82), but low for the exterior case. The experimental strain values at the same lifetime for the glass are almost three times higher than for carbon in Figure 77, with a slightly reduced ratio for the external case in Figure 79. The reason that the glass exceeds the predicted 1.9 times higher strain for the same lifetime compared with carbon may relate to the slightly higher G_{IIc} for glass in Table 1 and the mode mixity present for the internal case (Figure 83). However, agreement with experimental data is good considering the approximate nature of the model geometries and the static loading discussed earlier.

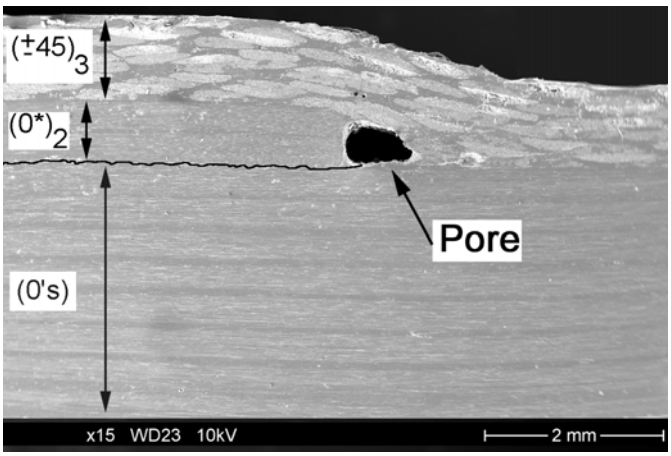

Figure 80. Photograph of delamination crack growing from pore ahead of double ply drop (see Fig. 21), carbon 0^o plies, compression fatigue (crack path enhanced).

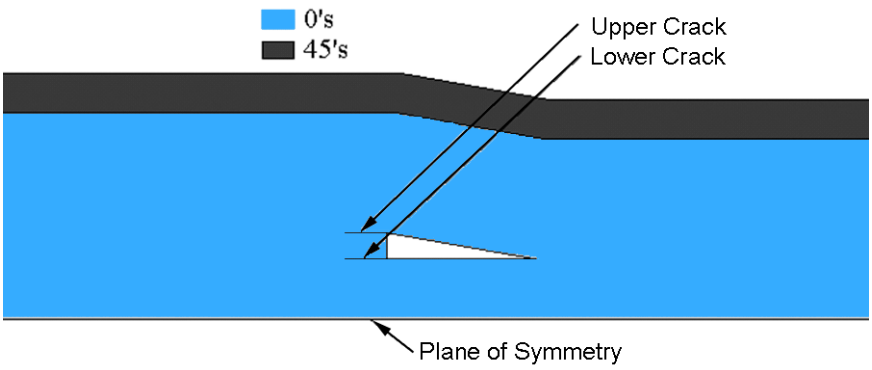

Figure 81. Finite element model showing internal ply drop, delamination cracks and pore ahead of ply drop.

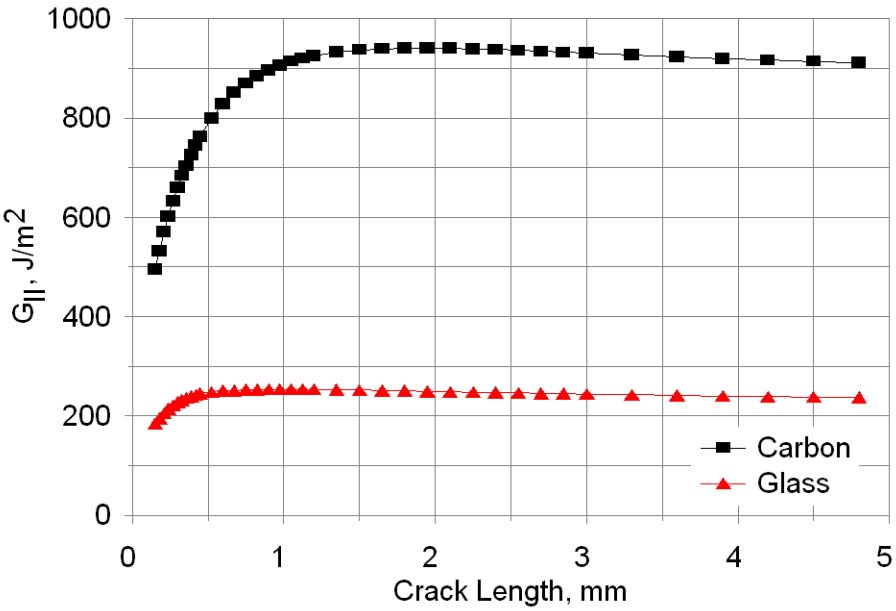

Figure 82. Comparison of glass and carbon FEA results for internal ply drop under tensile load, total G_{II} component for both cracks ($G_I \approx 0$), thin side strain = 0.5%.

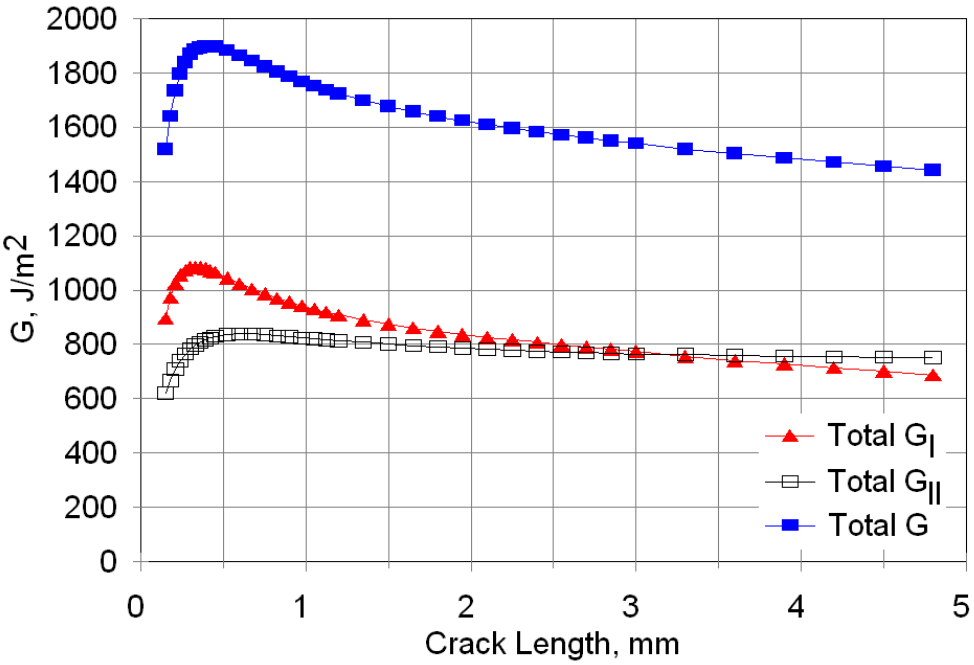

Figure 83. Same FEA case as Figure 82, but compression load (same strain), carbon 0° plies.

5.6 Design Implications

These results indicate that delamination at ply drops under fatigue loading can occur at relatively low applied strain levels for carbon fiber laminates. Delamination at ply drops in glass fiber wind turbine blades has not been widely observed, but has been cited as a factor in a blade failure study [72]. The results of this study indicate potential problems for ply drops involving ply thickness on the order of 0.6 mm for carbon fibers. This would represent relatively thin plies for infusion processes, but relatively thick plies for prepreg, where most aerospace prepreg ply thicknesses are on the order of 0.15 mm.

It is evident from these results and discussion that, for the same delamination resistance, substantially thicker ply drops can be used for glass than for carbon, in terms of allowable strains. If carbon and glass blades are designed to the same stiffness, then the design strains should be similar assuming the designs are fatigue sensitive. For carbon, with excellent in-plane fatigue resistance, ply drop delamination may be a limiting factor unless the plies are very thin, if thickness tapering is used. Manufacturing innovations for rapidly placing thin plies may be important if carbon is to be used in blade structures.

Methodologies for the design and analysis of delamination problems in composites have been validated using finite element analyses [20, 23-25]. A number of strategies for improving delamination resistance have been demonstrated [24]; the most direct is to increase the resin toughness [5, 53, 76].

SECTION 6. INFUSED COMPLEX STRUCTURED COUPONS

6.1 Concepts

The prepreg ply drop results from Section 5 were used to design a complex structured coupon for resin infusion studies which would provide a useful test of the performance of various infusion resins and fabrics for complex structure including ply drops, but also depending on the in-plane performance of the fabrics. While FEA based fracture mechanics can be an effective technology for analyzing ply drops and designing against delamination as described in Section 5, its complexity in application limits its usefulness in wind blades. Despite the complexity, basic mode delamination test data as in Table 12 provide a basis for materials selection in blades, and FEA based simulations of delamination in realistic blade structural representations could identify more basic static and fatigue materials parameters which warrant consideration.

The concept involved in developing the complex structured coupon is to bring the ply drop technology from Section 5 into a context which is more useful for infused blades. The coupon shown in Figures 9, 22 and 23 (and internal structure in Figure 2b) represents the complex blade composite structure in areas of thickness tapering, and may also provide useful qualitative trends for other structural detail areas. Based on the FEA results discussed in Section 5.5, the primary delamination crack in this geometry (with the ply drops on the surface of the 0^o stack) propagates into the thick side in mode II. However, the in-plane response of the plies, particularly matrix cracking of the biax layers, interacts with and can limit the delamination growth. Various infusion resins and fabrics are compared in this context, and the quantitative effects of thicker ply drops, useful in manufacturing, can be established. Loads to produce damage in this study were lower than in the prepreg tests (Section 5), due to the use of glass fibers and thick plies. This allows testing over a full range of tension and compression static and fatigue tests without the need for the end loading used for thick laminates in Section 5, which limited those results to compression. Although nonsymmetrical, the coupon design allows static and fatigue results for damage development and progression to be expressed in terms of allowable blade strains or knockdown factors.

6.2 Static Tests

Test results for the Complex Laminate coupon under static loading are given in Figures 84-89. Sample images of the damage development sequence during the fatigue lifetime of a specimen are given in Figure 84 (and the associated time-lapse movie). This sequence is similar for static tests as the load is increased toward failure. The damage geometry for most coupons is illustrated in Figure 85. The sequence of damage progression under tensile loading is as follows for both static and fatigue loading:

1. A crack forms in the resin, across the ends of the ply drops
2. Delaminations L_1 and L_2 grow along the dropped plies, into the thick side; L_2 only grows a short distance and arrests.
3. Matrix cracking (L_4) develops and spreads in the ±45 plies adjacent to the ply drops
4. Delamination L_3 develops and spreads into the thin section, as an extension of L_1

5. After damage spreads globally along the specimen, separation in the ±45 and 0° plies near the ply drops progresses to produce complete failure.

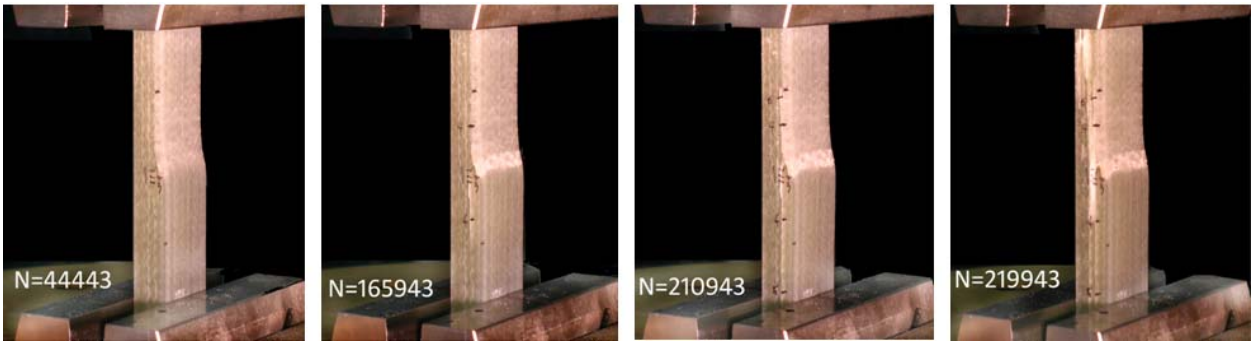

Figure 84. Images of damage in complex coupon with VE-1 resin, two ply drops, maximum load 44.5 kN, R = 0.1, at four cycle levels, N = 44443, 165943, 210943, 219943.

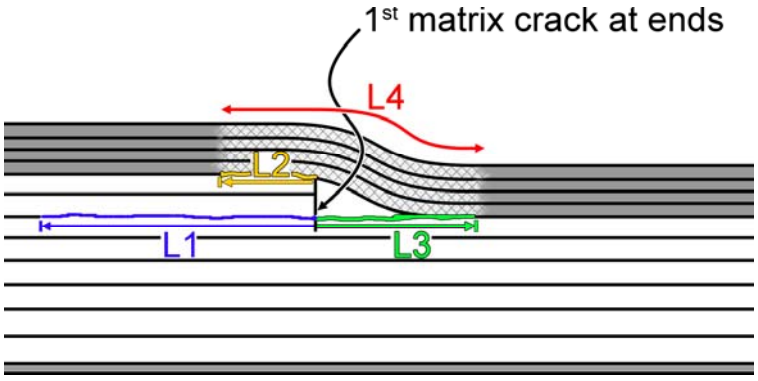

Figure 85. Schematic of various damage components and extents in complex coupon.

This progression through (4) was similar for all cases, but most tests were terminated prior to (5). Under compressive fatigue loading the matrix crack across the ends of the dropped plies, (1) above, was delayed until significant delamination slowly developed. The damage then spread rapidly after the matrix at the dropped ply ends formed a series of oriented cracks.

The static and fatigue response of the complex coupon depends on a variety of more basic properties of the resin and reinforcing fabrics, which, together with geometric factors, determine the overall performance. This and previous studies (Section 5) suggest the mechanisms involved in this damage sequence, and the relevant materials parameters. From linear FEA solutions (Figure 24) the stress fields and delamination modes change sign under compression relative to tension loading; shear stresses and deflections change direction. Thus, tensile matrix cracking at the ply ends is suppressed in compression, and shear amplitudes are essentially doubled (with a direction change) in reversed vs. tensile loading. In the damage sequence, the matrix cracking at the ply ends releases the dropped plies to delaminate more freely for a short distance, unloading their strain energy, until this process is restricted by the ±45 plies. When the ±45 plies form

matrix cracks and soften, the delamination L_1 is able to grow more extensively, and L_3 forms. Meanwhile, the 0^o and $\pm 45^o$ plies are subjected to accumulating damage, and may fail in a progression through the thickness, completely separating the coupon. The various damage components are expected to depend on matrix strength and toughness, $\pm 45^o$ ply crack resistance, and 0^o ply longitudinal strength and fatigue resistance. Prediction of the detailed damage progression requires a full simulation based on a complete set of component properties and geometry.

Figures 86 and 87 give static test results for the primary delamination length, L_1, as a function of applied load. The results in Figure 86 for different resins with two ply drops indicate the same ordering of resin delamination resistance as presented for other types of tests, such as Figure 68 and Table 12, epoxy>vinyl ester>polyester for base resin types. The toughened vinyl ester, VE-2, displays significantly greater resistance compared with the base vinyl ester VE-1. In contrast to the plain ±45 laminates in Figures 40, 56 and 57, the complex laminates show much greater sensitivity to the resin. The data in Figure 87 indicate a strong sensitivity of the static delamination load to the number of plies dropped at the single location for EP-1 resin, corresponding to a total thickness transition range of about 1-4 mm for the 1, 2, and 4 plies dropped. The dropped thickness effect shown here is consistent with that found for prepreg laminates with thinner plies (about 0.3 mm) in Section 5. Section 5, and other studies, demonstrated that the strain energy release rates are approximately proportional to the thickness of material dropped, excluding shape effects, so that delamination loads should vary approximately proportionally with the square root of the thickness of dropped material (Eq. 16). When the Figure 87 delamination length is plotted against the load times the square root of the number of ply drops, Load × $(PD)^{1/2}$, in Figure 88, the data for the one and two ply drop cases show good correlation, while the four ply drop case falls at somewhat higher load.

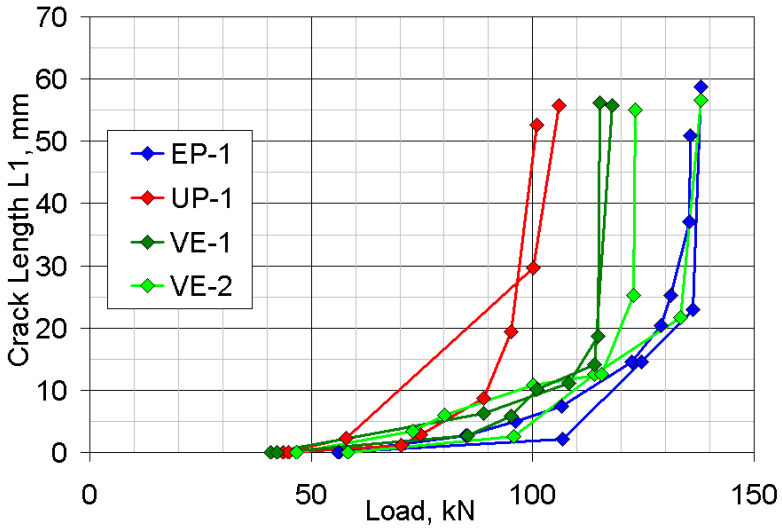

Figure 86. Static data for delamination growth vs. applied load for various resins, complex coupon with two ply drops.

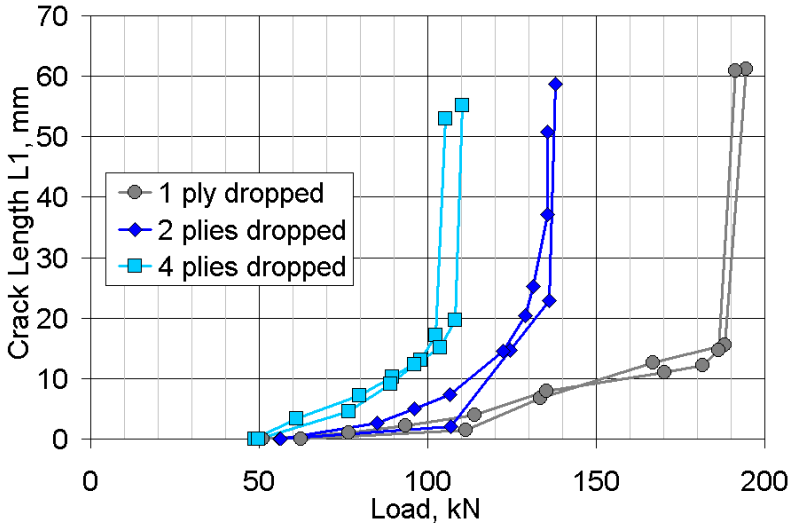

Figure 87. Static delamination growth vs. load for complex coupon with one, two and four plies dropped, resin EP-1.

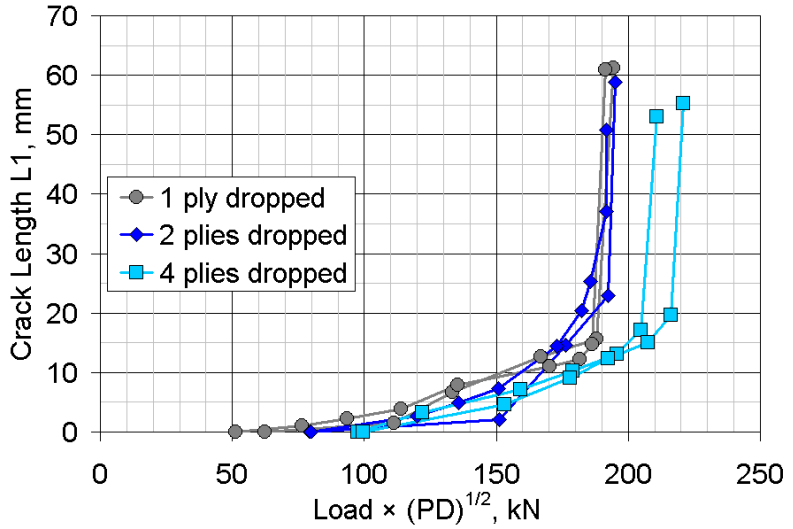

Figure 88. Static delamination growth vs. load × $(PD)^{1/2}$ for complex coupon with one, two and four plies dropped, resin EP-1 (PD is the number of unidirectional plies dropped at a single position).

Figure 89 gives a comparison of the static load curves for two biax fabrics, fabric M from Figures 86 and 87 and fabric L, which does not contain mat (Table 2), with the same fabric uni-fabric D. The stronger and stiffer (in the load direction) fabric M (Figure 39) results in increased damage resistance as expected, considering the significance of the biax plies in the damage sequence. The added strength with fabric M comes at a price, as the thickness and amount of resin are increased with the mat layer, see Figure 2 and Table 1. The two biax fabrics provide about the same weight of total glass per ply (Table 2).

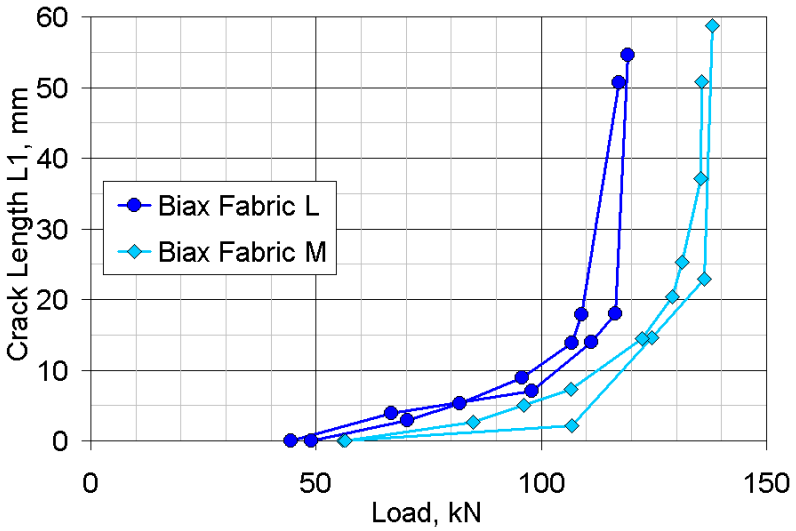

Figure 89. Effect of biax fabric type on static damage growth response, two ply drops, epoxy EP-1.

6.3 Fatigue Results

Figures 90-97 present the fatigue results for delamination growth in complex coupons as a function of resin, applied load, thickness of material dropped and R-value, and biax fabric. Results for the different resins are consistent with the static data, as are those for the thickness of dropped material, Figures 90, and 92 and 93, respectively. The effect of maximum load on the damage growth is significant, as expected (Figure 91).While the delamination rate in fatigue is generally reported to vary with some power of the strain energy release rates [5, 11, 25, 26 and 73], and the strain energy release rates (G_I and G_{II}) to vary with the square of the load, a full simulation of the progression of all of the damage components is necessary to fully predict the results for load and dropped thickness variations.

The effects of loading condition for tensile, reversed, and compressive fatigue (R = 0.1, -1 and 10) for the EP-1 and UP-1 resins with two ply drops in Figures 94 and 95 again highlights the sensitivity to reversed loading as well as resin. This is consistent with both the ±45 laminates (Figure 58 and 59) and data for prepreg laminate delamination in Mode II (Section 5). The comparison of biax fabrics in Figure 96 is consistent with the static data, Figure 89.

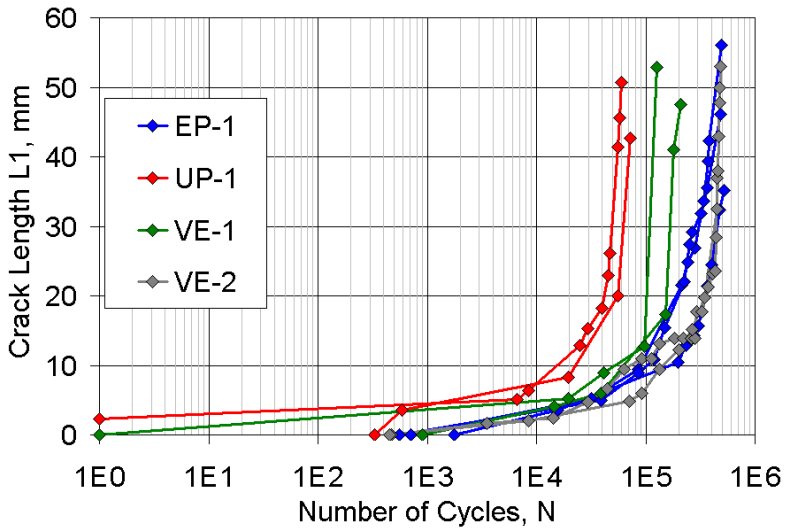

Figure 90. Delamination growth in fatigue for various resins, complex coupon with two plies dropped, maximum load 44.5 kN, R = 0.1.

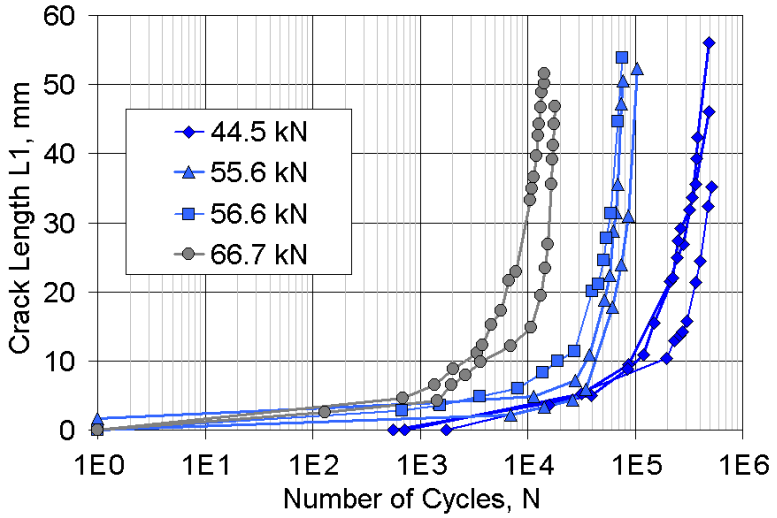

Figure 91. Effect of maximum load variation on delamination growth in fatigue, complex coupon with two plies dropped, resin EP-1, R = 0.1.

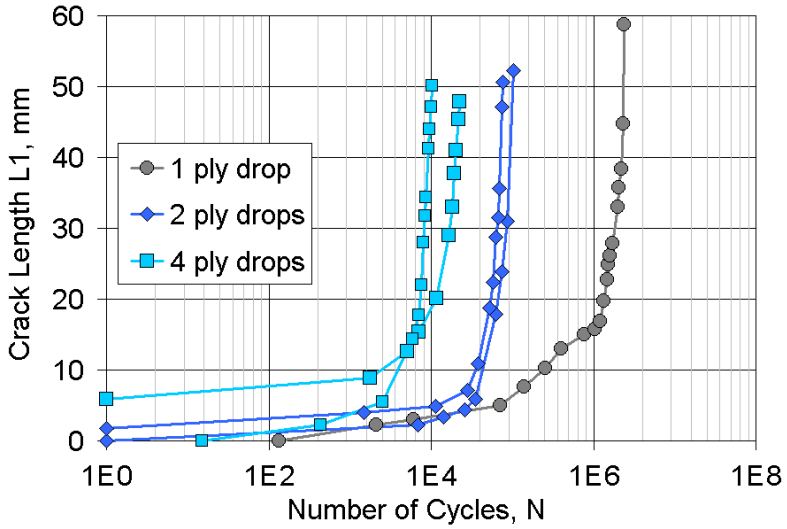

Figure 92. Effect of number of plies dropped on delamination growth in fatigue, resin EP-1, with a maximum load of 55.6 kN, R = 0.1.

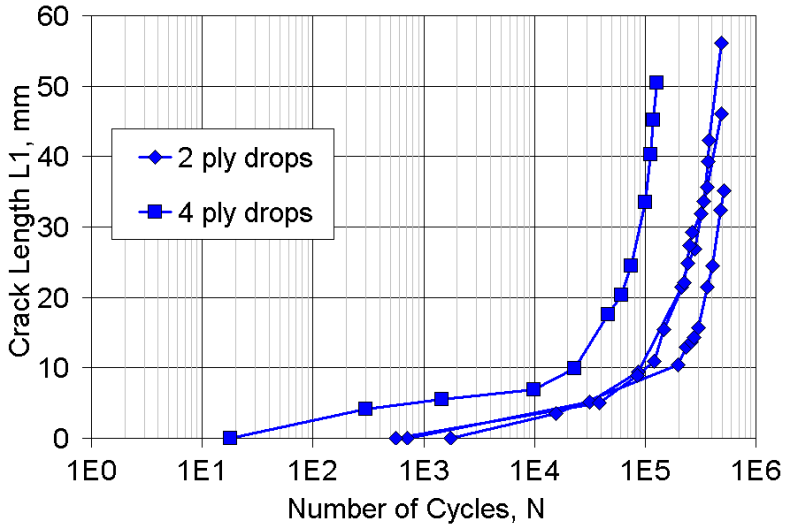

Figure 93. Effect of number of plies dropped on delamination growth in fatigue, resin EP-1, with a maximum load of 44.5 kN, R = 0.1.

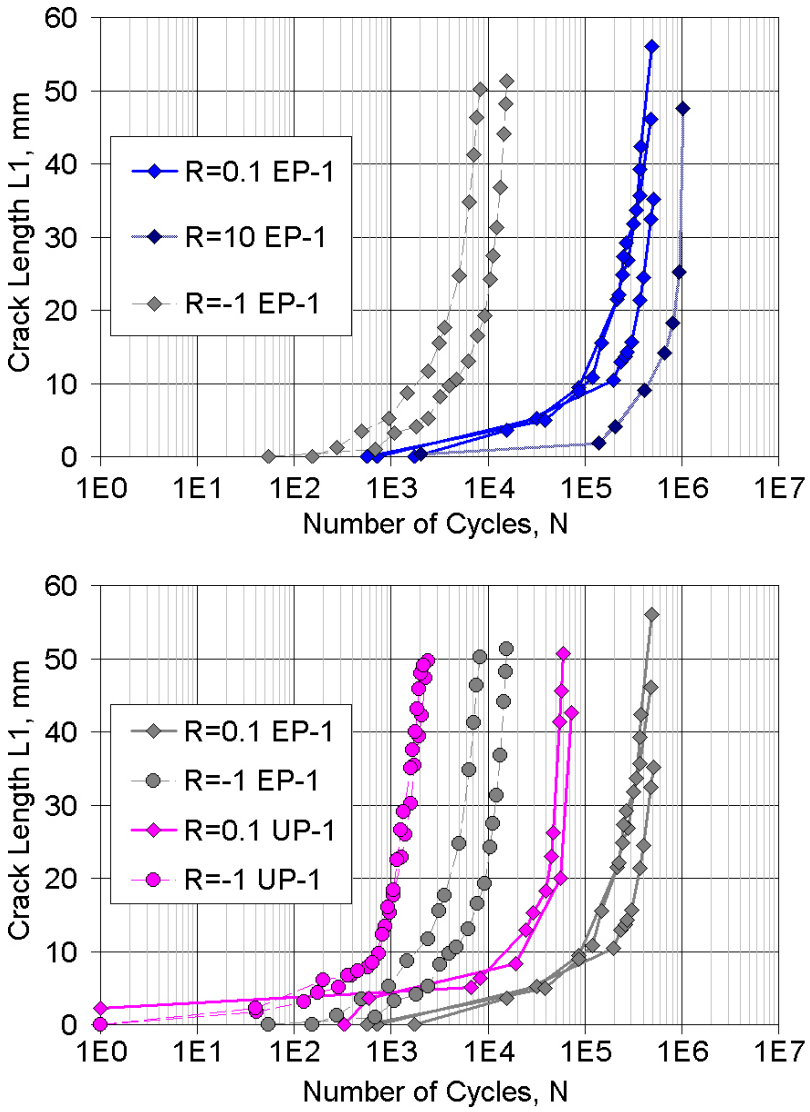

Figure 94. Effect of R-value on delamination growth, complex coupon with two plies dropped, with a maximum force of 44.5 kN: (top) epoxy EP-1 at R = 0.1, -1 and 10; and (bottom) comparison of EP-1 and UP-1 resins, R = 0.1 and -1.

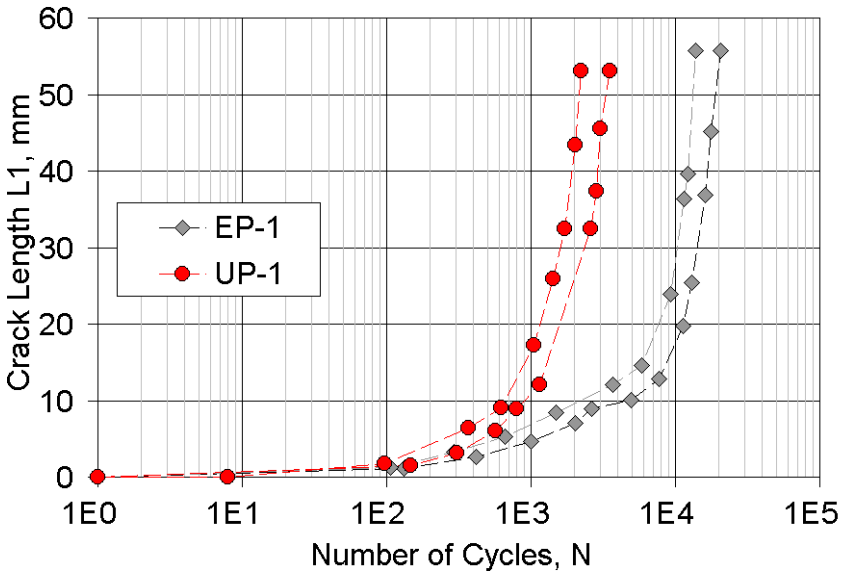

Figure 95. Effect of resin on reversed loading fatigue with a single ply drop, EP-1 epoxy and UP-1 polyester, R=-1, maximum load 55.6 kN.

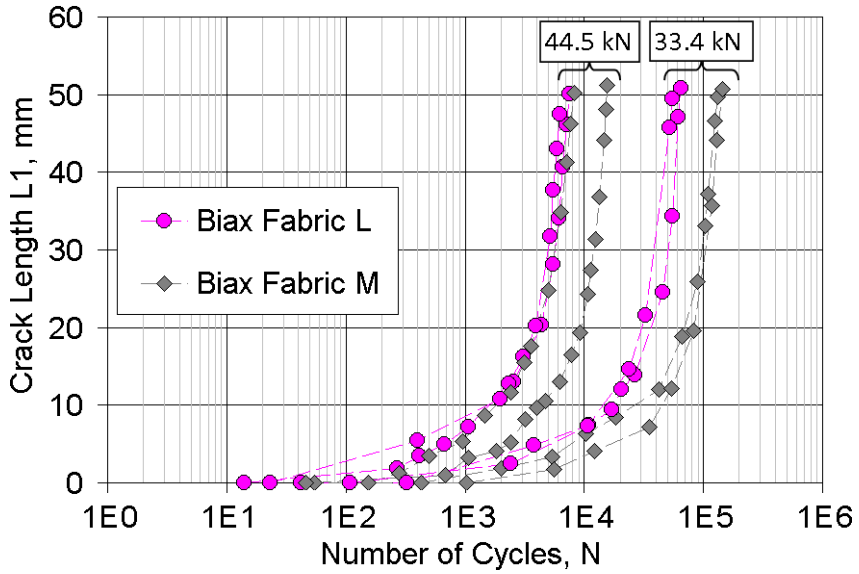

Figure 96. Effect of biax fabrics L vs. M on damage growth in fatigue, R = -1, 44.5 kN maximum force, two ply drops, epoxy EP-1.

A comparison of the data for various cases of complex laminates with the plain laminate data trends in Figures 43 and 57 is shown in Figure 97, using average initial strains on the thin side of the specimen from Figures 24 and 25. The knockdown in strain level for the complex laminates with ply drops, relative to plain ±45 laminates is evident in these results. All complex laminates with more than a single ply dropped fail before the plain ±45 laminates at the same strain level. The single ply drop case is not as clearly dominated by the dropped ply effects. A similar comparison of complex coupon data to plain 0^o fabric dominated multidirectional laminate data from Figure 43 is also shown. This figure allows a comparison of the lifetime of various complex

coupons with plain structural multidirectional laminates in terms of strain for different resins, and number of plies dropped at a single location. Figure 97 allows assessment of the penalties incurred by cost-reducing approaches of selecting lower performance resins and dropping more plies at a particular location instead of staggering single ply drops. While the penalties are real, their effects on allowable strains appear moderate.

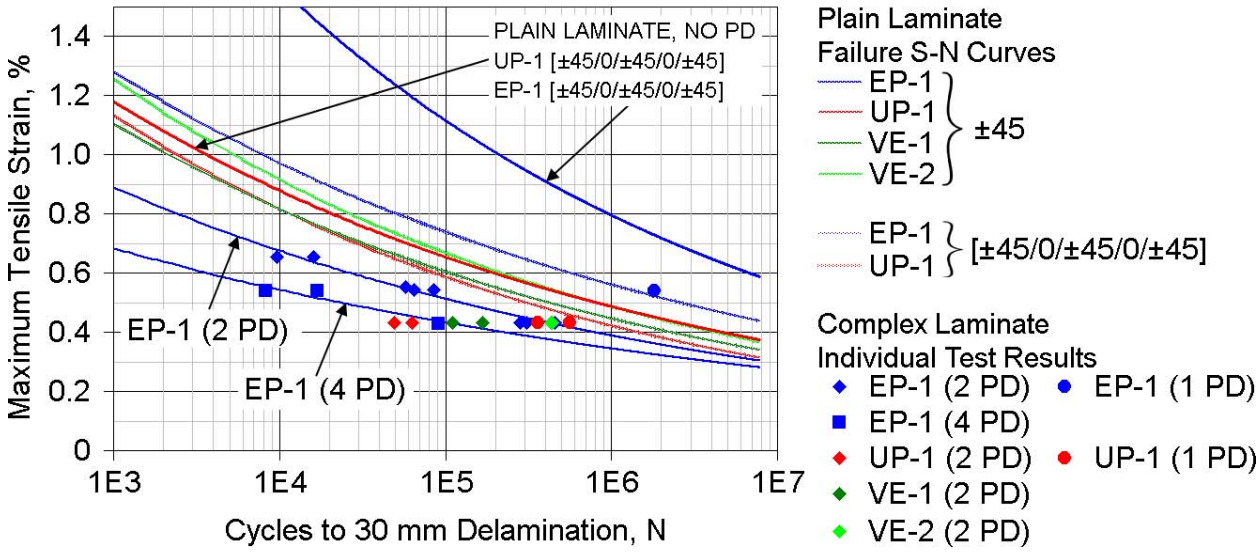

Figure 97. Average thin-side maximum initial strain vs. cycles to produce 30 mm delamination for complex coupon, compared with strain-cycles trend lines for plain laminates with no ply drops, R = 0.1.

Table 14. Static and Fatigue Results for Complex Coupons
(a) Static Test Results

Designation	Biax fabric	Resin	PD*	Thickness of thin section, mm	Load For L_1 = 30 mm, kN	Nominal axial strain** at L_1 = 30 mm (%)
PD1CDMEP-1	M	EP-1	1	11.39	189	1.862
PD2CDMEP-1	M	EP-1	2	11.25	135	1.334
PD4CDMEP-1	M	EP-1	4	11.15	106	1.042
PD2CDLEP-1	L	EP-1	2	10.48	147	1.505
PD2CDMUP-1	M	UP-1	2	10.94	99	0.973
PD2CDMVE-1	M	VE-1	2	10.44	115	1.139
PD2CDMVE-2	M	VE-2	2	11.15	129	1.274

Table 14. (cont) Static and Fatigue Results for Complex Coupons
(b) Fatigue Test Results

Designation	Biax fabric	Resin	PD*	Maximum absolute load, kN	Nominal maximum axial strain**, %	R	Cycles to L_1 = 30 mm
PD1DMEP-1.55.01	M	EP-1	1	55.6	0.54	0.1	1822904
PD2DMEP-1.55.01	M	EP-1	2	55.6	0.54	0.1	74686
PD4DMEP-1.55.01	M	EP-1	4	55.6	0.54	0.1	12595
PD2DMEP-1.44.01	M	EP-1	2	44.5	0.43	0.1	348518
PD4DMEP-1.44.01	M	EP-1	4	44.5	0.43	0.1	90688
PD2DMEP-1.56.01	M	EP-1	2	56.6	0.55	0.1	57330
PD2DMEP-1.66.01	M	EP-1	2	66.7	0.66	0.1	12832
PD2DMEP-1.44.10	M	EP-1	2	44.5	-0.46	10	956520
PD2DMEP-1.33.-1	M	EP-1	2	33.4	0.32	-1	100939
PD2DMEP-1.44.-1	M	EP-1	2	44.5	0.46	-1	8844
PD1DMEP-1.55.-1	M	EP-1	1	55.6	0.54	-1	12333
PD2DLEP-1.33.-1	L	EP-1	2	33.4	0.35	-1	45271
PD2DLEP-1.44.-1	L	EP-1	2	44.5	0.47	-1	5319
PD2DMUP-1.44.01	M	UP-1	2	44.5	0.43	0.1	56301
PD1DMUP-1.44.-1	M	UP-1	1	44.5	0.45	-1	9249
PD1DMUP-1.55.-1	M	UP-1	1	55.6	0.54	-1	2418
PD2DMUP-1.44.-1	M	UP-1	2	44.5	0.46	-1	1485
PD2DMVE-1.44.01	M	VE-1	2	44.5	0.43	0.1	138046
PD2DMVE-2.44.01	M	VE-2	2	44.5	0.43	0.1	436187

*PD is the number of unidirectional plies dropped at a single location (Fig. 22)

**The nominal axial strain is the initial average value through the thickness along line (h) in Fig. 24 and 25 at a load of 44.5 kN Strains at other applied loads are adjusted proportionally from the value at 44.5 kN; strains are from a linear elastic FEA solution with no damage present.

SECTION 7. ADHESIVE JOINTS

7.1 Concepts

The static and fatigue testing of adhesive joints is pursued either using strength concepts for generic joint geometries such as lap shear, or else using fracture mechanics concepts which address crack propagation (see Section 2.2.5). While the latter provides more fundamental adhesives characterization in terms of the resistance to crack growth and is necessary if considering large cracks in blade adhesives, joint strength testing addresses the critical effects of crack initiation and naturally occurring flaws, and may provide more meaningful results for tougher adhesives. These approaches have been considered in recent developments for wind blade adhesives standards and test programs [77-79].The approach in this study was to develop a lap shear test which would be applicable under various loading conditions and produce failure initiation within the adhesive in most cases, so that different adhesives could be compared. The test was designed to be compatible with conventional servo-hydraulic test systems and hydraulic grips. The desired test method attributes are listed in Section (3.2.5), along with a description of the test characteristics and development. Various joint test parameters have been explored.

The development of the more generic lap shear test was preceded by testing of a large population of simulated blade web joint specimens prepared by an industry partner (Section 7.3). This test series allowed identification of the major blade joint parameters (including flaws) influencing strength statistics and fatigue life for this class of joint designs.

7.2 MSU Notched Lap Shear Fatigue Test Results

7.2.1 Lap Shear Static Results

Static test results have been obtained for several geometries, peel plies, adhesives, displacement rates and adhesive thicknesses to explore the effects of various test parameters on the static strength. The baseline geometry and FEA results are given in Figures 26-28. The Hexion adhesive ADH-1 was used as a baseline adhesive for most these studies, with selected comparisons to several other adhesives. Strength results are obtained at a test rate of 0.025 mm/s except as noted, and the apparent shear strength is calculated from the maximum load to complete separation.

Early iterations of the test method included the use of other geometries and laminates. When notches were cut close to the opposite laminate surface (Figure 26) it was difficult to control whether the notch root penetrated the laminate surface; and results were inconsistent. On the other hand, notches which penetrated the adhesive less deeply often resulted in crack initiation at the upper laminate interface, inside the laminate surface, which was less desirable in comparing different adhesives. In initial tests biax laminates were more likely to fail below the first ply of the adherend, rather than in the adhesive, so the results presented here are for unidirectional laminate adherends of fabric F with resin EP-1, nominally 5 mm thick (Figure 28).

Figure 98 gives a series of bar charts with standard deviation markers for several static test comparisons; at least five test results were included for each case, except where noted. The apparent lap shear strength, τ_{app}, is calculated for each case from Eq. (17); it should be noted that failure is associated with the local stress concentration area at the notch root in Figure 27, so the average shear stress has limited physical meaning except in comparisons with other results from the same geometry (see Fig. 26).

$$\tau_{app} = F/ W \times L \tag{17}$$

where F is the applied force, W is the width (about 25 mm) and L is the overlap length (either 12.7 mm or 25.4 mm).

Figure 98 (a) gives different mixing batch results for adhesive ADH-1, all taken from the same containers. The slight variations between mixing batches should be taken into account when considering comparisons of other parameters. The hand mixing of very viscous adhesive and hardener, while done carefully, is not precise, and resulting porosity varies somewhat between batches. Adhesive joints are well known [30] to be sensitive to interface preparation, which, for wind blades may be a surface produced by the removal of the peel ply shown in Figure 8. The type of peel ply used is reported [80] to significantly affect the joint strength for prepreg carbon/epoxy laminates in some instances. Figure 98 (b) indicates little effect of peel ply type for the three products evaluated, for adhesives ADH-1 and ADH-2. The peel ply is applied to both laminate surfaces, but the resin distribution layers are used only on the top, under the vacuum bag (Figure 8). Since the bottom (mold) side is more nearly flat than the top side, the bottom mold side is used as the bonding surface unless noted. No significant effect on joint strength was found for bonding on the mold side or the resin distribution layer side, so the data shown are for bonding on the mold side.

Figure 98 (c) provides data for several adhesives tested at two overlap lengths. As discussed in the FEA section which follows, the longer overlap length results in the mid-length section of the adhesive carrying low stresses relative to the notch areas, so the calculated average shear stress over the entire length is lower than for shorter lengths at the same load. If failure initiates near the notch at a similar local stress condition, then the longer overlap length will result in lower apparent shear strength from Eq. 17. The strength ratio for 25.4 mm length to 12.7 mm length ranges from 0.48 to 0.65. As noted earlier, the longer overlap length is desirable for observing crack initiation and growth modes in fatigue.

The mode of failure under tensile loading (Figure 28) is crack initiation in the adhesive at the notch root, growth through the adhesive to the opposite interface, and then growth along the laminate interface either inside the adhesive or just inside the adherend surface. Under compressive loading the peel stress components reverse sign to compression, and the failure initiation site shifts to the interface. The crack appears to grow suddenly under compression, crossing the adhesive at approximately 45^{o} (consistent with the FEA predicted maximum tensile direction resulting from the mainly shear strain field), to the opposite laminate interface part way along the length. Figure 99 compares failed specimens under tension and compression loading, and Figure 98 (d) compares apparent shear strength values. The compressive strength is much

higher for the relatively brittle adhesive ADH-1, which appears to fail due to the local (tensile) peel stress component. The shear stresses are equal but in opposite direction under tensile and compressive loading for the same applied absolute force level, as discussed in Section 7.2.3.

The effect of adhesive thickness on apparent shear strength was determined for adhesive ADH-1, with the same 5 mm thick adherend laminates and a 25.4 mm overlap length. Figure 98(e) compares the joint strength under tensile load for three different adhesive layer thicknesses, nominally 3.25, 6.50 and 9.75 mm, and Figure 100 shows failed specimens of each. Failure initiates at about the same location on the notch radius for each case, and then propagates along the opposite interface, just inside the laminate surface, as noted earlier. A significant decrease in joint strength with increasing adhesive thickness is evident in Figure 98(e). This is consistent with the trend in Ref. 31 for thinner adhesive layers, and is somewhat steeper than reported for a broad range of adhesive thicknesses in Reference [81]. The thickness trend in Figure 98(e) is compared with an FEA based prediction in Section 7.2.3.

The performance of adhesives is generally recognized to be sensitive to time (creep) and temperature [37]. Data for three displacement rates for ADH-1 are given in Figure 98(f). These data show only a slight decrease in strength with increasing rate over the rate range of standard static tests and fatigue tests. A similar finding is reported for simulated blade joints in Section 7.3.1.

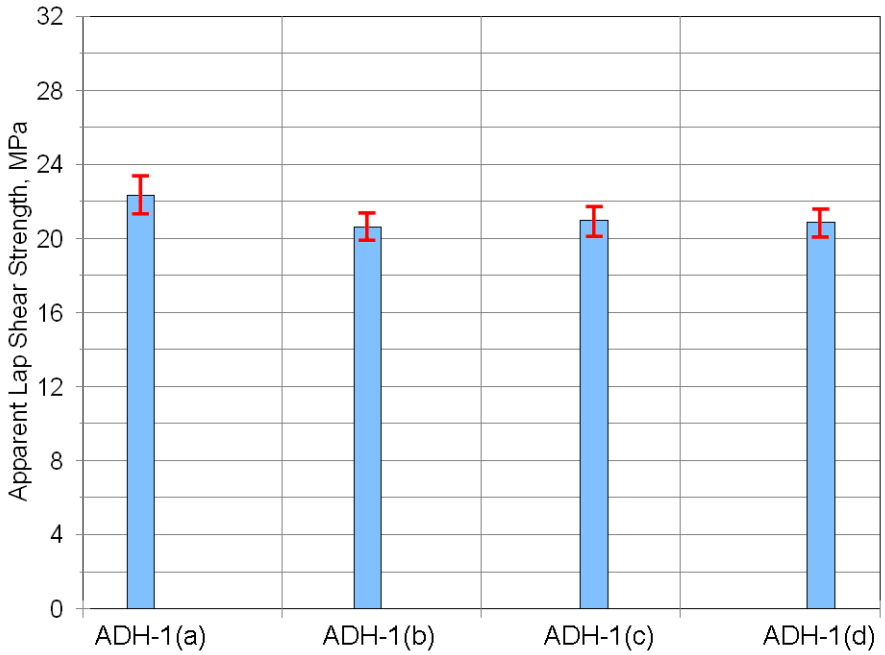

Figure 98(a). Repeatability of static strength results for three batches of adhesive ADH-1, overlap length 12.7 mm.

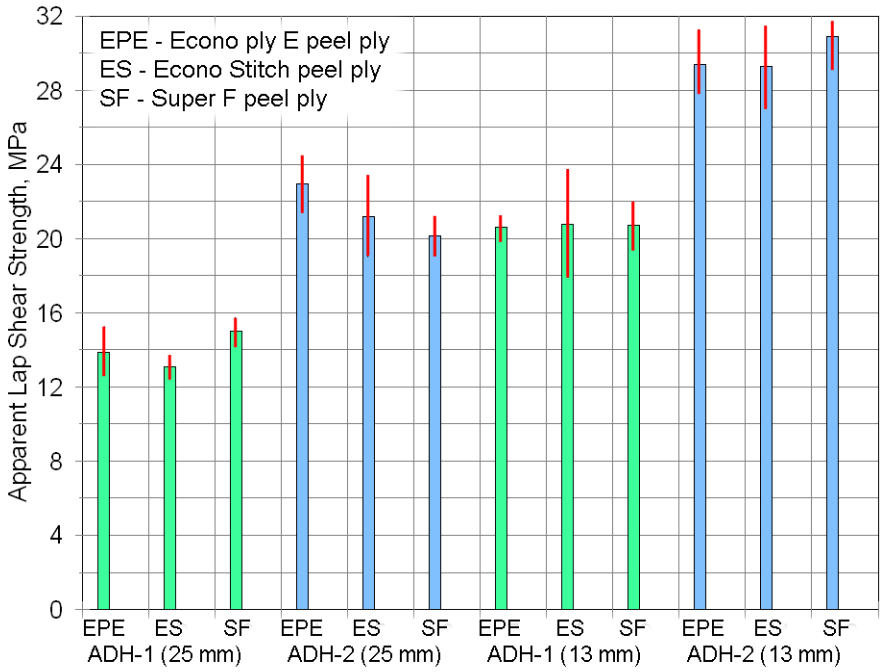

Figure 98(b). Effect of laminate peel ply for adhesives ADH-1 and ADH-2, 12.7 and 25 mm overlap length. ES- Econostitch, EPE- Econo ply E, SF - Super F.

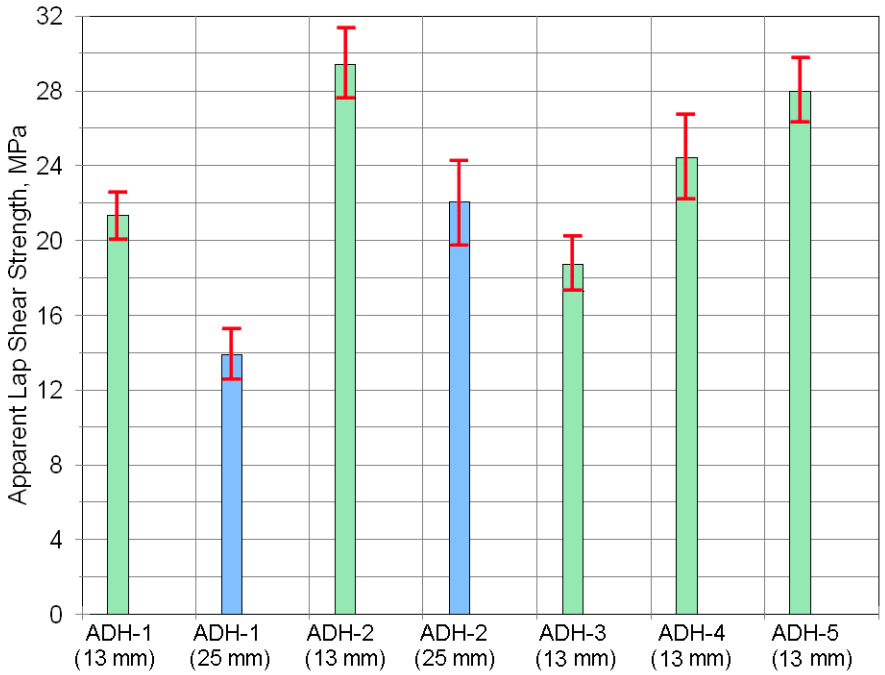

Figure 98(c). Comparison of various adhesives (Tables 3 and 4), 12.7 and 25.4 mm overlap length.

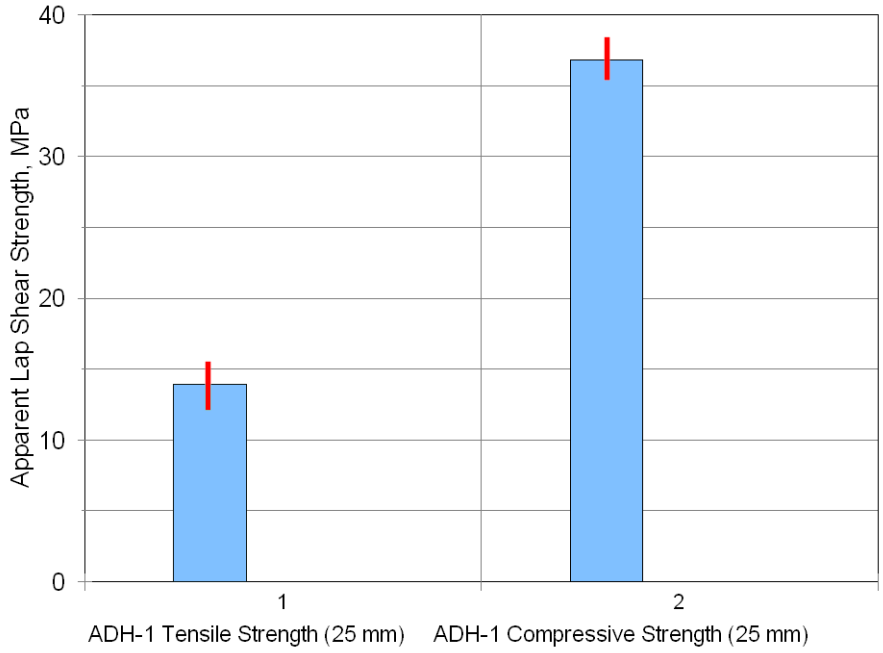

Figure 98(d). Comparison of tensile and compressive loading, ADH-1, 25.4 mm overlap length.

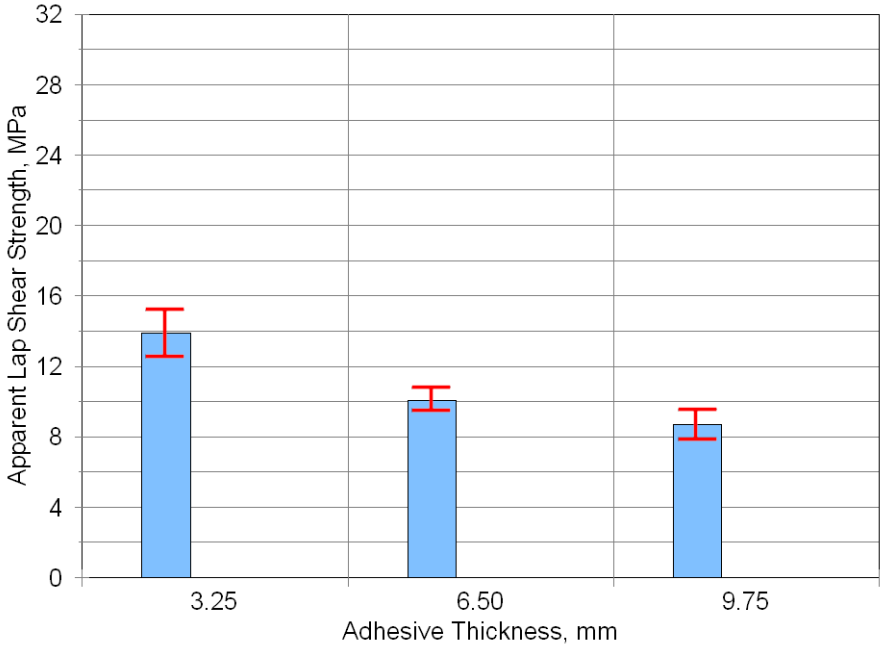

Figure 98(e). Effect of adhesive thickness for ADH-1, 25.4 mm overlap length.

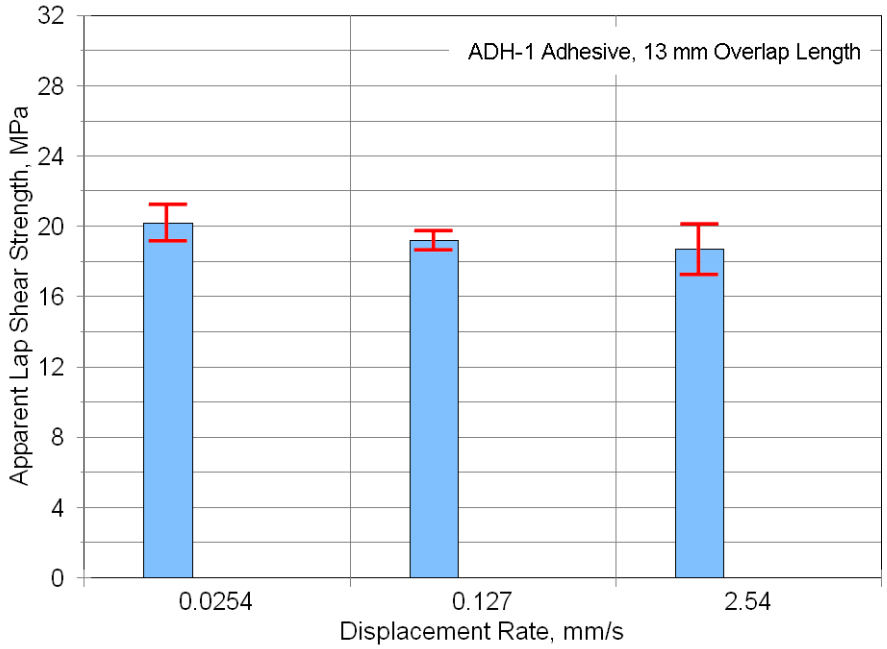

Figure 98(f). Effect of displacement rate, ADH-1, 12.7 mm overlap length.

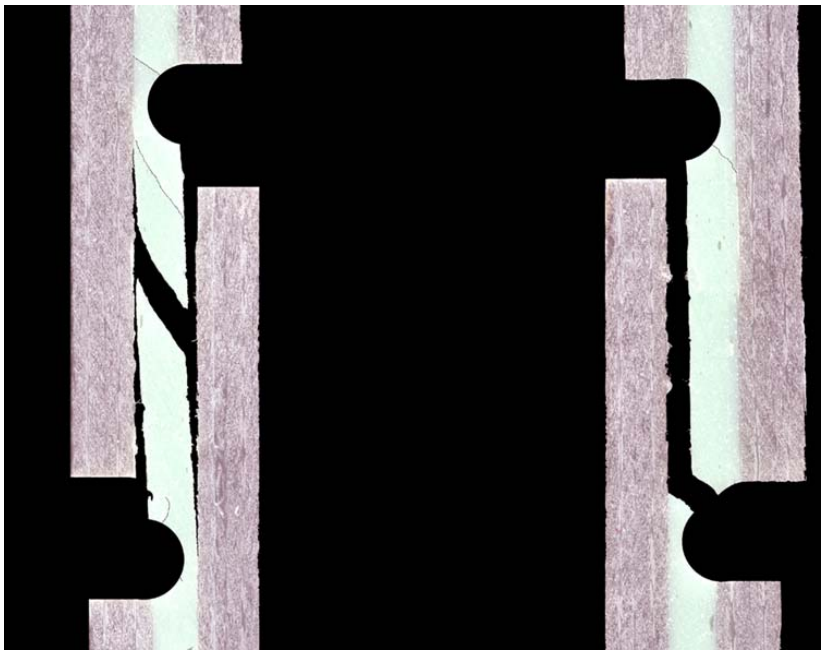

Figure 99. Failed specimens under tension (right) and compression loading, ADH-1, 25.4 mm overlap length.

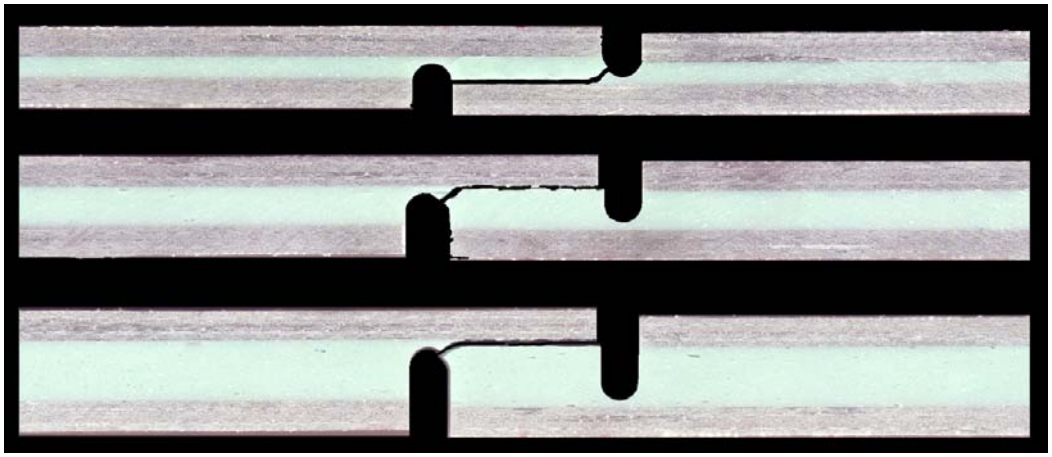

Figure 100. Failed coupons with 3.25, 6.50 and 9.75 mm thick adhesive layers, ADH-1, 25.4 mm overlap length.

7.2.2 Lap Shear Fatigue Results

The lap shear test specimen was designed with adequate stiffness to be used over a range of R-values including tension, reversed loading and compression. The static results indicate a significantly different behavior in compression, where peeling stresses become compressive, than under tensile loading. Reversed loading and compression data for adhesives have been very scarce in the literature, but are likely to be important for wind blades. In the linear range, at low loads, reversed loading produces reversed shear direction, but similar distribution, in the tensile and compressive parts of the cycle. Tensile (peel) stresses are high during the tensile load part, but mostly compression except for secondary areas, under the compressive part of the cycle. Further discussion of stress fields is presented in Section 7.2.3.

Figure 101 provides a comparison of tensile, reversed and compressive (R = 0.1, -1 and10) fatigue life data for the ADH-1 adhesive with the EP-1 resin unidirectional laminate adherends and 25.4 mm overlap length. The three loading conditions result in strongly differing fatigue response, with reversed loading the most fatigue sensitive. Compressive loading response is very fatigue resistant for this geometry and adhesive. The fatigue failure modes are similar to those under static loading, with reversed loading cracks initiating at the notch root (in the adhesive), similar in appearance to tension (Figure 28).

The mean curve fits following Eq. 10 are fit to the fatigue data only. The fatigue sensitivity in terms of approximate lifetime range at about 50% of the static strength are similar to a 4 mm thick general aviation paste adhesive under room temperature dry conditions, Figure 4-19 in Ref. 37. Little effect of test frequency in the 2 to 10 Hz range was reported in that study; the frequency for the tests in Figure 101 varied from 1-6 Hz. The fatigue trends given in Figure 101 are steeper (higher absolute value of the exponent B in Eq. 10) compared to the simulated blade web joints in Section 7.3, as discussed there [17].

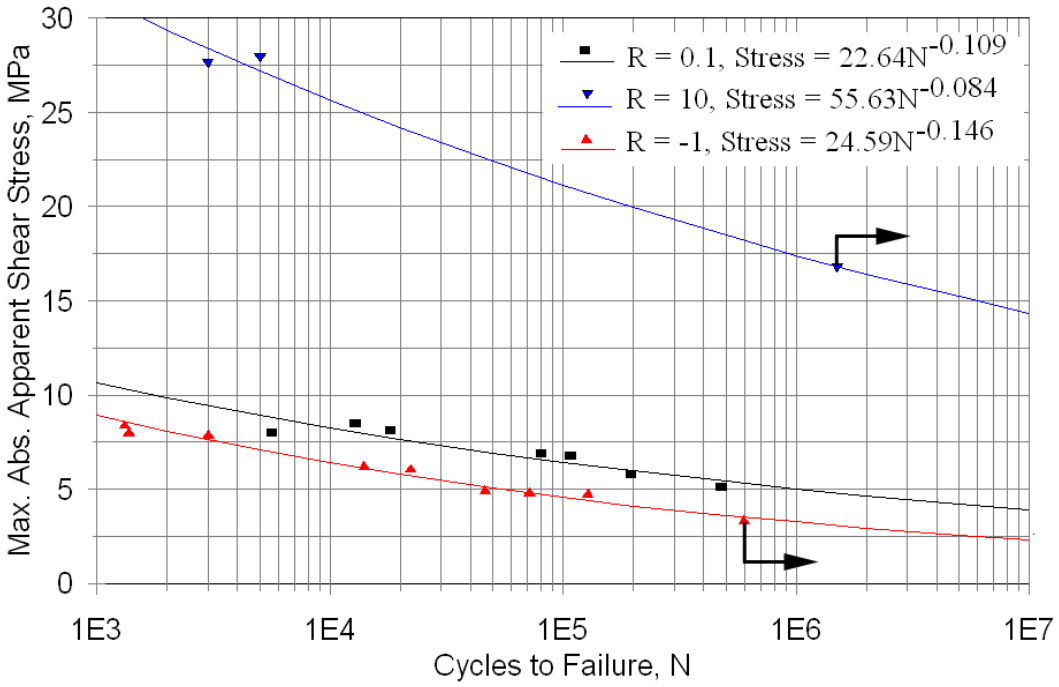

Figure 101. Lap shear fatigue data and curve fits for tensile, reversed and compressive loading (R = 0.1, -1 and 10), adhesive ADH-1, 3.25 mm adhesive thickness, 25.4 mm overlap length.

7.2.3 FEA of Lap Shear Test

A finite element study was carried out in parallel with the experimental work to assist in test development and the interpretation of results. The test geometry and elastic FEA maximum tensile strain maps were given in Figures 26 and 27. The general character of the strain distribution is similar to that in other joint geometries, with an elastic stress concentration area in the notch root, and more uniform stresses and strains away from the adhesive edge. Figure 102 gives typical mesh details near the notch root, and Table 15 gives analysis details and assumed adhesive properties.

Most structural paste adhesives show significant nonlinear response prior to failure. Tomblin, et al, have reported on the in-situ shear response of several paste adhesives [36]. Adhesive properties for this FEA study were determined from tensile tests on 3.25 mm thick bulk adhesive cast sheets. Figure 103 gives typical tensile and compressive stress-strain curves for the neat ADH-1 adhesive, and Figure 104 gives the multi-linear representation used in the nonlinear FEA runs. The actual tensile failure strains in the tensile tests varied significantly from specimen to specimen (Figure 103), with cracks initiating at pores as was also observed in the lap shear tests. The adhesive is stronger and more ductile in compression.

Figures 105 and 106 give elastic FEA maximum principal (tensile) strain maps of the two overlap length cases and three adhesive thicknesses, respectively, all for an applied tensile load of 4.45 kN. Shear strain and various stress maps have a similar appearance. The maximum tensile strain in the notch root area from the FE results is 58% higher for the 12.7 mm overlap geometry than for the 25.4 mm overlap, for the same applied force of 4.45 kN (Eq. 17). This would suggest lower apparent shear strength, τ_{app} at failure, for the longer overlap, as reported in Figure 98. The force at failure should be significantly higher for the longer overlap since the overlap length, L, is twice as long. Similarly, for the same force (and the same τ_{app} due to the same 25.4 mm length), the maximum elastic tensile strain increases as the adhesive thickness increases.

To predict joint strength trends from FEA analysis, it is assumed that failure occurs at a local value of the maximum tensile strain at the notch root (ignoring porosity). The average static apparent shear strength of the standard 3.25 mm thick, 25.4 mm overlap length, ADH-1 case was 13.6 MPa, yielding an applied force of 8.95 kN from Eq. 17. At this applied force, the maximum calculated local tensile strain at failure, ε_1, was 0.01428 for the elastic analysis, and 0.01524 for the nonlinear analysis. These calculated strains are consistent with the tensile stress-strain data (ultimate tensile strains) in Figure 103. The FEA runs were then redone for the other length and thicknesses (assuming the same local maximum tensile strain component at failure as for the standard case), to back-calculate a predicted load and apparent shear stress at failure for these cases. Table 16 indicates good agreement between predicted and experimental strengths for the 12.7 mm long and 6.50 and 9.75 mm thick adhesive joint cases. Figure 107 compares the experimental thickness data with the FEA predictions. The consistency of the neat adhesive stress-strain data, fracture surfaces (crack origin at the predicted location and normal to the maximum tensile stress), and agreement between predicted and experimental trends suggest that the local maximum tensile strain is a suitable failure criterion for this adhesive and geometry. The calculated joint stiffness variation with adhesive thickness given in Table 17 indicates that significant deflections will occur as adhesive thickness increases, for the same load. Adhesive thickness effects would be reduced somewhat if bending of the adherends were suppressed, as by very thick or high modulus laminates, but trends would be similar (Table 18).

Table 15. Lap shear adhesive joint finite element analysis details

Element description	ANSYS Plane 183, 8-node quadlilateral (large deflections, nonlinear material options)
Material Properties	Laminate: E_x = 41.7 GPa; E_y = 14.1 GPa; G_{xy} = 4.7 GPa; ν_{xy} = 0.263 Adhesive: E = 2.62 GPa, ν = 0.35 (nonlinear follows stress-strain curve)
Mesh	25 elements through adhesive thickness, more with pores
Boundary Conditions	Imposed displacement on grip area to top of notch

If the adhesive behaved in a more ductile fashion, and the local strain could achieve higher levels, the problem would become strongly nonlinear. Figure 108 gives von Mises stress maps for six increasing loads as yielding and deformation occur. As expected, the stress field becomes more uniform across the joint length. Under compressive loading the adhesive shows a

significantly higher yield resistance (Figure 103). The maximum tensile strain map (Figure 109, same absolute force as Figure 102) now shows much reduced tensile stresses as expected, with the maximum tensile stress point shifted to the interface. Application of the maximum local tensile strain criterion as used in tension now predicts the compressive load joint apparent shear strength of 50.9 MPa.

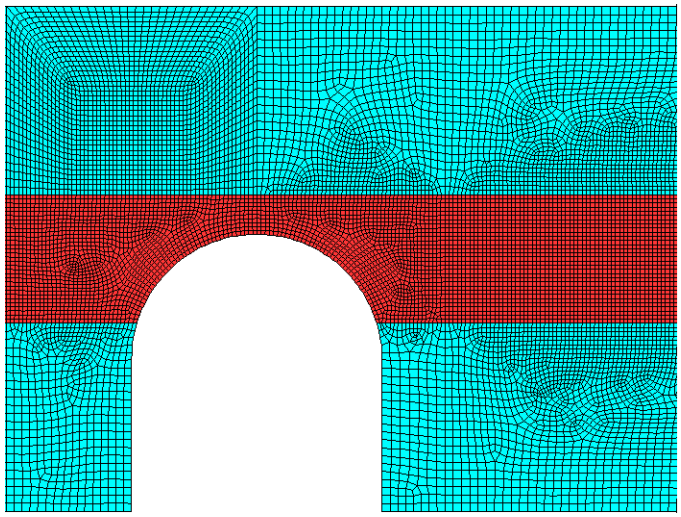

Figure 102 Typical finite element mesh near notch radius.

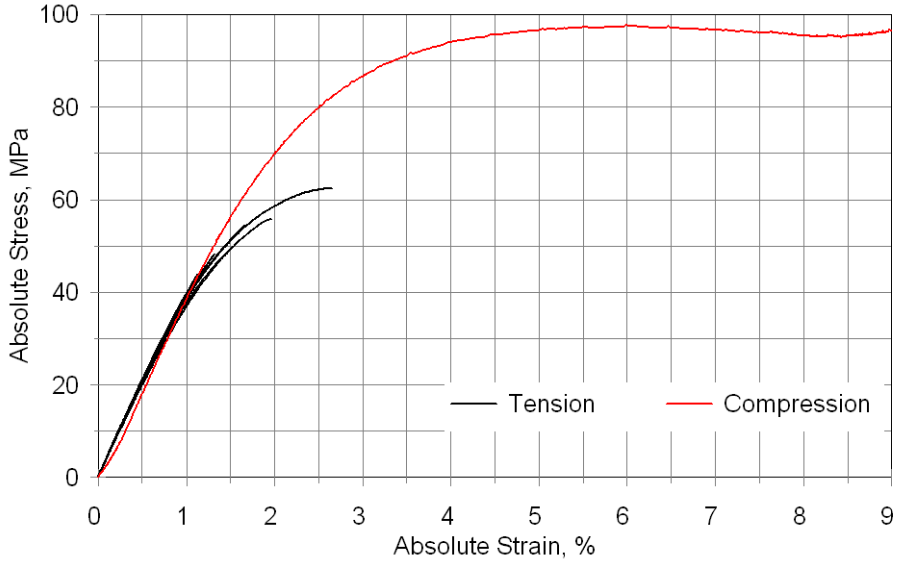

Figure 103. Tension and compression stress-strain test results for adhesive ADH-1, neat adhesive cast samples.

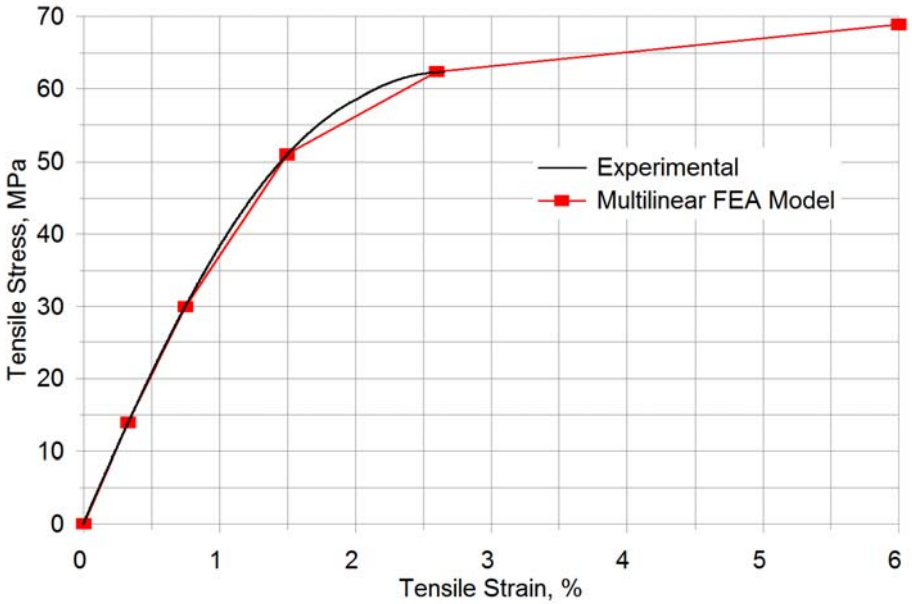

Figure 104. Nonlinear tensile stress-strain representation

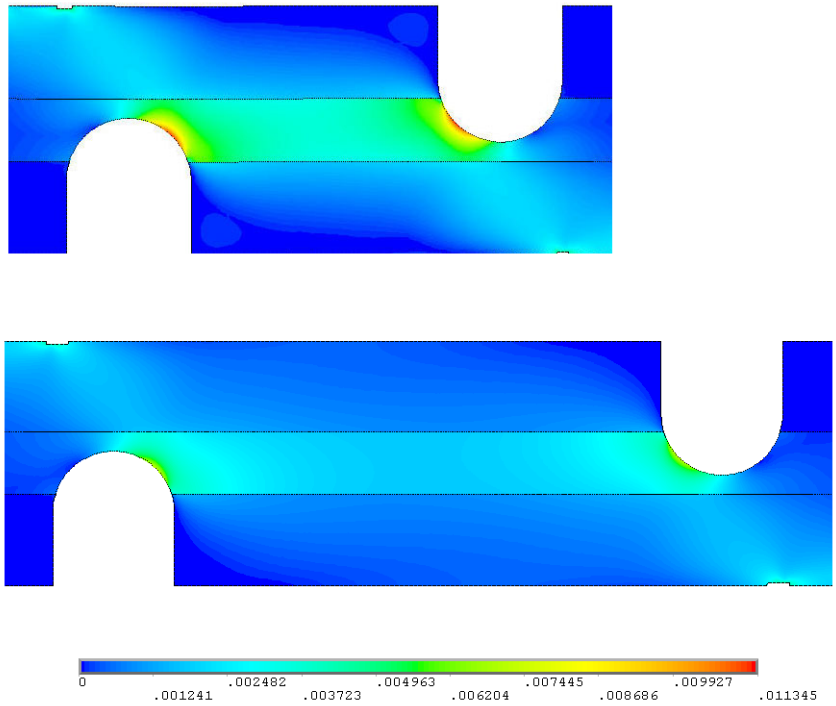

Figure 105. Maximum principal strain maps for 3.25 mm thick adhesive with overlap lengths of 12.7 mm and 25.4 mm (elastic solution at a force of 4.45 kN).

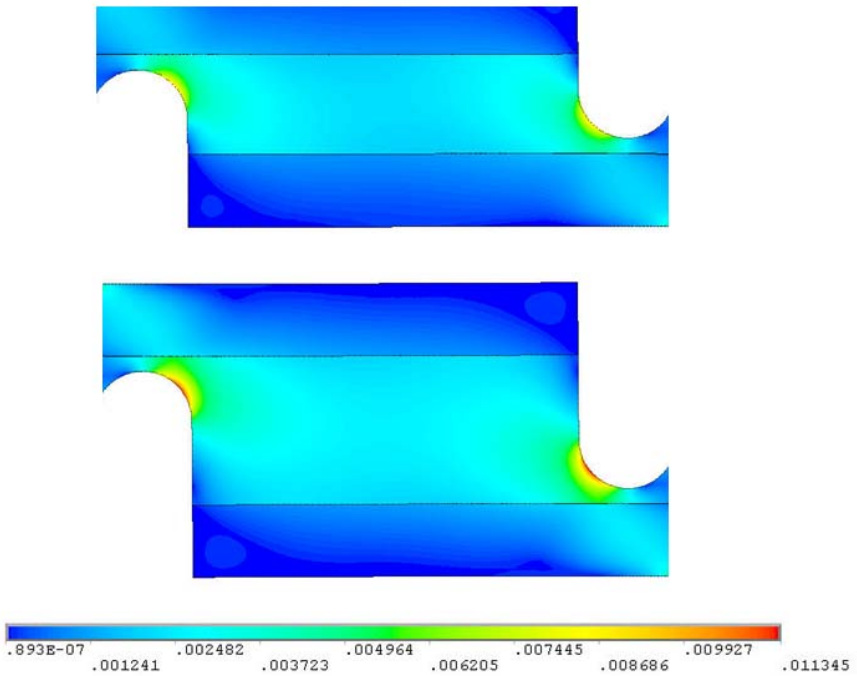

Figure 106. Maximum principal strain maps of 6.50 mm and 9.75 mm thick adhesives, overlap length 25.4 mm (elastic solution at a force of 4.45 kN).

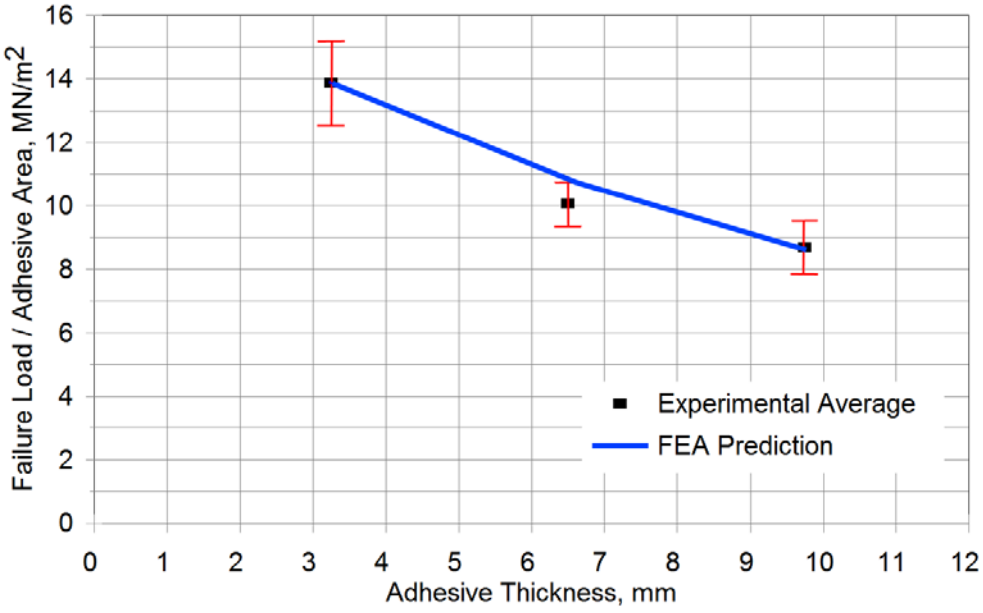

Figure 107. Experimental vs. FEA predicted apparent shear strength as a function of adhesive thickness, 25.4 mm overlap length.

Table 16. Experimental and FEA predicted apparent shear strength as a function of overlap length and adhesive thickness (FEA based on 25.4 mm long, 3.25 mm thick case).

Loading	Overlap length, mm	Thickness, mm	Apparent shear strength, MPa		
			Experimental data	Linear prediction*	Nonlinear prediction**
tension	*25.4*	*3.25*	*14.1*	*14.1*	*14.1*
tension	25.4	6.5	10.2	11.0	11.0
tension	25.4	9.75	8.81	8.76	8.79
tension	12.7	3.25	21.6	17.8	17.9
compression	25.4	3.25	37.3	50.9	- -

* failure strain = 0.01428 ** failure strain = 0.01524

Table 17. Variation of joint stiffness with adhesive thickness, 25.4 mm overlap length, effect of restraining adherend bending (elastic FEA).

Adherend boundary	Adhesive thickness, mm	Stiffness, kN/mm
free	3.25	73.4
free	6.50	49.5
free	9.75	34.4
bending suppressed	3.25	80.9
bending suppressed	9.75	50.1

7.2.4 Nonlinear Response and Pores

As noted earlier, the actual adhesives used in blades necessarily have very high viscosity to reduce slump during assembly. This characteristic results in significant porosity as explored in more detail for simulated blade joints. The effects of porosity have been addressed briefly here, including nonlinear modeling. Figure 110 gives a typical strain map (with different adhesive properties) for a joint containing a circular pore. Local maximum strains under both linear and nonlinear modeling occur at the pore border rather than at the machined radius. Figure 111 gives the maximum strain variation as a function of pore size and location. While little effect is seen for pore size, local strain increases significantly as the pore edge position approaches the machined radius. Thus, the anticipated effect of pores in the lap joints is to reduce joint strength if the pore is located near the machined radius. The failure location is expected to be at the pore edge when the pore is in the vicinity of the machined radius under tensile loading, which is frequently observed.

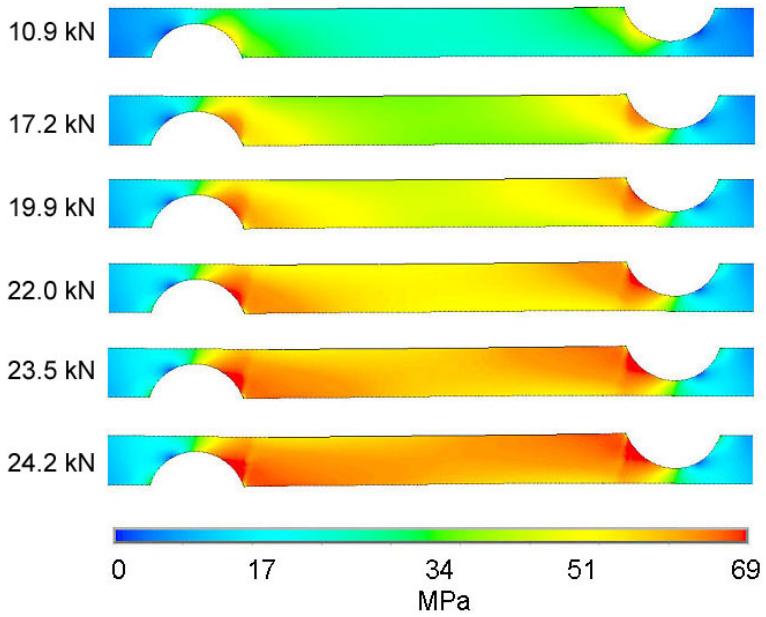

Figure 108. Nonlinear FEA results for von Mises stress maps (adhesive layer only) at increasing tensile loads, 25.4 mm overlap, 3.25 mm adhesive thickness.

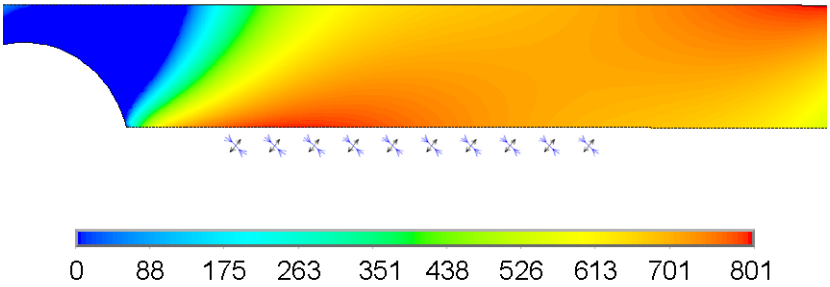

Figure 109. Maximum tensile stress map for compressive loaded specimen with strain field direction along interface, 25.4 mm overlap length, 4.45 kN force.

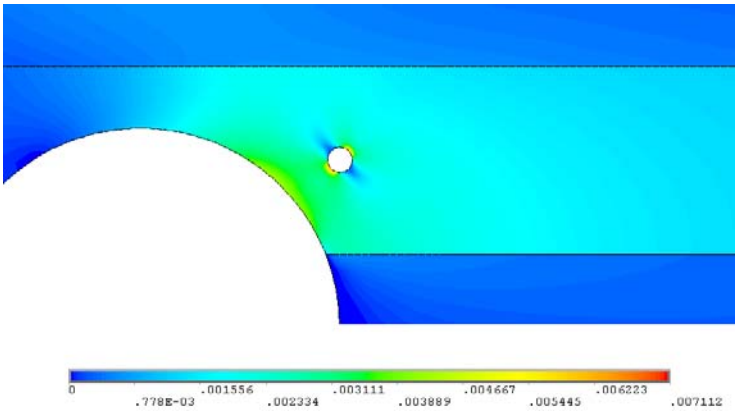

Figure 110. Maximum tensile strain map with pore, 1.5 kN.

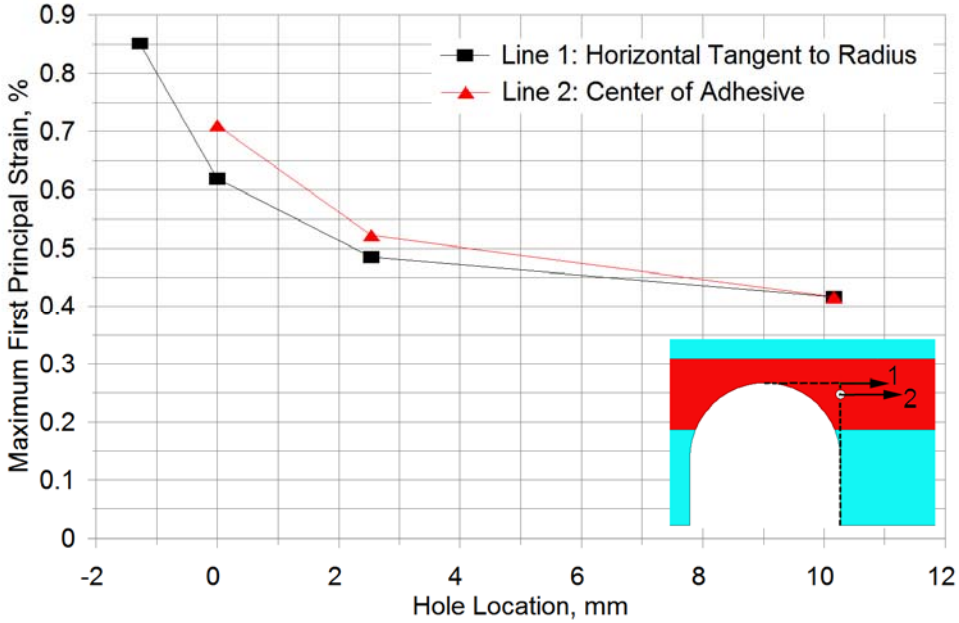

Figure 111 Maximum tensile strain vs. pore center location along lines 1 and 2 as shown, 1-mm circular pore diameter, 1.5 kN tensile load.

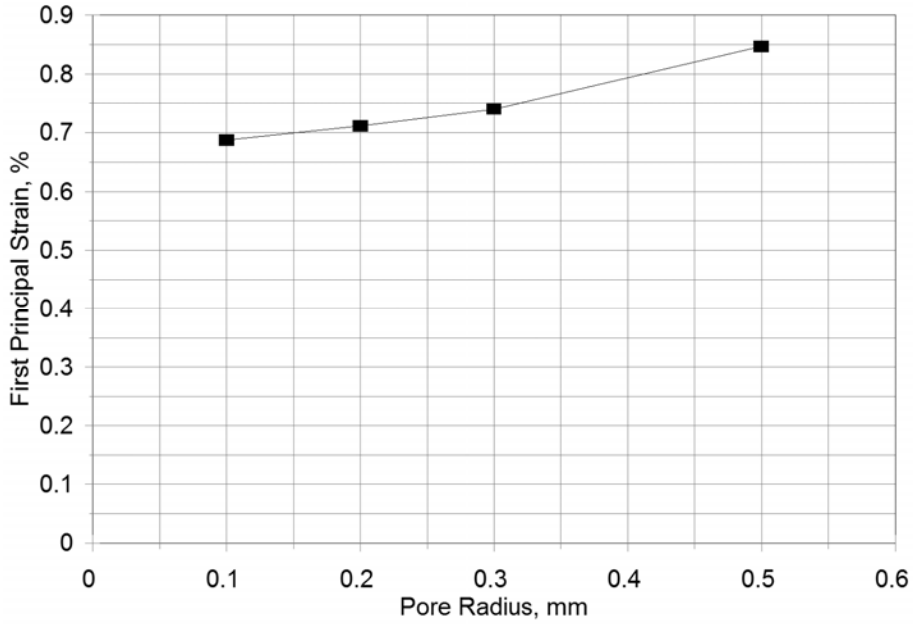

Figure 112. Effect of pore size on maximum tensile strain, 1.5 kN.

7.3 Simulated Blade Joint Geometries

7.3.1 Static Tests

Table 18 gives the static strength parameters for the four geometries described in Section 3.2.6 and Figures 11, 29 and 30. All data are normalized by the mean static strength (failure load per unit width) for Geometry A tested at the slow rate. As noted in Table 18, the number of coupons tested for each geometry was 20 at the slow (test standard) rate and 15 at the fast (fatigue) rate. The number of joint tests was twice these values, due to the doubled joint configuration (Fig. 11). The test-by-test strength variation for each of the geometries is given in Figure 113(a-d). The causes of the strength variations are addressed in detail later, but nearly all static test crack origins and initial growth areas were cohesive, within the adhesive layer. Individual test results are available in the March, 2009 update of the database [1].

Table 18. Static normalized strength data (normalized by the Geometry A, slow static average strength)

Geometry	Test Rate (mm/s)	Normalized Mean Strength	95/95 Normalized Strength	S.D.	COV (%)	No. Coupons	n
A	0.025	1.00	0.687	0.145	15	20	40
A	12.6	0.956	0.590	0.162	17	15	30
B	0.025	0.977	0.572	0.188	19	20	40
B	12.6	0.940	0.454	0.215	23	15	30
C	0.025	4.06	3.516	0.252	6	20	40
C	12.6	3.89	3.075	0.362	9	15	30
D	0.025	2.86	2.078	0.362	13	20	40
D	12.6	2.77	1.505	0.560	20	15	30

The 95/95 confidence limit is calculated following References 16 and 79 as the one-sided tolerance limit:

$$95/95 \text{ strength} = \text{mean strength} - c_{1-\alpha,\gamma}\,\text{S.D.} \qquad (18)$$

where S.D. is the standard deviation and the parameter $c_{1-\alpha,\gamma}$ is tabulated in Reference 79 as a function of the confidence level (1-α), probability, γ , and the number of joints, n.

The static data show several trends. The effects of test rate are relatively small, with slightly lower average strengths at the slow rate in each case. Paste adhesives in general are materials with significant time effects inherent to their mechanical response, particularly at temperatures approaching their glass transition temperature, but this was not evident in this test series or in the previous series.

The statistical content of the data in Table 18 and Figure 113 varies between different geometries. The reinforced geometries (C and D) are significantly higher in average strength and show reduced coefficients of variation compared to the corresponding base geometries (A and

B). Coefficients of variation are higher for the 90° specimens of both types (Geometries B and D), compared to the 45° specimens (Geometries A and C). The fast test speed results in slightly higher coefficients of variation than the slow speed for all geometries (the fast data include only 15 tests compared with 20 for the slow speed, for all geometries).

Of significance is the presence of a few particularly low strength specimens in most data sets, which reduce the 95/95 strength values (Table 18). No data have been censored from the calculations for Table 18, even though the low values may include flaws not representative of blades, such as poorly (hand) mixed adhesive and the occurrence of flaws which intersect the machined ends of the coupons; these could induce three-dimensional stresses not characteristic of the continuous webs in typical blades. The causes of low strength values are discussed in detail later.

Considering the datasets for the unreinforced specimens, the average strength values are very close for Geometries A and B (2.3% lower for B), but the 95/95 strength is 17% lower for B, which contains two results less than 60% and one additional less than 70% of the average. These very low test results are out of the 70 static tests run on the two unreinforced geometries; the total joints tested for these two geometries, due to the doubled configuration with two joints per specimen (Figure 11), was 140. The two lowest strength values were both associated with poorly cured adhesive areas as discussed later. If the lowest strength result for the slow rate, Geometry B, is not included, the average strength becomes equal to that for Geometry A, and the 95/95 strength increases to 0.665. For the reinforced geometries, C and D, Geometry C shows but a single value below 80% of the average for the two test rates combined, while Geometry D shows four values below 70% of the average for D, for the two test rates combined.

The scatter in the data for these test series may reflect variations in the test specimen geometry, mixing of the two part adhesive, porosity, unbonded areas or other factors as discussed later. Other data for paste adhesives using standard types of lap shear geometries show coefficients of variation ranging up to 20% [35-37], and the lap shear static strength results in Figure 98 ranged in COV from 3% to 14%.

7.3.2 Fatigue Tests

Fatigue results for the four geometries are presented in Figures 114-116. All fatigue data are plotted as normalized force/width vs. log cycles to failure (complete separation); the normalized force/width is the value of force/width for the particular test divided by the average static failure force/width for Geometry A at the slow rate. Thus, as with Figure 113, all fatigue data are plotted relative to the Geometry A (45°, unreinforced) data. The slow static data are plotted at one cycle for comparison. The mean lifetime for the fatigue data is then fit to the power law in Eq. (10), expressed here as:

$$F/F_o = A\, N^B \qquad (19)$$

and

$$B = -1/n \qquad (20)$$

where F_o is the slow static average strength for Geometry A, F is the maximum normalized force/width for the individual test, N is the cycles to failure, A is the one-cycle intercept of the curve fit, and B is the fit exponent, which is often expressed as -1 times its inverse, 1/n, to be consistent with fatigue crack growth literature [83].

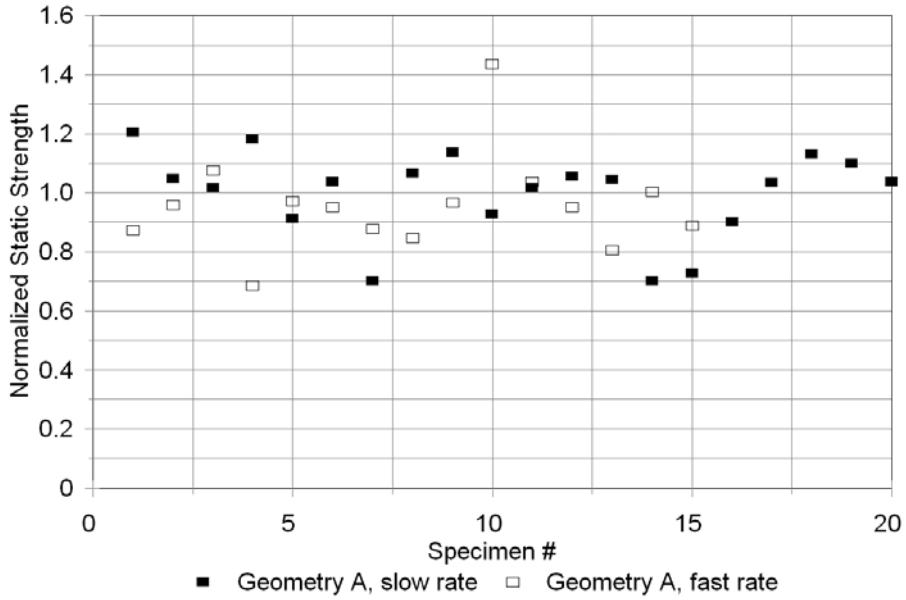

Figure 113. Strength distribution for Geometries A-D, fast and slow test rates, strength normalized by Geometry A slow rate average strength. Figure 113(a). Static strength, Geometry A.

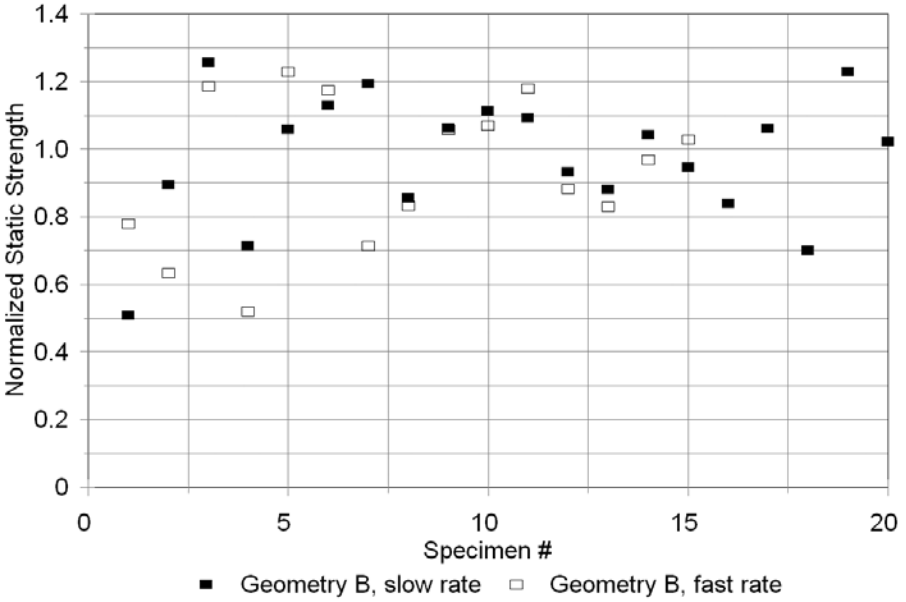

Figure 113(b). Static strength, Geometry B

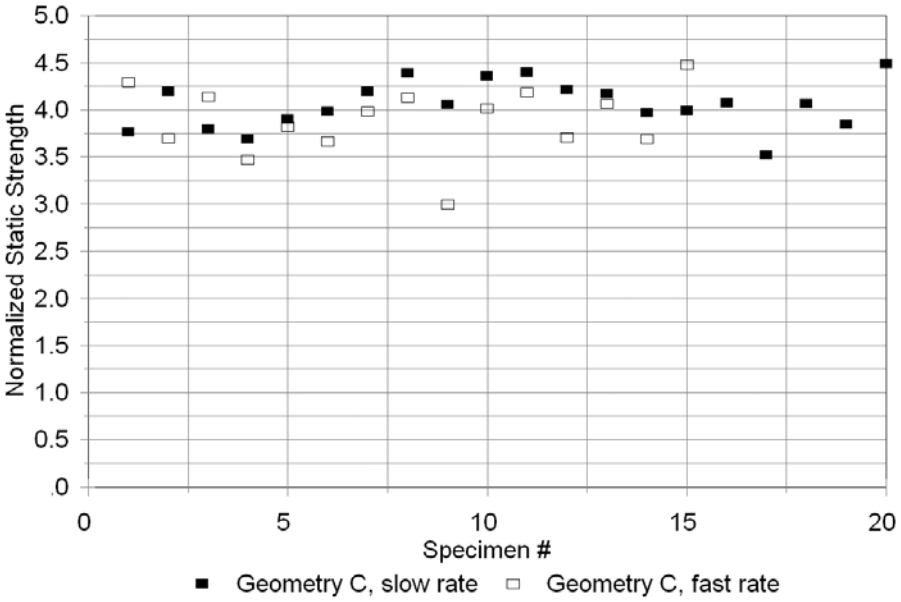

Figure 113(c). Static strength, Geometry C.

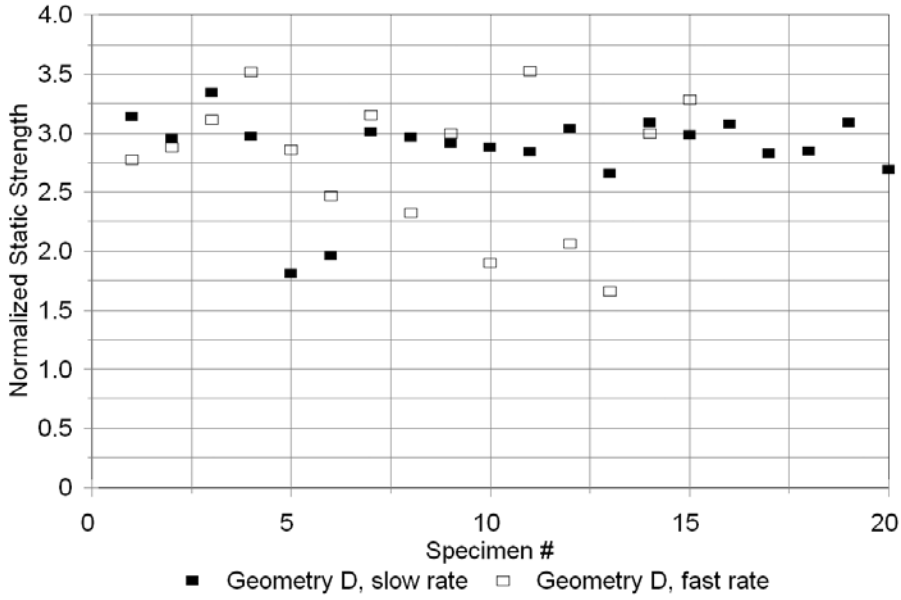

Figure 113(d). Static strength, Geometry D.

The results in Figure 114 indicate little difference in tensile fatigue resistance between the unreinforced Geometries A and B, similar to the static strength results in Table 18. Curve fit parameters given on the figures show similar fatigue exponents for the two cases. Like the static data, the fatigue results show significant scatter. The fatigue exponents, B in Eq. 19, are generally lower than those for typical fiberglass laminates, indicating reduced fatigue sensitivity (Table 9). S-N curve fits were not reported for other known fatigue data for thick paste adhesives [37] but the fatigue lives for a brittle adhesive system were a similar per cent of the average strength in the 10^5 cycle range to those in Figure 115.

Figure 115 gives tensile and reversed loading results for Geometry C. Like the static data, these results show significantly increased loads and reduced scatter relative to the unreinforced geometries. Fatigue exponents are higher than for Geometries A and B, indicating steeper S-N curves, but still in the range reported for most laminates (Table 9). Results for Geometry D in Figure 116 show reduced exponents but increased scatter relative to Geometry C, consistent with the static data, with one very short lifetime specimen consistent with the low static strength specimens.

The data for reversed loading, R = -1, for Geometry C reflect a change in failure mode from cohesive in the adhesive for all other geometry and load cases, to interlaminar in the adherend; the fatigue exponent, B, increases to -0.011. Under reversed loading Geometry D failed in a manner consistent with the static and tensile fatigue tests. Specimens of Geometries A and B, with thinner web material, could not be tested in reversed loading due to web buckling in compression. The shift to an adherend failure mode for Geometry C is not surprising, since ±45 laminates like the web used in this study are much less fatigue resistant under reversed loading, apparently due to the full reversal of the internal lamina shear stress direction in the individual 45^o plies as described in Section 4. Figures 58 and 59 illustrate this effect for typical ±45 glass/epoxy laminates loaded in-plane, comparing R = 0.1, and -1 fatigue datasets as a function of maximum strain. The exponents, B, for R = 0.1 and -1 are both about -0.124 (similar to Geometry C at R = -1), but strain levels are much lower for R = -1.

Table 19 compares the static strength, fatigue exponent and normalized strength at 10^6 cycles for the four geometries under tensile fatigue. Although the S-N curves are steeper for the reinforced geometries (C and D), these geometries are significantly stronger than the unreinforced geometries over the tested lifetime range.

Table 19. Comparison of static strengths and curve fit parameters for R = 0.1 (Eq. 19 and 20), for different geometries.

	Average normalized* static strength	Fatigue curve exponent, B	Fatigue curve exponent, n	Normalized* strength at 10^6 cycles
Geometry A	1.00	-0.0378	26.4	0.385
Geometry B	0.977	-0.0494	20.2	0.383
Geometry C	4.06	-0.0827	12.1	1.73
Geometry D	2.86	-0.0768	13.0	1.27

*Static strengths for the slow test rate, normalized by the average strength for Geometry A; fatigue parameters calculated from the fit equations given on Figs. 115-117.

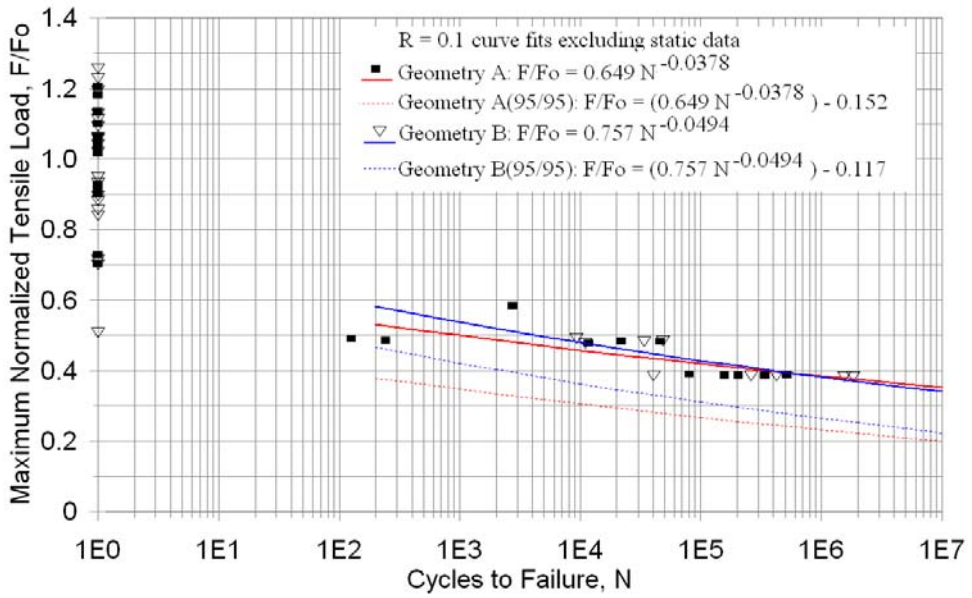

Figure 114. Tensile fatigue data and curve fits for Geometries A and B, R = 0.1, load normalized by the average static failure load for Geometry A, slow rate.

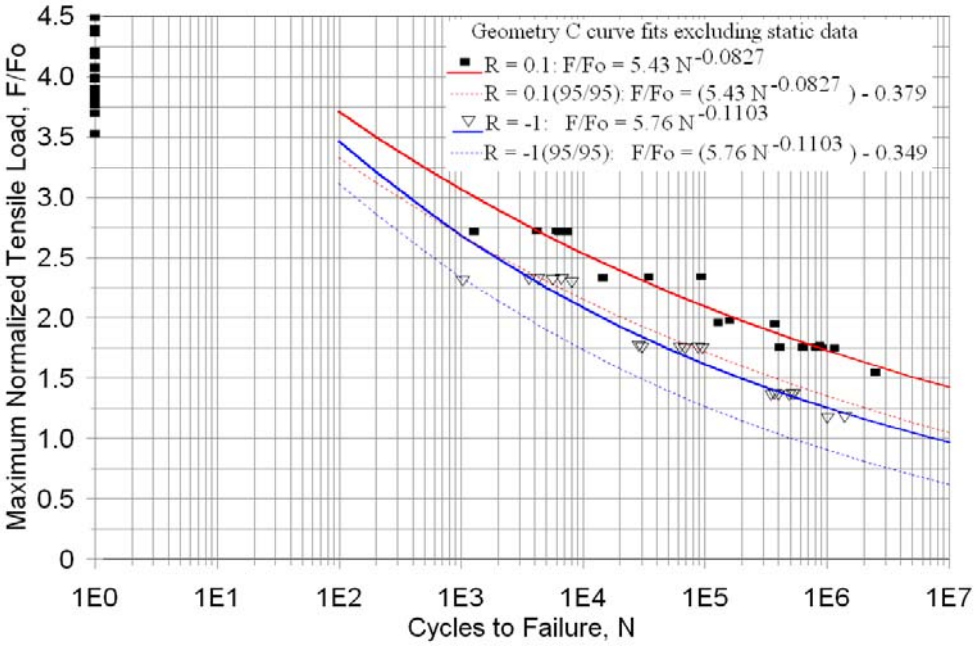

Figure 115. Tensile (R = 0.1) and reversed (R = -1) load fatigue data for Geometry C, load normalized by the average failure load for Geometry A, slow rate.

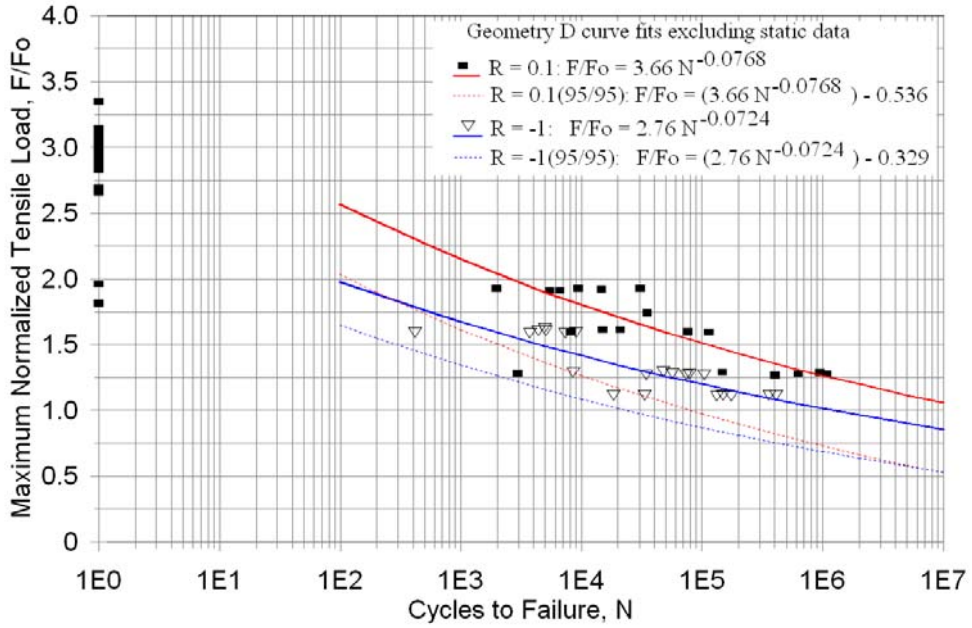

Figure 116. Tensile (R = 0.1) and reversed (R = -1) load fatigue data for Geometry D, Load normalized by the average static load at failure for Geometry A.

7.3.3. Failure Modes

Failure modes are characterized generally by the position of the crack origin (where it could be determined from fracture surface markings), the position of the crack (cohesive in the adhesive, interfacial between adhesive and adherend, or interlaminar in the adherend) [31, 37] and the position of subsequent propagation of the crack. Stable fatigue cracking could be observed visually, with magnification, during the late stages of many fatigue tests for Geometries C and D. Fracture surfaces also could be interpreted in many cases as to crack initiation sites and the progression of the crack [83]. Also described in this section are flaws observed on the fracture surface and on cross-sections of specimens.

Flaws fell into five categories in addition to minor geometric imperfections:

1. pores in the adhesive
2. pores in the adherend near the adhesive interface
3. unbonded or partially bonded areas between the adhesive and adherend
4. partially cured adhesive areas
5. pores in the laminate surface

Virtually all specimens contained visible pores in the adhesive, as reported for other paste adhesives in Section 7.2, but most were not involved in the failure process. Unbonded and partially bonded areas were evident as shinny regions on the adherend fracture surface. Partially cured areas also had a distinct appearance on the fracture surface and were often sticky to the touch (adhesive mixing was by hand in small batches, unlike typical blade manufacture, so the partially cured areas may not be representative of blades). Unbonded and partially cured areas were not observed for all geometries; different geometries were fabricated at different times.

Fracture surfaces were studied at low magnification for selected specimens of all four geometries, for specimens having low, average, and high strength and fatigue lifetime. Typical cases of pores at the fracture origin and partially cured areas were found for the weaker specimens for Geometries A and B, shown in Figure 117. Fatigue failure modes were generally similar to static failure modes. Failure for all of the Geometry A specimens started cohesively in the adhesive near Point A, the sharp corner in Figure 29, where there is a significant stress concentration due to the geometry, discussed in the next section. In most cases the crack followed the path shown in Figure 30, propagating across the adhesive, then into the adherend, where it propagated in an interlaminar mode to produce joint separation, similar to literature reports [31] and to the notched lap shear tests. A few of the partially cured specimens failed entirely in a cohesive mode in the adhesive (Figure 117). Lower strength values for Geometry A specimens were associated with either poorly cured areas or pores very close to the stress concentration at Point A; typical cases are shown in Figure 118. Since Geometry A specimens usually failed at the sharp corner (Point A, Fig 29), the detailed shape of the corner is also a likely source of variability; the crack origin was often slightly above Point A when the corner was not sharp, as for the strong specimen in Figure 117. This was not analyzed in detail.

Most Geometry B specimens failed in the vicinity of Point B in Figure 29, with the crack again propagating across the adhesive in a cohesive mode, then into the adherend (Figure 30). Crack

origins were mostly at pores in this general area. A few poorly cured cases were also found, notably including the lowest strength specimen in both the slow and fast rate datasets. The second weakest specimen in the slow dataset failed at a large pore in the surface of the laminate, adjacent to the adhesive.

Fracture origins for Geometry C and D specimens under static loading were most commonly observed at stress concentration points, mainly adjacent to the wedge block, at pores, or at unbonded areas between the adhesive and adherend; poorly cured adhesive areas were not observed in these geometries. Cracks initially propagated either in a cohesive mode in the adhesive or in an adhesive/cohesive mode near the interface, but usually slightly into the adhesive. As for Geometries A and B, most of the cracks shifted to an interlaminar mode in the adherend for much of their growth. The single low static strength specimen for Geometry C failed from a large unbonded area. Many other specimens with unbonded areas showed near-average strength. The lowest strength specimens for Geometry D were associated with poorly bonded areas adjacent to the wedge block, and appeared interfacial in growth mode.

Fatigue failures for Geometry C were similar to static failure modes at R = 0.1, with large fatigue cracks observed in the final stages of lifetime. Evidence of fatigue cracks on the fracture surfaces could be identified from the texture, but with difficulty. The failure mode changed to interlaminar in the adherend under reversed loading, R = -1, with large interlaminar fatigue cracks in the adherend observed prior to failure. Fatigue failures for Geometry D generally followed similar modes to the static tests for both R-values. The individual outlier points for each R-value were associated with large, apparently poorly bonded areas on the wedge block surface.

Figure 117. Fracture surfaces of Geometry A specimens, Point A, Figure 29 is at the bottom of the adhesive in each case, with crack propagation toward the top. Left, stronger than average specimen, no major flaws; center, weaker specimen, two large pores along edge of adhesive; right, weakest specimen, poorly cured adhesive (cohesive mode over entire surface).

7.3.4. Finite Element Results

Finite element modeling was carried out on Geometries A and B only, to help in understanding some of the experimental trends. As noted earlier, the two geometries were similar in average static strength, but Geometry B showed greater scatter. This result is partly explained by the poorly cured areas of B for the lowest strength specimens, but there also appeared to be added association with porosity. FEA modeling was carried out in plane stress, two dimensions in

ANSYS with plane 183, 8-node quadratic elements, with linear elastic assumptions (which is a simplification considering the nonlinearity discussed earlier). Elastic constants for the adhesive were assumed as E = 2.618 GPa, G = 0.971 GPa, ν = 0.35, and for the adherends, $E_1 = E_2 = 11.7$ GPa, $G_{12} = 3.1$ GPa, and $\nu_{12} = 0.187$. All results are presented for an applied load equal to the average failure load , Geometry A, at the low rate. Figure 29 gives the overall geometry including the sharp corner at Point A which is associated with a high stress concentration. A typical maximum strain map is given in Figure 118, for the maximum tensile strain in the joint. The stress concentration at Point A (Fig. 29) is seen to be extremely localized compared with the lap shear geometries such as Figure 105.

First, the adhesive strain distribution in the absence of flaws is considered. The tensile and shear strains are given in Figures 119 and 120, respectively, for four variations in geometry studied, which included Geometries A (45^o) and B (90^o), as well as for additional wedge block angles of 30^o and 60^o. Strains are plotted from Point A, along the line indicated in Figure 29. The assumed sharp corner at Point A results in a mesh dependent maximum strain value as Point A is approached. The closest point plotted on the figures is one element away from Point A. Considering the maximum tensile strain, the results in Figure 119 indicate strains in the vicinity of Point A on the order of twice as high for Geometry A as for Geometry B, suggesting that Geometry B would be significantly stronger. This is contradicted by the observed average experimental static strengths in Table 18, and fatigue strengths in Figure 115, which are similar for Geometries A and B; the reasons for this difference are addressed by considering the effects of pores and failure location.

The most common crack initiation location for Geometry A was Point A in Figure 29, as expected from the local stress concentration. The most common crack initiation location for Geometry B was in a region around Point B in Figure 29, where the strains are lower than at Point A in the absence of an additional stress concentrator. FEA solutions were carried out with several pore sizes, shapes and locations, as depicted in Figure 121, with a typical mesh shown in Figure 122. The variation in maximum tensile strain with distance from Point A, along axis in Figure 29, is given for several pore locations in Figure 123. As the pore approaches Point A, the maximum strain at Point A is seen to increase above the value with no pore present, so that the strength would be expected to drop, but only for pores which are close to Point A. The strain at the edge of the pore remains below the value at Point A until the pore actually intersects the edge of the adhesive. Thus, the effect of pores on the strains in Geometry A is to raise the strain at the geometric strain concentration when the pore is close to the corner. Otherwise, pores have no significant effect on the failure process.

Figures 124 and 125 explore the behavior of Geometry B, which showed about the same average strength as for Geometry A, but with more scatter. As noted above, the strains at the adhesive corner, Point A, are lower than for Geometry A. Failures were usually observed along the area of Point B in Figure 29, at pores. Figure 124 indicates that the maximum strains for Geometry B shift to the edge of pores in this vicinity. Results in Figure 125 indicate high strains for elliptical pores close to the edge of the adhesive (plotted along a line parallel to the axis in Figure 29, but starting at Point B). The local strains with pores now appear to be similar to those for Geometry A in Figure 123. The increased scatter for this geometry is apparently the result of a shift to a more flaw dominated strength, where the presence and variability in severity of pores

in the relatively large area around Point B is greater than the variability in geometry and pore incidence near Point A for Geometry A. An accurate prediction of joint strength in both geometries would require more detailed study including nonlinear effects. Prediction of fatigue life would require treatment of the crack initiation process; stable fatigue crack propagation was not observed for these two geometries in the experiments, but would likely be a significant factor for larger structures and more complex joint geometries, like Geometries C and D.

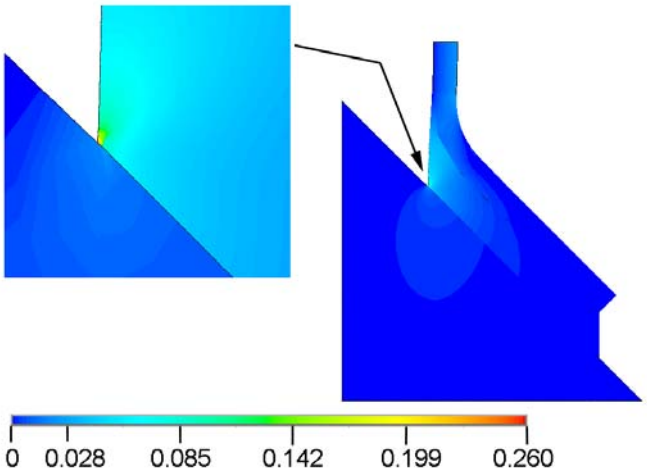

Figure 118. Maximum tensile strain distribution for Geometry A; expanded view shows stress concentration at Point A (Figure 29).

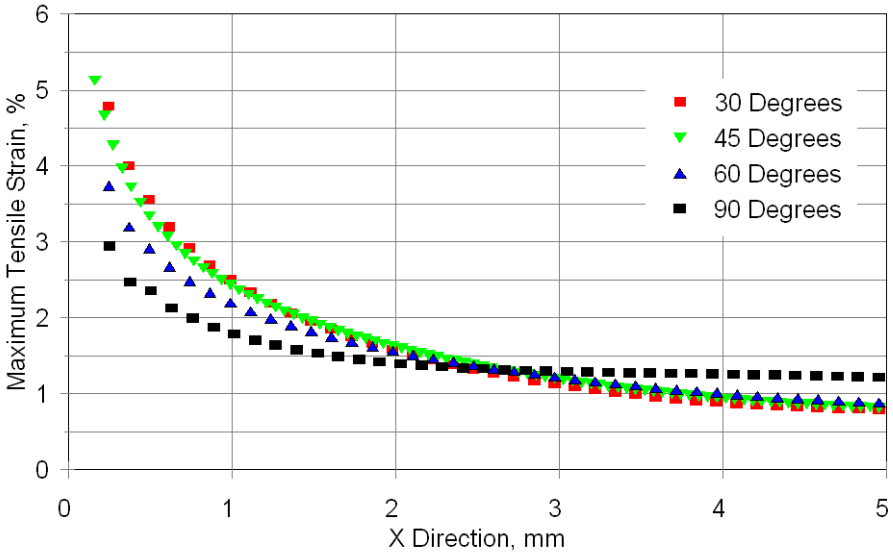

Figure 119. Maximum tensile strain distribution across the adhesive along the x-coordinate at Point A in Figure 29 for four wedge block angles. Geometries A and B are 45^{o} and 90^{o}, respectively.

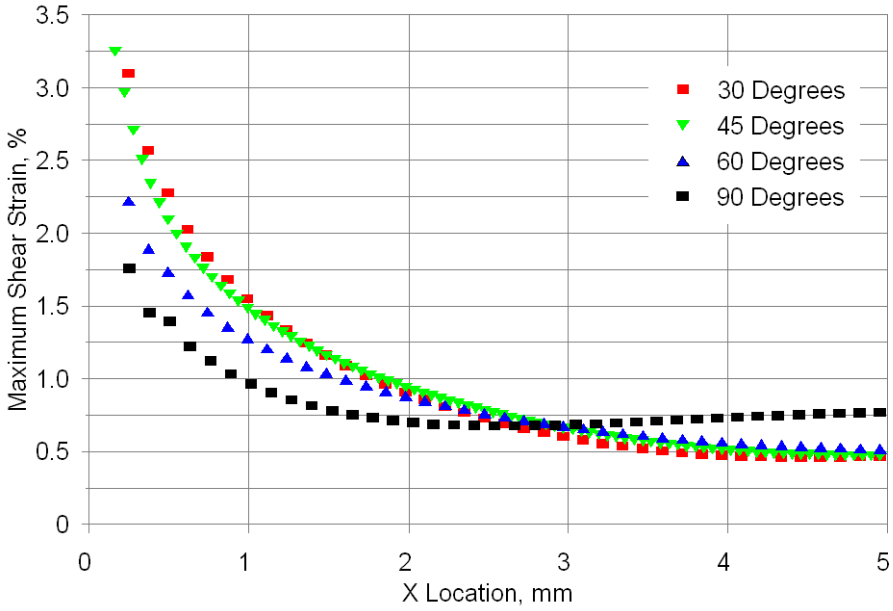

Figure 120. Maximum shear strain distribution corresponding to Figure 119.

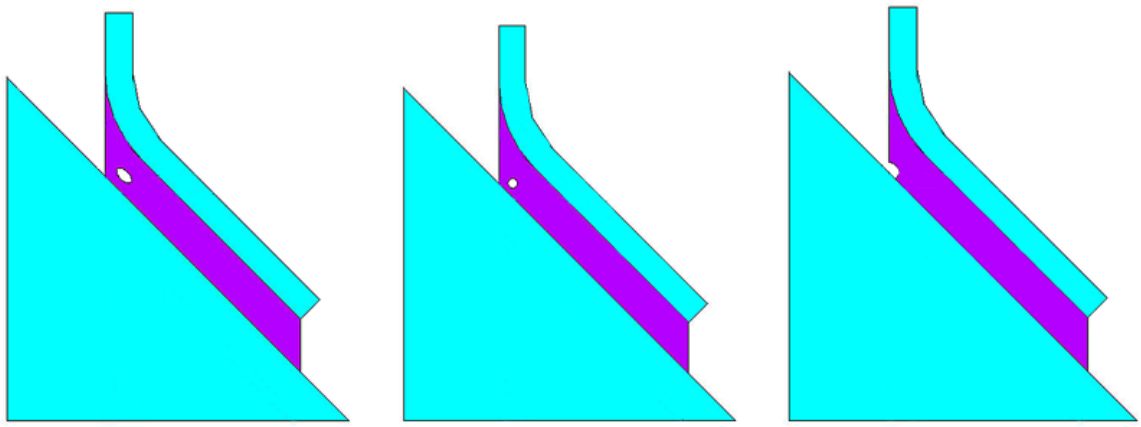

Figure 121. Typical pore geometries, ellipse, circle, intersecting circle.

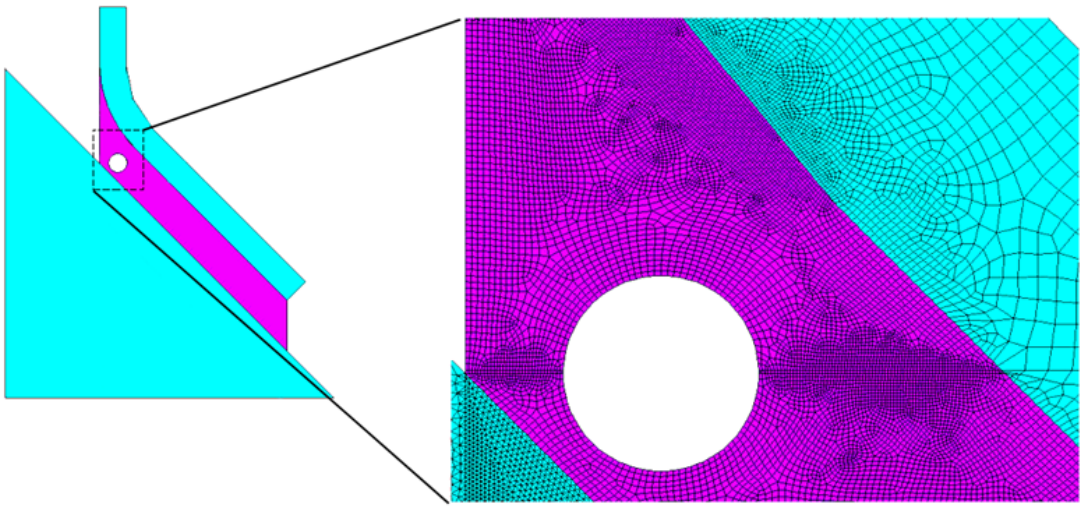

Figure 122. Typical mesh pattern around hole and corner.

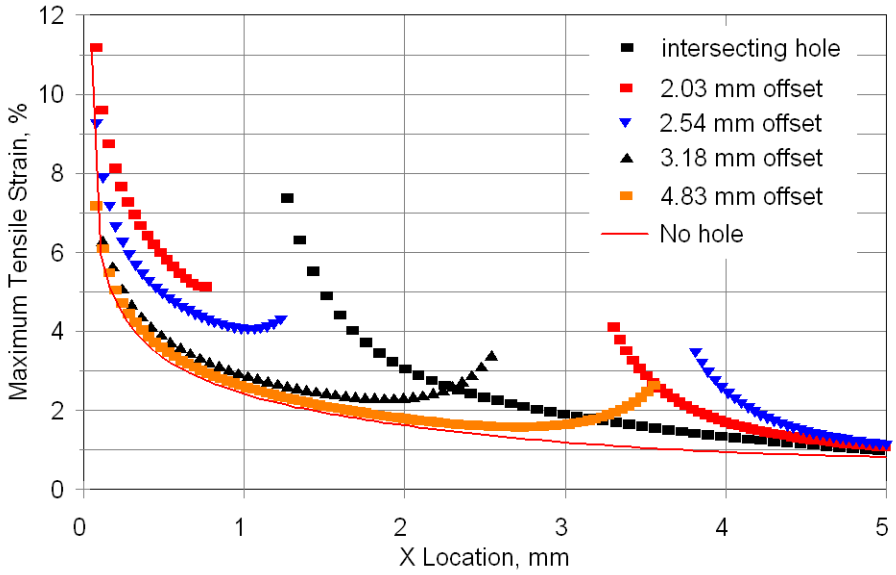

Figure 123. Maximum tensile strain across adhesive along x-coordinate (from Point A in Figure 29) for 2.5 mm diameter circular pores centered in various positions, Geometry A (offset is the distance to the pore center from x = 0; intersecting hole center is at Point A, X=0, Figure 29).

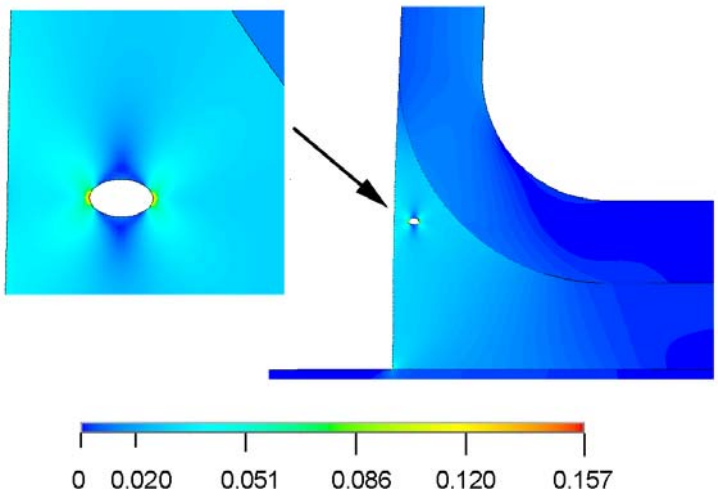

Figure 124. Tensile strain distribution at small elliptical hole in Geometry B specimen near Point B in Figure 29.

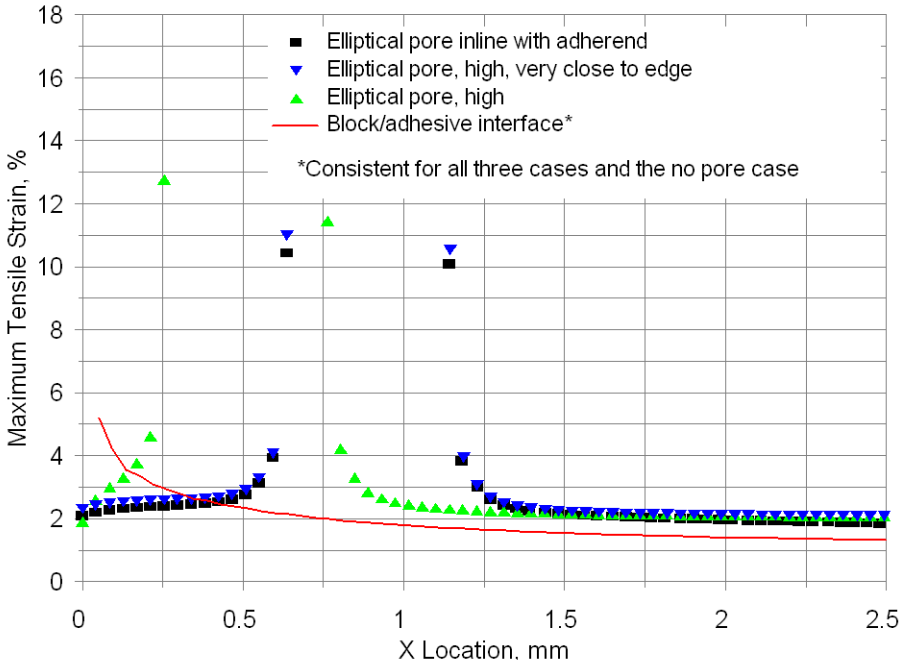

Figure 125. Maximum tensile strain for elliptical holes, Geometry B, plotted along block interface and near Point B in Figure 29.

7.4 Adhesive joint tests for small turbine tower connection

Notched lap shear tests similar to those described in Section 7.2 have been conducted with the laminate adherend on one side replaced by A36 steel in two thicknesses, 2.8 mm and 4.8 mm; steel surfaces were sand-blasted and cleaned with acetone prior to assembly. (In preliminary tests, when the steel adherends were only surface cleaned with acetone, the steel interfaces failed at low apparent shear stress.) The lap joint was assembled from continuous unidirectional 5-mm thick fabric D/polyester UP-3 laminate on one side (Figure 126) and 25.4 mm wide steel bar stock strips on the other. Gaps were left in the bar stock for the notch to be cut into the adhesive; the second notch was cut normally.

Static strength results are given in Figure 127 at one cycle. For the 4.8 mm steel thickness, the average apparent shear strength was 14.0 MPa with ADH-2 compared with 33% lower, 9.4 MPa for ADH-3. A similar 37% decrease in joint strength for ADH-3 relative to ADH-2 was shown with laminate-to-laminate joints (EP-1 resin laminates), at 12.7 mm overlap length, in Figure 98(c). For the same 25.4 mm overlap length with ADH-2, the steel-to-laminate strength was 37% lower than the all-laminate joints. FEA results similar to Figure 27 showed 35% reduced maximum strain at the laminate notch relative to the value at the notch through the steel, consistent with the experimental findings. Failure originated at the root of the notch through the steel side, propagating to and then along the laminate adherend in the manner described previously (Figure 28).

Fatigue data for the steel-to laminate joint are given in Figure 127. Compared with the tensile fatigue data fit (B = -0.109, Eq. 10) for the all-laminate joint data for ADH-1 from Figure 101, the steel-to laminate trends show somewhat reduced fatigue sensitivity.

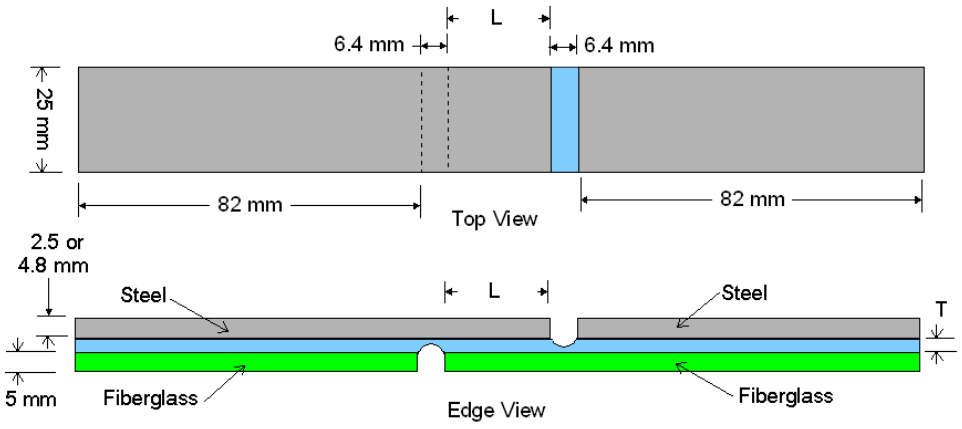

Figure 126. Notched lap shear steel-to-laminate joint schematic, L = 25.4 mm.

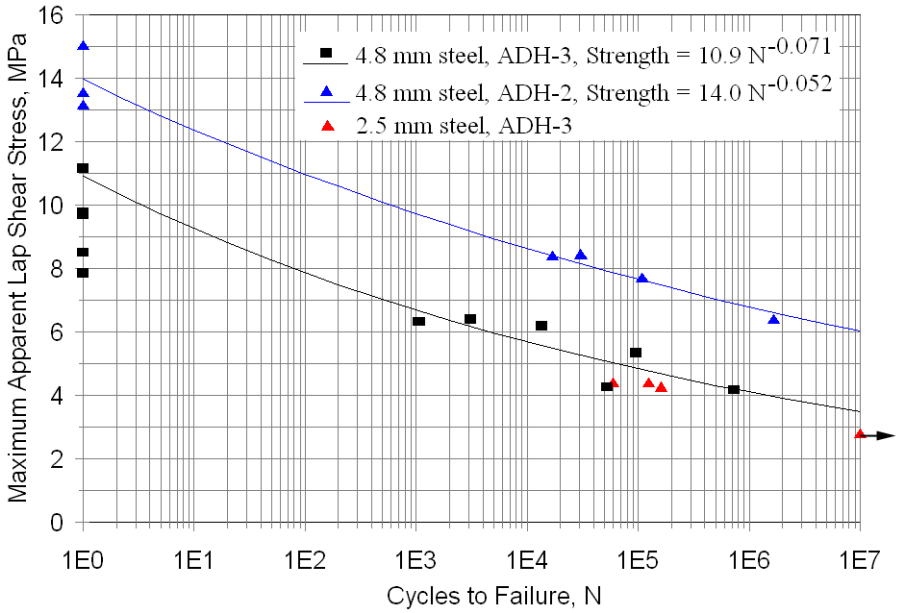

Figure 127. Comparison of ADH-2 and ADH-3 in steel-to-laminate fatigue, R = 0.1, 25.4 mm overlap length.

SECTION 8. SPAR-CAP SPLIT TESTS

The study reported in this section was intended to shed some light on the effect of different levels of off-axis material in resisting split propagation parallel to the mostly unidirectional fibers of thick laminates, as often used in spar caps. The test specimen shown in Section 3.5 is similar to a compact tension specimen used in fracture toughness testing, and has been used for that purpose with composites [84]. As will be shown, the matrix cracking/delamination zones which develop with the laminates used in this test are so extensive as to preclude the use of classical linear fracture mechanics to represent the results, so the data are presented here as load-deflection and load-crack growth curves (cohesive zone modeling [85] has not been attempted, but might be appropriate). Since the specimen planar dimensions are held constant, the maximum load gives a good measure of the split resistance. (Some success has also been reported representing these data in terms of the dissipated energy [86]). Details of the materials and processing can be found in Section 3.1.5 and 3.2.7.

Figure 128 gives photographs of several glass fiber specimens after a pin displacement (Figure 31) of 13 mm, at which point the notch has extended significantly. The extensive matrix crack/delamination zone is evident for all laminates except the unidirectional case. Figure 129 shows the 90^o ply of a $[(90)_7/\pm45/(90)_5]_S$ laminate, where the surface 90^o plies have been polished after testing. The unidirectional 90^o material forms several splits underneath the ±45's in multidirectional cases. These are typical failure modes for the glass fiber laminates. While the carbon fiber laminates cannot be seen as easily, their failure modes are similar in nature (not shown).

Three data sets have been obtained, one each for fiberglass laminates based on D155 90^o plies and A260 90^o plies, both with DB120 ±45 plies, and carbon 90^o plies with glass ±45 plies. The fiberglass laminates were processed by VARTM while the carbon hybrid laminates were processed from prepreg. Tables 5 and 20 give the details for each laminate. The specimen geometry results in relatively low fracture loads, which allows the use of thicker than usual laminates. All specimens were about 10 mm thick, so the results should be representative of spar-cap behavior.

Numerical and graphical results are presented in Table 20 and Figures 129 - 133. The load-displacement curves are generally similar for each material system (Figures 130 - 132). Tests were continued until a maximum load had been clearly defined. The unidirectional cases, $(90)_n$, show co-linear crack growth at relatively low forces. The addition of even 10% off-axis plies greatly increases the maximum load. Maximum load versus per cent off-axis plies is given in Figure 133. One notable difference between the glass and carbon 90's is that the addition of low amounts of off-axis plies, less than 10%, has a much greater effect on the glass cases (Figures 130 and 131) than for carbon (Figure 132). The unidirectional carbon starts (100% 90's) at about twice the maximum force compared with the glass cases, but the effect of off-axis (glass) plies on the carbon is much less, resulting in significantly lower maximum forces for the carbon at off-axis contents above 5%. The high modulus of the carbon results in only moderate improvements from the off-axis plies. The crack opening displacement (COD) at the maximum force is much lower for the carbon. Higher stiffness off-axis material may be required for carbon spar caps.

A major concern of this study was to determine whether the extent of dispersion of the off-axis plies in the otherwise unidirectional spar-cap would have a significant effect. Figure 133 indicates little difference between placing all of the off-axis plies on the surface, as with a unidirectional spar-cap sandwiched between skin-type off-axis lay-ups, and dispersing the off-axis plies throughout the thickness. Based on other studies, this conclusion might change if the specimens were subjected to fatigue loading; this is planned for future studies.

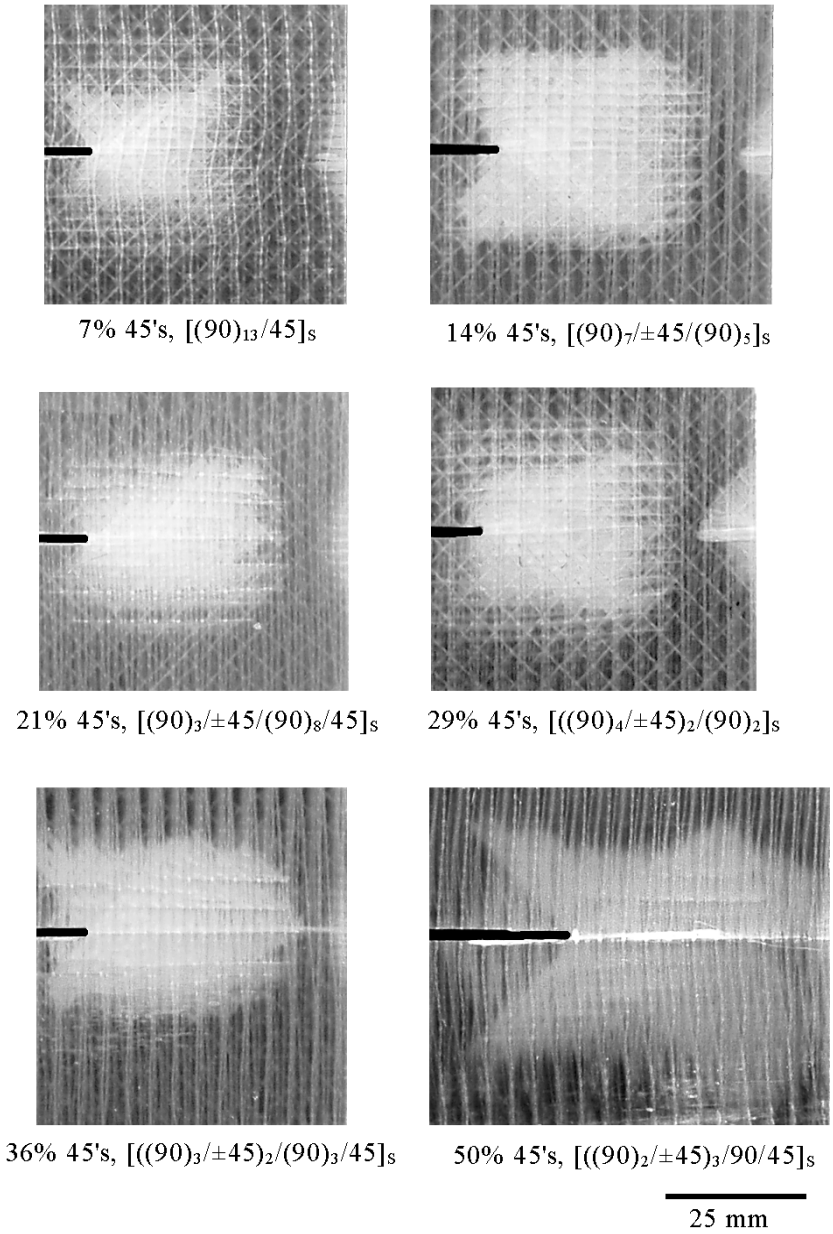

Figure 128. Reflected light photographs of damage in compact tension coupons after loading to a COD displacement of approximately 13 mm, D155 Coupons.

Table 20. Summary of Spar Cap Split Tests.

Material Lay-up	% 0^O	% 90^O	% 45^O	Thickness, mm	ao, mm	Maximum Load, kN
D155 Glass Fiber with UP-4 resin (V_F = 48 %)						
$(90)_{28}$	0	100	0	12.6	26	0.803
$(90)_{14}/0/(90)_{13}$	3.6	96.4	0	12.7	64	3.419
$((90)_2/0)_{4S}$	28.6	71.4	0	10.9	64	22.19
$(90/0)_{7S}$	50	50	0	12.6	64	15.54
$(0/90)_{7S}$	50	50	0	12.6	64	14.67
$[(90)_{13}/45]_S$	0	92.9	7.1	12.7	64	3.593
$[(90)_7/\pm45/(90)_5]_S$	0	85.7	14.3	12.7	64	6.210
$[((90)_4/\pm45)_2/(90)_2]_S$	0	71.4	28.6	12.7	64	10.462
$[((90)_2/\pm45)_3/90/45]_S$	0	50	50	12.7	64	10.836
A260 (0's), *DB120 (±45's) and DB240 (±45's) Glass Fiber with UP-4 resin (V_F = 48 %)						
$(90)_{16}$	0	100	0	11.5	64	0.891
$(\pm45^*/(90)_7)_S$	0	94.7	5.3	11.0	64	2.374
$(\pm45/(90)_7)_S$	0	88.8	11.2	11.8	64	5.240
$((\pm45)_2/(90)_6)_S$	0	78.7	21.3	11.5	64	7.646
$(\pm45/(90)_4/\pm45/(90)_2)_S$	0	78.7	21.3	11.1	64	6.250
$((\pm45/(90)_2)_3/90/(-/+45/(90)_2)_2/-/*45)$	0	66.4	33.6	11.3	64	7.798
$(\pm45)_2/(90)_5/\pm45/-/+45/(90)_6/(-/+45)_2$	0	66.4	33.6	10.9	64	8.598
$(\pm45/90)_4)/90/(90/-/+45)_4$	0	55.2	44.8	11.8	64	10.080
$(\pm45)_4/(90)_9/(-/+45)_4$	0	55.2	44.8	11.7	64	8.879
NCT307-D134600 Newport Carbon fiber prepreg 0° plies and NB307-D1-7781-497A Newport Glass prepreg ±45° plies (V_F = 53 %)						
90_{42}	0	100	0	13.2	62	1.688
$90_{20}/\pm45/90_{20}$	0	95.9	4.1	12.8	63	1.788
$[90_{13}/\pm45/90_6]_S$	0	91.7	8.3	12.3	65	2.488
$[90_9/\pm45]_3\ /90_9$	0	87.4	12.6	11.9	65	2.988
$[(90_7/\pm45)_2\ /90_3]_S$	0	83.1	16.9	11.9	63	3.692
$[(90_3/\pm45)_4\ /90)]_S$	0	65.3	34.7	10.8	65	4.849
$[(90_2/\pm45)_5\ /90]_S$	0	56.1	43.9	9.8	64	5.609
$[(90_4/(\pm45)_2)_2\ /(90)_3/\pm45]_S$	0	56.1	43.9	9.8	65	5.525
$[\pm45]_{21}$	0	0	100	11.4	65	7.335

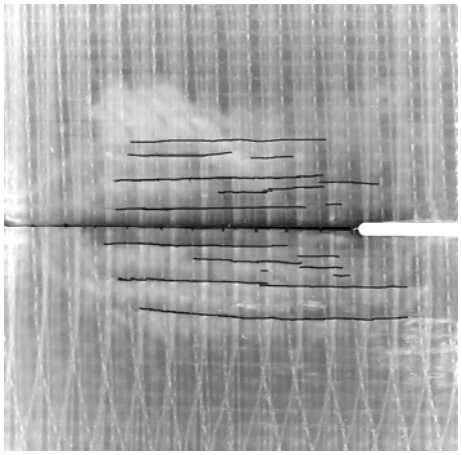

Figure 129. Photograph of 90^{O} Ply Multiple Splitting in Delamination region in a $[(90)_7/\pm45/(90)_5]_S$ Laminate.

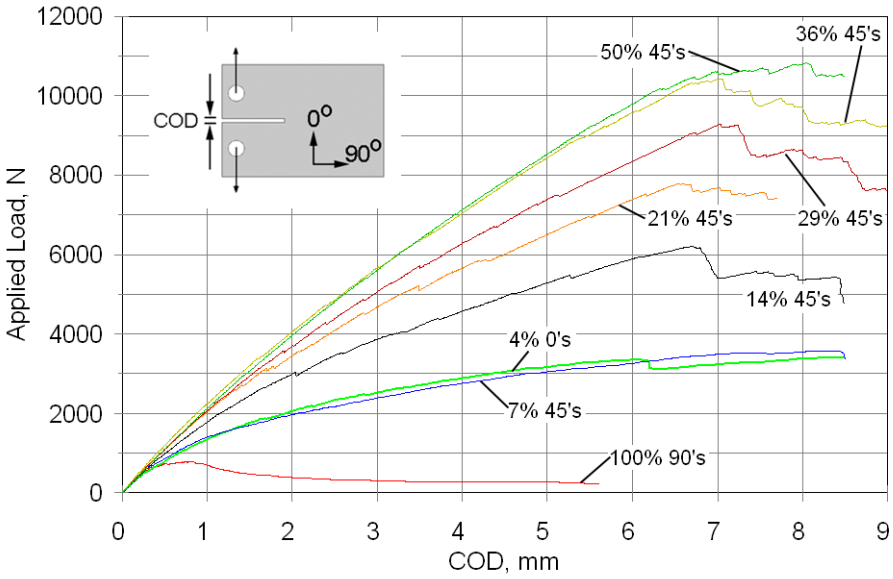

Figure 130. Applied load versus COD for D155 glass fiber coupons with various amounts of D155 0^{o} and ±45 plies with remainder being D155 90^{o} degree plies.

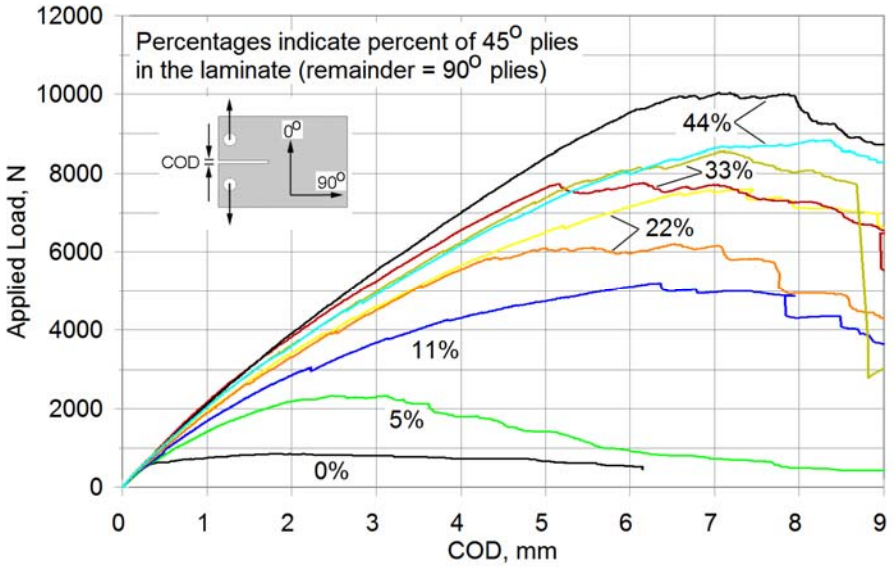

Figure 131. Applied load versus COD for A260/DB240 glass fiber coupons with various amounts of ±45^{O} plies with remainder being 90^{O} degree plies.

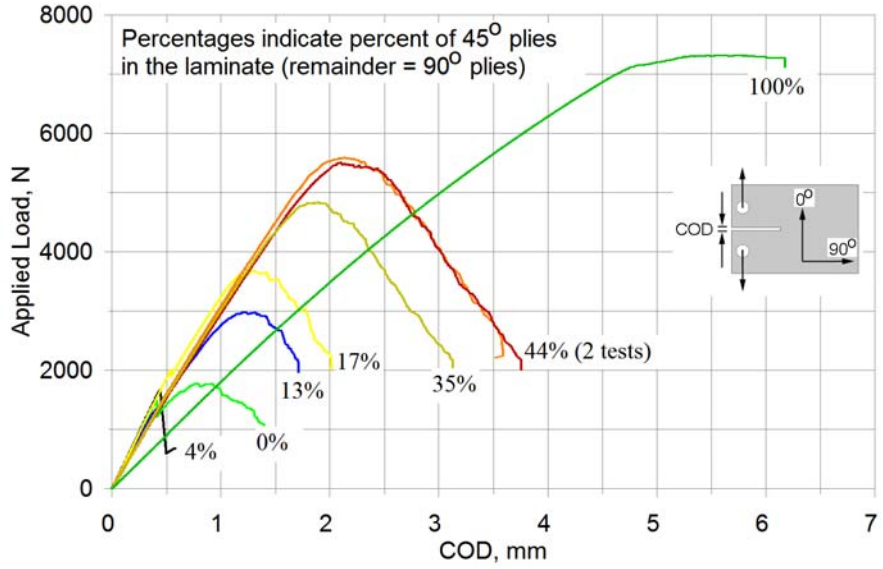

Figure 132. Applied load versus COD for coupons with various amounts of glass fiber ±45^{O} plies with remainder being 90^{O} degree carbon fiber plies.

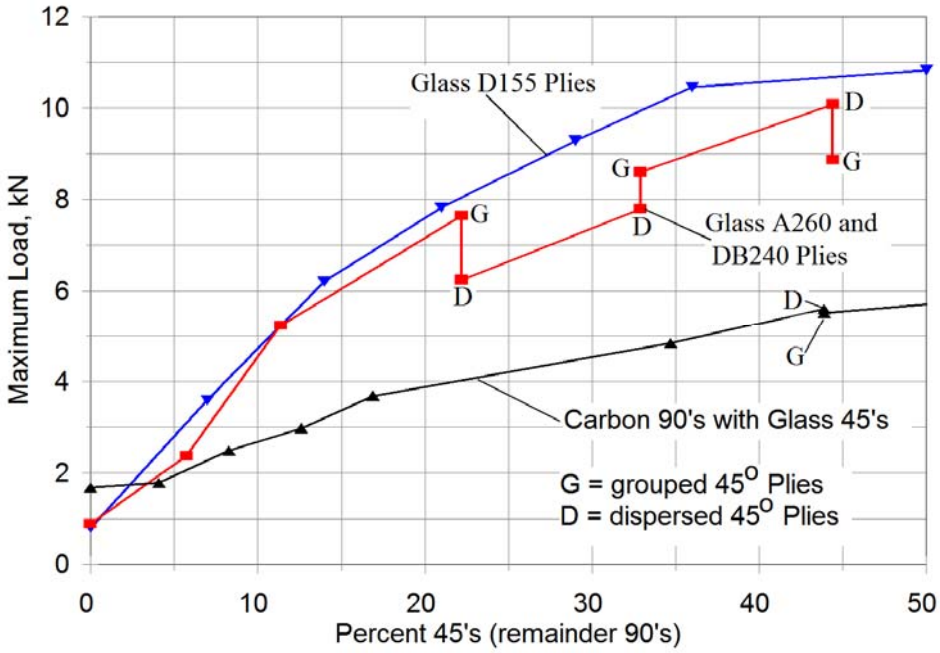

Figure 133. Summary of maximum loads versus percent ±45^{O} plies for glass and carbon compact tension coupons.

SECTION 9. LAMINATES WITH pDCPD RESIN

9.1 Resin, Laminates and Testing

Resin pDCPD is a new type of thermoset with very low viscosity and high toughness [87]. Laminates were prepared by Materia Inc. to MSU specifications as to fabrics and layup using several versions of the resin; typical results are presented in this section. Fabrics D and L (Table 2(b)) were infused (without resin distribution layers) into unidirectional (0_4) and ($\pm 45_3$) laminates with fabric D, and multidirectional (±45/0/±45/0/±45), and complex laminate (Figure 22) configurations, the latter two with uni-fabric D and biax fabric L. Test specimens were prepared at MSU from plates supplied by Materia; test methods followed those described in Section 3.

9.2 Results and Discussion

Test data for each case are compared with typical epoxy resin results. The static multidirectional modulus, strength and ultimate strain properties listed in Table 21, and stress-strain curves shown in Figures 134 and 135, generally indicate similar in-plane mechanical properties for the epoxy and pDCPD. The slightly higher fiber content for the pDCPD laminates is reflected in the stress-strain curve in Figure 134; the higher simulated shear stress-strain curve (ASTM D3518) appears to reflect greater matrix cracking resistance in the pDCPD.

The most notable difference between the epoxies and the pDCPD in Table 21 is the much higher delamination resistance, G_{Ic}, for the pDCPD. The G_{Ic} value of 1729 J/m^2 is in the range of very highly toughened epoxies like F185 [76] and high performance thermoplastics like PEEK (APC2)[66, 76]. G_{IIc} values for the un-toughened epoxies are generally high, reflecting the complex cracking mechanism involved in crack advance [66]. Tough resins like PEEK [66] and pDCPD deform in a ductile manner in both modes, and have similar high toughness values in modes I and II.

The tensile fatigue performance of the multidirectional pDCPD laminates is similar to that for the various epoxy resins using the highest performance uni-fabric D, as shown in Figure 136. The pDCPD data fall near or above those for the epoxy laminates having similarly high fiber contents. The compressive fatigue results given in Figure 137 show slightly improved compressive fatigue resistance for the pDCPD.

The higher toughness of pDCPD relative to typical epoxies like EP-1 is reflected in their relative performance in the complex structured coupon (Section 6). The data given in Figure 138 indicate a significant increase of about 30% in the static load to produce large-scale delamination for the pDCPD relative to the epoxy. The pDCPD also shows higher reversed loading fatigue cycles for the same damage length in Figure 139. The differences in Figure 139 are clearer in Figure 140, where the cycles are plotted on a linear rather than log scale. At the intermediate load level (33.4 kN), the pDCPD lifetime is about three times as long for the greater damage lengths.

Table 21. Average Static Properties for Infused Multidirectional Laminates, and G_{Ic} and G_{IIc} for Unidirectional Laminates

Resin	EP-1 epoxy (TT1A laminate)	pDCPD
Thickness, mm	4.24	4.07
V_f, %	55.6	60.1
Elastic Modulus E, GPa	29.7	30.3
Tensile Strength, MPa	910	928
Ult. Tensile Strain, %	3.2	3.1
Compressive Strength, MPa	-670	-632
Ult. Compressive Strain, %	-2.2	-2.1
G_{Ic}, J/m^{2*}	330	1729
G_{IIc}, J/m^{2*}	3446	2910

*Unidirectional fabric D laminate ($0_2/0_2$), 0/0 interface, EP-1 V_f = 60%, and pDCPD V_f = 64%.

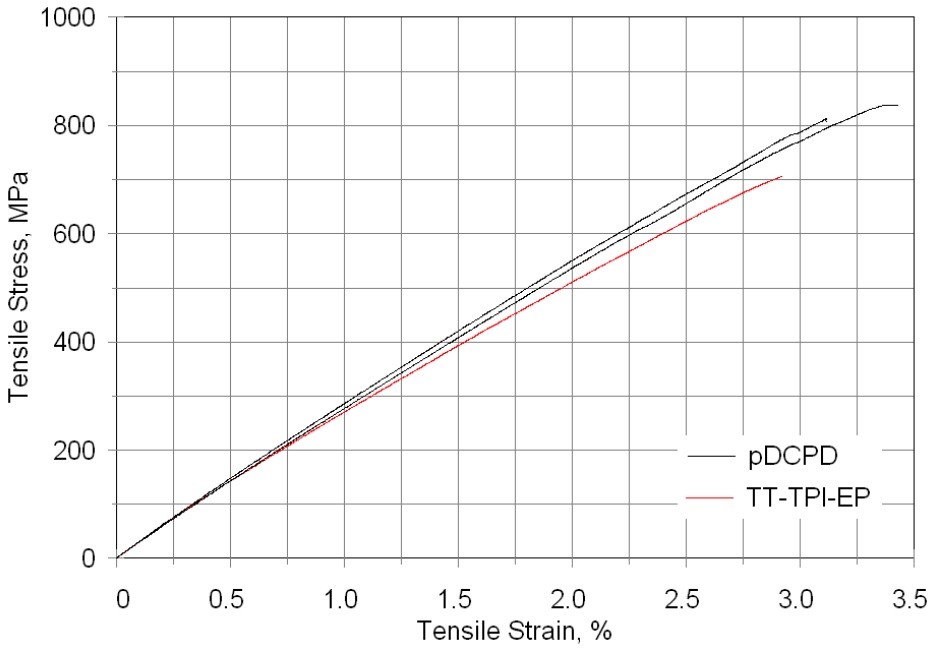

Figure 134. Typical Tensile Stress-Strain Curves for pDCPD and Epoxy Multidirectional Laminates

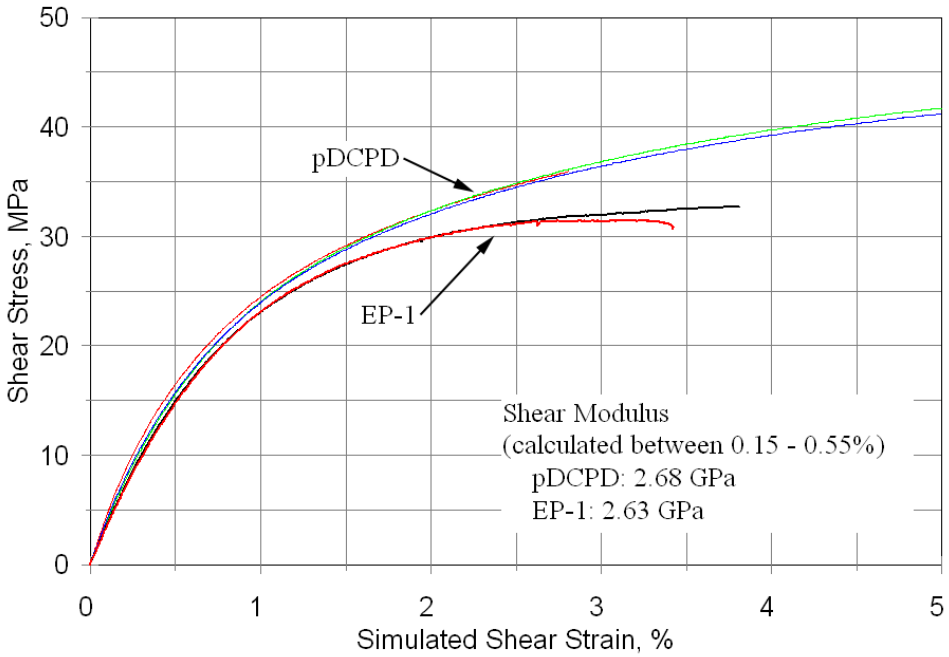

Figure 135. Simulated Shear Stress-Strain Curves, ±45 Fabric D.

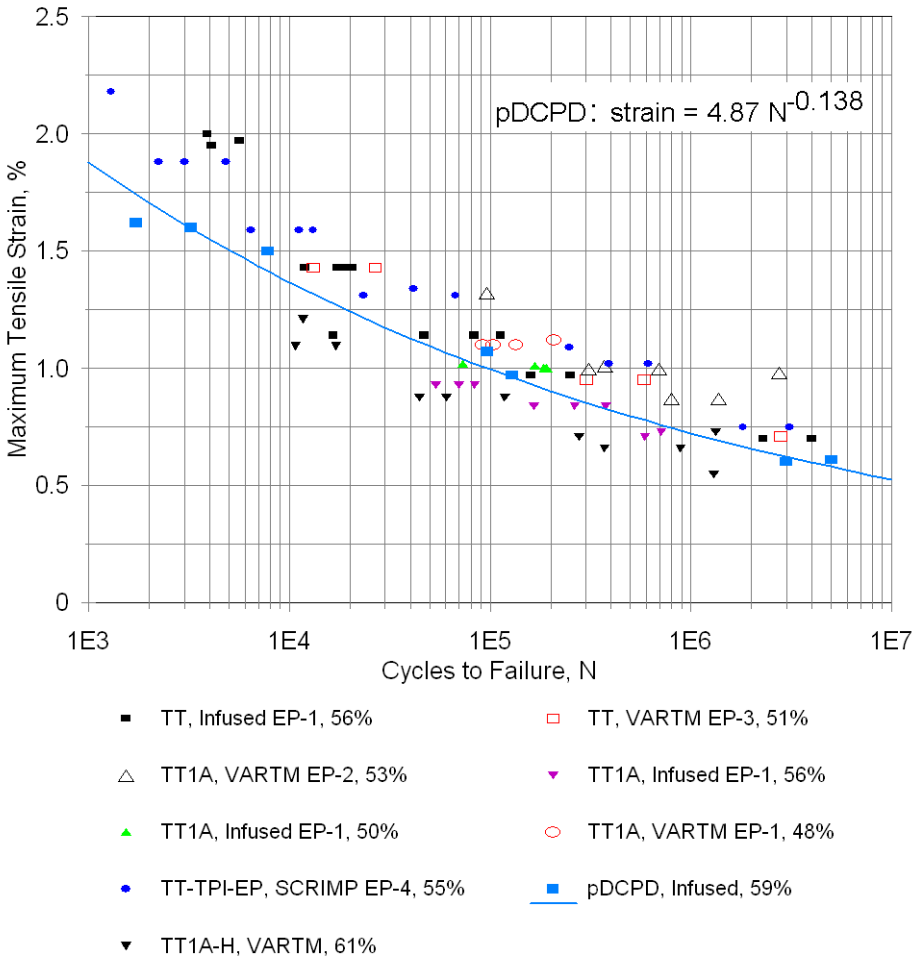

Figure 136. Tensile Fatigue Data and Trend Line for pDCPD Multidirectional Laminate Compared with Various Epoxy Data from Figure 50, R = 0.1; All Laminates Use the Same Uni-fabric D.

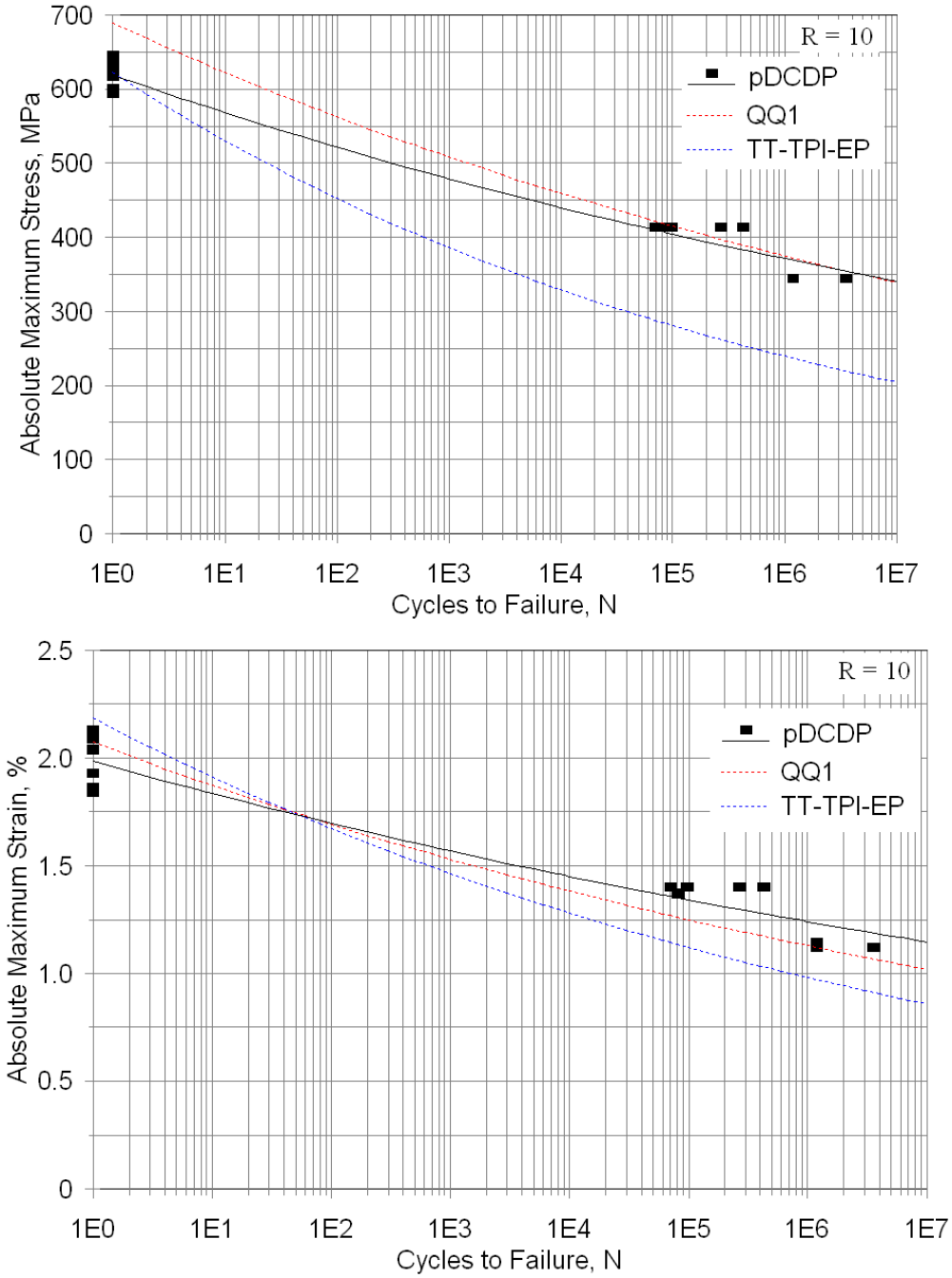

Figure 137. Compression Fatigue Data and Trend Lines for pDCPD Multidirectional Laminate Compared with Trend Lines for Epoxy Laminates QQ1 and TT-TPI-EP from Figure 41(b), R = 10.

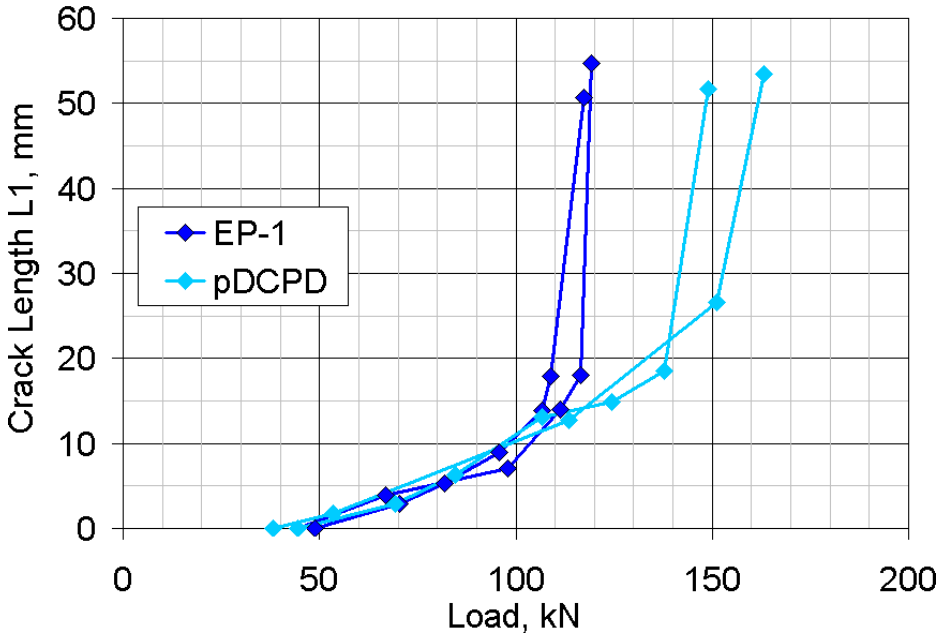

Figure 138. Comparison of pDCPD and EP-1 Epoxy (Figure 89, Biax Fabric L) Resins for Static Damage Growth vs. Applied Load, Complex Structured Laminate, Two Ply Drops.

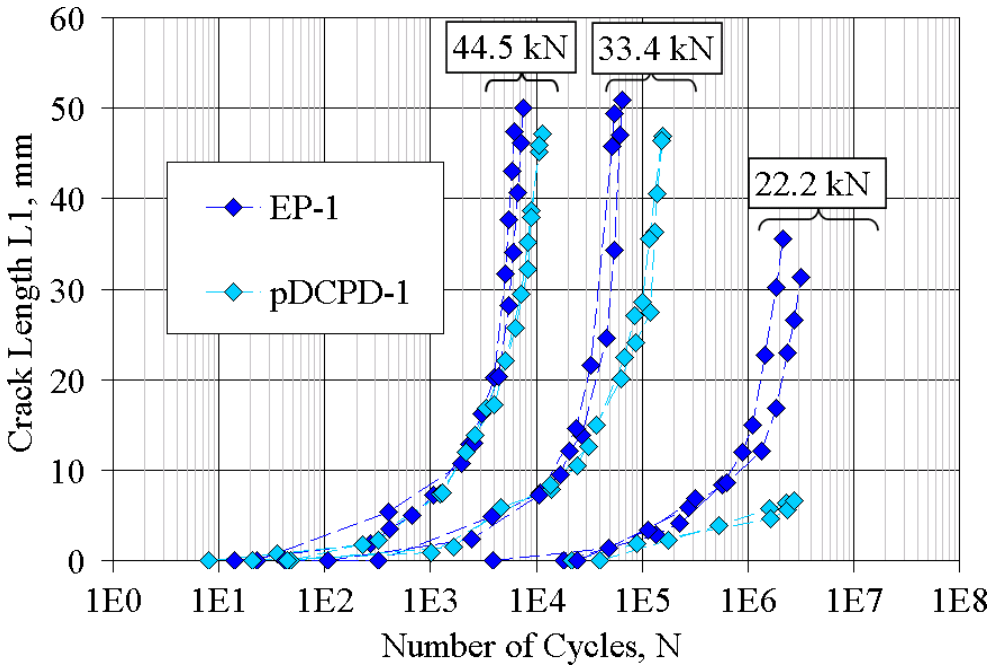

Figure 139. Comparison of pDCPD and EP-1 Epoxy (Figure 96, Biax Fabric L) Resins for Reversed Loading Fatigue Damage Growth, Complex Structured Laminate, Two Ply Drops, R = -1.

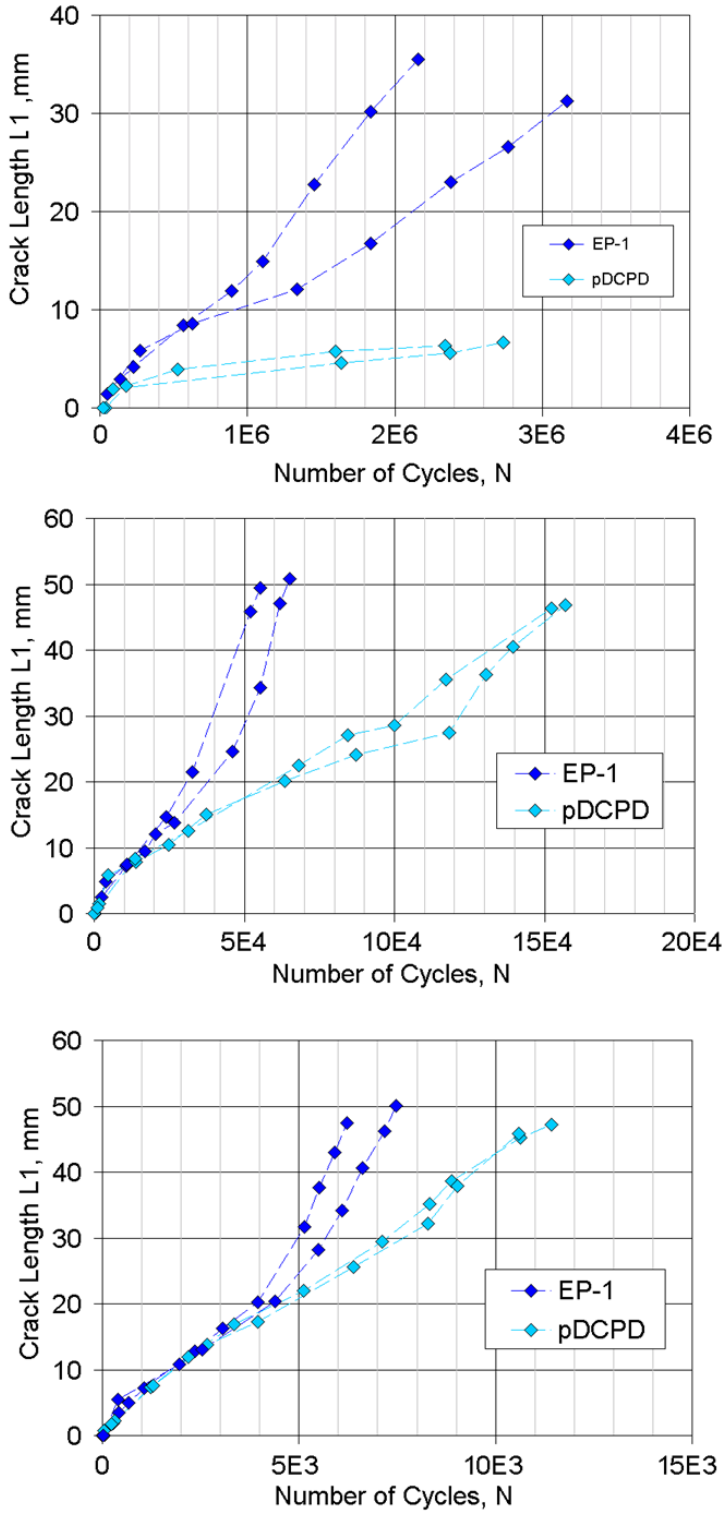

Figure 140. Results from Figure 139 Plotted on a Linear Cycles Scale for Maximum Absolute Loads of 22.2 kN (Top), 33.4 kN (Middle) and 44.5 kN (Bottom), R = -1.

SECTION 10. SUMMARY and CONCLUSIONS

10.1 Test Methods

Test methods for standard laminates which contain no specialized structure like ply drops have been developed over decades by standards organizations. Some of the test methods require modification for particular blade materials, as described in Section 2 and earlier reports [2, 5, 6]. Maintaining desired gage section failures becomes difficult and sometimes impossible for stronger, thicker laminates with compressive and reversed loading R-values [2, 13]. Specimen size (tension tests) and the presence of tabs in the gage section had insignificant effects on fatigue results for typical laminates. Static test rates do influence the strength for most fiberglass laminates; most fatigue test series included static data determined at the higher typical fatigue displacement rate (13 mm/s), which produced a 13% to 30% static strength increase relative to standard static rates (0.02 mm/s). Test methods for ply delamination resistance, G_{Ic} and G_{IIc}, are now standardized for opening (Mode I) and in the process of standardization for shearing (Mode II), and mixed mode; all require simulated flaws to be fabricated between the plies of the laminate.

The fatigue resistance of blades depends most strongly on the performance of structural detail areas including structure containing ply drops for thickness tapering (where ply delamination may occur), adhesive joints, and sandwich core structure used for buckling resistance. This report contains significant new test methods for the first two topics: (1) complex structured coupons containing ply drops and (2) adhesive joints of two different types, notched lap shear for generic adhesives studies, and simulated blade web joints. These structural detail test methods were developed (with FEA) to provide desired failure modes, identifiable stress and strain states which could be related to blade design, and convenient fabrication and test requirements. The test coupons are nonsymmetrical through the thickness to represent blade structure and also to allow greater material thickness for the same testing machine load requirements. The test methods allow loading in compression without buckling, so that compression and reversed loading fatigue resistance can be characterized.

Experience with the complex test coupon geometries has been favorable. Results are reproducible, easily analyzed by FEA, and directly useful without detailed analysis, in quantifying materials selection (especially resin and adhesive). While more complicated to fabricate and test than simple laminate coupons, they are very cost effective relative to larger blade substructure tests. Nonsymmetrical specimens induce varying degrees of bending moments in the grip system. Relatively thick coupons clamped in heavy (130 kg) grips with lateral constraints top and bottom result in manageable levels of out-of-plane displacement and stress state complications. The demands of providing meaningful materials comparisons in the face of the multitude of materials options for infused blades require test comparisons of this type.

10.2 Standard Blade Laminates

Static and fatigue data are provided for multiple combinations and lay-ups of 16 resins, 15 fabrics (including three types of fiber), three prepregs, and five adhesive systems, with several process and fiber content variations, tested under various loading conditions and directions. All

but a few historical baseline cases are of current or potential interest for blades. Individual test conditions and results are available either in the March, 2009 or March, 2010 updates of the SNL/MSU/DOE Fatigue of Composite Materials Database [1]. Fiber content has major effects on laminate stiffness and strength, and also on tensile fatigue resistance. Fiber volume contents for vacuum infused laminates depend on fabric construction, ranging around 45-50% for biax fabrics, 55-65% for uni-fabrics and 50-60% for multidirectional laminates; fiber weight contents are significantly higher. The various sections of this report present detailed comparisons and analysis of the performance of selected representative cases for each material group and test type.

10.2.1 Static Tests

Static strength and modulus data are provided for most laminates listed, while ply elastic constants and strengths for use in stress analysis, as well as interlaminar toughness data, are provided for selected infused fabrics and prepreg materials. Stress-strain curves in principal directions are also included for selected fabrics and multidirectional laminates.

Blade stiffness is a primary design driver which is proportional to material elastic modulus for a particular geometry. Longitudinal and multidirectional laminate elastic modulus is a direct product of the modulus of the fibers. Relative to glass fiber laminates, carbon increases the modulus by about a factor of three (while reducing density) and WindStrand increases the modulus by about 15%. Resin modulus has generally secondary effects, notably on the transverse and shear ply moduli and on the longitudinal compressive strength; the many resins included in this study showed little effect on laminate initial (low strain) modulus values.

As the stress and strain are increased in tension, the first damage observed is local cracking in the resin matrix. Matrix cracking, whether under static or fatigue loading, decreases the laminate stiffness slightly for longitudinal and multidirectional laminates, but significantly for transverse or shear direction loading. For the multidirectional laminates in this study, matrix cracking occurs primarily in the biax plies. Polyester resins are less resistant to matrix cracking than are epoxy resins. Small amounts of transverse fiber or, particularly, mat, significantly improve transverse ultimate strength (and biax fabric strength), but the transverse and shear moduli decrease dramatically at the matrix cracking strain. The rapid softening of biax fabrics in tension at strains above the matrix cracking point results in strongly nonlinear stress-strain curves. The constraints in multidirectional laminates greatly reduce the effects of the biax ply nonlinearity. Compressive stress-strain behavior for biax fabrics shows much reduced presence of matrix cracking compared with tension, but the response remains strongly nonlinear.

10.2.2. Fatigue Behavior

Fatigue results include fiber and matrix effects, fabric architecture effects for multidirectional and biax laminates, mean load (R-value) effects, constant life diagrams, predicted spectrum loading laminate comparison, and laminates for small turbine towers. The results show superior performance for carbon fiber laminates relative to glass under all loading conditions. Biax and multidirectional WindStrand laminates performed on a par with the best glass laminates. Polyester resin tensile fatigue curves showed a reduction of about 35% to 45% in stress and

strain at a million cycles lifetime relative to epoxy, with multidirectional glass laminates. Vinyl ester performance relative to epoxy was slightly poorer in tensile fatigue but better in compressive fatigue. Biaxial fabric fatigue was sensitive to direction and construction, but not significantly sensitive to resin type, although toughened epoxy EP-8 was relatively resistant and polyester UP-1 was slightly inferior to most vinyl esters and epoxies.

Multidirectional glass laminates under tensile fatigue loading are very sensitive to fiber content and small details in fabric construction. Laminates based on uni-fabric D retained good fatigue performance, in terms of fatigue exponent and strain capacity at 10^6 cycles, to significantly higher fiber contents than did fabrics A, B or C for VARTM processing (Figure 48). All fabrics showed a transition to much lower strain capacity (and associated shift in fatigue exponent) above some fiber content range. That range for fabric D laminates was around 55-60% fiber by volume, on the high side of infusion processed blades, while the transition occurred at or below 45% fiber volume for the other fabrics using VARTM processing. The fabric D laminates approach the upper limit defined by some prepreg laminates in the infusion fiber content range. Uni-fabric C, similar in weight and construction to fabric D, performed on a par with fabric D for infused laminates at 50% fiber by volume, but performed less well when VARTM processed. The performance of fabric D laminates was relatively insensitive to the epoxy resin used and the process details (VARTM, SCRIMP and infusion through resin distribution layers, Figures 7 and 8). Slightly reduced performance was observed for both VARTM and infusion processing as the fiber volume content rose to 56 to 60% for fabric D laminates (Figure 50).

For the same maximum loads, reversed loading is more damaging than tension or compression for all laminates, but particularly for biax laminates where shear effects are most significant. The lifetime of multidirectional laminates appears to follow similar trends and strain levels as do the biax fabric layers (Figure 50); however, a full understanding of the limiting factors involved in laminate fatigue failure require further study.

Large data-sets for three laminates at various loading conditions (six to thirteen R-values) have been developed: DD16 (an early, low fiber content glass/polyester); QQ1 (glass/epoxy with fabric B); and P2B, (carbon/epoxy prepreg with biax glass surfacing plies). The S-N datasets were then assembled into constant life (Goodman) diagrams in Figures 63-65 and the Appendix, covering all mean stress and stress-amplitude combinations, from which the expected mean and 95/95 lifetime can be determined for each cycle in a typical blade loads spectrum. The comparisons of laminates QQ1 and P2B in Figures 63 and 64 show the dominance of carbon fibers in terms of stress. In terms of strain the glass performs better at low cycles, but the tensile fatigue sensitivity of QQ1 is very damaging for tension containing cycles at long lifetimes.

The DD16 data, and a European OPTIMAT program glass/epoxy CLD, were used by Nijssen [2] in spectrum loading predictions which also included extensive residual stress experiments and lifetime model development. Sutherland and Mandell also used the DD16 data to explore fatigue data requirements for spectrum load predictions [16, 63] and to test the accuracy of various linear and nonlinear cumulative damage models for lifetime predictions under spectrum loading. This report includes lifetime predictions under the WISPERX spectrum for laminates DD16, QQ1 and P2B (Figures 66 and 67). While carbon performs particularly well, laminate QQ1 shows significant effects of the poor tensile fatigue resistance at high cycles which is

characteristic of many glass laminates at fiber contents above 45-50% by volume. Similar data for fabric D laminates are not yet available, but would be much improved over QQ1 at these fiber contents.

10.2.3 Delamination Resistance

Delamination between plies is an issue in areas with significant third-dimension stress components, as at ply drops and other structural detail areas. The initiation and growth of cracks which separate plies of a composite structure are best treated by fracture mechanics concepts and test methods. The resistance to delamination is characterized through experimental opening mode I and shearing mode II tests which allow determination of the critical strain energy release rates G_{Ic} and G_{IIc}. Mixed Mode I and II testing has also been carried out, since typical delamination crack fronts are mixed mode.

Delamination resistance is a resin-dominated property which correlates with neat resin toughness. Data in this report are consistent with earlier findings that G_{Ic} and G_{IIc} are consistently higher for typical epoxy resins than for polyester resins, with vinyl esters intermediate between the two. Mixed mode results (Figure 68) show the same trend with resin type. Toughened versions of resins such as VE-2, show greater delamination resistance than do the base resins, VE-1. Delamination testing under fatigue loading usually involves determining crack growth rates as a function of the maximum or range of G_I or G_{II} [5, 25]. Crack growth rates are typically a power law function of G_I or G_{II}.

Many industries, including wind blades, do not design their products using fracture mechanics, which requires a strategy of assumed (inspectable) flaw size, inspection periods and complex analysis. Instead, interlaminar toughness may be used as a qualitative resin selection criterion. The following sections (10.3 and 10.4) address an alternate approach which is compatible with wind blade technology, where ply drops which cause delamination are included in coupon static and fatigue tests, and data can be treated in the usual fashion, as knockdowns on allowable stresses or strains. Thus, the resin sensitive delamination resistance is quantified in terms of its effect on coupon static or fatigue performance, without requiring the use of fracture mechanics analysis.

10.3 Prepreg Ply Drops

This study explored the basic geometric and materials parameters involved with ply drops. Detailed finite element analysis of a broad range of geometries for ply drops, ply joints, and material transitions can be fount in a thesis by Wilson [59], available on the MSU fatigue program website (www.coe.montana.edu/composites/). Only selected representative FEA results are included in this report (Figures 82 and 83).

The results indicate that ply drops in carbon fiber laminates can lead to ply delamination at relatively low applied strains under fatigue loading (Figure 70). Findings were similar for various loading conditions including tension, compression and reversed loading, and in compression, for relatively thin and thick laminates. Ply drops involving ply thicknesses of about 0.3 mm had adequate fatigue resistance with carbon fibers, while ply thicknesses of 0.6 mm and greater

delaminated at maximum strains of 0.3% and below at one million cycles. By contrast, glass laminates using the same resin and prepreg manufacturing delaminated at strains about three times higher than for carbon (Figure 79); slightly higher stresses were required to delaminate the carbon compared with glass.

The various trends with materials and geometry can be understood from both approximate strength of materials estimates and the detailed FEA results. Differences between carbon and glass fiber performance in ply drops relates to differences in G_I and G_{II} levels resulting primarily from the higher elastic modulus of the carbon laminates.

10.4 Complex Structured Coupon with Ply Drops

The concept in this study was to develop a complex structured coupon test for infused laminates which was representative of tapered blade structure, containing ply drops with their inherent resin sensitivity. The resulting test method was then used to compare the performance of different resin types and ply drop thicknesses, under tension, compression and reversed loading, in terms of both damage growth characteristics and strain knockdowns.

The complex coupon with ply drops provides a basis for comparing infusion blade material and lay-up parameters for a case which is more representative of real blade structure than are plain laminate tests. The sequence of damage initiation and growth depends on both in-plane properties of the fabric layers and interlaminar properties, the latter dominated by the resin. The test coupon geometry FEA indicates only minor effects of non-symmetry, which allows for double the thickness compared with earlier symmetrical coupons. Results from the static and fatigue tests indicate improved performance for the epoxy system EP-1 relative to the vinyl ester VE-1 or polyester UP-1; the toughened vinyl ester, VE-2, is significantly improved relative to the base VE-1 (Figures 86-95). The results for various resins with the complex coupon are consistent with data for interlaminar Modes I and II tests.

The results show significantly higher knockdowns for greater thicknesses of dropped material (4 vs. 2 vs. 1 plies dropped at the same position, for approximately 1.3 mm thick plies, Figure 96). The results also show much increased fatigue sensitivity under reversed fatigue loading compared with either tensile or compressive loading alone, for both epoxy and polyester resins. In terms of fabrics, complex coupon test data show better performance with biax fabric M compared with fabric L under static and fatigue loading (Figures 89 and 96), despite the opposite trend in fatigue for the biax fabrics when tested alone (Figure 60).

10.5 Adhesive Joints

10.5.1 Notched Lap Shear Joints

The notched lap shear joint test method produced consistent results for several high viscosity paste adhesives for a range of adhesive thicknesses (3 mm-9 mm), overlap lengths (12.7 and 25.4 mm), laminate adherends, laminate peel plies and loading conditions (tension, compression and reversed loading). Failure initiated under tension and reversed loading as a crack in the notch root area, at a stress concentration in the adhesive, then propagated along the interface, either inside the laminate surface or on the peel ply interface (Figures 27 and 28). Compressive failures

appeared to initiate at the interface in an area of local tensile stress, then propagate diagonally across the adhesive and along the interfaces (Figure 99). Linear and nonlinear finite element predictions correlated with the various results for geometric effects, using measured neat adhesive stress-strain data.

The static results for typical blade adhesive ADH-1 show the following (Figure 98):

1. Coefficients of variation in the 5% range within a single mixed batch, and small variations between batches.
2. Little effect of peel ply type for three common products.
3. Significant variations in apparent shear strength for different adhesives.
4. Higher strength for the shorter overlap (12.7 mm) compared with the longer overlap length (25.4 mm) used in fatigue tests.
5. Much higher apparent shear strength for compressive loading than for tension, despite the same shear stresses in each case (failure correlates with the maximum local tensile (peel) strain).
6. A significant decrease in joint strength as the thickness of the adhesive increases from approximately 3 mm to 9 mm.
7. Only a slight strength decrease when the loading rate was increased by a factor of 100.

Fatigue data were obtained for adhesive ADH-1 under static, reversed and compressive loading. Crack propagation was observed only in the last few cycles, so the fatigue life was initiation dominated. Lifetime scatter in fatigue appears low from the limited data available to date, despite the fact that most cracks initiated at pores in the adhesive, near the notch root. Fatigue sensitivity, in terms of curve fit exponents, was lowest for compression, highest for reversed loading.

Finite element results correlated well with the measured thickness effect using the maximum local tensile (peel) strain as a failure criterion (Figure 107). Less accurate but approximate correlations were obtained for the overlap length effect and for compression loading (Table 16). FEA modeling of pore size and location effects show less effect of pore size than for the proximity of the pore to the notch root stress concentration location.

10.5.2 Simulated Blade Joints

Simulated blade joint studies involved testing of a simulated web joint geometry using test coupons fabricated by an industry partner. Baseline and reinforced geometries were included in the series of over 250 tests of four geometries, two static loading rates, and two fatigue loading conditions. The test geometries are representative of typical blade web joints using a relatively brittle, thick paste adhesive. Various flaws and failure modes have been identified, and some have been explored with finite element modeling. The following conclusions were reached:

1. The 140 static test results indicate that the average strengths are similar for Geometries A (45^o) and B (90^o), while the corresponding reinforced geometries, C and D, are significantly stronger, with lower coefficients of variation. Geometry B produced significantly greater strength scatter than Geometry A, which reduced its 95/95 strength. Most of the difference

between Geometries A and B could be related to several poorly cured adhesive specimens. Static strengths were insensitive to differences in test rate (0.025 mm/s vs. 12.6 mm/s).

2. Tensile fatigue results show relatively low fatigue sensitivity in terms of fatigue exponent, for Geometries A and B. Geometries C and D showed somewhat greater sensitivity in terms of fatigue exponent, but fatigue strengths at 10^6 cycles were significantly higher than for the unreinforced geometries. Reversed tension-compression loading produced a shift in failure mode to interlaminar in the adherend, with greater fatigue sensitivity, for Geometry C. This is consistent with the greater fatigue sensitivity under reversed loading relative to tensile loading, of typical $\pm 45^o$ laminates used in the adherends. Reversed loading could not be tested for Geometries A and B due to adherend buckling under compressive loads of the thinner adherends.

3. Flaws, crack origins and failure modes were described for each geometry and loading condition, with emphasis on Geometries A and B. Most crack origins and initial growth were cohesive in the adhesive, shifting to interlaminar in the adherend as the cracks extended. For Geometry A, cracks initiated mostly at the major geometric stress concentration, Point A in Fig. 29. Lower strength specimens either contained pores in the adhesive close to Point A or else regions of poorly cured adhesive. Pores were common in most specimens in apparently random locations. Crack initiation in Geometry B specimens was mostly above the stress concentration point, near Point B in Fig. 29; pores could be observed at the crack origin in most cases. Poorly cured adhesive was present in a few specimens of Geometries A and B, including the weakest specimens, apparently related to hand mixing of the very viscous adhesive in small batches. Poorly bonded adhesive/adherend interface areas were the most common flaw in weaker specimens of Geometries C and D, where poorly cured adhesive was not observed. As noted above, the failure mode shifted to interlaminar in the adherend for reversed loading with Geometry C.

4. Finite element results showed a significantly higher strain concentration at Point A for Geometry A than for Geometry B. Pores near to Point A in Geometry A increase the strain at Point A, but do not shift the maximum strain location. For Geometry B, failure origins shifted to the edges of pores in the area of Point B in Fig. 29, away from the sharp corner. Maximum strains in these joints are at the pore ends. Joint strength and lifetime for Geometry B are then functions of pore size and location, over a larger volume of the adhesive than for Geometry A, possibly contributing to the increase in scatter.

5. For geometries like A and B, joint strength and lifetime (in the absence of other flaws like poorly cured or poorly bonded areas) is a function of the severity of the geometric strain concentrations inherent to the joint geometry, combined with pore location and severity. If the geometric strain concentration is lower, then failure may be dominated by pores, and would then be dependent on their severity and distribution, possibly leading to increased scatter and reduced 95/95 strength. Changes in adhesive ductility due to adhesive composition or environmental conditions may shift this behavior [37].

10.6 Spar Cap Split Tests

The split tests are not an accepted test method for composites, but the results provide a meaningful comparison of the split resistance of primarily unidirectional spar caps constructed with different materials, manufacturing methods, and axial material content. Of the unidirectional cases, the carbon prepreg is clearly superior to the glass laminates, probably reflecting a higher transverse strength. When low levels of off-axis materials are added, the laminates with glass 90^o material improve rapidly to split resistance levels higher than for comparable carbon laminates. Developing improved split resistance in carbon spar caps may require stiffer off-axis material. The dispersion of off-axis material is relatively unimportant.

The results of these static tests suggest that glass spars should contain at least 15% off-axis material, including any bonded skins or webs. Carbon spars require further study to optimize the amount (and stiffness) of off-axis materials. Fatigue testing is needed to more fully explore the splitting resistance.

10.7 Laminates with pDCPD Resin

The new pDCPD resin has very low viscosity and high toughness. Standard laminate data show similar static strength and modulus, with greatly increased interlaminar toughness, G_{Ic}, relative to the baseline epoxy. The tensile fatigue resistance for multidirectional laminates based on Fabrics D and L is similar to that for epoxy laminates with similar fiber content, while the compressive fatigue resistance is slightly improved over epoxy. Performance in the complex structured coupon with ply drops is significantly improved over the baseline epoxy for both static and fatigue loading.

REFERENCES

1. Mandell, J.F. and Samborsky, D.D., "DOE/MSU Fatigue of Composite Materials Database, 2009 update (www.sandia.gov/wind/other/973002upd0309.pdf).

2. Nijssen, R.P.L., "Fatigue Life Prediction and Strength Degradation of Wind Turbine Rotor Blade Composites," Contractor Report SAND2006-7810P, Sandia National Laboratories, Albuquerque, NM, 2006.

3. Griffin, D., "Blade System Design Study Part II: Final Project Report (GEC)," Contractor Report SAND2009-0686, Sandia National Laboratories, Albuquerque, NM (2009).

4. Mandell, J.F. and Samborsky, D.D., "Analysis of the DOE/MSU Database: Fatigue of Composite Materials for Wind Turbine Blades," Final Report DOE Grant DE-FG04-01AL67287, 2004.

5. J.F. Mandell, D.D. Samborsky, and D.S. Cairns, "Fatigue of Composite Materials and Substructures for Wind Turbine Blade," Contractor Report SAND2002-0771, Sandia National Laboratories, Albuquerque, NM, (2002).

6. J.F. Mandell and D.D. Samborsky, "DOE/MSU Composite Material Fatigue Database: Test Methods, Materials, and Analysis," Contractor Report SAND97-3002, Sandia National Laboratories, Albuquerque, NM (1997).

7. Mandell, J.F., Reed, R.M. Jr. and Samborsky, D.D., "Fatigue of Fiberglass Wind Turbine Blade Materials," Contractor Report SAND92-7005, Sandia National Laboratories, Albuquerque, NM (1992).

8. N.K. Wahl, J.F. Mandell, D.D. Samborsky, "Spectrum Fatigue Lifetime and Residual Strength for Fiberglass Laminates," Report SAND2002-0546, Sandia National Laboratories, Albuquerque, NM (2002).

9. J.F. Mandell, D.D. Samborsky, D.W. Combs, M.E. Scott and D.S. Cairns, "Fatigue of Composite Material Beam Elements Representative of Wind Turbine Blade Substructure," Report NREL/SR-500-24374, National Renewable Energy Laboratory, Golden, Co (1998).

10. R. P. L. Nijssen, "OptiDAT - Fatigue of Wind Turbine Blade Materials Database," 2006, (www.kc-wmc.nl/ optimat_blades).

11. Samborsky, D.D., Wilson, T.W., Agastra, P., and Mandell, J.F., J. Sol. Energy Eng., 2008 130, paper 031001.

12. Mandell, J.F., Samborsky, D.D. and Agastra, P., Proc. SAMPE 2008, Long Beach, CA, paper L238, 2008.

13. Samborsky, D.D., Wilson, T.J. and Mandell, J.F., J. Sol. Energy Eng., 2009, 131, paper 011006.

14. Samborsky, D. D., Wilson, T. J. and Mandell, J. F., Proc. 2007 ASME Wind Energy Symposium, Paper AIAA-07-67056, AIAA/ASME, Reno, NV, 2007.

15. D. D. Samborsky, P. Agastra and J. F. Mandell, Proc. 2008 ASME Wind Energy Symposium, Paper AIAA-2008-1346, ASME/AIAA, Reno, NV, 2008.

16. Sutherland, H. J. and Mandell, J. F., "Optimized Goodman Diagram for the analysis of Fiberglass Composites Used in Wind Turbine Blades," ASME J. Solar Energy Engineering, 127:563-569, 2005

17. Samborsky, D.D., Sears, A., Mandell, J.F. and Kils, O., "Static and Fatigue Testing of Thick Adhesive Joints for Wind Turbine Blades," paper AIAA-2009-1550, AIAA/ASME, Orlando, 2009.

18. Agastra, P., Samborsky, D.D. and Mandell, J.F., "Fatigue Resistance of Fiberglass Laminates at Thick Material Transitions," paper AIAA-2009-2411, AIAA SDM Conf., Palm Springs, 2009.

19. Grimes, G.C. and Dusablon, E.G., "Study of Compression Properties of Graphite/Epoxy Composites with Discontinuities," Composite Materials: Testing and Design (Sixth Conference), ASTM STP 787, I.M. Daniel Ed., American Society for Testing and Materials, Philadelphia, 1982, pp. 513-538.

20. Trethewey, B.R., Gillespie, J.W., Jr. and Wilkins., "Interlaminar Performance of Tapered Composite Laminates," Proceedings of the American Society for Composites, Fifth Technical Conference, June 11-14, 1990, p. 361.

21. Ochoa, O.O., and Chan, W.S., "Tapered Laminates: A Study on Delamination Characterization," Proceedings of the American Society for Composites, Third Technical Conference, September 25-29, 1988, p. 633.

22. Meirinhos, G., Rocker, J., Cabanac, J-P, Barrau, J-J., "Tapered Laminates Under Static and Fatigue Tension Loading," Composites Science and Technology, 62 (2002), pp. 597-603.

23. Murri, G.B., Salpekar, S.A., and O'Brien, T.K., "Fatigue Delamination Onset Prediction in Unidirectional Tapered Laminates," Composite Materials: Fatigue and Fracture (Third Volume), ASTM STP 1110, T.K. O'Brian, Ed., American Society for Testing and Materials, Philadelphia, 1991, pp. 312-339.

24. Cairns, D.S., Mandell, J.F., Scott, M.E., Maccagnano, J.Z., "Design Considerations for Ply Drops in Composite Wind Turbine Blades," 1997 ASME Wind Energy Symposium, ASME/AIAA, AIAA-97-0953, pp. 197 - 208. (1997).

25. Mandell, J.F., Cairns, D.S., Samborsky, D.D., Morehead, R.B., and Haugen, D.J., J. Sol. Energy Eng., 2003, 125, paper 009304.

26. Murri, G.B., Schaff, J.R., Dobyns, A.L.," Fatigue Life Analysis of Hybrid Composite Tapered Flexbeams," NASA LaRC Technical Library Digital Repository http://hdl.handle.net/2002/15079

27. Vizzini, A. J. and Lee, S. W., "Damage Analysis of Composite Tapered Beams," Journal of the American Helicopter Society, 40 (2), Apr. 1995, pp. 43-49.

28. Avery, D. P., Samborsky D. D., Mandell, J. F. and Cairns, D. S., "Compression Strength of Carbon Fiber Laminates Containing Flaws with Fiber Waviness," 2004 ASME Wind Energy Symposium, ASME/AIAA., AIAA-2004-0174, pp. 54-63, (2004)

29, Mandell, J.F., Samborsky, D.D., Wang, L., and Wahl, N.K., "New Fatigue Data for Wind Turbine Blade Materials," Journal of Solar Energy Engineering, ASME, Vol. 125, No. 4, pp. 506-514. November 2003.

30. Petrie, E.M., “Handbook of Adhesives and Sealants, Second Edition,” McGraw-Hill, New York, 2007.

31. Tomblin, J., Harter, P., Seneviratne, W., and Yang, C., “Characterization of Bondline Thickness Effects in Adhesive Joints,” J. Composites Tech. and Res., 24:80-92, 2002.

32. Kinloch, A.J., and Osiyemi, S.O., “Predicting the Fatigue Life of Adhesively-Bonded Joints,” J. Adhesion, 43:79-90, 1993.

33. Curley, A.J., Hadavinia, H., Kinloch, A.J. and Taylor, A.C., “Predicting the Service Life of Adhesively - Bonded Joints,” Inter. J. Fracture, 103:41-69, 2000.

34. ISO Standard 9664:1993(E), “Adhesives - Test Methods for Fatigue Properties of Structural Adhesives in Tensile Shear,”.

35. Tomblin, J., Yang, C. and Harter, P, “Investigation of Thick Bondline Adhesive Joints,” FAA Report DOT/FAA/AR-01/33, June, 2001.

36. Tomblin, J., Seneviratne, W., Escobar, P. and Yap, Y., “Shear Stress-Strain Data for Structural Adhesives,” FAA Report DOE/FAA/AR-02/97, November, 2002.

37. Tomblin, J., Seneviratne, W., Escobar, P. and Yap, Y., “Fatigue and Stress Relaxation of Adhesives in Bonded Joints,” FAA Report DOE/FAA/AR-03/56, October, 2003.

38. Goland, M. and Reissner, E., “The Stresses in Cemented Joints,” J. Appl. Mechanics, 11:17-27, 1944.

39. Hart-Smith, L.J., “Developments in Adhesives 2,” Kinloch, A.J., ed., Applied Science Publications, London, 1981.

40. Sancaktar, E., “Fracture Aspects of Adhesive Joints: Material, Fatigue, Interphase and Stress Concentrations,” J. Adhesion Sci. and Tech., 9:119-147, 1995.

41. Ripling, E.J., Mostovoy, S. and Patric, R.L., “Application of Fracture Mechanics to Adhesive Joints,” Adhesion, ASTM STP 360, ASTM, Phil., p.5, 1963.

42. Johnson, W.S. and Mall, S., “A Fracture Mechanics Approach to Designing Adhesively Bonded Joints,” NASA Technical Memorandum 85694, NTIS, Springfield, VA, 1983.

43. Jablonski, D. A., “Fatigue Crack Growth in Structural Adhesives,” J. Adhesion, 11:125-143, 1980.

44. Luckyram, J. and Vardy, A. E., “Fatigue Performance of Two Structural Adhesives,” J. Adhesion, 26:273-291, 1988.

45. Harris, J.A. and Fay, P.A., “Fatigue Life Evaluation of Structural Adhesives for Automotive Applications,” 12:9-18, 1992.

46. Metzinger, K. E. and Guess, T. R., “Single Cycle and Fatigue Strengths of Adhesively Bonded Lap Joints,” 1999 ASME Wind Energy Symposium, AIAA/ASME, 1999, pp 21-31.

47. Sancaktar, E., “Fatigue and Fracture Mechanics,” Engineered Materials Handbook, Vol. 3, Adhesives and Sealants, p. 501, ASM International, Materials Park OH, 1990.

48. Sancatar, E., “Mixed-Mode Fatigue Failure in Structural Adhesives,” Fatigue and Fracture Mechanics: Twenty-Ninth Volume, ASTM STP 1332, T. L. Panontin and S. D. Sheppard, Eds., American Society for Testing and Materials, West Conshohocken PA, 1999.

49. Quaresimin, M. and Ricotta, M., “Fatigue Behavior and Damage Evolution of Single Lap Bonded Joints in Composite Material,” Composites Science and Technology, 66:176-187, 2006.

50. Broughton, W.R. and Mera, R.D., “Review of Life Prediction Methodology and Adhesive Joint Design and Analysis Software,” National Physical Laboratory, London, June 1997.

51. Ashcroft, I.A. and Shaw, S.J., “Mode I Fracture of Epoxy Bonded Composite Joints 2. Fatigue Loading,” Internat. J. Adhesion and Adhesives, 22,151-167, 2002.

52. Agastra, P., "Mixed Mode Delamination of Glass Fiber/Polymer Matrix Composite Materials", Masters Thesis, Chemical and Biological Engineering Department, Montana State University, 2003.

53. Hunston, D.L., Moulton, R.J., Johnson, N.J., and Bascom, W.D., "Matrix Resin Effects in Composite Delamination: Mode I fracture Aspects," Toughened Composites, ASTM STP 937, Norman J. Johnson, Ed., American Society for Testing and Materials, Philadelphia, 1987, pp. 74-94.

54. Friedrich, K., ed., “Composite Materials Series, Vol. 6, Application of Fracture Mechanics to Composite Materials,” R. B. Pipes, series ed., Elsevier, New York (1989).

55. Cairns, D.S., ASTM J. Composites Technology and Research, 14, 1992, pp 37-42.

56. Russell, A.J. and Street, K.N., in “Delamination and Debonding of Materials, STP 876,” W.S. Johnson, Ed., ASTM, Phil., 1985, pp. 349-370.ASTM

57. Williams, J.G., Composite Sci. and Tech., 35, 1989, pp 367-376.

58. Mandell, J.F., D.D. Samborsky, N.K. Wahl, and H.J. Sutherland, “Testing and Analysis of Low Cost Composite Materials Under Spectrum Loading and High Cycle Fatigue Conditions,” Conference Paper, ICCM14, Paper # 1811, SME/ASC, 2003.

59. Wilson, T.J., "Modeling of In-Plane and Interlaminar Fatigue Behavior of Glass and Carbon Fiber Composite Materials," MS Thesis, Department of Mechanical Engineering, Montana State University, 2006.

60. Sutherland, H.J., and P.S. Veers, “The Development of Confidence Limits For Fatigue Strength Data,” 2000 ASME Wind Energy Symposium, AIAA/ASME, 2000, pp. 413-423.

61. ASTM, E739-91, Standard Practice for Statistical Analysis of Linear or Linearized Stress-Life (S-N) and Strain-Life (e-N) Fatigue Data, ASTM, Conshohocken, PA.

62. Echtermeyer, T., E. Hayman, and K.O. Ronold, “Estimation of Fatigue Curves for Design of Composite Laminates,” Composites-Part A (Applied Science and Manufacturing), Vol. 27A, No. 6, 1996, p. 485.

63. H. J. Sutherland and J. F. Mandell, Wind Energy, 8, 93 (2005).

64. Paquette, J., van Dam, J. and Hughes, S., “Structural testing of 9 m carbon fiber wind turbine research blade,” 45th AIAA Aerospace Sciences Meeting and Exhibit, Reno, NV 2007.

65. Tanaka, K., and Tanaka, H., "Stress-Ratio Effect on Mode II Propagation of Interlaminar fatigue Cracks in Graphite/Epoxy Composites," Composite Materials: Fatigue and Fracture (Sixth Volume), ASTM STP 1285, E.A. Armanios, Ed., ASTM, 1997, pp. 126-142.

66. Russell, A.J. and Street, K.N., “The effect of matrix toughness on delamination: static and fatigue fracture under Mode II shear loading of graphite fiber composites,” Toughened Composites, ASTM STP 937, N. J. Johnston, Ed., American Society for Testing and Materials, Phil., 1987, pp. 275-294.

67. Jacob, G.C., Hoevel, B., Pham, H.Q., Dettloff, M.L., Verghese, N.E., Turakhia, R.H., Hunter, G., Mandell, J.M. and Samborsky, D.D., “Technical advances in epoxy technology for wind turbine blade composite fabrication,” SAMPE Fall Technical Conf., Wichita, KS, 2009.

68. Nagarajan, M. and Mandell, J.F., “Improving fatigue performance of wind blade materials,” Windpower 2009, AWEA, Chicago, 2009.

69. J.F. Mandell, D.D. Samborsky, M. Li., R. Orozco, and D.S. Cairns, Proc. of the 2000 ASME Wind Energy Symposium, ASME/AIAA, New York, 2000, pp. 354-366.

70. Reeder, J. R., and Crews, J. H., Jr., “The Mixed Mode Bending Method for Delamination Testing,” AIAA Journal, Vol. 28, No. 7, July 1990, pp. 1270-1276.

71. Mandell, J.F., "Fatigue Behavior of Short Fiber Composite Materials," The Fatigue Behavior of Composite Materials, K.L. Reifsnider, Ed., Elsevier, Ch. 7, 1991.

72. Musial, W., Berry, D., Mandell, J., Ashwill, T., and Hartman, D., “Advances in Blade Design and Material Technology,” Windpower 2005, American Wind Enenergy Association, 2005.

73. Krugar, R., and Konig, M., Composite Materials: Fatigue and Fracture, ASTM STP 1285, E. A. Armanios, Ed., American Society for Testing and Materials, Philadelphia (1997) pp.162-178.

74. O'Brien, T.K., "Composite Interlaminar Shear Fracture Toughness, GIIC: Shear Measurement or Sheer Myth?," Composite Materials: Fatigue and Fracture, Seventh Volume, ASTM STP 1330, R.B. Bucinell, Ed., American Society for Testing and Materials, Philadelphia,1998, pp. 3-18.

75. Ramkumar, R. L. and Whitcomb, J. D., Delamination and Debonding of Materials, ASTM STP 876, W. S. Johnson, ed., American Society for Testing and Materials, Philadelphia (1985).

76. Johnson, W.S. and Mangalgiri, P.D., "Influence of the resin on interlaminar mixed mode fracture," Toughened Composites, ASTM STP 937, N. J. Johnston, Ed., American Society for Testing and Materials, Phil., 1987, pp. 295-315.

77. DNV Offshore Standard DNV-OS-J102, "Design and manufacture of wind turbine blades, offshore and onshore wind turbines," Det Norske Veritas, Norway (2006).

78. Nuin, I., et. al., "Fracture mechanics techniques for the design of structural components with adhesive joints for wind turbines," F M Paper 461, EWEC, 2009.

79. Holmes, J.W., Sorensen, B.F. and Brondsted, P., "Reliability of wind turbine blades: an overview of materials testing," Windpower Shanghai, 2007.

80. Flinn, B. and Phariss, M., "The effect of peel ply surface preparation variables on bond quality," DOT/FAA/AR-06/28, U.S. DOT/FAA, Wash. D.C., August, 2006.

81. Wetzel, K.K., "Defect tolerant design of wind turbine blades," EWEC, 2009.

82. Natrella, M. G., "Experimental Statistics," National Bureau of Standards Handbook 91, National Bureau of Standards, Gaithersburg, MD, August, 1963.

83. Broek, D., Elementary Fracture Mechanics, p. 276, Martinus Nijhoff Publishers, Dordrecht, The Netherlands, 1982.

84. J.F. Mandell, F.J. McGarry, S.S. Wang, J. Im, J. Composite Materials, Vol. 8, 1974, P. 105.

85. Harper, P.W. and Hallett, S.R., "Cohesive zone length in numerical simulations of composite delamination," Engineering Fracture Mechanics, vol 75 (2008), pp. 4774-4792.

86. Cairns, D.S., Ritter, W., Norris, P., Mandell, J., "A new Methodology for Wind Turbine Blade/Materials/Structural Characterization," 2004 ASME Wind Energy Symposium, ASME/AIAA., AIAA-2004-0175, pp. 64-75, (2004).

APPENDIX. DETAILED DATA AND ANALYSIS FOR LAMINATES QQ1 AND P2B

This Appendix presents more complete axial and transverse data, statistics, and constant life diagrams for glass/epoxy laminate QQ1 and carbon hybrid laminate P2B in axial and transverse directions, taken from Wilson [59].

A1. Fatigue Data, Fit Parameters, and Statistical Treatment

A.1.1 Fiberglass Laminate QQ1, Axial Direction

The majority of the data sets for the different R-values of QQ1 were fit with power law equations through all of the fatigue data. For two R values, however, better fits to the higher cycle data were obtained by fitting equations to truncated fatigue data sets. For R = -1, the data fit were at a stress level that produced failures over 10 cycles. For R = 0.5, the data were truncated at a stress level that produced failures on the order of 500 cycles or greater. Table A1 gives the fit parameters. Figure A1 through Figure A3 show these fits. Static tensile, R = 1.0, data were not available for materials QQ1 (or P2B) so stress rupture predictions were not made. As with DD16, the fatigue model trend is shown in the static range, but only the static mean or 95/95 limit line represents the static data.

Table A1: Fit parameters for material QQ1, axial direction (fit to all fatigue data, except fit to data for stresses which produce failure above 10 cycles (R = -1) and 500 cycles (R = 0.5).

R-value	Static failure mode	95/95 Static strength, MPa	Mean fit parameters		95/95 fit parameters	
			A	B	m	b-tol
10	Compression	595.5	690.4	-0.0445	-0.0445	2.796
-2	Compression	595.5	697.6	-0.0600	-0.0600	2.795
-1	Compression	595.5	931.2	-0.1378	-0.1378	2.902
-0.5	Tension	758.4	1172.6	-0.1407	-0.1407	3.012
0.1	Tension	758.4	1327.6	-0.1556	-0.1556	3.056
0.5	Tension	758.4	1358.9	-0.1313	-0.1313	3.092

The exponent, B, for material QQ1 has a higher absolute value in the range R = -1 to 0.5 than for DD16, showing increased tensile fatigue sensitivity. The compression dominated exponents are similar to DD16.

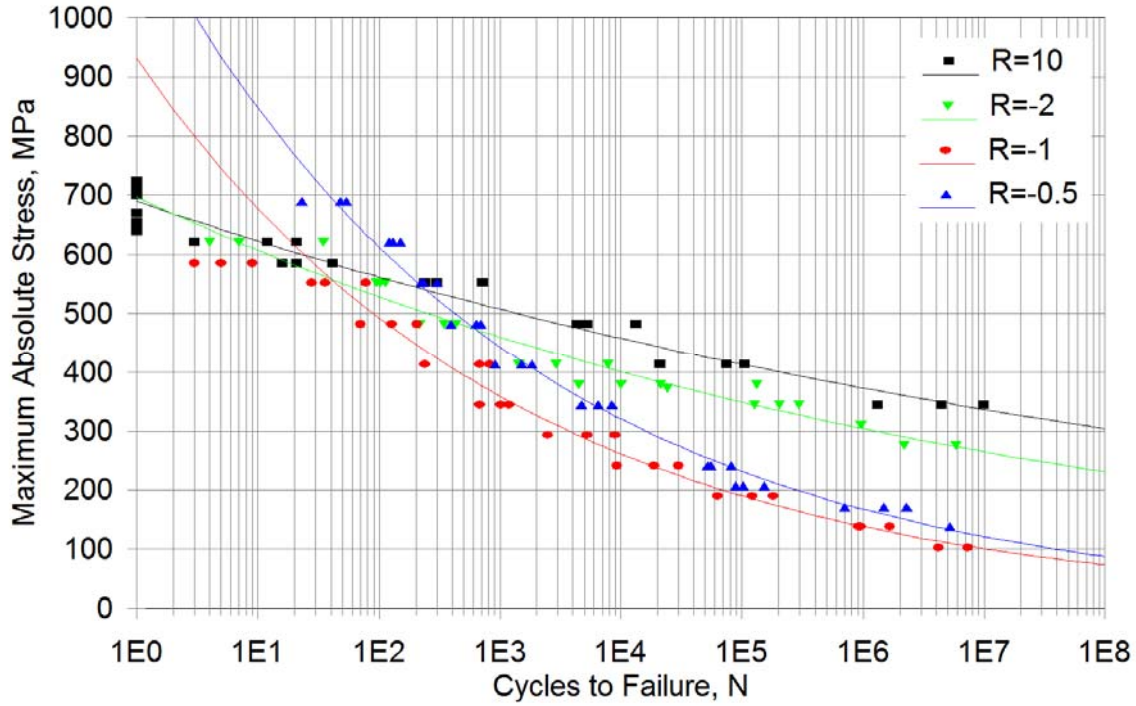

Figure A1: Compression and mixed fatigue, mean power law fits (material QQ1, axial direction).

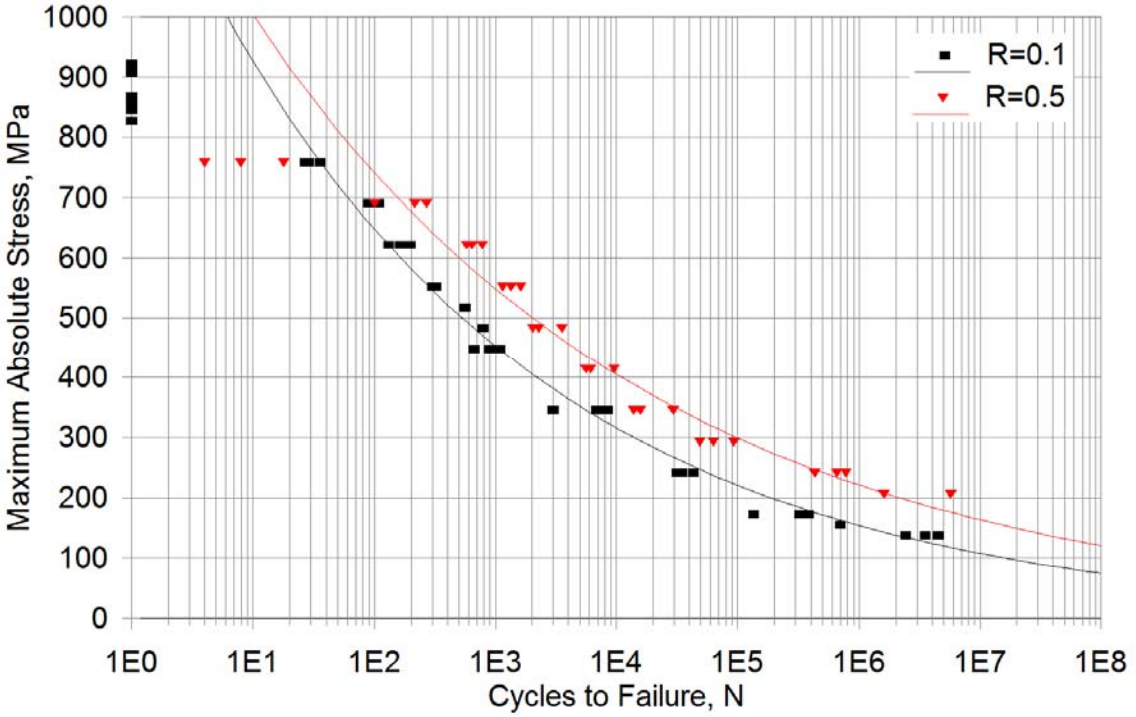

Figure A2: Tensile fatigue, mean power law fits (material QQ1, axial direction).

A.1.2 Fiberglass Laminate QQ1T, Transverse Direction

Material QQ1T (material QQ1 loaded in the transverse direction) is modeled with power laws fit though all of the data. Parameters are given in Table A2 and mean fits are shown in Figure A3 and A4. The lower absolute value of B than for the axial direction shows slightly reduced fatigue sensitivity, compared with the axial direction (Table A1).

Table A2: Fit parameters for material QQ1T, transverse direction (fit to all static and fatigue data).

R - Value	Static failure mode	95/95 Static strength , MPa	Mean fit parameters		95/95 Fit parameters	
			A	B	m	b-tol
10	Compression	232.7	238.6	-0.0434	-0.0434	2.331
-2	Compression	232.7	280.9	-0.1042	-0.1042	2.399
-1	Compression	232.7	174.7	-0.1170	-0.1170	2.169
-0.5	Tension	127.7	165.7	-0.1087	-0.1087	2.138
0.1	Tension	127.7	145.4	-0.0806	-0.0806	2.105
0.5	Tension	127.7	154.9	-0.0709	-0.0709	2.138
0.7	Tension	127.7	140.7	-0.0480	-0.0480	2.091

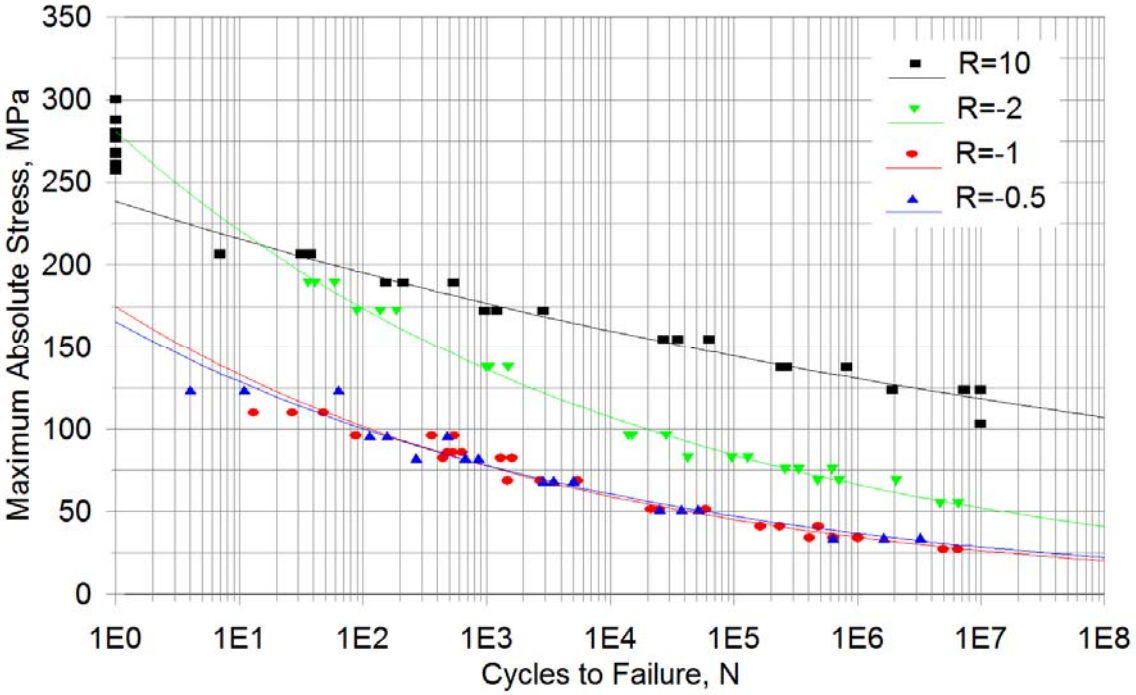

Figure A3: Compression and mixed fatigue, mean power law fits (material QQ1T, transverse direction).

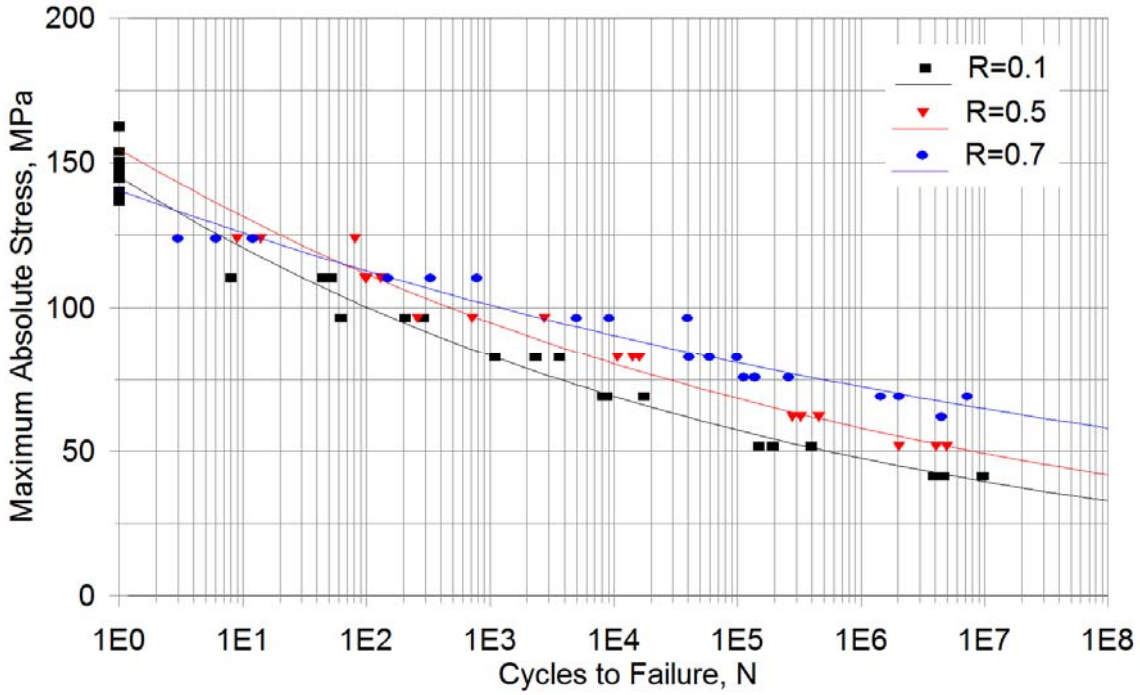

Figure A4: Tensile fatigue, mean power law fits (material QQ1T, transverse direction).

A.1.3 Carbon/Glass Hybrid Laminate P2B, Axial Direction

Material P2B test data are all relatively flat compared to the fiberglass laminates and tend to fall into two distinct bands. Fully tensile tests perform better than compressive or mixed loading. P2B data show a fairly flat, linear slope when plotted on a log-linear plot. To determine what type of equation better fits the data, both a logarithmic and power law equation was fitted to each data set. Residual squared values were compared to indicate which form of equation better fit the data. These are shown in Table A3.

Table A3: Comparison of Residual Squared Values for Equation fits for Material P2B (Fit to All Static and Fatigue Data).

R- Value	Logarithmic fit	Power law fit
10	0.8407	0.8729
-2	0.9140	0.9161
-1	0.9301	0.9361
-0.5	0.8102	0.8422
0.1	0.8633	0.8740
0.5	0.7516	0.7766
Mean	0.8517	0.8697

The residual squared values in Table A3 show that the P2B data are better fit with a power law equation. Unlike the fiberglass materials, the fits were done for all of the data, both fatigue and static tests. Basing the 95/95 fit equations on stress as the distributed parameter at a defined

lifetime (Eq. 12-15), rather than distributed lifetime at a defined stress, allows the static data to be included in the fit, which appears justified for the P2B data since the parameter A in the mean fit (Table A4) is close to the ultimate tensile and compressive strengths (1564 MPa and -1047 MPa, respectively, Table 9). Mean fits are shown in Figure A5 and Figure A6. The fatigue sensitivity, B, is significantly lower for all R-values compared with the corresponding axial fiberglass data (Table A1).

Table A4: Fit Parameters for material P2B, axial direction (fit to all static and fatigue data).

R - Value	Static failure mode	95/95 Static strength, MPa	Mean fit parameters		95/95 Fit parameters	
			A	B	m	b-tol
10	Compression	914.2	1038.7	-0.0217	-0.0217	2.973
-2	Compression	914.2	1052.4	-0.0394	-0.0394	2.970
-1	Compression	914.2	1045.0	-0.0385	-0.0385	2.967
-0.5	Compression	914.2	1043.0	-0.0239	-0.0239	2.973
0.1	Tension	1301.1	1531.3	-0.0202	-0.0202	3.145
0.5	Tension	1301.1	1515.6	-0.0148	-0.0148	3.147

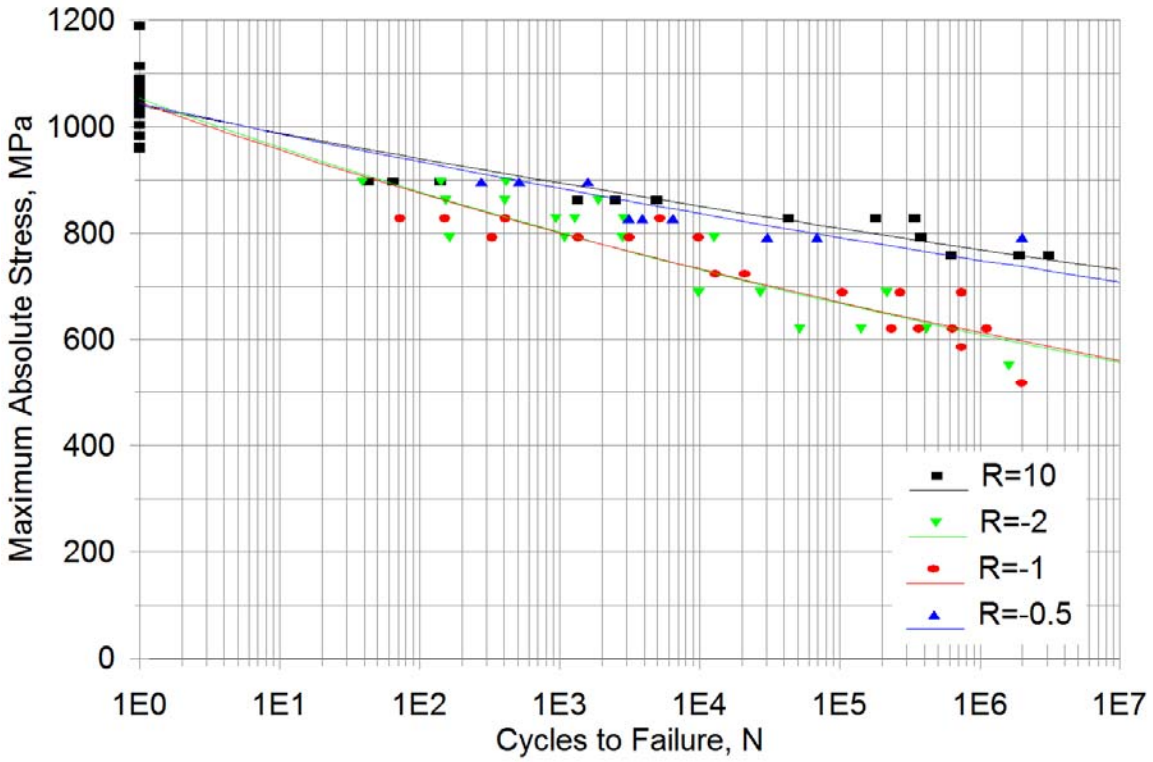

Figure A5: Compression and mixed fatigue, mean power law fits (material P2B, axial direction).

Of note in Figure A5 is the fact that tension dominated mixed fatigue (R = -0.5) data extrapolates to the compressive static strength, not the tensile static strength. Carbon fiber composites tend to show relative weakness to compression.

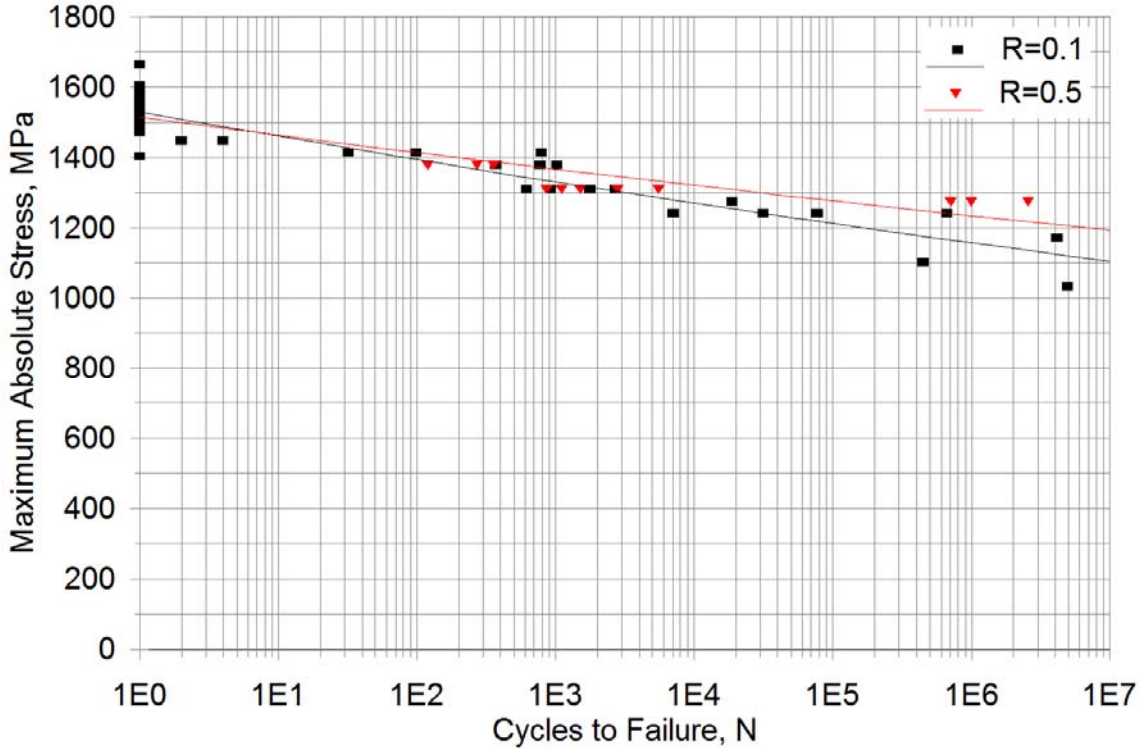

Figure A6: Tensile fatigue, mean power law fits (material P2B, axial direction).

A.1.4. Carbon/Glass Hybrid Laminate P2BT, Transverse Direction

Material P2BT test data show a distinct lower band of tension dominated failures and significantly higher compression performance. P2BT is modeled with a power law fit through the fatigue data only, with parameters given in Table A5 and fits shown in Figure A7 and Figure A8. Again, the fatigue sensitivity is lower than for the glass laminate, Table A2, although the strengths and modulus of the glass are higher, reflecting the different lay-ups and the backing strands in the glass fabric.

Table A5. Fit parameters for material P2BT in the transverse direction (fit to all fatigue data).

R- Value	Static failure mode	95/95 Static strength, MPa	Mean fit parameters		95/95 Fit parameters	
			A	B	m	b-tol
10	Compression	218.6	217.2	-0.0408	-0.0408	2.308
-2	Compression	218.6	170.5	-0.0856	-0.0856	2.189
-1	Tension	71.9	86.6	-0.0717	-0.0717	1.872
-0.5	Tension	71.9	82.5	-0.0689	-0.0689	1.838
0.1	Tension	71.9	81.8	-0.0518	-0.0518	1.846
0.5	Tension	71.9	87.9	-0.0423	-0.0423	1.869
0.7	Tension	71.9	80.1	-0.0214	-0.0214	1.856

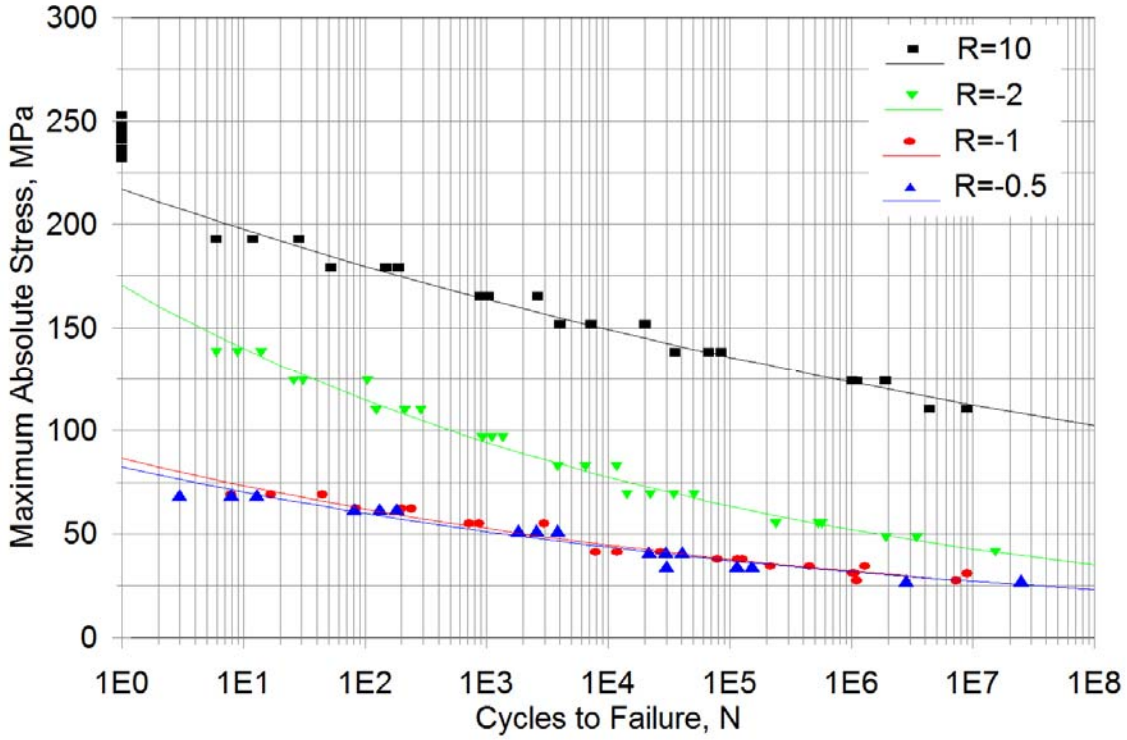

Figure A7: Compression and mixed fatigue, mean power law fits (material P2BT, transverse direction).

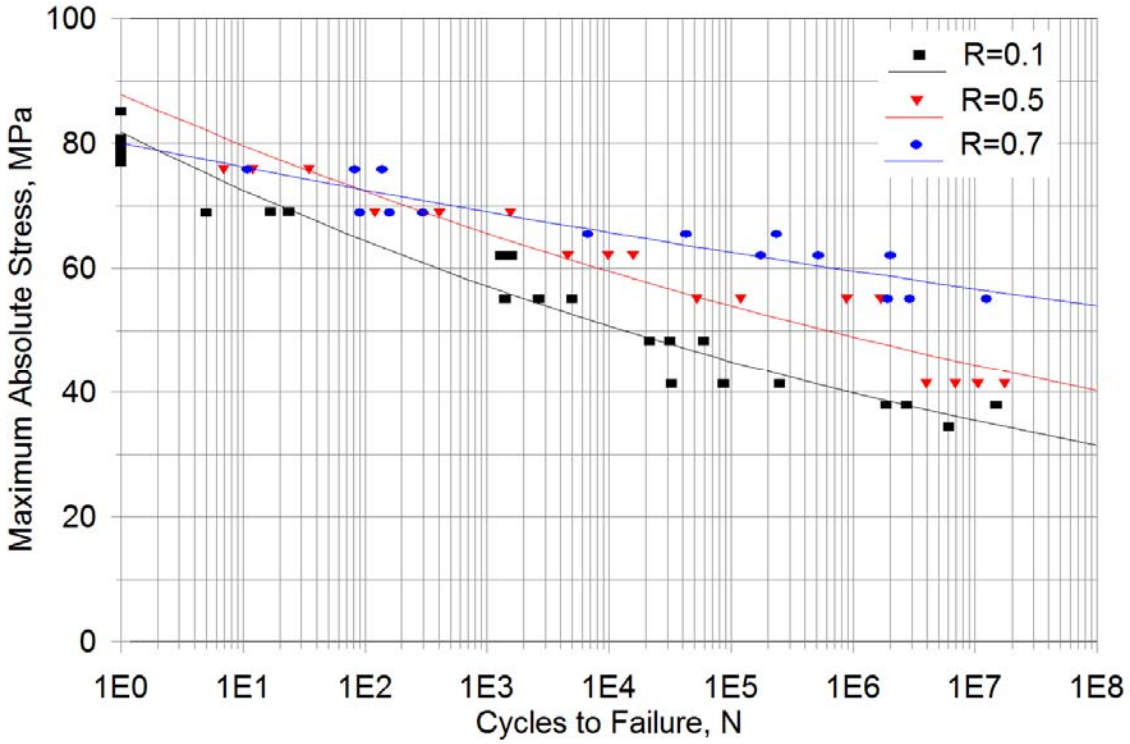

Figure A8: Tensile fatigue, mean power law fits (material P2BT, transverse direction).

A2. Constant Life Diagrams

A.2.1 CLD Construction

Composite materials generally have differing susceptibility to tension dominated and compression dominated fatigue loading, as is evident in the foregoing. A method of graphically displaying the fatigue life of a material at different ratios of mean and alternating stresses is the constant life diagram, also commonly known as a Goodman diagram.

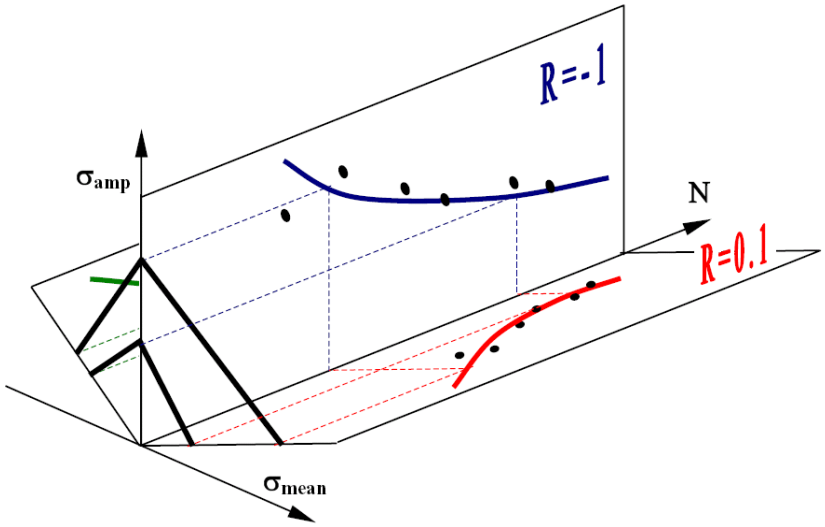

Figure A9: Schematic of the relationship between S-N curves and constant life diagrams [2]

Constant life diagrams (CLD's) for the materials considered in this study are displayed below. Each of these diagrams is normalized to the mean static tensile strength. Normalized mean stress is plotted on the abscissa and normalized alternating stress is on the ordinate. Figure A9 is a schematic showing the relationship of constant life diagrams to stress-life curves [2]. Each plane represents a stress-life curve at one R value; thus, the constant life diagram is a way to display fatigue data from many R values in one diagram. Radial lines mark the different R values. Constant life contours circumscribe the origin; a logarithmic decade of cycles to failure typically separates each one. The CLD can be used in design for assigning damage for each cycle in a load spectrum, from the mean stress and stress amplitude for that cycle.

Constant life diagrams representing both the mean life and 95/95 tolerance life are given for the materials in this report. Fatigue tests are generally run to the order of one million (10^6) cycles or less. The following constant life diagrams include extrapolations beyond this region. To differentiate, extrapolated life lines, on the order of 10^7 and 10^8 cycles, are shown as dotted lines in the diagrams. The extrapolation using fatigue models has not been validated for the specific laminates used in this study. Extrapolation of the 95/95 fits is particularly uncertain, but is a practical necessity in predicting the response under spectrum loading.

In general, the one cycle line is determined by the static model. In the case of the mean constant life diagram this is the mean UTS or UCS, while in the case of the 95/95 constant life diagram it is the 95/95 static tensile or compressive strength. In some cases the cyclic model would predict one cycle failure at a lower stress than determined by the static properties. In this case the one cycle line is plotted from the static data rather than the fatigue model. An exception to the use of the static model to determine the one cycle line is the stress rupture model used for material DD16. In this case, the lowest critical condition of the two models in [59] is used. The stress rupture model is based on a time under load criterion, and depending on the frequency used to predict failure, may predict failure at a lower stress than the static strength. The high ramp rates used in the static tests reduce the influence of the stress rupture phenomenon.

A.2.2 CLD for Fiberglass Laminate DD16, Axial Direction

Two constant life diagrams are shown in Figures A10 and A11 for material DD16 because of the influence of loading frequency on the tensile end of the diagram due to the inclusion of the stress rupture model described in Reference 59. Diagrams of 1 Hz and 10 Hz loading frequencies are included.

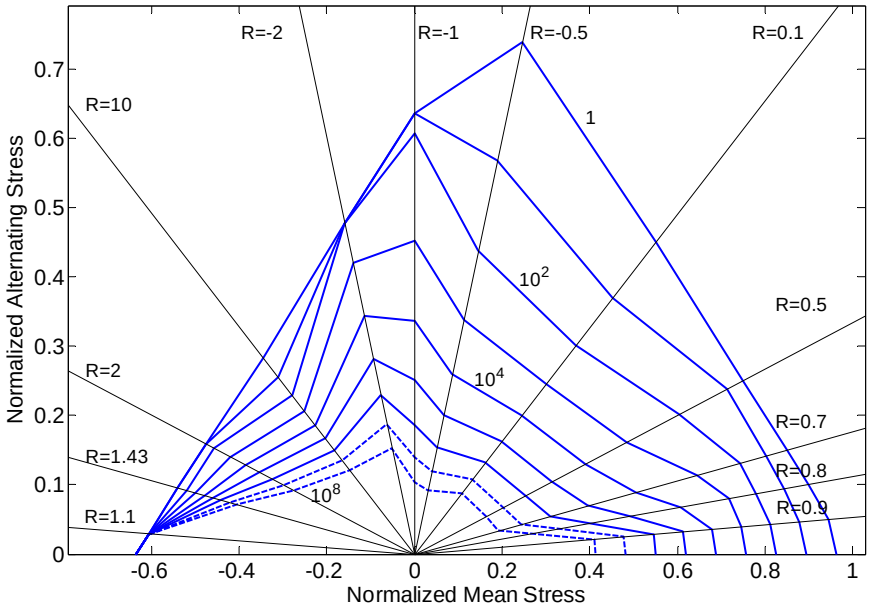

Figure A10: Mean axial constant life diagram for material DD16, 1 Hz frequency.

Figure A10, a constant life diagram for material DD16, shows results for a 1 Hz loading case. Note the difference between the 10 cycle life line in the region of positive normalized mean stress in this case, and the 10 Hz case, shown as Figure A11. The 10 Hz case more closely represents results found in the fatigue testing, as test frequencies tended to be closer to 10 Hz than to 1 Hz [6]. Figures A12 and A13 give the corresponding 95/95 CLD's.

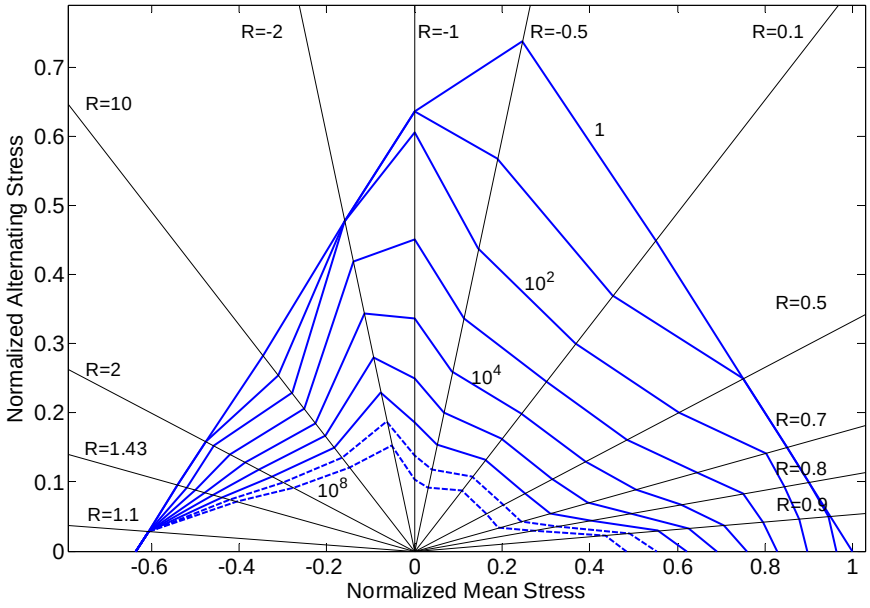

Figure A11: Mean axial constant life diagram for material DD16, 10 Hz frequency.

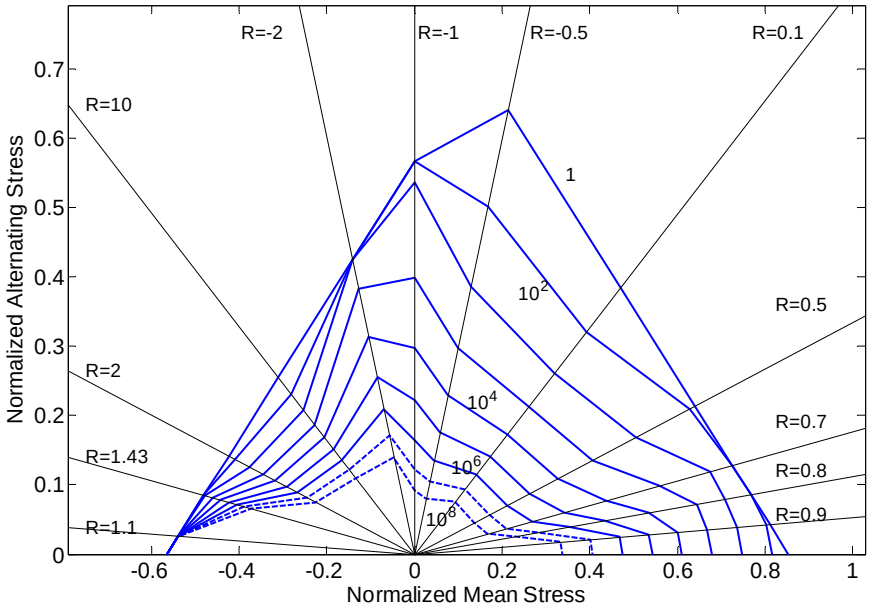

Figure A12: 95/95 Axial constant life diagram for material DD16, 1 Hz frequency.

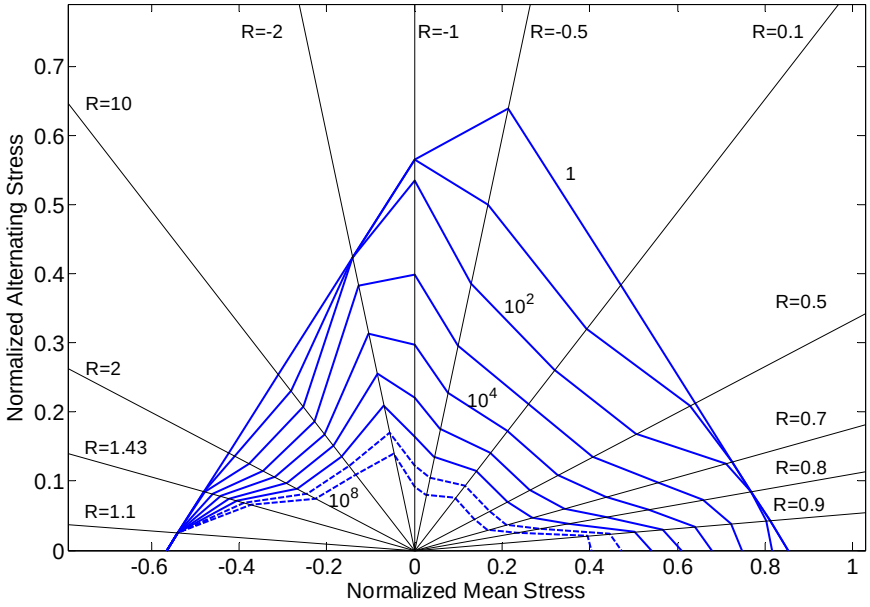

Figure A13: 95/95 Axial constant life diagram for material DD16, 10 Hz frequency.

A.2.3 CLD for Fiberglass Laminate QQ1, Axial Direction

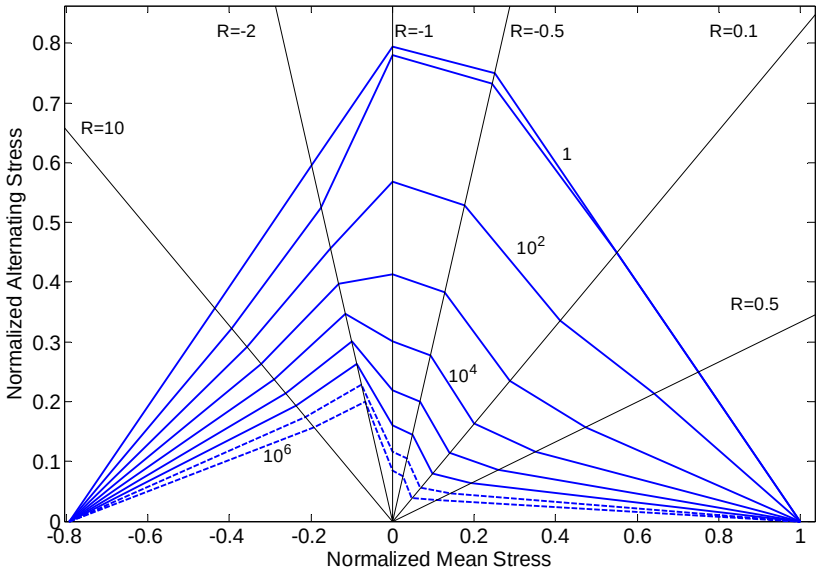

Figure A14. Mean axial constant life diagram for material QQ1.

The mean axial constant life diagram for material QQ1, Figure A14, shows that fatigue performance for this fiberglass composite is generally similar to the DD16. The higher fiber content material produces a more severe transition between the tension and compression dominated regimes. Thus, the damage done by a cycle with some amplitude is very sensitive to the mean stress at reversed loading R-values. Tension is much more damaging than compression at high cycles; much less so at low cycles. The CLD in Figure A14 is the most extreme known for any laminate in the tension-compression transition region [2, 5]. The 95/95 CLD in Figure A15 is also extreme in this respect, with very low mean and alternating stresses at high cycles. A measure of the extreme tensile fatigue sensitivity is the 95/95 maximum stress at 10^8 cycles for R = 0.1 of 64.8 MPa, which is only 7.5% of the mean UTS of 869 MPa.

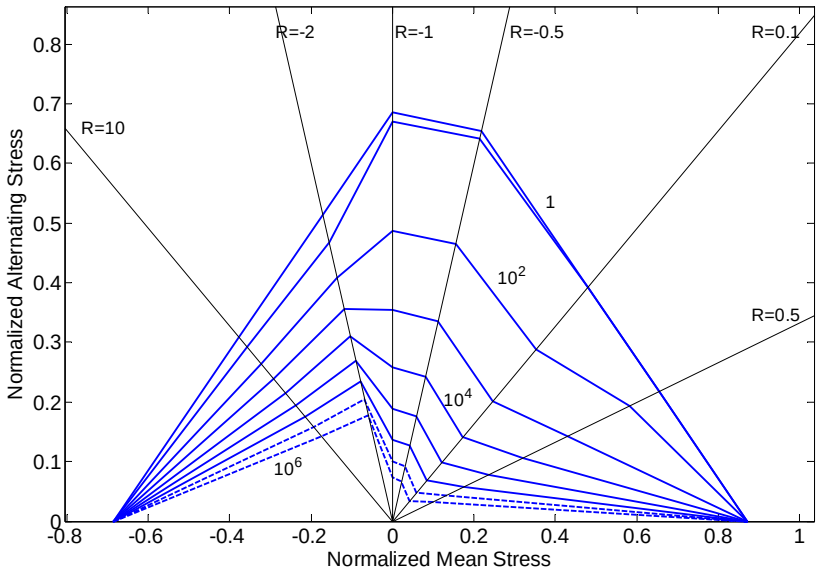

Figure A15: 95/95 Axial constant life diagram for material QQ1.

A.2.4 Fiberglass Laminate QQ1T, Transverse Direction

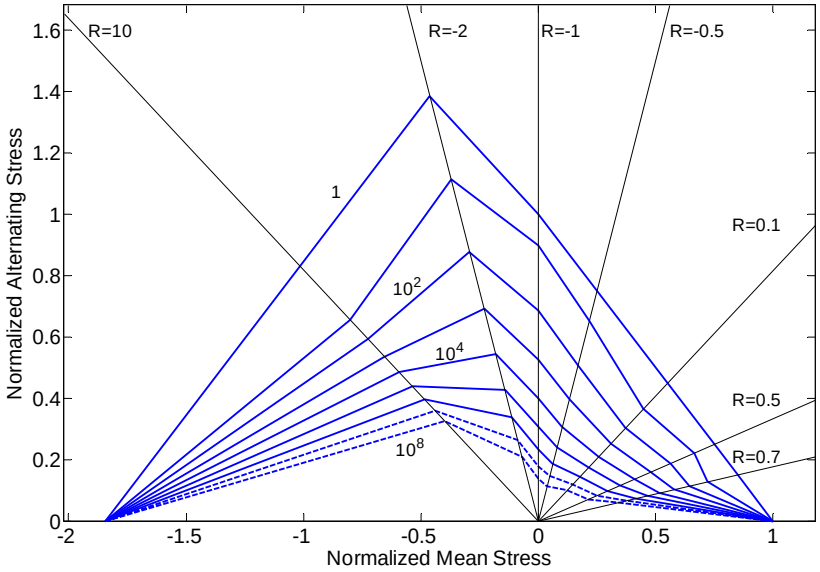

Figure A16: Mean transverse constant life diagram for material QQ1T.

The transverse constant life diagrams for fiberglass laminate QQ1T (Figure A16 and A17) are distorted toward higher strength and fatigue resistance in compression, as is typical for the transverse direction of composites. These results may be used to predict matrix cracking in blades, in combination with shear data which are not currently available.

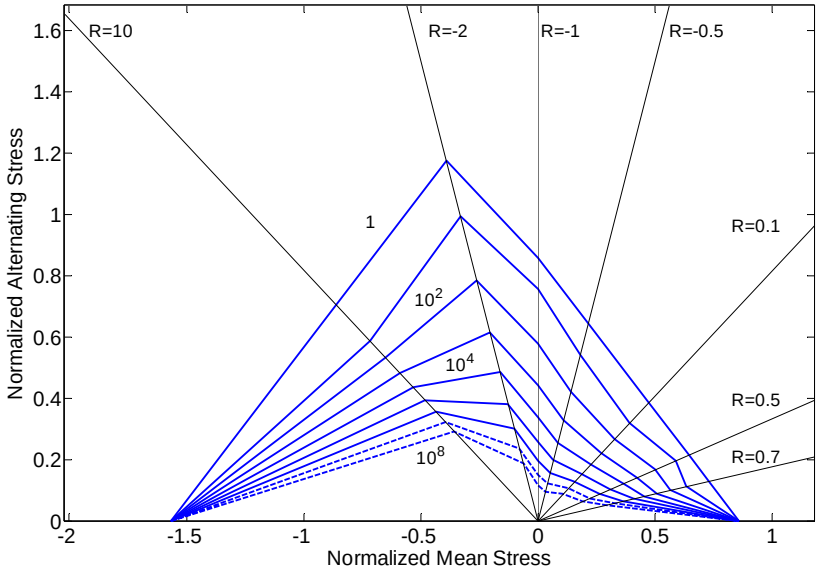

Figure A17: 95/95 Transverse constant life diagram for material QQ1T.

A.2.5 Axial Carbon/Glass Hybrid Laminate P2B

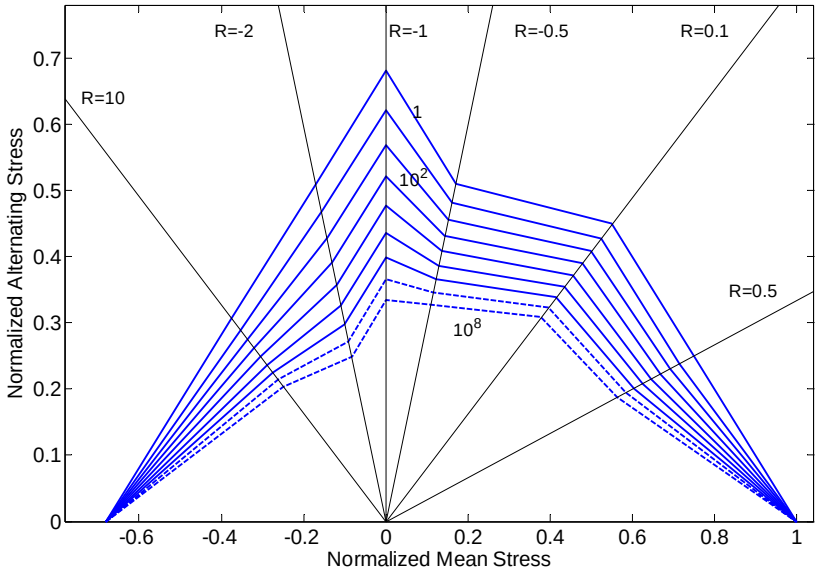

Figure A18: Mean axial constant life diagram for material P2B.

The constant life diagram for carbon fiber based material P2B in the axial direction (Figure A18 and A19) reflects a similar ratio of compression to tensile strength compared with fiberglass QQ1, but greatly improved fatigue resistance at all R values. The life lines between R = -0.5 and 0.1 show a mode change, but without the extreme distortion evident for QQ1. Compression drives the failure for R = -0.5 in P2B, which is tension dominated for QQ1. The greatest limitation with carbon in blades may be the much lower static ultimate compressive strains compared with glass, as discussed elsewhere [11].

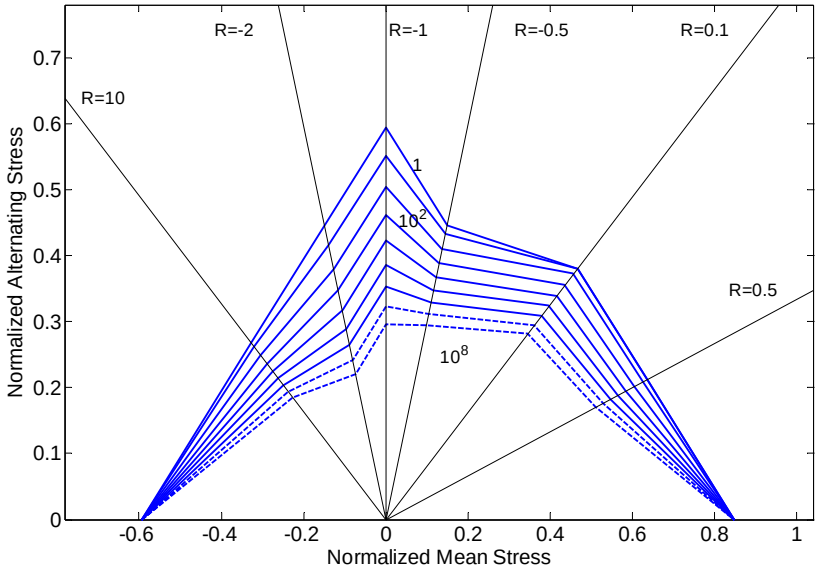

Figure A19: 95/95 Axial constant life diagram for material P2B.

A.2.6 Carbon/Glass Hybrid Laminate P2BT, Transverse Direction

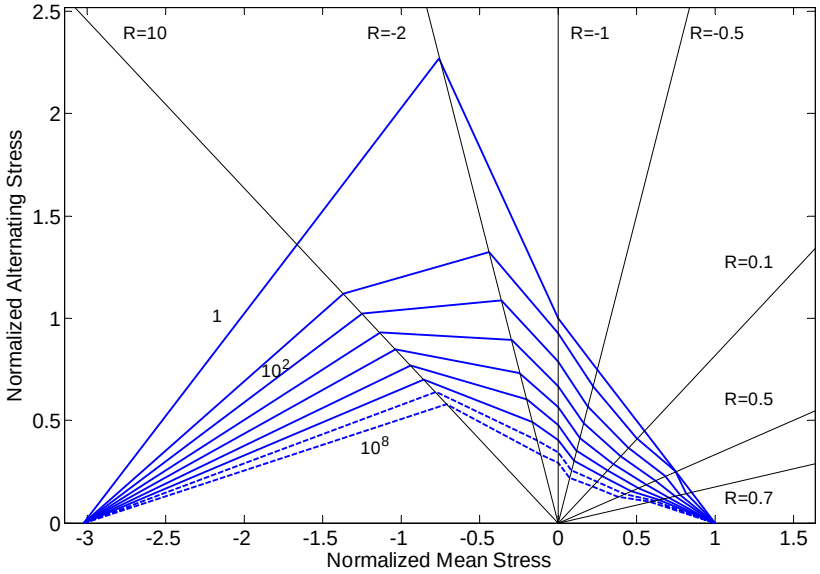

Figure A20: Mean transverse constant life diagram for material P2BT.

The mean constant life diagram of carbon based P2BT, shown in Figure A20, is similar in shape to that for fiberglass material QQ1T, also tested in the transverse direction. As noted earlier, QQ1T has higher strength values due to the different contents of plies in various directions and the higher transverse modulus for glass versus carbon.

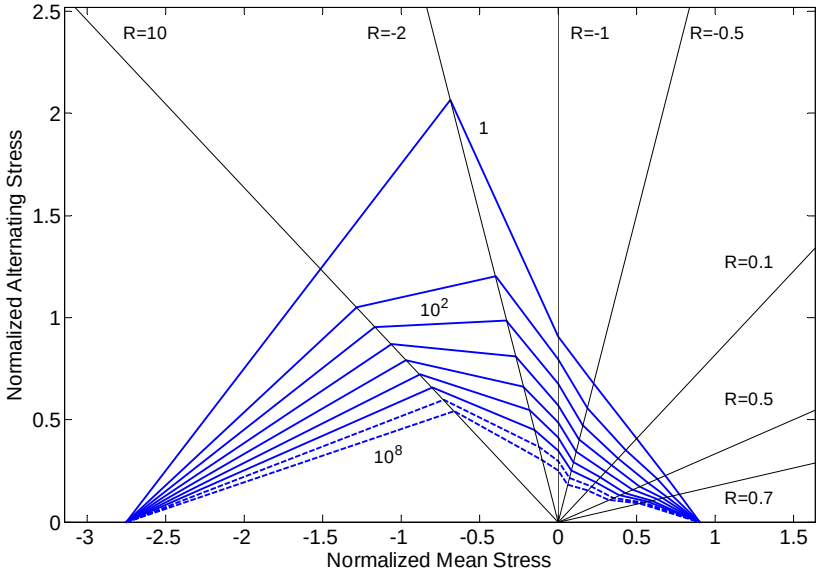

Figure A21: 95/95 Transverse constant life diagram for material P2BT.

DISTRIBUTION:

Cecelia Sterling (15)
Office of Wind and Hydropower Technologies
EE-2B Forrestal Building, U.S. DOE
1000 Independence Ave. SW
Washington, DC 20585

Warren Ault
LM Glasfiber ND Inc.
117 N. Jefferson Street, Suite 400
Chicago, IL 60661

Benjamin Bell
Garrad Hassan America, Inc.
45 Main Street, Suite 302
Peterborough, NH 03458

Keith Bennett
U.S. Department of Energy
Golden Field Office
1617 Cole Boulevard
Golden, CO 80401-3393

Derek Berry
TPI Composites, Inc.
373 Market Street
Warren, RI 02885-0328

Gunjit Bir
NREL/NWTC
1617 Cole Boulevard MS 3811
Golden, CO 80401

Garrett Bywaters
Northern Power Systems
182 Mad River Park
Waitsfield, VT 05673

Doug Cairns (3)
Montana State University
Dept. of Mechanical & Industrial Eng.
College of Engineering
Bozeman, MT 59717-3800

David Calley
Southwest Windpower
1801 West Route 66
Flagstaff, AZ 86001

Jamie Chapman
Texas Tech University
Wind Science & Engineering Research Center
Box 41023
Lubbock, TX 79409-1023

Joe Cohen
Princeton Economic Research, Inc.
1700 Rockville Pike, Suite 550
Rockville, MD 20852

C. Jito Coleman
Northern Power Systems
182 Mad River Park
Waitsfield, VT 05673

S. Finn
GE Global Research
One Research Circle, Rm. K1-3C12A
Niskayuna, NY 12309

Trudy Forsyth
NREL/NWTC
1617 Cole Boulevard MS 3811
Golden, CO 80401-3393

Brian Glenn
Clipper Windpower Technology, Inc.
6305 Carpinteria Ave. Suite 300
Carpinteria, CA 93013

Dayton Griffin
Global Energy Concepts, LLC
1809 7th Ave., Suite 900
Seattle, WA 98101

Thomas Hermann
Odonata Research LLC
2813 Wild Plum Ct.
Columbia, MO 65201-3520

D. Hodges
Georgia Institute of Technology
270 Ferst Drive
Atlanta, GA 30332

Adam Holman
USDA - Agricultural Research Service
PO Drawer 10
Bushland, TX 79012-0010

D.M. Hoyt
NSE Composites
1101 N. Northlake Way, Suite 4
Seattle, WA 98103

Scott Hughes
NREL/NWTC
1617 Cole Boulevard MS 3911
Golden, CO 80401

Kevin Jackson
Dynamic Design Engineering, Inc.
123 C Street
Davis, CA 95616

Jason Jonkman
NREL/NWTC
1617 Cole Boulevard
Golden, CO 80401

Gary Kanaby
Northern Powers Systems
NPS Blades
1313 Day Marina Drive
National City, CA 91950

Scott Larwood
1120 N. Stockton St.
Stockton, CA 95203

Wendy Lin
GE Global Research
One Research Circle
Niskayuna, NY 12309

Steve Lockard
TPI Composites, Inc.
8501 N. Scottsdale Rd.
Scottsdale, AZ 85253

James Locke
Collier Research Corp.
760 Pilot House Dr. Ste. A
Newport News, VA 23606

John F. Mandell (5)
Montana State University
302 Cableigh Hall
Bozeman, MT 59717

Steve Mikel
Suzlon Wind Energy Corporation
620 3rd Avenue SE
Pipestone, MN 56164

Walt Musial
NREL/NWTC
1617 Cole Boulevard MS 3811
Golden, CO 80401

Library (5) NWTC
NREL/NWTC
1617 Cole Boulevard
Golden, CO 80401

Byron Neal
USDA - Agricultural Research Service
PO Drawer 10
Bushland, TX 79012

Steve Nolet
TPI Composites, Inc.
373 Market Street
Warren, RI 02885-0367

Energy Research Centre of the Netherlands
T.S. Obdam
PO Box 1
1755 ZG Petten
The Netherlands

Tim Olsen
Tim Olsen Consulting
1428 S. Humboldt St.
Denver, CO 80210

Ian Prowell
University of California-San Diego
9500 Gilman Drive #0085
San Diego, CA 92093-0085

Jim Richmond
MDEC
3368 Mountain Trail Ave.
Newberg Park, CA 91320

Dan Samborsky
Montana State University
302 Cableigh Hall
Bozeman, MT 59717

Scott Schreck
NREL/NWTC
1617 Cole Boulevard MS 3811
Golden, CO 80401

Brian Smith
NREL/NWTC
1617 Cole Boulevard MS 3811
Golden, CO 80401

J. Sommer
Molded Fiber Glass Companies/West
9400 Holly Road
Adelanto, CA 92301

Fred Stoll
WebCore Technologies, LLC.
8821 Washington Church Rd.
Miamisburg, OH 45069

Herbert J. Sutherland
HJS Consulting
1700 Camino Gusto NW
Albuquerque, NM 87107-2615

Andrew Swift
Texas Tech University
Wind Science & Engineering Research Center
PO Box 41023
Lubbock, TX 79409-1023

Robert W. Thresher
NREL/NWTC
1617 Cole Boulevard MS 3811
Golden, CO 80401

Steve Tsai
Stanford University
Aeronautics & Astronautics
Durand Bldg. Room 381
Stanford, CA 94305-4035

Case P. van Dam
Dept. of Mechanical & Aeronautical Eng.
University of California, Davis
One Shields Avenue
Davis, CA 95616-5294

Jeroen van Dam
Windward Engineering
NREL/NWTC
1617 Cole Boulevard
Golden, CO 80401

Paul Veers
NREL/NWTC
1617 Cole Boulevard MS 3811
Golden, CO 80401

Kyle Wetzel
Wetzel Engineering, Inc.
PO Box 4153
Lawrence, KS 66046-1153

Mike Zuteck
MDZ Consulting
601 Clear Lake Road
Clear Lake Shores, TX 77565

Habib Dagher
Advanced Structures & Composite Center
University of Maine
5793 AEWC Bldg. Room 142
Orono, ME 04469-5793

Rogier Nijssen
Knowledge Centre WMC
PO Box 43
1770 AA Wieringerwerf
The Netherlands

Internal Distribution

MS 0346 T.J. Baca, 1523
MS 0372 J.M. Redmond, 1525
MS 0557 T.W. Simmermacher, 1523
MS 0557 D.T. Griffith, 1523
MS 1124 J.R. Zayas, 6120
MS 1124 T.D. Ashwill, 6121 (20)
MS 1124 M. Barone, 6121
MS 1124 D.E. Berg, 6121
MS 1124 J. Berg, 6122
S.M. Gershin, 6122 (Electronic)
MS 1124 R.R. Hill, 6122
MS 1124 R. Jepsen, 6122
MS 1124 W. Johnson, 6121
MS 1124 B. Karlson, 6121
MS 1124 D.L. Laird, 6121
MS 1124 B. Lucero, 6121
MS 1124 B. McKenney, 6121
MS 1124 A. Ogilvie, 6121
MS 1124 J. Paquette, 6121
MS 1188 V. Peters, 6121
MS 1124 B. Resor, 6121
MS 1124 J. Roberts, 6122
MS 1124 M.A. Rumsey, 6121
MS 1124 J. White, 6121
MS 1108 D. Wilson, 6122
Technical Library, 9536 (Electronic)
MS 1124 Wind Library, 6121 (20)
MS 9018 Central Technical Files, 8945-1